



# Optimisation de la modélisation RANS d'écoulements cavitants

Xinlei Zhang

## ► To cite this version:

Xinlei Zhang. Optimisation de la modélisation RANS d'écoulements cavitants. Autre. Ecole nationale supérieure d'arts et métiers - ENSAM, 2019. Français. NNT : 2019ENAM0060 . tel-02611790

**HAL Id: tel-02611790**

**<https://pastel.hal.science/tel-02611790>**

Submitted on 18 May 2020

**HAL** is a multi-disciplinary open access archive for the deposit and dissemination of scientific research documents, whether they are published or not. The documents may come from teaching and research institutions in France or abroad, or from public or private research centers.

L'archive ouverte pluridisciplinaire **HAL**, est destinée au dépôt et à la diffusion de documents scientifiques de niveau recherche, publiés ou non, émanant des établissements d'enseignement et de recherche français ou étrangers, des laboratoires publics ou privés.

École doctorale n° 432 : Sciences des Métiers de l'ingénieur

**Doctorat ParisTech**

**T H È S E**

pour obtenir le grade de docteur délivré par

**l'École Nationale Supérieure d'Arts et Métiers**

**Spécialité “ Génie énergétique ”**

*présentée et soutenue publiquement par*

**Xinlei ZHANG**

le 16 Décembre 2019

**Optimisation de la Modélisation RANS D'écoulements Cavitants**

Directeur de thèse : **Olivier COUTIER-DELGOSHA**

Co-encadrement de la thèse : **Thomas GOMEZ**

**Jury**

**Mme. Paola CINNELLA**, Professeur, Arts et Métiers ParisTech

**M. Pietro Marco CONGEDO**, Professeur, INRIA

**M. Jean-Camille CHASSAING**, Professeur, Sorbonne Université

**M. Marcello MELDI**, Maître de conférences,

Ecole Nationale Supérieure de Mécanique et d'Aérotechnique (ENSMA)

**M. Heng XIAO**, Professeur, Virginia Tech

**M. Thomas GOMEZ**, Professeur, Université de Lille

**M. Olivier COUTIER-DELGOSHA**, Professeur, Arts et Métiers ParisTech / Virginia Tech

Président

Rapporteur

Rapporteur

Examineur

Examineur

Examineur

Examineur

**T  
H  
È  
S  
E**

# Acknowledgements

First of all, I would express my heartfelt gratitude to my supervisors. I am extremely grateful to Prof.Olivier Coutier-Delgosha for accepting and trusting me to work on this project. I thank him for the persistent guidance and support during the past three years. His academic enthusiasm and encouragement kept me constantly engaged with this work. At the same time, I warmly thank my co-supervisor, Prof.Thomas Gomez, not only for his guidance on my research, but also for his kindness and patience. Also, I would like to express my sincere appreciation to Prof.Heng Xiao for advising my work. He shared his knowledge and research experience without any hesitate, and I have benefited profoundly from my association with him.

I sincerely thank Prof.Paola Cinnela, Prof.Pietro Marco Congedo, Prof.Jean-Camille Chassaing, and Prof.Marcello Meldi for joining my jury and providing me helpful suggestions for my thesis and future works. I would like to give special thanks to Prof.Congedo and Prof.Chassaing for being the reporters of this thesis.

I am also thankful for the other collaborators. I thank Mr.Carlos Michelen-Strofer for fruitful discussions on our collaborated works and giving me a lot of tips about coding. Thanks to Dr.Ilyass Khelifa for providing me experimental data of non-cavitating flows. Thanks to Mr.Guangjian Zhang for providing me the X-ray experimental data of cavitating flows.

My appreciation extends to all colleagues at Arts et Métiers ParisTech and Virginia Tech for beneficial discussions on this work and their help in my life, especially, Mr.Yuzhi Li, Mr.Lei Shi, Mr.Ben Zhao, Mr.Zhongshu Ren, Mr.Yang Zeng, Dr.Jinlong Wu, Dr.Guangyao Wang, Dr.Yaguang Heng, Mr.Alberto Baretter, Mr.Kunpeng Long.

At last, I would like to express my deepest gratitude to my parents for their supports and sacrifices.





# Table of Contents

	Page
List of Tables	vii
List of Figures	ix
<b>1 Introduction</b>	<b>1</b>
<b>2 Review of Data Assimilation Methods</b>	<b>17</b>
2.1 Introduction . . . . .	17
2.2 Data assimilation problem statement . . . . .	17
2.3 Variational data assimilation method . . . . .	19
2.4 Kalman filter . . . . .	19
2.5 Ensemble-based data assimilation methods . . . . .	20
2.5.1 Ensemble Kalman filter . . . . .	21
2.5.2 Ensemble randomized maximum likelihood . . . . .	22
2.5.3 Ensemble Kalman filter with multiple data assimilation . . . . .	23
2.6 Hybrid data assimilation methods . . . . .	23
2.6.1 Hybrid methods . . . . .	23
2.6.2 Ensemble-based variational methods . . . . .	24
2.6.3 Iterative ensemble Kalman filter . . . . .	25
2.7 Particle filtering . . . . .	26
<b>3 Optimization of RANS Simulation with EnVar Method</b>	<b>29</b>
3.1 Introduction . . . . .	29
3.2 Data assimilation framework . . . . .	31
3.2.1 Ensemble-based variational scheme . . . . .	31
3.2.2 Fitting criterion . . . . .	33
3.3 Numerical setup . . . . .	34
3.3.1 CFD solver . . . . .	34
3.3.2 Data assimilation implementation . . . . .	34

## TABLE OF CONTENTS

---

3.4	Inlet velocity inference . . . . .	35
3.4.1	WallTurb Bump . . . . .	35
3.4.2	Venturi . . . . .	39
3.5	Model correction . . . . .	42
3.5.1	Correction in $k$ equation . . . . .	43
3.5.2	Correction in $\omega$ equation . . . . .	45
3.5.3	Correction in $k$ and $\omega$ equation . . . . .	48
3.6	Conclusion . . . . .	51
<b>4</b>	<b>Regularization of Ensemble Kalman Method</b>	<b>55</b>
4.1	Introduction . . . . .	55
4.1.1	Adjoint- vs. ensemble-based inversion methods . . . . .	56
4.1.2	Ill-posedness and regularization of inverse problems . . . . .	58
4.1.3	Related works and contributions of present work . . . . .	59
4.2	Methodology . . . . .	61
4.2.1	Equivalence between optimization and maximum a posteriori approaches	61
4.2.2	Derivation of the regularized ensemble Kalman method . . . . .	62
4.2.3	Implementing regularization procedure for an iterative ensemble Kalman method . . . . .	64
4.2.4	Generality and possible extensions to other ensemble Kalman methods .	67
4.3	Results . . . . .	67
4.3.1	Parameter estimation . . . . .	68
4.3.2	Field inversion . . . . .	73
4.3.3	RANS equations closure . . . . .	79
4.4	Conclusion . . . . .	84
<b>5</b>	<b>Iterative Ensemble Methods for UQ Problem</b>	<b>87</b>
5.1	Introduction . . . . .	87
5.1.1	Bayesian uncertainty quantification for CFD . . . . .	87
5.1.2	Ensemble-based data assimilation methods . . . . .	89
5.1.3	Objective of the present work . . . . .	90
5.2	Ensemble-based data assimilation methods . . . . .	90
5.2.1	Minimization problem . . . . .	91
5.2.2	EnKF . . . . .	92
5.2.3	EnRML . . . . .	93
5.2.4	EnKF-MDA . . . . .	93
5.2.5	Remarks . . . . .	94
5.3	Scalar case . . . . .	96
5.3.1	Problem statement . . . . .	96

5.3.2	Results . . . . .	97
5.4	RANS equation . . . . .	101
5.4.1	Problem statement . . . . .	101
5.4.2	Methodology . . . . .	102
5.4.3	Case details . . . . .	103
5.4.4	Results . . . . .	104
5.5	Conclusion . . . . .	106
<b>6</b>	<b>Towards for Cavitation</b>	<b>109</b>
6.1	Introduction . . . . .	109
6.2	Governing equations . . . . .	111
6.2.1	Turbulence models . . . . .	112
6.2.2	Reboud correction . . . . .	114
6.2.3	Phase model . . . . .	115
6.3	Numerical evaluation of current SST-based models . . . . .	116
6.3.1	Numerical setup . . . . .	116
6.3.2	Comparison results . . . . .	117
6.3.3	Discussion . . . . .	119
6.4	Modified Reboud correction . . . . .	123
6.5	Validation . . . . .	126
6.6	Conclusion . . . . .	128
<b>7</b>	<b>Conclusions and Perspectives</b>	<b>131</b>
7.1	Conclusions . . . . .	131
7.2	Perspectives . . . . .	132
<b>A</b>	<b>Comparison of optimization methods and test case in Venturi with EnVar method</b>	<b>135</b>
A.1	Comparison between BFGS and Newton-CG . . . . .	135
A.2	Test case of inlet velocity inference in Venturi . . . . .	136
<b>B</b>	<b>Derivation of REnKF and sensitivity study of algorithmic parameters</b>	<b>139</b>
B.1	Derivation of regularized ensemble Kalman method . . . . .	139
B.2	Sensitivity studies of algorithmic parameters in regularization . . . . .	141
<b>C</b>	<b>Derivation of EnKF and EnRML</b>	<b>143</b>
C.1	Derivation of EnKF . . . . .	143
C.2	Derivation of EnRML . . . . .	144
<b>D</b>	<b>List of publications</b>	<b>147</b>

## TABLE OF CONTENTS

---

<b>Bibliography</b>	<b>149</b>
---------------------	------------

# List of Tables

Table	Page
3.1 Data assimilation results for inlet velocity inference . . . . .	35
3.2 Summary of DA experiments for model correction inference . . . . .	43
4.1 Summary of the constraints used in the parameter estimation problem. . . . .	70
4.2 Results of the baseline and regularized inference with different constraints. . . . .	71
5.1 Schematic comparison of EnKF, EnRML and EnKF-MDA . . . . .	95
6.1 Summary of simulation results with different turbulence model with comparison to the experiments . . . . .	117
6.2 Summary of slope of cavitating mixing layer for four different flow condition with comparison of experimental data and the results of fitting formula. . . . .	125
B.1 Summary of inferred parameter $\omega$ with different $\chi_0$ , $S$ , and $d$ for the equality constraint (Case C1) in the parameter estimation problem. The values in bold indicate the reference. . . . .	141
B.2 Summary of inferred parameter $\omega$ with different $\chi_0$ , $S$ , and $d$ for the inequality constraint (Case C2) in the parameter estimation problem. The values in bold indicate the reference. . . . .	142



# List of Figures

Figure	Page
1.1 Examples of cavitation effects in hydraulic machinery. Adopted from [33] . . . . .	2
1.2 The different cavitation patterns. Adopted from [6, 17, 110] . . . . .	3
1.3 Road map of the thesis . . . . .	6
1.4 Exemples d'effets de cavitation dans les machines hydrauliques. Extrait de [33] . .	10
1.5 Les différents modèles de cavitation. Extrait de [6, 17, 110] . . . . .	11
1.6 Feuille de route de la thèse . . . . .	15
3.1 Schematic illustration of EnVar method . . . . .	33
3.2 Mesh of WallTurb Bump . . . . .	36
3.3 Data assimilation results about the inferred inlet velocity and the prediction in $C_f$ : (a) (b) for the prior of parabolic velocity; (c) (d) for the prior of flat velocity . . .	38
3.4 Data assimilation results of cost function $J$ and $J_{ob}$ : (a)(b) for the prior of parabolic inlet velocity; (c)(d) for the prior of flat inlet velocity . . . . .	38
3.5 Velocity $U$ field with the first guess of parabolic velocity for prior(a), posterior(b) and DNS(c) . . . . .	39
3.6 Mesh of the Venturi-type section . . . . .	40
3.7 Data assimilation results of velocity at inlet(a) and velocity at $x = 0.0008m$ (b) . .	41
3.8 Data assimilation results of cost function $J$ (a) and $J_{ob}$ (b) . . . . .	41
3.9 Velocity $u$ field for prior(a), posterior(b) and experiment(c) . . . . .	42
3.10 Variance $\sigma(x)$ of $\beta_c$ in TKE transport equation . . . . .	44
3.11 Data assimilation results of cost function $J$ (a) and $J_{ob}$ (b) . . . . .	45
3.12 Comparison in velocity $u$ (a) and TKE (b) along profiles among prior, posterior and experiment . . . . .	46
3.13 Inferred $\beta_c$ profiles . . . . .	47
3.14 variance $\sigma(x)$ of $\beta_c$ in $\omega$ transport equation . . . . .	47
3.15 data assimilation results in cost function $J$ (a) and $J_{ob}$ (b) . . . . .	47
3.16 Comparison in velocity $u$ (a) and TKE (b) along profiles among prior, posterior and experiment . . . . .	49
3.17 Inferred $\beta_c$ profiles . . . . .	50

3.18	Data assimilation results of cost function $J(a)$ and $J_{ob}$ (b) . . . . .	50
3.19	Comparison in velocity $u$ (a) and $k$ (b) along profiles among prior, posterior and experiment . . . . .	51
3.20	Inferred $\beta_c$ profiles in $k$ equation . . . . .	52
3.21	Inferred $\beta_c$ profiles in $\omega$ equation . . . . .	52
3.22	Contour plots of velocity $u$ (first column) and TKE (second column): (a)(b) prior; (c)(d) posterior with correction in $k$ transport equation; (e)(f) posterior with correction in $\omega$ transport equation; (g)(h) posterior with correction in both $k$ and $\omega$ transport equation; (i)(j) experiment . . . . .	53
4.1	Schematics of ensemble Kalman methods by using ensemble Kalman filtering (EnKF) as example. The proposed regularization scheme consists of an additional correction $\delta$ , defined in Eq. (4.17), to the forecast states $\mathbf{x}^f$ before the Kalman correction. Such a correction enforces constraints and is equivalent to penalty term $\lambda \ \mathcal{G}[\mathbf{x}]\ _{\mathbf{W}}^2$ in adjoint methods as in Eq. (4.11). Our contribution that differentiates the present method to baseline ensemble Kalman methods is highlighted in red/grey box. The Kalman correction in the regularized EnKF has the identical form as that in standard EnKF except that it acts on the pre-corrected states $\tilde{\mathbf{x}}^f$ . . . . .	65
4.2	Contour plot of the discrepancy $J[\omega]$ . The two groups of local minimums are indicated with the red/gray cross “+” (Group I) and the red/gray circle (Group II). . . . .	70
4.3	Results of paramter estimation problem using the baseline and proposed regularized methods with different constraints. For all methods three different prior means (green/gray dots) are considered. (a) Baseline case; (b) Case C2: proposed method with $G[\omega] = h_1[\omega]$ where penalty function is indicated by the black straight line ; (c) Case C2: proposed method with $G[\omega] = \phi[h_{in1}[\omega]]$ . The blue/gray region indicates where the constraint is inactive; (d) Case C3: proposed method with $G[\omega] = \phi[h_{in1}[\omega]] + \phi[h_{in2}[\omega]]$ . The blue/gray region indicates where the constraint is inactive. With the baseline method, different priors converge to the different local minima. With the proposed regularized method all priors can converge to the true local minimum (1, 1), indicated as blue/gray triangle. . . . .	72
4.4	First 5 KL modes in the diffusion case scaled by their corresponding eigenvalues. . . . .	75
4.5	<b>Prior samples</b> of diffusivity $\mu$ (top) and corresponding output fields $u$ (bottom) for different number of modes. . . . .	76
4.6	Inferred diffusivity by using the <b>baseline methods</b> (left column; panels a, b, and d) and the <b>proposed regularized methods</b> (right column; panels c and e) for different number of modes. . . . .	77
4.7	Comparison of inferred KL coefficients for <b>the diffusion case</b> by using the baseline method and the regularized method with 20 modes. . . . .	78



4.8	Errors in the inferred diffusivity in <b>the diffusion case</b> for the baseline method and the regularized methods as a function of number of modes used in the field representation. . . . .	78
4.9	Contour plots of first 8 modes from KL decomposition for the periodic hills case. The modes are scaled by their corresponding eigenvalues. . . . .	80
4.10	Prior realizations of eddy viscosity $\nu_t$ and propagated streamwise velocity $U_1$ for the periodic hills case. The locations of the observations are indicated by crosses ( $\times$ ). . . . .	81
4.11	Inferred eddy viscosity field and propagated streamwise velocity field for the baseline and regularized methods using 200 modes. . . . .	82
4.12	Contour plots of the inferred (posterior) eddy viscosity $\nu_t$ with with the baseline and regularized methods using 200 modes. . . . .	83
4.13	Magnitudes of the inferred KL coefficients for the periodic hills case using the baseline and regularized methods with 200 modes. . . . .	83
4.14	Error in the inferred eddy viscosity in the <b>periodic hill case</b> by using the baseline and regularized methods as a function of the number of modes used in the field representation. Note that a logarithmic scale is used for the errors. . . . .	84
5.1	Schematic of Bayesian uncertainty quantification. Bayesian approach can combine the prior information (red dashed line) and the data to quantify the posterior uncertainty (blue solid line) in the quantities of interest as well as the input. . . .	88
5.2	Joint PDFs with <b><math>10^6</math> samples</b> in comparison of Bayes, EnKF, EnRML, and EnKF-MDA for the scalar case. . . . .	98
5.3	Marginal PDFs for $x$ with <b><math>10^6</math> samples</b> in comparison of EnKF, EnRML, EnKF-MDA, and Bayes for the scalar case. . . . .	98
5.4	Joint PDFs with <b><math>10^2</math> samples</b> in comparison of Bayes, EnKF, EnRML, and EnKF-MDA for the scalar case . . . . .	99
5.5	Marginal PDFs for $x$ with <b><math>10^2</math> samples</b> in comparison of EnKF, EnRML, EnKF-MDA, and Bayes for the scalar case. . . . .	99
5.6	Results of prior joint PDF with large ( $10^6$ ) and small ( $10^2$ ) ensemble size for the scalar case . . . . .	100
5.7	Comparison of analytic gradient and ensemble gradient. The light/pink shaded region represents analytic gradient and the dark/blue shaded region represents ensemble gradient. (a): $10^6$ samples; (b): $10^2$ samples . . . . .	101
5.8	Prior ensemble realization of velocity profiles at 8 locations, in comparison to DNS and baseline. The location of observation is indicated with crosses( $\times$ ). . . . .	104
5.9	Data assimilation Results with EnKF, EnRML, and EnKF-MDA in comparison to baseline and DNS for the turbulent flow in a periodic hill. . . . .	105

5.10	The 95% credible intervals of the prior (light/pink shaded region) and posterior (dark/blue shaded region) samples of velocity profiles for the turbulent flow in a periodic hill . . . . .	107
6.1	a cycle of cavitation behaviour . . . . .	114
6.2	Plot of the Reboud correction function . . . . .	115
6.3	Plot of barotropic state law for the mixture . . . . .	116
6.4	The geometry of the Venturi-type section. The red, numbered line in the enlarged window indicate the profiles for comparison. . . . .	117
6.5	Time evolution of cavity shape with different turbulence models. The color indicate the minimum void fraction in each cross section, from the Venturi throat. . . . .	118
6.6	Shape of time-averaged cavity. . . . .	119
6.7	The contour plots of time-averaged turbulent kinetic energy with different turbulence models compared to the experiments. . . . .	120
6.8	Comparison in turbulent kinetic energy between the different turbulent models and experiments with Reboud correction along profiles. . . . .	120
6.9	Time-averaged Reynolds shear stress with Reboud correction. . . . .	121
6.10	Comparison in Reynolds shear stress between the different turbulent models and experiments with Reboud correction. . . . .	121
6.11	time-averaged Reynolds shear stress without Reboud correction. . . . .	122
6.12	Comparison in Reynolds shear stress between the different turbulence models and experiments without Reboud correction. . . . .	122
6.13	The schematic of two measured window for comparison . . . . .	124
6.14	The comparison of the Reboud correction with $n = 10$ (red line), the Bradshaw assumption with $c = 0.1$ (blue line) and experimental data (grey dots) . . . . .	124
6.15	Fitting slope of the cavitating mixing layer . . . . .	125
6.16	Experimental comparison at window 1. Red line: the Reboud correction with $n = 10$ ; blue line: the Bradshaw assumption with $c = 0.1$ ; grey dots: experimental data; blue dots: modified Reboud correction. . . . .	126
6.17	Experimental comparison at window 2: Red line: the Reboud correction with $n = 10$ ; blue line: the Bradshaw assumption with $c = 0.1$ ; grey dots: experimental data; blue dots: modified Reboud correction. . . . .	127
6.18	Numerical comparison of the modified Reboud correction with experiment and original Reboud correction in Reynolds shear stress. . . . .	127
6.19	Comparison in velocity and density with modified Reboud correction and original Reboud correction. . . . .	128
7.1	The schematic diagram of data-driven modeling with data assimilation and machine learning . . . . .	133

A.1	evolution of cost function between BFGS and Newton-CG. left: with parabolic inlet velocity; right: with flat inlet velocity . . . . .	135
A.2	Results in inference of inlet velocity and prediction in $C_f$ : (a) (b) for prior parabolic velocity; (c)(d) for prior flat velocity . . . . .	136
A.3	Data assimilation results to infer the inlet velocity in Venturi . . . . .	137



# Chapter 1

## Introduction

Hydrodynamic cavitation in liquid flows is partial vaporization observed when the liquid experiences an abrupt pressure drop. This phenomenon affects high-speed internal flows in rotating machinery, external flows on fast marine vehicles, and, more generally, any hydraulic system where the flow is submitted to local accelerations. Cavitation is obtained in various application areas, such as propellers and appendices of high speed ships or submarines in ocean engineering, pumps of nuclear plants and space rocket cryogenic engines, and hydraulic dams. Major detrimental effects of cavitation in these applications include a loss of efficiency and the inception of instabilities, vibrations, noise, and erosion. Instabilities are mostly generated by the adverse pressure gradient in the wake of cavitation, which induces large-scale secondary flows and shedding of bubble clouds. The collapse of these bubbles generates a combination of pressure waves and micro-jets that repeatedly impact the walls of the hydraulic device, which is responsible for the noise and the erosion. On the other hand, cavitation can also have positive effects in diverse contexts. For instance, cavitation generated at the tip of underwater vehicles is used to create a layer of gas between the walls and the liquid flow, which strongly reduces the friction coefficient. It results in a significant drop of the drag that noticeably increases the vehicle speed. Cavitation can also be used for lithotripsy via the shock pulse produced by the collapse of cavitation bubble clusters. To benefit from this phenomenon through preventing the negative effects as well as triggering the positive ones, we have to gain insights into the physical mechanisms and thus control the behavior of cavitation. Some examples of cavitation effects are shown in Fig. 1.1.

The experimental measurements and numerical simulations are common tools to investigate cavitating flows. Experiments in multiphase flows with high void fraction, like cavitating flows, are generally challenging: non-intrusive measurements based on optical imaging, like particle image velocimetry (PIV), are made difficult by the opacity of the liquid/vapor mixture, and the strong reflection of any incident light on the cavitation bubbles. Specific techniques have to be used, like the use of fluorescent particles in PIV, or X-ray imaging instead of optical imaging. The cost and the complexity of such experiments make numerical simulations very appealing as

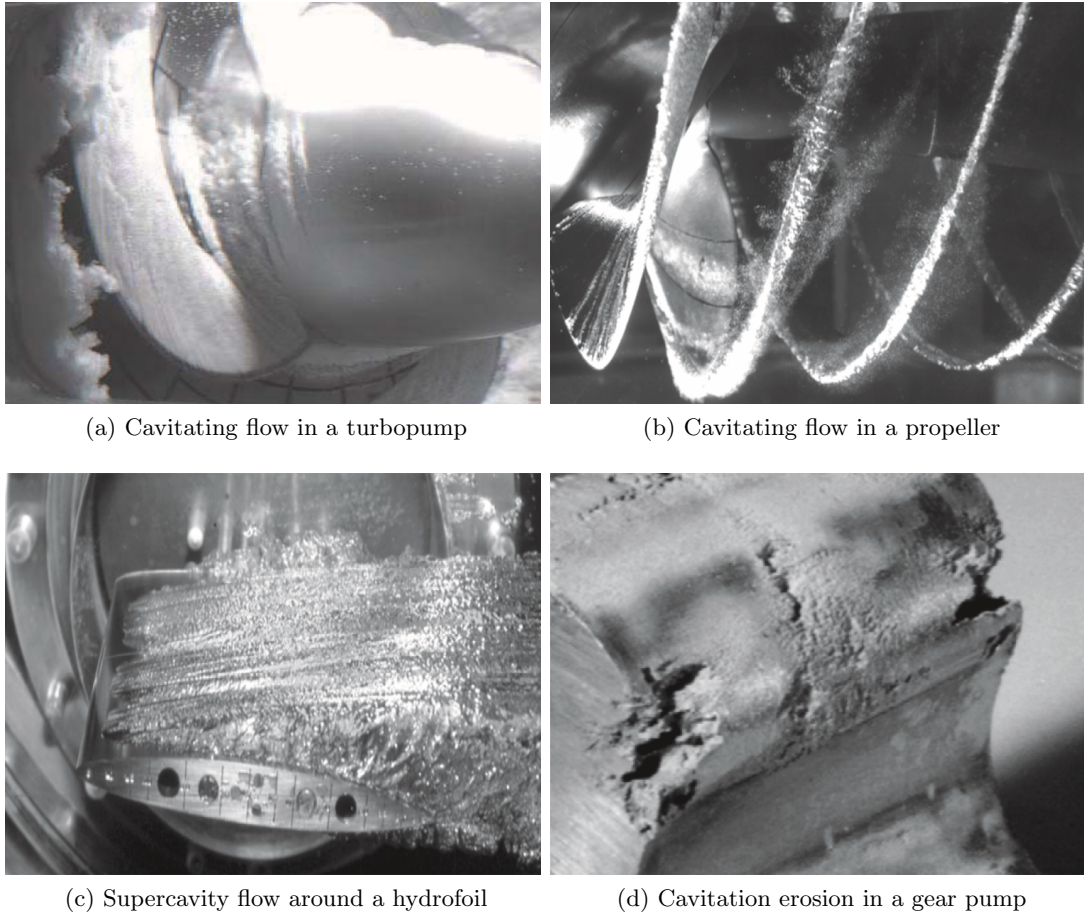


Figure 1.1: Examples of cavitation effects in hydraulic machinery. Adopted from [33]

a complementary approach to investigate the physics of this phenomenon.

To numerically simulate the turbulent cavitating flow, the most common approach is to couple the Reynolds averaged Navier–Stokes (RANS) method with cavitation or phase change models. High-fidelity turbulence methods, such as large eddy simulation (LES) and direct numerical simulation (DNS), have also been introduced into the cavitation simulation. They generally provide more accurate results for a much higher computational cost. For instance, Dittakavi et al. [36] conducted the LES in the Venturi nozzle by using the dynamic Smagorinsky model and analyzed the effects of cavitation on each term in the vorticity transport equation. Huang et al. [69] performed the LES simulation with Wall-Adapting Local Eddy-viscosity (WALE) model in the Clark Y hydrofoil and demonstrated the strong correlation between the cavity and vorticity structure through the analysis of the vorticity transport equation. Ji et al. [74, 76] adopted the WALE LES to investigate the interaction of turbulence and cavitation in unsteady cavitation and showed that the cavitation could prompt the vortex production. Gnanaskandan and Mahesh [57] used the LES with a homogeneous mixture model and showed

the simulation results in void fraction could have a good agreement with experimental data. Žnidarčič [157] proposed a fast, novel DNS algorithm to better investigate the cavitation–turbulence interaction. Despite the development of these high-fidelity methods, they are still not practical for many engineering applications, mainly due to the prohibitive computational cost. Hence, the RANS method is still the primary tool for cavitation simulations.

Conversely, the current framework combining the RANS approach and homogeneous cavitation modelling cannot, in general, accurately predict the different types of cavitating flows. The unsteady cavitation patterns can be roughly divided into:

- (a) **attached/sheet cavitation:** cavity forms on a wall due to a local flow acceleration, and remains mostly steady, with possible fluctuations and shedding at various scales. This type of cavitation is shown in Fig. 1.2a.
- (b) **cloud cavitation:** the main part of the cavitation periodically detaches from the wall, forms large scale clouds of bubbles, and sheds downstream, where they collapse as soon as the pressure re-increases. This is the most aggressive flow pattern regarding cavitation-induced erosion, and also the one that will likely generate noise, vibrations, and pressure fluctuations. This cavitation pattern is presented in Fig. 1.2b.
- (c) **shear cavitation:** the formed vapor structures are immediately detached from the wall, and no attached cavity can be observed on the wall. This cavitation type is shown in Fig. 1.2c.

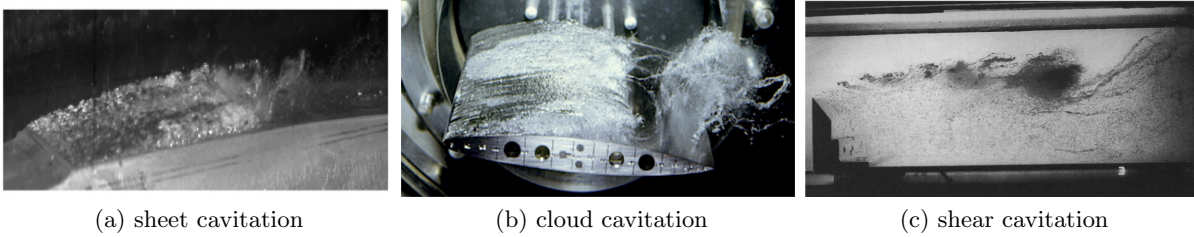


Figure 1.2: The different cavitation patterns. Adopted from [6, 17, 110]

In some specific cases like cloud cavitation, a fair general agreement with the experiments can be obtained [32, 52], but local comparisons of the void fraction or velocity profiles usually exhibit a poor agreement with the available experimental measurements [18]. In addition, the other configurations of cavitating flows, such as attached cavitation or shear cavitation, are usually not accurately predicted [6, 34].

The poor predictive performance of current methods can be due to many aspects.

- (i) First, the RANS framework has inherent limitations due to the use of the Boussinesq assumption, isotropic turbulence, etc. That will affect the predictive performance for

the turbulent cavitating flows. Specifically, cavitating flows are typically the separated recirculating flow with adverse pressure gradient, while it is well known that the RANS model cannot confidently predict this type of flow. Additionally, most of the RANS models are validated only for simple flows. However, in the cavitating flows, the use of homogeneous cavitation models results in large density gradients and high compressibility effects, which are usually not in the range of validity of these models. Besides, RANS models usually overestimate the turbulent viscosity in many cavitating flow configurations [27, 35, 155], which leads to that the unsteady effects, including fluctuations at multiple scales, are also complicated to handle by current RANS methods.

- (ii) Second, most of the existing cavitation model uses a homogeneous approach where the slip velocity between the two phases is neglected, the pressure is assumed to be the same in the liquid and vapor, and surface tension and bubble/bubble interactions are not considered. The commonly used models are based on the hypothetical state law (barotropic model), the empirical methods (such as Merkle model [104], Kunz model [87]), or deduced from single bubble dynamics (such as Schnerr-Sauer model [128], Singhal model [131]). Specifically, the barotropic model describes the vaporization behavior based on a pre-set pressure interval  $\Delta p_v$ . If the local pressure is higher than the vaporization pressure  $p_v + \frac{1}{2}\Delta p_v$ , the local density is considered as pure liquid. Oppositely, if the local pressure is lower than  $p_v - \frac{1}{2}\Delta p_v$ , the local density is regarded as vapor. Between the two pressure limits, a sinusoidal function usually is used to define the phase transition. Different from the barotropic model, the empirical models and the bubble dynamics based models estimate the mixture density by solving a void fraction transport equation as:

$$(1.1) \quad \frac{\partial \beta}{\partial t} + \nabla \cdot (\beta U) = m^+ + m^-,$$

where  $\beta$  is the void fraction,  $U$  is velocity,  $m^+$  and  $m^-$  represent the vaporization and condensation term, respectively. One advantage of these methods, compared to the barotropic model, is that both the vaporization and condensation process can be taken into account. The difference between the empirical model and the model based on bubble dynamics lies in the estimation for the vaporization and condensation process. The empirical model is based on the difference between local pressure and vaporization pressure. Moreover, as for the Kunz and Merkle model, the empirical coefficients,  $C_{\text{prod}}$  and  $C_{\text{dest}}$ , are introduced to control the magnitude of the vaporization and condensation term, respectively. While the bubble dynamics based models are deduced from the Rayleigh–Plesset equation, which describes the behavior of a spherical bubble in a pressure field. Based on that, the vaporization and condensation terms in Eq. 1.1 are modeled by assuming the bubbles in cavitating flows are spherical and have the same initial radius. Generally, all these cavitation models are under several assumptions and problematic to describe the behavior of natural cavitation bubble clusters accurately.



- 
- (iii) Moreover, it has been demonstrated by numerous works that there exist strong interactions between turbulence and cavitation. For instance, the cavitation can prompt the vortex production [74], enlarge the turbulent boundary layer thickness [127], and arise additional dissipation [35]. Specific changes of the standard turbulence models to take into account these interactions have to be applied but still need further investigations.

Conclusively, we have not yet fully understood the physics of both turbulence and cavitation, not mentioning the interaction between cavitation and turbulence. To improve the prediction from both sides of the turbulence model and the cavitation model is too ambitious so far. On the other hand, the work of [57] showed that better turbulence models (LES) combined with the same homogeneous cavitation models could provide predictive results in remarkably good agreement with experimental data, which suggests that the RANS models need to be primarily improved, more than the cavitation models. Hence, before we investigate the cavitation–turbulence interaction, it is crucial to have a better turbulence model to take into account large, fast changes of properties in terms of compressibility and viscosity, and the fluctuations at different scales in cavitating flows. Specifically, the cavitating flow is usually characterized by strong unsteadiness, the flow separation caused by adverse pressure gradient, and large pressure/density gradient, while RANS methods perform poorly on the flow with these characterizations. With the improvement to tackle these issues, the RANS model is possible to recover the field information of cavitating flows accurately. Therefore, this work intends to focus on the optimization of RANS models, more specifically 2-equations RANS models, and improve the overall performance with the optimal RANS methods for non-cavitating and cavitating flows.

To improve the accuracy of simulations for cavitating flows, the conventional approach is to apply better RANS models proposed in the turbulence community and deduce novel cavitation models embedding more physical insights into the mass transfer. Different works have been conducted to improve the predictive performance of RANS models based on physical knowledge. For instance, the  $k$ - $\epsilon$ ,  $k$ - $\omega$ , and  $k$ - $\omega$  shear stress transport (SST) model were proposed successively in the past decades and have been introduced in cavitation simulations. [27, 84] In recent years, the hybrid RANS/LES methods, for instance, detached eddy simulation (DES) and scale-adaptive simulation (SAS) model, which resolve the flow based on local turbulence length scale, are developed rapidly and used to predict unsteady cavitating flows [34]. Nevertheless, the development of the RANS model has been stagnant for the last two decades. There is still no universal models that can make a satisfactory prediction at an affordable computational cost for different types of flows. It is mainly due to that the knowledge about turbulence is still limited, and also the computational power is not feasible for the high-fidelity simulation of flows in industrial applications, which both barrier us to further improve the prediction. Hence, for specific flows, we often have to tune the dozens of turbulence models to achieve a balance between the simulation accuracy and the computational cost, which is very laborious.

In view of the fact that the development of the physical model has encountered the bottleneck, in the past few years, the data-driven methods, including data assimilation and machine learning, draw more and more attention in the turbulence community. Data assimilation is widely applied in diverse context (e.g., geoscience, weather forecasting, fluid mechanics, etc.). This method can integrate the low fidelity simulation with limited observations from experiments or high-fidelity simulations, and thus used for different purposes, such as state estimation, uncertainty quantification (UQ), and inference of empirical parameters or underlying source terms in RANS models. Another data-driven method, machine learning, is getting highlighted in the CFD field in recent years. Different from data assimilation, this technique does not need to embed the physical model and can build a functional mapping between the input features and the quantities of interest, e.g., model discrepancy, with offline training data. It is very promising to augment the turbulence modeling and construct a predictive model for the model-form discrepancy based on the underlying model information extracted with data assimilation.

In this work, we explore to improve the RANS model from two different directions: inverse modeling and empirical modeling. The road map of this work is shown in Fig. 1.3. The inverse modeling aims to extract the underlying model information from the data, and thus we can use this information to assist the RANS modelling. While the empirical modeling is to gain additional physical insight from the data, and further, we can embed the new physical understanding into the existing models to improve the prediction.

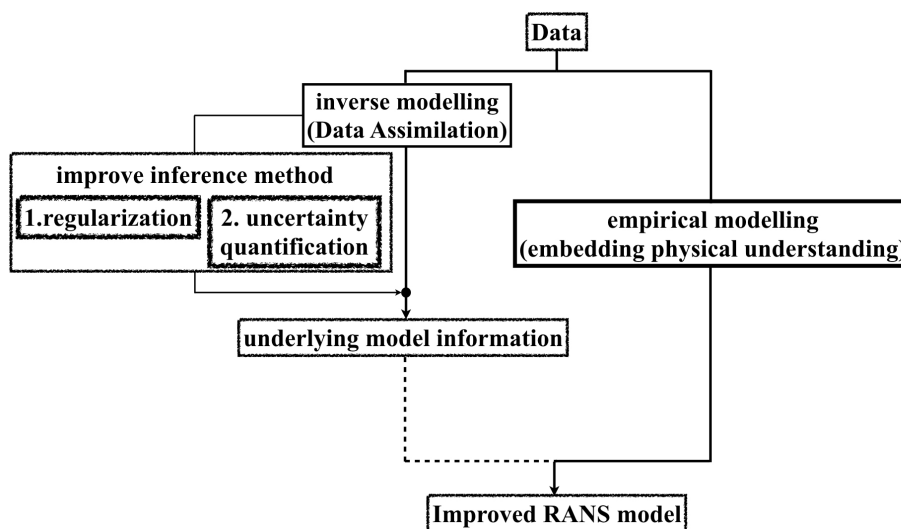


Figure 1.3: Road map of the thesis

As for the inverse modeling, we mainly focus on the data assimilation approach and investigate the applicability of diverse DA methods into complex CFD problems with the ultimate goal of improving the RANS models for cavitating flows. In concrete, with the data assimilation method, we attempt to quantify the unknown model-form uncertainties associated

---

with the Reynolds stress (i.e., underlying model corrections, and discrepancy in the Reynolds stress or the eddy viscosity), based on the high-fidelity data. These latent fields are not measurable straightforwardly from experiments, but they embed the main source of model-form uncertainties we need to quantify.

To achieve the goal, we first introduce a hybrid data assimilation method, namely ensemble-based variational (EnVar) method, to improve the simulation in the convergent-divergent channel, which is extensively used for the investigation of cavitating flows. We incorporate the high fidelity data (the DNS results and PIV experimental data) with  $k-\omega$  SST turbulence model to infer optimal boundary condition and underlying model corrections, thereby improving the predictive performance in the non-cavitating flows.

Although the EnVar method is robust and can improve the numerical predictions significantly, two issues are observed in the inference results and have to be addressed before further applying into cavitating flows: one is the ill-posedness of the field inversion problem, and another one is the uncertainty information loss. Concretely, when inferring the entire field from limited observation, it increases significantly the ill-posedness of the inverse problem where many possible model parameters can result in a satisfactory result in the observation space. That makes it very challenging to obtain good inferences with existing DA approaches. To this end, concerning the ill-posedness of the field inversion problem, we propose a novel ensemble-based data assimilation technique, namely regularized ensemble Kalman filter, to constrain the analysis step with auxiliary prior knowledge and thus provide more physical, accurate inference results. Another issue about the uncertainty information loss is observed in both EnVar and ensemble Kalman filter. For the EnVar, the resampling around the updated posterior mean at each iteration will only retain the sample mean and ignore the statistical information. While the ensemble Kalman filter is typically adopted for the dynamic systems and will underestimate the posterior uncertainty when used for the stationary systems due to data repeatedly use. To this end, we investigate different widely used data assimilation techniques and evaluate their performance as an efficient, approximate Bayesian UQ method for CFD applications.

Regarding the empirical modeling, we conduct the RANS simulation with the advanced two-equation turbulence model ( $k-\omega$  SST and SST-SAS) and compare the results with reliable X-ray experimental measurements in the cavitating flows. Motivated by the results, we propose a novel eddy viscosity modification to improve the prediction in Reynolds shear stress by further considering the effects of cavitation on the boundary layer.

The thesis includes firstly the literature review focusing on different data assimilation methods and their applications since they are the main optimization methods used in this work. In Chapter 3, a hybrid data assimilation method, namely ensemble-based variational data assimilation method, is adopted for the Bayesian optimization of turbulent flow in the convergent-divergent channel. In Chapter 4, a regularized ensemble Kalman method is proposed to regularize the inference results with additional constraints on the inferred field. In Chapter 5,

the performance of different ensemble-based data assimilation methods is assessed and discussed for uncertainty quantification problems in CFD applications. In Chapter 6, we evaluate the performance of different RANS methods on the simulation of cavitating flows and propose a modification to better consider the effects of cavitation on the turbulence. Finally, we summarize the conclusions and discuss the potentials and challenges in the applicability of data-driven techniques for future investigations of cavitating flows.

# Résumé

La cavitation hydrodynamique dans les écoulements liquides est une vaporisation partielle observée lorsque le liquide subit une chute de pression brutale. Ce phénomène affecte les écoulements internes à grande vitesse dans les machines tournantes, les écoulements externes sur les appendices de bateaux et les systèmes de propulsion et, plus généralement, tout système hydraulique où l'écoulement est soumis à des accélérations locales. La cavitation est obtenue dans divers domaines d'application, tels que les hélices et les appendices de navires rapides ou de sous-marins dans le domaine naval, les pompes de centrales nucléaires, les moteurs cryogéniques dans le domaine spatial, ou encore les barrages hydrauliques. Les principaux effets néfastes de la cavitation dans ces applications comprennent une perte d'efficacité et le déclenchement d'instabilités, de vibrations, de bruit et d'érosion. Les instabilités sont principalement engendrées par le gradient de pression défavorable dans le sillage de la cavitation, qui induit des écoulements recirculants à grande échelle et le détachement de nuages de bulles. L'implosion de ces bulles engendre une combinaison d'ondes de pression et de micro-jets qui impactent de façon répétitive les parois de l'objet qui induit la cavitation, provoquant notamment les problèmes de bruit et d'érosion. D'un autre côté, la cavitation peut également avoir des effets positifs dans divers contextes. Par exemple, la cavitation engendrée volontairement au nez des véhicules sous-marins peut être utilisée pour créer une couche de gaz entre les parois et l'écoulement liquide, ce qui réduit fortement le coefficient de frottement. Il en résulte une baisse importante de la traînée, ce qui augmente sensiblement la vitesse du véhicule. La cavitation peut également être utilisée pour la lithotripsie via l'onde de pression produite par le collapse des bulles de vapeur. Pour limiter les effets négatifs dans certains cas, tout en recherchant les effets positifs dans d'autres, il est nécessaire de mieux comprendre les mécanismes physiques des instabilités de cavitation, pour finalement les contrôler. Quelques exemples d'effets de la cavitation sont présentés dans la Fig. 1.4.

Les mesures expérimentales et les simulations numériques sont des outils courants pour étudier les écoulements cavitants. Les expériences dans les écoulements multiphasiques à fraction de vide élevée, comme les écoulements cavitants, sont généralement difficiles: les mesures non intrusives basées sur l'imagerie optique, comme la Vélocimétrie par Image de Particules (PIV), sont rendues difficiles par l'opacité du mélange liquide / vapeur et la forte réflexion de toute lumière incidente sur les bulles de cavitation. Des techniques spécifiques doivent être utilisées,

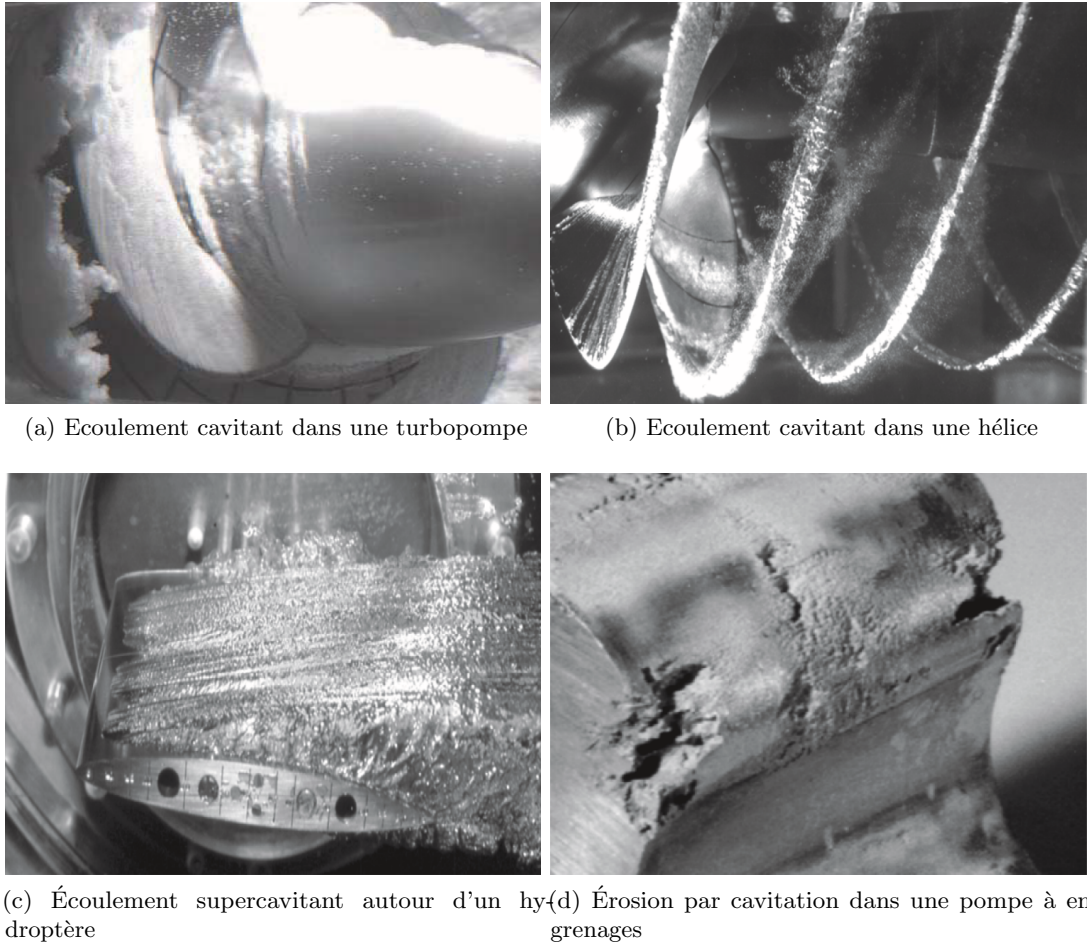


Figure 1.4: Exemples d'effets de cavitation dans les machines hydrauliques. Extrait de [33]

comme l'utilisation de particules fluorescentes en PIV, ou l'imagerie par rayons X au lieu de l'imagerie optique. Le coût et la complexité de telles expériences rendent les simulations numériques très attrayantes en tant qu'approche complémentaire pour étudier les mécanismes physiques.

Pour simuler numériquement un écoulement cavitant turbulent, l'approche la plus courante consiste à coupler l'approche RANS (Reynolds Averaged Navier-stokes equations) avec des modèles de cavitation ou de changement de phase. Des méthodes de turbulence haute fidélité, telles que la simulation des grandes échelles (LES) et la simulation numérique directe (DNS), ont également été introduites dans la simulation de cavitation. Elles fournissent généralement des résultats plus précis pour un coût de calcul beaucoup plus élevé. Par exemple, Dittakavi et al. [36] ont effectué une LES dans un Venturi en utilisant le modèle dynamique de Smagorinsky, et ils ont analysé les effets de la cavitation sur chaque terme dans l'équation de transport de tourbillon. Huang et al. [69] ont effectué la simulation LES avec le modèle Wall-Adapting Local Eddy-viscosity (WALE) sur l'hydrofoil Clark Y et ont démontré la forte corrélation entre la

structure de la cavité et celle des tourbillons, par l'analyse de l'équation de transport de la vorticit . Ji et al. [74, 76] ont  galement adopt  le mod le WALE pour  tudier l'interaction de la turbulence et de la vapeur en r gime de cavitation instationnaire, et ils ont montr  que la cavitation pouvait favoriser la production de vortex. Gnanaskandan et Mahesh [57] ont utilis  l'approche LES avec un mod le de m lange homog ne et ont montr  que les r sultats de simulation en termes de fraction volumique de vapeur  taient en bon accord avec les donn es exp rimentales.  nidar i  [157] a propos  un nouvel algorithme DNS rapide pour mieux  tudier l'interaction cavitation-turbulence. Malgr  le d veloppement de ces m thodes haute fid lit , elles ne sont toujours pas pratiques pour de nombreuses applications d'ing nierie, principalement en raison du co t de calcul prohibitif. Par cons quent, la m thode RANS est toujours l'outil principal pour les simulations de cavitation.

Inversement, le cadre actuel combinant l'approche RANS et la mod lisation homog ne de la cavitation ne peut pas, en g n ral, pr dire avec pr cision les diff rents r gimes d' coulements cavitants. Les mod les de cavitation instationnaires peuvent  tre principalement divis s en:

- (a) **cavitation attach e / stable**: la cavit  se forme sur une paroi en raison d'une acc l ration locale de l' coulement et reste g n ralement stable, avec des fluctuations et des d tachements possibles   diff rentes  chelles. Ce type de cavitation est illustr  dans Fig. 1.5a.
- (b) **cavitation avec nuages de bulles**: la partie principale de la cavitation se d tache p riodiquement de la paroi, formant des nuages de bulles   grande  chelle qui sont convect s en aval, o  ils implosent d s que la pression augmente   nouveau. Il s'agit du sch ma d' coulement le plus agressif en ce qui concerne l' rosion induite par la cavitation, et  galement celui qui g n rera des niveaux  lev s de bruit, de vibrations et de fluctuations de pression. Ce mod le de cavitation est pr sent  dans Fig. 1.5b.
- (c) **cavitation de cisaillement**: les structures de vapeur form es sont imm diatement d tach es de la paroi, et aucune cavit  attach e ne peut  tre observ e. Ce type de cavitation est illustr  dans Fig. 1.5c.

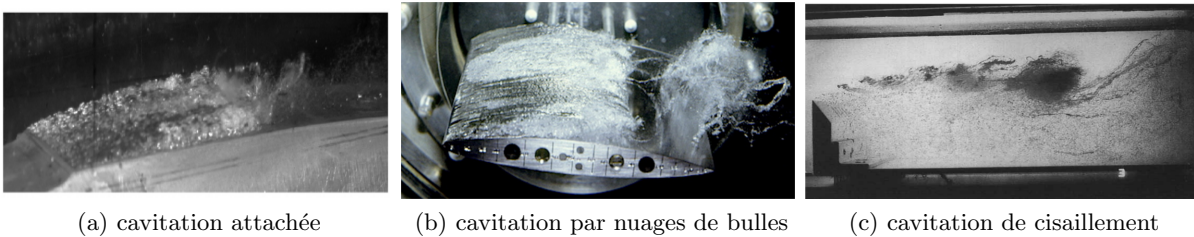


Figure 1.5: Les diff rents mod les de cavitation. Extrait de [6, 17, 110]

Dans certains cas sp cifiques comme la cavitation instable, un accord g n ral correct avec les exp riences peut  tre obtenu [32, 52], mais les comparaisons locales de la fraction volumique de

vapeur ou des profils de vitesse présentent généralement un mauvais accord avec les mesures expérimentales disponibles [18]. De plus, les autres configurations d'écoulements de cavitation, telles que la cavitation attachée ou la cavitation de cisaillement, ne sont généralement pas prédites de façon satisfaisante [6, 34].

Cette mauvaise performance des méthodes actuelles peut être due à de nombreux aspects.

- (i) Premièrement, le cadre RANS a des limites inhérentes en raison de l'utilisation de l'hypothèse de Boussinesq et de la notion implicite de turbulence isotrope. Il s'ensuit des difficultés générales à prédire la structure des écoulements cavitants. Plus précisément, les écoulements cavitants engendrent généralement des écoulements détachés et des recirculations liés à un gradient de pression défavorable en aval de la cavité, ce qui est typiquement une configuration d'écoulement dans laquelle les modèles RANS ont montré de fortes limitations. De plus, la plupart de ces modèles ne sont validés que pour des écoulements incompressibles simples. Cependant, dans la modélisation de la cavitation, l'utilisation de modèles homogènes entraîne des gradients de densité élevés et de forts effets de compressibilité, qui ne sont généralement pas dans la plage de validité de ces modèles. En outre, les modèles RANS surestiment généralement la viscosité turbulente dans de nombreuses configurations d'écoulements cavitants [27, 35, 155], ce qui conduit à une mauvaise prédiction des effets instationnaires, aussi bien les évolutions périodiques à grande échelle que les fluctuations à plus haute fréquence.
- (ii) Deuxièmement, la plupart des modèles de cavitation existants utilisent une approche homogène où la vitesse de glissement entre les deux phases est négligée, la pression est supposée être la même dans le liquide et la vapeur, et la tension de surface ainsi que les interactions entre bulles ne sont pas prises en compte. Les modèles couramment utilisés sont basés soit sur une loi d'état pour le mélange (modèle barotrope), des méthodes empiriques de détermination de termes sources de vapeur (telles que le modèle Merkle [104], le modèle Kunz [87]), ou déduites de la dynamique d'une seule bulle (comme le modèle Schnerr–Sauer [128], modèle Singhal [131]). Plus précisément, le modèle barotrope décrit le phénomène de changement de phase sur un intervalle de pression prédéfini  $\Delta p_v$ . Si la pression locale est supérieure à la pression de vaporisation  $p_v + \frac{1}{2}\Delta p_v$ , la densité locale est considérée comme liquide pur. À l'opposé, si la pression locale est inférieure à  $p_v - \frac{1}{2}\Delta p_v$ , la densité locale est considérée comme de la vapeur. Entre ces deux limites de pression, une fonction sinusoïdale est généralement utilisée pour définir la transition de phase. À la différence du modèle barotrope, les modèles empiriques et les modèles basés sur la dynamique des bulles estiment la densité du mélange en résolvant une équation de transport pour la fraction volumique de vapeur comme:

$$(1.2) \quad \frac{\partial \beta}{\partial t} + \nabla \cdot (\beta U) = m^+ + m^-,$$



---

où  $\beta$  est la fraction volumique de vapeur,  $U$  est la vitesse,  $m^+$  et  $m^-$  représentent respectivement le terme source de vaporisation et de condensation. Un avantage de ces méthodes, par rapport au modèle barotrope, est que les processus de vaporisation et de condensation peuvent être pris en compte séparément, avec éventuellement un décalage entre les variations de pression et de densité. La différence entre le modèle empirique et le modèle basé sur la dynamique des bulles réside dans la technique d'estimation du taux de vaporisation et de condensation. Les modèles empiriques sont basés sur la différence entre la pression locale et la pression de vapeur saturante. Des coefficients (constantes),  $C_{\text{prod}}$  et  $C_{\text{dest}}$ , sont introduits pour contrôler respectivement l'amplitude du terme de vaporisation et de condensation. Les modèles basés sur la dynamique des bulles sont déduits quant à eux de l'équation de Rayleigh-Plesset, qui décrit le comportement d'une bulle sphérique dans un champ de pression. Sur cette base, les termes de vaporisation et de condensation dans Eq. 1.2 sont modélisés en supposant que les bulles dans les écoulements cavitants sont sphériques et ont toutes le même rayon initial. Généralement, ces modèles incluent des hypothèses fortes (bulles qui n'interagissent pas et ne se déforment pas) pour pouvoir être appliqués à des nuages de bulles de vapeur.

- (iii) De plus, il a été démontré par de nombreux travaux qu'il existe de fortes interactions entre turbulence et cavitation. Par exemple, la cavitation peut provoquer la production de vorticit  [74], augmenter l' paisseur de la couche limite turbulente [127] et provoquer une dissipation suppl mentaire [35]. Des modifications sp cifiques des mod les de turbulence standard pour prendre en compte ces interactions doivent  tre appliqu es mais n cessitent encore des investigations suppl mentaires.

En conclusion, la physique de la turbulence et de la cavitation est loin d' tre comprise enti rement, sans parler de l'interaction entre la cavitation et la turbulence. Am liorer simultan ment l'efficacit  du mod le de turbulence et du mod le de cavitation est jusqu'  pr sent trop ambitieux. D'un autre c t , les travaux de [57] ont montr  que de meilleurs mod les de turbulence (LES) combin s avec les m mes mod les de cavitation homog nes pouvaient fournir des r sultats pr dictifs en tr s bon accord avec les donn es exp rimentales, ce qui sugg re que les mod les RANS doivent  tre principalement am lior s, plus que les mod les de cavitation eux-m mes. Par cons quent, avant d' tudier l'interaction cavitation-turbulence, il est crucial d'avoir un meilleur mod le de turbulence, pouvant prendre en compte les changements importants et rapides de propri t s en termes de compressibilit  et de viscosit , et les fluctuations   diff rentes  chelles des  coulements cavitants. Plus pr cis ment, les  coulements cavitants sont g n ralement caract ris s par une forte instabilit , une s paration caus e par un gradient de pression d favorable, et des variations rapides de densit  et de pression, alors que les m thodes RANS fonctionnent mal dans ces conditions. Ce travail vise   se concentrer sur l'optimisation des mod les RANS, plus sp cifiquement les mod les RANS   2  quations, et   am liorer les

performances globales par des méthodes d’assimilation de données en conditions non cavitantes et cavitantes.

Pour améliorer la précision des simulations des écoulements de cavitation, l’approche conventionnelle consiste à appliquer de meilleurs modèles RANS proposés dans la communauté de la turbulence et à déduire de nouveaux modèles de cavitation intégrant davantage de physique dans l’expression des termes de transfert de masse. Différents travaux ont été menés pour améliorer les performances prédictives des modèles RANS basés sur les connaissances physiques. Par exemple, les modèles  $k$ - $\epsilon$ ,  $k$ - $\omega$  et  $k$ - $\omega$  shear stress transport (SST) ont été appliquées successivement ces dernières décennies aux simulations de cavitation. Récemment les méthodes hybrides RANS/LES, telles que Detached Eddy Simulation (DES) et Scale-Adaptive Simulation (SAS), qui prennent en compte une échelle des turbulence locale, se sont développée rapidement et ont été appliquées aux écoulements instationnaires cavitants [34]. Néanmoins, le développement du modèle RANS stagne depuis deux décennies. Il n’existe toujours pas de modèles universels capables de faire une prédiction satisfaisante à un coût de calcul abordable pour différents types d’écoulements. Cela est principalement dû au fait que les connaissances sur la turbulence sont encore limitées et que la puissance de calcul n’est pas réalisable pour la simulation haute fidélité des écoulements dans les applications industrielles. Par conséquent, pour des écoulements spécifiques, il est souvent nécessaire de tester différents modèles de turbulence et choisir finalement un compromis entre précision de la simulation et le coût de calcul, ce qui est très laborieux.

Compte tenu du fait que le développement des modèle physique a stagné au cours des dernières années, les méthodes basées sur l’analyse de données, y compris l’assimilation de données et l’apprentissage automatique, attirent de plus en plus l’attention dans la communauté de la turbulence. L’assimilation de données est largement appliquée dans divers contextes (par exemple, géoscience, prévisions météorologiques, mécanique des fluides, etc.). Cette méthode peut intégrer la simulation basse fidélité à des observations limitées issues d’expériences ou de simulations haute fidélité, et elle est utilisée pour la quantification de l’incertitude (UQ) et la détermination de paramètres empiriques ou de termes sources sous-jacents dans les modèles RANS. Une autre méthode, l’apprentissage automatique, a émergé dans le domaine de la CFD ces dernières années. Différente de l’assimilation de données, cette technique n’a pas besoin d’incorporer le modèle physique et peut créer une correspondance fonctionnelle entre les caractéristiques d’entrée et les quantités d’intérêt. Il semble très prometteur de combiner les deux approches, i.e. améliorer la modélisation de la turbulence et construire un modèle prédictif sur la base des informations du modèle sous-jacent extraites avec l’assimilation des données.

Dans ce travail, nous explorons l’amélioration du modèle RANS par deux techniques différentes et complémentaires : la modélisation inverse d’une part, et une approche empirique d’autre part. La feuille de route générale de ce travail est présentée sur la Fig. 1.6. La modélisation inverse vise à extraire des informations supplémentaires sur le modèle à partir de comparaisons

entre calculs et mesures de référence, et ainsi à améliorer la modélisation RANS. La modélisation empirique quant à elle vise à obtenir une meilleure compréhension de la physique, pour l'intégrer dans les modèles existants et améliorer la prédiction.

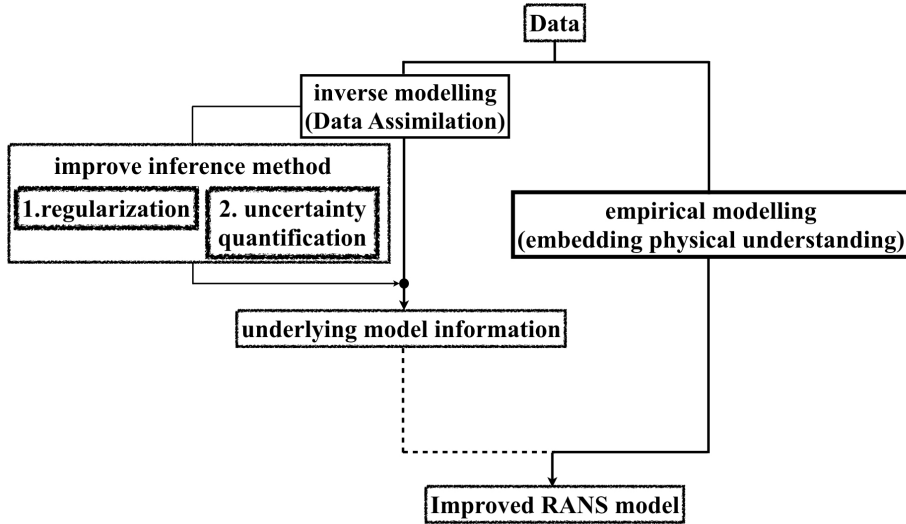


Figure 1.6: Feuille de route de la thèse

En ce qui concerne la modélisation inverse, nous nous concentrons principalement sur l'approche d'assimilation de données (DA) et étudions l'applicabilité de diverses méthodes DA dans des problèmes CFD complexes, dans le but final d'améliorer les modèles RANS pour les écoulements cavitants. Concrètement, avec la méthode d'assimilation de données, nous essayons de quantifier les incertitudes du modèle associées aux composantes du tenseur de Reynolds (i.e., les corrections du modèle et les écarts dans le tenseur de Reynolds ou la viscosité turbulente), sur la base de données haute fidélité. Ces champs ne sont pas mesurables directement à partir d'expériences, mais ils intègrent la principale source d'incertitudes du modèle, que nous devons quantifier.

Pour atteindre cet objectif, nous introduisons d'abord une méthode hybride d'assimilation de données, à savoir la méthode variationnelle basée sur l'ensemble (EnVar), pour améliorer la simulation dans le canal convergent-divergent, qui est largement utilisée pour l'étude des écoulements de cavitation. Nous incorporons les données haute fidélité (les résultats DNS et les données expérimentales PIV) avec le modèle de turbulence  $k-\omega$  SST pour déduire la condition aux limites optimale et les corrections du modèle sous-jacent, améliorant ainsi les performances prédictives dans les écoulements sans cavitation.

Bien que la méthode EnVar soit robuste et puisse améliorer considérablement les prédictions numériques, deux problèmes sont observés dans les résultats d'inférence et doivent être résolus avant de s'appliquer plus avant aux écoulements cavitants: d'une part le problème d'inversion de champ est mal posé, et d'autre part on observe une perte d'information sur l'incertitude. Concrètement, quand on infère un champ complet à partir d'observations limitées, de nombreux

paramètres différents du modèle peuvent aboutir à un résultat satisfaisant dans l'espace d'observation. Il est donc très difficile d'obtenir de bonnes inférences avec les approches DA existantes. Pour résoudre ce problème, nous proposons une nouvelle technique d'assimilation de données basée sur une méthode d'ensemble, à savoir un filtre de Kalman d'ensemble régularisé, pour contraindre l'étape d'analyse avec des connaissances préalables auxiliaires et ainsi fournir des résultats d'inférence plus physiques et plus précis. . Un autre problème concernant la perte d'informations d'incertitude est observé à la fois dans EnVar et dans le filtre de Kalman. Pour l'EnVar, le rééchantillonnage autour de la moyenne postérieure mise à jour à chaque itération ne conservera que la moyenne de l'échantillon et ignorera les informations statistiques. Alors que le filtre de Kalman d'ensemble est généralement adopté pour les systèmes dynamiques et sous-estimera l'incertitude postérieure lorsqu'il est utilisé pour les systèmes stationnaires en raison de l'utilisation répétée des données. À cette fin, nous étudions dans ce mémoire différentes techniques d'assimilation de données largement utilisées et évaluons leurs performances en tant que méthode bayésienne efficace pour les applications de CFD.

En ce qui concerne la modélisation empirique, nous effectuons la simulation RANS avec des modèles de turbulence à deux équations ( $k$ - $\omega$  SST et SST-SAS) et comparons les résultats avec des mesures expérimentales par imagerie de rayons X fiables dans les écoulements de cavitation. Sur la base de ces résultats, nous proposons une nouvelle modification de la viscosité turbulente pour améliorer la prédiction de la contrainte de cisaillement de Reynolds en considérant davantage les effets de la cavitation sur la couche limite.

La thèse comprend tout d'abord une revue bibliographique portant sur les différentes méthodes d'assimilation de données et leurs applications car ce sont les principales méthodes d'optimisation utilisées dans ce travail. Dans le chapitre 3, une méthode hybride d'assimilation de données, à savoir la méthode d'assimilation d'ensemble de données variationnelles, est adoptée pour l'optimisation bayésienne de l'écoulement turbulent dans un canal venturi convergent-divergent. Dans le chapitre 4, une méthode de Kalman régularisée est proposée pour régulariser les résultats d'inférence avec des contraintes supplémentaires sur le champ déduit. Dans le chapitre 5, la performance de différentes méthodes d'assimilation de données basées sur un ensemble est évaluée et discutée pour les problèmes de quantification de l'incertitude dans les applications CFD. Dans le chapitre 6, nous évaluons les performances de différentes méthodes RANS sur la simulation des écoulements cavitants et proposons une modification pour mieux prendre en compte les effets de la cavitation sur la turbulence. Enfin, une synthèse des travaux clot ce mémoire, où les problèmes subsistants et les champs d'applications des techniques d'assimilation de données sont discutés pour le cas particulier des écoulements cavitants.

## Chapter 2

# Review of Data Assimilation Methods

### 2.1 Introduction

Data assimilation (DA) is widely used in the field of geoscience and meteorology to seek for the optimal state estimate via combining the theoretic/physical model with sparse observations. Also, it has been increasingly leveraged for the inference problem, for instance, to determine the initial or boundary condition or find out optimal system parameters with consideration of available data. This technique can be applied for either dynamic or stationary systems, and in this work, we focus on the stationary scenario. Numerous methods mainly based on Kalman filter and variational method have been developed. In this chapter, we give a brief review of different data assimilation schemes mainly for the time-independent scenario, with emphasis on the DA schemes adopted in the present work.

### 2.2 Data assimilation problem statement

The problem we intend to solve with DA can be briefly sorted by three different purposes. First is the state estimation problem to estimate the state of the system by reducing the mismatch between the model forecasting and the observation. The second is Bayesian uncertainty quantification problems where the interest is not only to capture the most confidential value (mode) but also estimate the posterior statistics of the state inputs as well as the model outputs with given noised data. The final one is the inference problem to infer the latent field or parameters of interest by incorporating the observation data. Before illustrating the DA problem, two sources of information, i.e., the model and the observation, need to be further explained. The model is the theoretical/physical description of the system but inaccurate to some extent, for instance, the RANS model in CFD applications. The observation is the *intuitive*

description via observations or measurements on the system. Conventionally, the model and observation are both discretized in space, as we will do in this work.

In the discrete formulation, it is assumed that the state of the system, for instance, the fluid velocity, can be expressed as  $\mathbf{x} \in \mathbb{R}^M$  where  $M$  is the dimension of the state after discretization. The forward model is to propagate the state vector into the observation space, which can be expressed as:

$$(2.1) \quad \hat{\mathbf{y}} = \mathcal{H}[\mathbf{x}],$$

where  $\mathcal{H} : \mathbb{R}^M \rightarrow \mathbb{R}^D$  is generally the nonlinear model operator mapping the state space to observation space. Note that the model hereby is the perfect model, and the model error is not considered in this thesis. The noised observations can be represented as the observation vector  $\mathbf{y}_o \in \mathbb{R}^D$  and formulated as:

$$(2.2) \quad \mathbf{y}_o = \mathcal{H}[\mathbf{x}^+] + \epsilon,$$

where  $\epsilon$  is the observation noise, accounting for the epistemic and aleatoric uncertainty in the measurements as well as the deficiency of the observation operator;  $\mathbf{x}^+$  is the reference trajectory projecting to observation via the operator  $\mathcal{H}$ . In most cases, the dimension of the state vector is much higher than that of observation, i.e.,  $M \gg D$ . The information from data is insufficient to fully describe the system, and DA is capable of utilizing these information to propagate from observed to unobserved areas and estimate the state of the system by incorporating the model. The theoretical foundation of DA is the Bayes' theorem as:

$$(2.3) \quad p(\mathbf{x} | \mathbf{y}) = \frac{p(\mathbf{y} | \mathbf{x})p(\mathbf{x})}{p(\mathbf{y})},$$

where  $p(\mathbf{x})$  is the prior distribution, reflecting the knowledge before taking the new observation into account,  $p(\mathbf{y} | \mathbf{x})$  is the likelihood of data conditioned on the state  $\mathbf{x}$  of the system, and  $p(\mathbf{y})$  is the marginal distribution of the data,  $p(\mathbf{y}) = \int p(\mathbf{y} | \mathbf{x})p(\mathbf{x})d\mathbf{x}$ . It can be simply illustrated as the posterior distribution is proportional to the prior and the likelihood of data given the system model. Note that the distribution  $p(\mathbf{y})$  is independent on the state  $\mathbf{x}$  and can be regarded as a normalization constant. To obtain the full distribution of posterior, it typically needs at least millions of samples, which is not practical for most partial-differential-equations-based systems. To this end, in data assimilation, maximum a posteriori (MAP) estimate is used to capture the peak of the posterior instead of the full posterior distribution, thus reducing the amount of the sampling. Therefore, presuming that the prior and posterior are both Gaussian distributed, the problem can be formulated as:

$$(2.4) \quad p(\mathbf{x} | \mathbf{y}) \propto p(\mathbf{x})p(\mathbf{y} | \mathbf{x}) = e^{-J}$$

In the above formula,  $J$  is the cost function as:

$$(2.5) \quad J = \frac{1}{2} \|\mathbf{x}^a - \mathbf{x}^f\|_{\mathbf{P}}^2 + \frac{1}{2} \|\mathbf{y} - \mathcal{H}[\mathbf{x}^a]\|_{\mathbf{R}}^2,$$

where  $\mathbf{P}$  is the model error covariance,  $\mathbf{R}$  is the observation error covariance,  $\|*\|_{\mathbf{A}}^2 = *^\top \mathbf{A}^{-1} *$ , and the superscript  $a$  and  $f$  stands for analysis and forecast, respectively. Therefore, the DA problem is equivalent to find the optimal state vector  $\mathbf{x}$  to minimize the cost function and reduce the mismatch with data in the observation space.

In the following sections, we give a brief review of different data assimilation techniques, including the variational DA methods, ensemble-based DA methods, hybrid DA methods, and the particle filter.

## 2.3 Variational data assimilation method

The variational data assimilation method equates the maximum a posterior estimation as the minimization of the cost function (2.5) under the Gaussian assumption on the prior and likelihood function. To minimize the objective function  $J$ , the 3D variational data assimilation method [24] adopts the gradient-based optimization technique. The gradient of the cost function can be derived by differentiating (2.5) with respect to the state  $\mathbf{x}^a$  as follows:

$$(2.6) \quad \nabla J = \mathbf{P}^{-1}(\mathbf{x}^a - \mathbf{x}^f) + (\mathcal{H}'[\mathbf{x}^a])^\top \mathbf{R}^{-1}(\mathbf{y} - \mathcal{H}[\mathbf{x}^a]),$$

where the  $\mathcal{H}'[\mathbf{x}^a]$  is the Jacobian of the observation operator. At the minimum, the gradient should vanish as zero. Hence, we can obtain the optimal point from:

$$(2.7) \quad \mathbf{P}^{-1}(\mathbf{x}^a - \mathbf{x}^f) = -(\mathcal{H}'[\mathbf{x}^a])^\top \mathbf{R}^{-1}(\mathbf{y} - \mathcal{H}[\mathbf{x}^a]).$$

The value that minimizes the cost function corresponds to the mode of the posterior distribution. For dynamic systems, the forecast model need to be embedded to propagate the system state in time. Thus, the 3DVar can be extended to be 4DVar method (e.g., [53, 136, 158]) by introducing Lagrangian associated with the forecast model. The reader is referred to [70] for further details.

Numerous works based on the variational method have been investigated in CFD applications. For instance, Gronsksis et al. [61] used variational methods to infer inflows and initial conditions for DNS simulations. Foures et al. [51] proposed a DA framework based on the variational formulation to reconstruct the mean velocity field by finding the optimal forcing term. Mons et al. [107] applied the variational DA method to reconstruct the flow around a cylinder in the presence of coherent gust, through inferring the inlet and initial conditions. Symon et al. [134] reproduced the flow over an idealized airfoil by incorporating the PIV experimental data with the variational method.

## 2.4 Kalman filter

The original Kalman filter [78] can be derived from the Bayesian formulation under several assumptions (i.e., the statistical error is Gaussian, both observational and dynamical models

are linear). Accordingly, the dynamical and observational models can be rewritten as:

$$(2.8) \quad \begin{aligned} \mathbf{x}_k &= \mathbf{M}_{k-1}\mathbf{x}_{k-1} + \eta_k; & \eta_k &\sim \mathcal{N}(0, \mathbf{Q}_k) \\ y_k &= \mathbf{H}\mathbf{x}_k + \epsilon_k; & \epsilon_k &\sim \mathcal{N}(0, \mathbf{R}_k), \end{aligned}$$

where  $\mathbf{Q}_k$  is the dynamic model error covariance, the dynamic model error  $\eta_k$  and observation error  $\epsilon_k$  are subjected to zero mean multivariate normal distribution  $\mathcal{N}$ . The derivation is similar to variational method through equating the MAP to the minimization of the cost function, and the details are omitted for clarity. The Kalman filter can be divided into two steps: the forecast step and analysis step. The forecast step is to propagate the current state and covariance matrix to the next time as:

$$(2.9) \quad \mathbf{x}_{k+1}^f = \mathbf{M}_k \mathbf{x}_k^a, \quad \mathbf{P}_{k+1}^f = \mathbf{M}_k \mathbf{P}_k^a \mathbf{M}_k^\top + \mathbf{Q}_{k+1}$$

The analysis step is to update the state and covariance through:

$$(2.10) \quad \begin{aligned} \mathbf{K}_k &= \mathbf{P}_k^f \mathbf{H}^\top (\mathbf{R} + \mathbf{H} \mathbf{P}_k^f \mathbf{H}^\top)^{-1} \\ \mathbf{x}_k^a &= \mathbf{x}_k^f + \mathbf{K}_k (y_k - \mathbf{H} \mathbf{x}_k^f) \\ \mathbf{P}_k^a &= (\mathbf{I} - \mathbf{K}_k \mathbf{H}) \mathbf{P}_k^f \end{aligned}$$

Given the model operator  $(\mathbf{H}, \mathbf{M})$ , error covariance matrix  $(\mathbf{Q}, \mathbf{R})$ , and initial state mean  $\mathbf{x}_0$  and covariance  $\mathbf{P}_0$ , the Kalman filter can sequentially estimate the state by assimilating the available data. The solution of the Kalman filter is also known as the *Best Linear Unbiased Estimator* (BLUE) [4].

However, the Kalman filter is not practical to be applied for large scale problems like fluid mechanics. Because it needs store and propagate in time the covariance  $\mathbf{P}$ , which presents a daunting computational burden [50]. Hence, the reduced-order Kalman filter is proposed when applying to CFD problems. For instance, Lee et al. [90] derived a feedback controller for drag reduction of turbulent channel flow. They applied a reduced model of the linearized Navier–Stokes equations to reduce the dimension of the system. Meldi and Poux [100] proposed the reduced-order Kalman filter based on the model reduction strategies to reduce the computational cost. The framework has been further applied in different flow configurations, including three-dimension unsteady flows.

## 2.5 Ensemble-based data assimilation methods

Ensemble-based DA method is an approximate Bayesian method with the Monte Carlos technique. The model error covariance is estimated with limited samples. This type of method includes ensemble Kalman filter or smoother and its variants. Here, we give a review of three widely used ensemble-based DA methods, namely ensemble Kalman filter, ensemble randomized maximum likelihood method, and ensemble Kalman filter with multiple data assimilation.



### 2.5.1 Ensemble Kalman filter

Among the ensemble-based DA methods, the most extensively used one is ensemble Kalman filter or smoother [48]. The difference between ensemble Kalman filter and smoother is that ensemble Kalman filter utilizes the data sequentially, while smoother consider the data at all times simultaneously. This method is motivated by the Kalman filter [140] which is derived from Bayesian formulation for linear systems under Gaussian assumption. It was initially proposed by Evensen [47] and further revised with an ensemble observation to avoid too low posterior variance by Burger et al. [15]. The method uses the Monte Carlo technique to prescribe the prior statistics around the first guess, and thus the error statistic is represented with an approximate ensemble state instead of storing the full covariance matrix. The state matrix can be expressed as:

$$(2.11) \quad \mathbf{X}_i^f = \{\mathbf{x}_{i,j}^f\}_{j=1}^M,$$

where  $M$  is the ensemble size,  $i$  is the iteration index,  $j$  is the sample index. Further, the model error covariance  $\mathbf{P}_i$  can be represented as:

$$(2.12) \quad \mathbf{P}_i = \frac{1}{M-1}(\mathbf{X}_i^f - \bar{\mathbf{X}}_i^f)(\mathbf{X}_i^f - \bar{\mathbf{X}}_i^f)^\top,$$

where  $\bar{\mathbf{X}}_i^f$  is the mean of the ensemble  $\mathbf{X}_i^f$ :

$$(2.13) \quad \bar{\mathbf{X}}_i^f = \frac{1}{M} \sum_{j=1}^M \mathbf{x}_{i,j}^f.$$

The update scheme for each ensemble sample  $\mathbf{x}_j$  at the time  $i$  can be formulated as:

$$(2.14) \quad \mathbf{x}_{i,j}^a = \mathbf{x}_{i,j}^f + \mathbf{K}(\mathbf{y}_{i,j} - \mathbf{H}\mathbf{x}_{i,j}^f),$$

where  $\mathbf{K}$  is the Kalman gain matrix  $\mathbf{K} = \mathbf{P}_i \mathbf{H}^\top (\mathbf{H} \mathbf{P}_i \mathbf{H}^\top + \mathbf{R})^{-1}$ ,  $\mathbf{H}$  is the tangent linear observation operator, and  $\mathbf{y}_{i,j}$  is the ensemble observation through adding the perturbation subject to Gaussian distribution with zero mean and covariance matrix  $\mathbf{R}$  to the measurement  $\mathbf{y}_o$ . The equation (2.14) can imply that the ensemble mean is updated in the similar form. It is shown by Evensen [46] and Burger [15] that the analyzed covariance matrix  $\mathbf{P}^a$  can be derived as:

$$(2.15) \quad \mathbf{P}^a = (\mathbf{I} - \mathbf{K}\mathbf{H})\mathbf{P}^f,$$

which proves that the ensemble Kalman filter is consistent with the Kalman filter. Since the covariance represented by the ensemble anomalies will be rank-deficient to substitute the full rank true one, it usually has to introduce the localization [65, 68, 115] and inflation [3, 92, 106] technique to consider the spurious correlations between the elements of the state variable. A body of work has explored to apply the EnKF into CFD problems for state estimate, inference as well as inverse uncertainty quantification. For instance, Colburn et al. [23] leveraged the EnKF

to estimate the turbulent channel flow at a low Reynolds number based on wall information. Kato et al. [79] used the EnKF to determine the optimal empirical parameters in the Spalart–Allmaras turbulence model. Xiao et al. [148] applied the method to quantify and reduce the model-form uncertainty associated with Reynolds stress.

### 2.5.2 Ensemble randomized maximum likelihood

The ensemble randomized maximum likelihood (EnRML) method was initially proposed by Gu et al. [62] to address the data assimilation application with nonlinear system models. They demonstrated the methods could have better results for nonlinear problems than the EnKF approach. Essentially, the state variable in this DA scheme is updated iteratively to minimize the cost function (2.5) via the Gauss–Newton method as:

$$(2.16) \quad \mathbf{x}_{i,j}^a = \mathbf{x}_{i,j}^f + \gamma \left( \frac{\partial J^2}{\partial^2 \mathbf{x}} \right)^{-1} \frac{\partial J}{\partial \mathbf{x}},$$

where  $\gamma$  is the parameter to adjust the step length. The derived update formulation can be expressed as follows:

$$(2.17) \quad \mathbf{x}_{i,j}^a = \gamma \mathbf{x}_{0,j}^f + (1 - \gamma) \mathbf{x}_{i,j}^f - \gamma \mathbf{P}_0 (\mathcal{H}'[\mathbf{x}_{i,j}^f])^\top (\mathbf{R} + (\mathcal{H}'[\mathbf{x}_{i,j}^f])^\top \mathbf{P}_0 \mathcal{H}'[\mathbf{x}_{i,j}^f])^{-1} (\mathcal{H}[\mathbf{x}_{i,j}^f] - y_j - \mathcal{H}'[\mathbf{x}_{i,j}^f](\mathbf{x}_{i,j}^f - \mathbf{x}_{0,j}^f)),$$

where  $\mathbf{P}_0$  is the initial ensemble covariance which is not changed with iterations, and  $\mathcal{H}'[\mathbf{x}]$  is the sensitivity matrix which is computed from the ensemble realizations at every iteration by solving:

$$(2.18) \quad \Delta d_i = \mathcal{H}'[\mathbf{x}_i^f] \Delta \mathbf{x}_i.$$

In the above formula,  $\Delta d_i$  and  $\Delta \mathbf{x}_i$  are deviation realizations of the predicted data and the deviation realizations of the state variables from the mean, respectively. The singular value decomposition is usually needed to calculate the inverse of  $\Delta \mathbf{x}_i$  since it is not full rank. The approximate sensitivity matrix is not accurate as the analytic gradient with adjoint code unless the ensemble variability is small and the ensemble size is large.

For highly nonlinear systems, it is necessary to iteratively update the state vector in order to have a satisfactory data match. Because the nonlinearity will increase the number of local minimums, and thus it is inevitable to have a “many to one” mapping and accordingly increase the ill-posedness of the problem. On the other hand, EnKF can be regarded as a full step of Gauss–Newton analysis where the linearization is introduced to circumvent the adjoint code [49], to the optimal point, which may change the solution of the nonlinear problem. The EnRML method leverages the Gauss–Newton to iteratively update the state variables, thus partly keeping the nonlinearity of the problem. Further, Chen and Oliver [20] describe the batch-EnRML as the iterative ensemble smoother to assimilate the data at different times for the highly nonlinear problem. This method has been applied extensively for history matching problem [21, 111] but has not gained attention in the CFD community.

### 2.5.3 Ensemble Kalman filter with multiple data assimilation

EnKF can be regarded as the Gauss–Newton method, where the averaged sensitivity matrix and a full step in the search direction are adapted. While a full Gauss–Newton step in the early iterations may arise overcorrections on the state variables when the model output is far from the data. From this point of view, Emerick et al. [44] proposed the ensemble smoother with multiple data assimilation to alleviate the drawbacks by inflating the observation errors. They demonstrated the outperformance of EnKF-MDA to EnKF for data match and uncertainty quantification.

From the Bayesian formulation, it can be illustrated to represent a single EnKF step with recursion of the likelihood as:

$$(2.19) \quad f(\mathbf{x} | \mathbf{y}) \propto f(\mathbf{x}) \prod_{i=1}^{N_{\text{mda}}} f(\mathbf{y} | \mathcal{H}[\mathbf{x}_{i-1}])^{\frac{1}{\alpha_i}}$$

The parameter  $\alpha_i$  is subject to  $\sum_{i=1}^{N_{\text{mda}}} \alpha_i = 1$  where  $N_{\text{mda}}$  is the total iteration number in one data assimilation window. The model and observation error covariance is estimated the same as in EnKF. Further, we can obtain the analysis scheme of EnKF-MDA as:

$$(2.20) \quad \mathbf{x}_{i,j}^a = \mathbf{x}_{i,j}^f + \mathbf{P}_i \mathbf{H}^\top (\mathbf{H} \mathbf{P}_i \mathbf{H}^\top + \alpha_i \mathbf{R})^{-1} (d + \sqrt{\alpha_i} \epsilon_{i,j} - \mathbf{H} \mathbf{x}_{i,j}^f)$$

The choice of  $N_{\text{mda}}$  can be constant or a decreasing function which need some trials and errors. Le et al. [89] proposed an adaptive ensemble smoother with multiple data assimilation to adaptively choose the inflation factor.

## 2.6 Hybrid data assimilation methods

Variational DA methods and the ensemble-based DA methods are now both intensively used. Ensemble-based DA methods aforementioned only perform the linear update in the search direction. Hence, for the nonlinear scenario, the variational method with optimization techniques can outperform to ensemble methods. On the other hand, variational methods need much extra effort for the adjoint code to calculate model derivation, while ensemble-based DA methods can give an estimation of the model gradient with the ensemble realizations, thus circumventing the need for the adjoint model. This motivates the occurrence of the hybrid data assimilation method to combine the variational methods and the ensemble-based methods, thereby keeping the merits from both. In this section, we give a brief introduction to three commonly used hybrid methods.

### 2.6.1 Hybrid methods

From Bayes' formulation, the posterior is analyzed from prior explicitly. Hence, the posterior results with data assimilation are very sensitive to the prior statistics. That is, the proper prior

statistics is critical for the performance and robustness of the Bayesian analysis. However, to characterize the prior statistics is significantly difficult [5]. To this end, Hamill and Snyder [64] proposed to blend the model error covariance from the variational method and that one from the ensemble-based DA method as:

$$(2.21) \quad \mathbf{P} = \alpha \mathbf{B} + (1 - \alpha) \mathbf{X}^f (\mathbf{X}^f)^\top,$$

where  $\mathbf{B}$  is the error covariance as in variational DA method and  $\mathbf{X}^f$  is the matrix of the ensemble anomalies. By changing the  $\alpha$  from 0 to 1, the covariance changed from the flow-dependent, ensemble-based covariance to the original covariance used in variational DA scheme. By doing so, the model covariance does not strictly depend on either of these two approaches, and the sampling error in the ensemble-based statistics can be alleviated by the added variational method. Zhang and Zhang [151] coupled the EnKF with 4DVar and demonstrated that this hybrid method is more effective than the EnKF and 4DVar on a Lorenz96 model.

### 2.6.2 Ensemble-based variational methods

The notable weakness of the variational method is the demand for the adjoint code, which needs the tedious task for complex computational models. While the ensemble-based method can give an estimation on the model derivative with the Monte Carlo samples, thereby circumventing the adjoint code, but use the optimization method implicitly. The ensemble-based variational method [94] is proposed to combine the variational data assimilation method with EnKF. The prior statistics are estimated with the Monte Carlo sampling technique, and the adjoint operator is estimated by the ensemble samples as the ensemble-based methods. Under several mild assumptions, this method transforms the problem to be the optimal control problem where the optimal control vector can be searched in the subspace with the explicit optimization approach, such as Gauss–Newton or BFGS method. On the other hand, only the ensemble mean is updated, and the distributions are re-estimated at each DA iteration, which can ease the influence from the improper prior and sample collapse.

In the EnVar scheme, the ensemble of state vector can be expressed as

$$(2.22) \quad \mathbf{X} = \bar{\mathbf{X}} + \mathbf{E}' \beta,$$

where  $\beta$  is the control vector.  $\mathbf{E}'$  is the ensemble anomalies as:

$$(2.23) \quad \mathbf{E}' = (\mathbf{X}_1 - \bar{\mathbf{X}}, \mathbf{X}_2 - \bar{\mathbf{X}}, \dots, \mathbf{X}_M - \bar{\mathbf{X}}).$$

Further, the cost function  $J$  is formulated as:

$$(2.24) \quad J = \frac{1}{2} \|\mathbf{X} - \bar{\mathbf{X}}\|_{\mathbf{P}}^2 + \frac{1}{2} \|\mathbf{d} - \mathbf{y}\|_{\mathbf{R}}^2,$$

where  $\mathbf{d}$  is the RANS realizations in observation space based on state vector  $\mathbf{X}$ ,  $\mathbf{y}$  is the observation. The difference between RANS prediction in observed quantities and the observation, weighed

by the ensemble covariance  $\mathbf{P}$  and observation error covariance  $\mathbf{R}$ , respectively.  $\mathbf{d}$  can be realized by the linearizations as in the following formulas:

$$(2.25) \quad \mathbf{d} = \mathcal{H}[\bar{\mathbf{X}}] + H' \beta$$

$$(2.26) \quad H' = (\mathcal{H}[\mathbf{X}_1] - \mathcal{H}[\bar{\mathbf{X}}], \mathcal{H}[\mathbf{X}_2] - \mathcal{H}[\bar{\mathbf{X}}], \dots, \mathcal{H}[\mathbf{X}_M] - \mathcal{H}[\bar{\mathbf{X}}]).$$

Using  $\mathbf{P} \simeq \frac{1}{N_{en}-1} E' E'^\top$  and substituting  $\mathbf{X}$  with Eq. (2.22), the cost function in Eq. (2.24) can be rewritten as a quadratic equation on control vector  $\beta$ :

$$(2.27) \quad J = \frac{1}{2}(M-1)\beta\beta^\top + \frac{1}{2}\|\mathcal{H}[\bar{\mathbf{X}}] + H'\beta - \mathbf{y}\|_{\mathbf{R}}^2.$$

The gradient and Hessian of  $J$  can be derived as:

$$(2.28) \quad \frac{\partial J}{\partial \beta} = (M-1)\beta + H'^\top \mathbf{R}^{-1}(\mathcal{H}[\bar{\mathbf{X}}] + H'\beta - \mathbf{y}),$$

$$(2.29) \quad \frac{\partial^2 J}{\partial^2 \beta} = (M-1)\mathbf{I} + H'^\top \mathbf{R}^{-1} H'.$$

In order to minimize the cost function (2.27), one iteration of gradient (downhill) method is performed with Eq. (2.28) and Eq. (2.29). The obtained  $\beta$  is used to update the state vector  $\alpha$  according to Eq. (2.22).

### 2.6.3 Iterative ensemble Kalman filter

Sakov et al. [126] proposed the iterative ensemble Kalman filter to address the strongly nonlinear system. They [12] further extended the approach as the iterative ensemble Kalman smoother to be comparable to 4DVar. To be simplified, the associated cost function for a stationary system can be formulated as:

$$(2.30) \quad J = \frac{1}{2}\beta\beta^\top + \|\mathbf{y} - \mathcal{H}[\bar{\mathbf{X}} + E'\beta]\|_{\mathbf{R}}^2,$$

where  $\beta$  is the control vector,  $E'$  is the ensemble anomalies;  $\mathcal{H}$  is system model which map the state to the observation space.

The minimization of the cost function can be performed in the subspace spanned by the ensemble realizations with different optimization approaches, such as Gauss–Newton method [10], Levenberg–Marquardt method [96], or the trust–region method [124]. Similar to EnVar, the update scheme with Gauss–Newton method can be formulated as:

$$(2.31) \quad \beta^a = \beta^f + \left( \frac{\partial^2 J}{\partial^2 \beta} \right)^{-1} \frac{\partial J}{\partial \beta}$$

However, the implementation of estimating  $\mathcal{H}'[E']$  is different from the EnVar based on the linear assumption. Sakov et al. advocate to use the finite-difference estimate of the tangent linear operate as follow:

$$(2.32) \quad H' = \frac{1}{\varepsilon} \left( \mathcal{H} [\bar{\mathbf{X}} + \varepsilon E'] - \frac{1}{M} \mathcal{H} [\bar{\mathbf{X}} + \varepsilon E'] \mathbf{1} \right),$$

where  $\mathbf{1} = [1, 1, \dots, 1]^\top$  is the vector of  $M$ , and  $\varepsilon \ll 1$  is the scaling factor or *bundle* variant. The anomalies update is computed using an approximate Hessian of this cost function, using the retrospective ensemble analysis as:

$$(2.33) \quad E'^a = \sqrt{M-1} E'^f \left( \frac{\partial J^2}{\partial^2 \beta} \right)^{-1/2} \mathbf{U},$$

where  $\mathbf{U}$  is the orthogonal matrix. IEnKS is well understandable at the theoretical level, and its performance has been supported by many numerical evidence (Lorenz models [10, 11], 2D turbulence [12] and 2D barotropic vorticity model [9]). It not only can keep the merits of 4DVar for nonlinear problems and but also that of EnKF for the flow dependence of the error statistics.

## 2.7 Particle filtering

The above derived ensemble-based methods are all the approximate Bayesian methods based on several mild assumptions (e.g., the linearization and the Gaussian distribution). As for the exact Bayesian analysis, the big obstacle is the calculation of conditioned probability density, at least for the high dimension cases. Moreover, within the approximate Bayesian method, the Gaussian assumption is applied for the prior and likelihood function. That may lead to wrong solutions when considering the strong nonlinearity and the non-Gaussian distribution in many realistic systems. Hence, the direct approach, namely particle filter (PF) or the sequential Monte Carlo, is proposed in the data assimilation community and worth attention for future investigations.

In PF, the posterior distribution can be expressed as a weighted sum of delta-Dirac masses. Each one is centered on  $\mathbf{x}_k^n$ .

$$(2.34) \quad p(\mathbf{x}_k | \mathbf{y}_{k-1:}) = \sum_{n=1}^N \omega_{k-1}^n \delta(\mathbf{x}_k - \mathbf{x}_k^n),$$

where  $\mathbf{x}^n$  refers to the  $n$  th particles (i.e., ensemble samples),  $\mathbf{y}_{k:}$  is the sequence of the observation from the far past to the current time  $k$ ,  $\mathbf{y}_{k:} = \mathbf{y}_k, \mathbf{y}_{k-1}, \dots, \mathbf{y}_0$ .  $\delta$  is the Dirac measure at the time  $k$ .  $\omega$  is the importance weight which needs to be normalized to one as:

$$(2.35) \quad \sum_{n=1}^N \omega_{k-1}^n = 1.$$

The analysis step in particle filter is constructed from the Bayes theorem:

$$(2.36) \quad p(\mathbf{x}_k | \mathbf{y}_{k:}) \propto p(\mathbf{x}_k | \mathbf{y}_{k-1:})p(\mathbf{y}_k | \mathbf{x}_k^n) = \sum_{n=1}^N \omega_{k-1}^n p(\mathbf{y}_k | \mathbf{x}_k^n) \delta(\mathbf{x}_k - \mathbf{x}_k^n).$$

Thus, the normalized importance weights can be expressed:

$$(2.37) \quad \omega_k^n \propto \omega_{k-1}^n p(\mathbf{y}_k | \mathbf{x}_k^n).$$

The proportionality factor in the above formula needs to take into account the condition that the normalized updated weights summing up to 1. By applying Chapman-Kolmogorov equation, the analysis can be further simplified as:

$$(2.38) \quad \begin{aligned} p(\mathbf{x}_{k+1} | \mathbf{y}_{k:}) &= \int d\mathbf{x}_k p(\mathbf{x}_{k+1} | \mathbf{x}_k) p(\mathbf{x}_k | \mathbf{y}_{k:}) \\ &= \sum_{n=1}^N \int d\mathbf{x}_k p(\mathbf{x}_{k+1} | \mathbf{x}_k) \omega_k^n \delta(\mathbf{x}_k - \mathbf{x}_k^n) \\ &= \sum_{n=1}^N \omega_k^n p(\mathbf{x}_{k+1} | \mathbf{x}_k^n). \end{aligned}$$

There are two approaches to implement the particle filtering. One is sequential importance sampling (SIS) particle filter or bootstrap PF [59] to obtain a delta-Dirac pdf from Eq. (2.38). For each particle, we sample  $\mathbf{x}_{k+1}^n$  from the density  $p(\mathbf{x}_{k+1} | \mathbf{x}_k^n)$  by simply forecasting  $\mathbf{x}_k^n$  from  $t_k$  to  $t_{k+1}$  using the (possibly stochastic) model associated with the transition density  $p(\mathbf{x}_{k+1} | \mathbf{x}_k)$ , which yields:

$$(2.39) \quad p(\mathbf{x}_{k+1} | \mathbf{y}_{k:}) \approx \sum_{n=1}^N \omega_k^n \delta(\mathbf{x}_{k+1} - \mathbf{x}_{k+1}^n)$$

The another one is sequential importance resampling PF which add the resampling step before the forecast to avoid the sample degeneracy. That is, when the effective particle number is less than the threshold one, we need resample  $N$  particles from current statistic with consideration of their importance weight to replace the origin particles. Then the equivalent weight  $\omega = 1/N$  is put on these new particles which yields:

$$(2.40) \quad p(\mathbf{x}_{k+1} | \mathbf{y}_{k:}) \approx \frac{1}{N} \sum_{n=1}^N \delta(\mathbf{x}_{k+1} - \mathbf{x}_{k+1}^n)$$





## Chapter 3

# Bayesian Optimisation of RANS Simulation with Ensemble-based Variational Method in Convergent–Divergent Channel

### 3.1 Introduction

Despite significant development of Computational Fluid Dynamics (CFD) for several decades, the high-fidelity resolution Direct Numerical Simulation (DNS) and Large Eddy Simulation (LES) is still computationally intractable for most applications, especially with high Reynolds numbers. Reynolds-Averaged Navier-Stokes (RANS) simulation will remain dominant for industrial applications in the near future. However, it has been noted that RANS model cannot make accurate predictions for the turbulent flows in the convergent-divergent channel where there exist mean curvature and pressure gradient, due to the ambiguous boundary condition and the inadequate turbulence model. On the other hand, experimental investigations have to be faced with the challenges of the sparse measurements in the limited observable field, noise contamination and insufficient resolution for the small scale flow. To address these issues, data assimilation (DA) approach widely used in the oceanography and geography gains the spotlights over the past few years in the turbulence community. Based on Bayes theorem, data assimilation can integrate the low-fidelity RANS calculation with the high-fidelity resolution from LES/DNS or sparse experimental measurements to infer the unknown boundary condition or underlying model information and thus optimize the RANS predictions.

Data assimilation can be sorted by variational data assimilation method, Ensemble Kalman Filter (EnKF) method, and hybrid methods. All these methods leverage the Maximum a Posteriori (MAP) estimation, while in the variational method, MAP is formulated as the

minimization of the cost function through adjoint optimal least square techniques. A body of works based on the variational method has demonstrated its inferential performance and robustness to replicate the flow status. A. Gronsksis et al. [61] established a data assimilation framework based on the variational method incorporating with adjoint optimization method to generate the inflows condition for DNS. Foures et al. [51] applied the variational method to minimize the discrepancy between the time-averaged velocity fields of a DNS resolution and an incompressible RANS simulation for the two-dimensional flow past a circular cylinder at a Reynolds number of  $Re = 150$ . S. Symon et al. [134] applied the variational method to reconstruct the flows with relatively high Reynolds number of 13500 around an idealized airfoil by assimilating the mean velocity field from time-averaged Particle Image Velocimetry (PIV) measurements.

Also, the EnKF method where the state statistics are updated with an ensemble of realizations, have been intensively applied to quantify and reduce the uncertainty in RANS simulation. Colburn et al.[23] used EnKF to estimate the near-wall turbulent flow based on the wall information from DNS resolution. Kato and Obayashi [79] applied EnKF to infer the optimal parameters in the Spalart-Allmaras turbulence model for zero-pressure gradient flat plate boundary layer at Mach number of 0.2 and Reynolds number of  $5 \times 10^6$ . They [80] also used the Ensemble Transform Kalman Filter to integrate the CFD and experimental fluid dynamics (EFD) to replicate the transonic turbulent flows over RAE 2822 airfoil and ONERA M6 wing through estimating the proper angle of attack, Mach number, and turbulent viscosity. Xiao et al. [148] introduced uncertainty in Reynolds stress directly and adopted an iterative ensemble Kalman method to reduce the model-form uncertainty in  $k$ - $\epsilon$  model for the flow over periodic hills and the flow in a square duct by assimilating very sparse observations.

Despite both the variational data assimilation method and EnKF have demonstrated their applicability for the Bayesian optimization of CFD problems, the intrusiveness of variational method makes it difficult to implement, and the high sensitivity to the prior statistics for EnKF causes the inference results prone to be inferior. Recently, a hybrid method, namely ensemble-based variational method(EnVar), gains attention to solve the inverse problem for CFD simulation with both robustness and non-intrusiveness. Mons et al. [107] first explored the applicability of this kind of data assimilation technique into unsteady flows with coherent gust and assessed the robustness of variational data assimilation method, Ensemble Kalman Smoother and EnVar method to reconstruct the flows around a cylinder. They demonstrated that the ensemble-based variational method could be robust as the variational method and circumvent the efforts on the adjoint model by estimating the prior statistics with ensemble realizations. Meanwhile, the inferential performance can be very satisfactory and is not very sensitive to prior and observation statistics comparing to ensemble Kalman smoother.

The current study investigates the applicability of the ensemble-based variational method to optimize the RANS simulation from the perspective of inferring improved inlet boundary

condition and underlying model corrections by incorporating with DNS resolution or sparse experimental observation. The test cases from low dimension ( $D=20$ ) to high dimension ( $D=2400$ ) of input parameters all demonstrated the merits of the proposed approach. It is worth noting that the limited observation from the PIV experimental measurements is also integrated with RANS simulation to recover the flow status.

The rest of this paper is structured as follows. The ensemble-based variational scheme is presented in Section 3.2. The CFD code and the practical implementation of the data assimilation framework are described in Section 3.3. The applications of this framework to infer inlet velocity and model corrections are presented in Section 3.4 and Section 3.5, respectively. Section 3.6 is dedicated to the conclusion and perspectives.

## 3.2 Data assimilation framework

### 3.2.1 Ensemble-based variational scheme

The ensemble-based variational method is a hybrid data assimilation approach that combines the variational data assimilation method with EnKF. Compared to the variational method, the formulation of EnVar uses a Monte Carlo ensemble to estimate the prior statistics thus circumventing the efforts on the adjoint operator. This method equates MAP to the optimal control problem where the optimal control vector is searched based on gradient-descent optimization to update prior information. Meanwhile, the prior distributions are re-estimated at each DA iteration thus counteracting the influence from the improper prior, while in EnKF scheme the Kalman gain matrix to update the prior distribution, is directly constructed from the approximated prior statistics.

The state vector is the input parameters, representing the quantities to be inferred. For simplification, the vector is assumed to be Gaussian distributed. The mean of this normal distribution corresponds to the initial guessed or prior state vector, and the vector can be expressed as

$$(3.1) \quad \alpha = \alpha^{(e)} + E' \beta ,$$

where  $\beta$  is the control vector with dimension of  $N_{en}$ .  $N_{en}$  is the ensemble size.  $E' = (\alpha^{(1)} - \alpha^{(e)}, \alpha^{(2)} - \alpha^{(e)}, \dots, \alpha^{(N_{en})} - \alpha^{(e)})$

Regarding the observation, it is the reference data (e.g., friction/pressure coefficient, velocity fields, and so on) from high-fidelity simulation or experiment that have a substantial influence on the inferred quantities. Random measurement noise in observation is assumed to be Gaussian distributed with zero mean, uncorrelated, and are characterized by the relative standard deviation  $\sigma_o$ . The observation  $y$  can be prescribed as

$$(3.2) \quad y = h(\alpha^+) + \epsilon ,$$

where  $h$  is the observation operator that maps the state space to observation space,  $\alpha^+$  is reference trajectory projecting to the observation and  $\epsilon$  is the possible random measurement

error.

Based on the Bayes theorem, to maximize the posterior is equivalent to minimize the cost function  $J$

$$(3.3) \quad p(\alpha | y) \propto p(\alpha)p(y | \alpha) \propto e^{-J} \rightarrow J = \frac{1}{2}\|\alpha - \alpha^{(e)}\|_{\mathbf{P}^{-1}}^2 + \frac{1}{2}\|d - y\|_{\mathbf{R}^{-1}}^2 ,$$

where  $d$  is the RANS realizations in observation space based on state vector  $\alpha$ ,  $y$  is the observation from DNS solutions or the experimental measurements,  $\|*\|_{\mathbf{P}^{-1}}^2 = *^\top \mathbf{P}^{-1}*$ ;  $\|*\|_{\mathbf{R}^{-1}}^2 = *^\top \mathbf{R}^{-1}*$ . As in (3.3), the cost function  $J$  is composed of two parts: the difference between the prior and its realizations, and the difference between RANS prediction in observed quantities and the observation, weighed by the model error covariance  $\mathbf{P}$  and observation error covariance  $\mathbf{R}$ , respectively.  $d$  can be realized by the linearizations as in the following formula:

$$(3.4) \quad d = h(\alpha^{(e)}) + H' \beta ,$$

$$H' = (h(\alpha^{(1)}) - h(\alpha^{(e)}), h(\alpha^{(2)}) - h(\alpha^{(e)}), \dots, h(\alpha^{(N_{en})}) - h(\alpha^{(e)})) .$$

Using  $\mathbf{P} \simeq \frac{1}{N_{en}-1} E' E'^T$  and substituting  $\alpha$  with (3.1), the cost function in (3.3) can be rewritten as a quadratic equation on control vector  $\beta$ :

$$(3.5) \quad J = \frac{1}{2}(N_{en} - 1)\beta\beta^\top + \frac{1}{2}\|h(\alpha^{(e)}) + H' \beta - y\|_{\mathbf{R}^{-1}}^2 .$$

The gradient and hessian of  $J$  can be derived straightforwardly as

$$(3.6) \quad \frac{\partial J}{\partial \beta} = (N_{en} - 1)\beta + H'^\top \mathbf{R}^{-1}(h(\alpha^{(e)}) + H' \beta - y) ,$$

$$(3.7) \quad \frac{\partial^2 J}{\partial^2 \beta} = (N_{en} - 1)I + H'^\top \mathbf{R}^{-1} H' .$$

In order to minimize the cost function (3.5), one iteration of Newton CG method is performed with (3.6) and (3.7). The obtained  $\beta$  is used to update the state vector  $\alpha$  according to (3.1). This iterative process is continued until the converge criterion is reached. The procedure of the ensemble-based variational method is shown in Figure 3.1 and the details can be summarized as follows:

*Step 1.* Give a first guessed or prior state vector  $\alpha^{(e)}$ , and prescribe the prior and observation statistics respectively;

*Step 2.* Realize  $N_{en}$  samples around the mean vector  $\alpha^{(e)}$ ;

*Step 3.* Propagate each sample of state vector to observation space through solving RANS equation;

*Step 4.* Analyze the control vector  $\beta$  by minimizing cost function with (3.6) and (3.7);

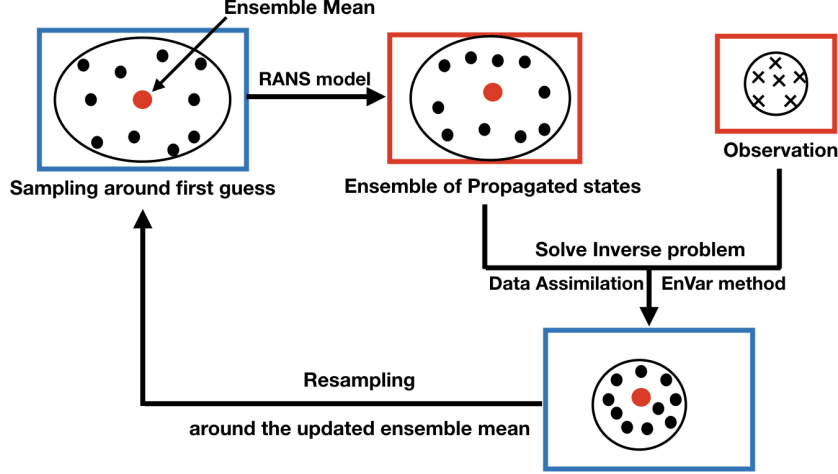


Figure 3.1: Schematic illustration of EnVar method

*Step 5.* Update the mean of state vector with the analyzed control vector  $\beta$  based on (3.1);

*Step 6.* Return to *Step 2* and resample around the updated ensemble mean until the fitting criterion or maximum iteration is reached.

### 3.2.2 Fitting criterion

The goal of the data assimilation approach is to best fit the numerical prediction with DNS or experiments. Hence in order to evaluate the optimal performance, it is first necessary to calculate the ratio of cost function value before and after the data assimilation process in order to assess the extent to which the cost function is reduced. The ratio of cost function  $J$  can be defined as:

$$(3.8) \quad r_J = \frac{J_{end}}{J_0} .$$

Moreover, the cost function is constituted of two parts as illustrated in the formula (3.5) and thus reduction of the cost function may not directly reflect the decrease of the discrepancy between the numerical prediction and the observation in the quantities of interest. Therefore, the formula (3.9) is introduced to measure this distance:

$$(3.9) \quad J_{ob} = \frac{1}{2} \|y - h(\alpha^{(e)})\|^2 ,$$

where  $\| \cdot \|$  is Euclidean norm. In this work, the data assimilation process is terminated as  $J_{ob} < 10^{-3}$ . The ratio of the assimilated and initial  $J_{ob}$  is also introduced to evaluate the efficiency of the optimization process

$$(3.10) \quad r_{J_{ob}} = \frac{J_{ob_{end}}}{J_{ob_0}} .$$

### 3.3 Numerical setup

#### 3.3.1 CFD solver

A 2D steady incompressible solver is used to perform the numerical simulations on two-equation RANS turbulence model. The governing equations can be expressed as:

$$(3.11) \quad \text{div}(F_c - F_v) = \mathbf{S} ,$$

$$\text{with } F_c = \begin{pmatrix} \rho u & \rho v \\ \rho u^2 + p & \rho uv \\ \rho uv & \rho v^2 + p \end{pmatrix} \text{ and } F_v = \begin{pmatrix} 0 & 0 \\ 2\mu S_{xx} + \tau_{xx} & 2\mu S_{xy} + \tau_{xy} \\ 2\mu S_{xy} + \tau_{xy} & 2\mu S_{yy} + \tau_{yy} \end{pmatrix} ,$$

where  $\rho$  is density;  $u$  and  $v$  is stream-wise and wall-normal mean velocity;  $F_c$  and  $F_v$  denote the convective and viscous flux densities;  $\mu$ ,  $S$  and  $\tau$  represent molecule viscosity, mean strain rate, and Reynolds stress respectively;  $\mathbf{S}$  is the source term.

The Reynolds stress term  $\tau$  is modelled by Menter's  $k - \omega$  SST model [102]. And the code uses the HPLA (Hybrid Linear / Parabolic Approximation) non-oscillatory second-order scheme for the convective term. The SIMPLE (Semi-implicit Method for Pressure-Linked Equations) algorithm is applied to solve the coupled mass and momentum conservation equations, on two-dimensional structured curvilinear-orthogonal meshes.

The non-slip condition is used on the wall. The first grid for all cases in this paper is well placed in the viscous layer and the wall function is not incorporated therefore to eliminate the effects of assumptive wall boundary condition.

#### 3.3.2 Data assimilation implementation

Firstly, an initial guess of the input parameter is given as prior, and then  $N_{en}$  samples are constructed around the first guess based on Gaussian process. To ensure the smoothness of the obtained samples, a non-diagonal covariance matrix to describe the prior distribution is prescribed as:

$$(3.12) \quad \Sigma_{i,j} = \sigma(x_i)\sigma(x_j)b^2 \exp\left(-\frac{\|x_i - x_j\|^2}{l_c^2}\right) ,$$

where the variance  $\sigma(x)$  is constructed based on the discrepancy between the prediction from initial RANS simulation and the observation in order to inform where large or small perturbations are expected;  $b$  refers to the characteristic values, for inlet velocity reconstruction

it is based on inlet bulk velocity while for model correction inference, it is taken as 1;  $l_c$  is constant correction length based on the height of the channel at inlet;  $x_i$  refers to the position of the  $i$ th control volume. With mean vector  $\alpha^{(e)}$  and covariance matrix  $\Sigma_{i,j}$ , the  $N_{en}$  samples around the first guess could be realized.

The observation error is assumed to be the uncorrelated Gaussian distribution with zero mean. For simplification, the covariance matrix  $R$  is constructed as a diagonal matrix based on the observation error which is defined as  $\epsilon\epsilon^\top$ . The resolution in the observation space is mapped from the state vector forwardly with CFD solver. The posterior is obtained by solving the Bayesian optimization problem based on the ensemble-based variational scheme. For the optimization method, Newton-CG is used to minimize the cost function.

### 3.4 Inlet velocity inference

The proper inlet velocity has critical implications for the performance of numerical prediction, and many forward methods have been proposed to generate the inflow condition for DNS and LES, such as the recycling-based method and synthetic turbulence generators [146], whereas high computational efforts are required in these methods. In this section, the ensemble-based variational method is explored to infer the inlet velocity profile based on the limited quantities from DNS resolution or experimental measurements. Two test cases are used to evaluate the performance of the data assimilation scheme on the reconstruction of the inlet velocity profile. The first one is turbulent flow in the WallTurb Bump where DNS dataset is available, and the other one is non-cavitating flow in Venturi where the experimental X-ray measurements can be considered as the reference data. A summary of data assimilation experiments for inlet velocity inference is given in Table 3.1.

Geometry	$\alpha$	Prior	$\dim(\alpha)$	$y$	$N_{en}$	$r_J$	$r_{J_{ob}}$
Bump	inlet velocity	parabolic	30	$C_f$	30	0.0025	0.20
		flat				0.002	0.157
Venturi		parabolic	20	$u$	20	$2.7 \times 10^{-4}$	$2 \times 10^{-5}$

Table 3.1: Data assimilation results for inlet velocity inference

#### 3.4.1 WallTurb Bump

##### 3.4.1.1 Flow configuration

The turbulent flow in WallTurb Bump [97] is one canonical flow and widely used to verify the performance of numerical methods [88][85][73]. The Reynolds number for this flow is 12600. The computational domain is  $-5.22 < x < 7.34; 0 < y < 2$ . In order to simulate this flow, the structured curvilinear-orthogonal mesh is generated with 125 cells in stream-wise direction and

60 cells in the normal-to-wall direction. The  $y^+$  of first mesh adjacent to the wall is around 1. The mesh of the WallTurb Bump is shown in Figure 3.2.

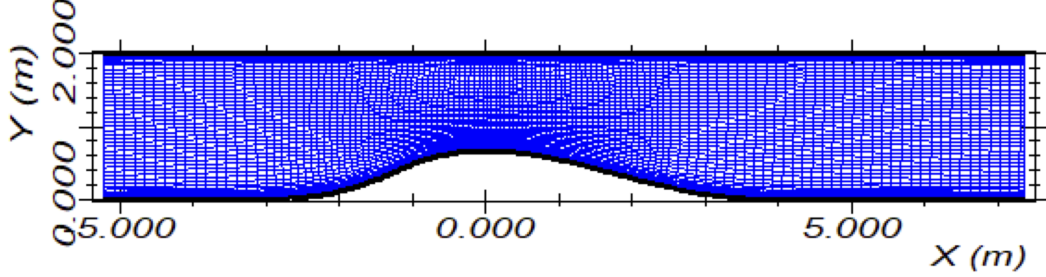


Figure 3.2: Mesh of WallTurb Bump

For the setup of data assimilation, the input parameters are the lower half of inlet velocity with the dimension of 30, and the ensemble size  $N_{en}$  is set to be consistent with the dimension of input space. The variance field  $\sigma$  is based on the discrepancy field of the prior inlet velocity and the DNS velocity with a multiplication of  $10^{-3}$ . The value of multiplication need some trials and errors since large variance will increase the spatial extent of subspace where the optimal solution is searched, and thus result in the instability of the optimization process, while too small variance will make the process robust but very slow.

In order to infer the inlet velocity profile for this case, the friction coefficient  $C_f$  is regarded as the observation in consideration of the strong correlation between the velocity and the friction coefficient. The skin friction coefficient is defined by:

$$C_f = \frac{\tau_w}{0.5\rho U_{ref}^2}$$

where  $\tau_w$  is the wall shear stress  $\tau_w = \mu \frac{du}{dy}|_{y=0}$  and  $U_{ref}$  is reference velocity, which is taken as the dimensionless inlet bulk velocity 1. Since presumably the friction coefficient is not sensitive to the inlet condition in the region with the bump where the flow encounters the strong pressure gradient, the observation is confined near the inlet region and exclude the part adjacent to the inlet. Thus, the observation includes the friction coefficient on the bottom wall from  $x = -4.2$  to  $-1.9$ , and the standard deviation of observation error is taken as  $5 \times 10^{-4}$ .

The Newton-CG method is applied to minimize the cost function. As in this case the ensemble size is quite small, the Hessian of the cost function can be explicitly expressed, and the Newton-CG is more robust compared to the quasi-Newton method with approximated Hessian matrix such as BFGS. The comparison of Newton CG and implicit BFGS method to infer inlet velocity for the bump is presented in Appendix A.1.



### 3.4.1.2 Physical constraints

Due to the non-uniqueness of the optimal solution, data assimilation process may result in the inferred inlet velocity losing physical meaning, for instance too high velocity adjacent to the wall and non-symmetric inlet velocity profile for this case, which may also bring about the divergence problem for CFD solver. Therefore, three constraints are given based on physical knowledge. Firstly, the dimensionless velocity at the first grid to the bottom wall is fixed at  $2 \times 10^{-3}$  via interpolation from DNS resolution to avoid the steep velocity gradient near the boundary and have a reasonable  $y^+$  at the inlet. Secondly, the reconstructed inlet velocity profile may lead to the variation of flux and accordingly change the flow condition. Therefore, the flux at the inlet is corrected after each data assimilation iteration, by multiplying the ratio of the updated flux and reference flux to ensure the flux constant. Besides, in this case, the inflow into the channel should be developed turbulent flow and presumably symmetric. On the other hand, only the friction coefficient on the bottom wall is considered as the observation; hence the inlet velocity near the top wall is not able to be recovered due to lack of information. Thus only the bottom half profile is taken as the input parameter, while another half is constructed by symmetric projection.

### 3.4.1.3 Results

Two different first guess is imposed as the prior inlet velocity: the parabolic and the flat profile. The assimilated results of inlet velocity and observed friction coefficient are presented in Figure 3.3 with the comparison to the prior and DNS. The inferred inlet velocity profiles are both quite close to the DNS data as shown in Figure 3.3(a)(c). Accordingly, the predictions in terms of friction coefficient presented in Figure 3.3(b)(d) also have a good agreement with DNS data in the observed region. Generally, both cases can obtain a good inference on inlet velocity and improve the prediction on  $C_f$  by assimilating the friction coefficient from DNS.

Figure 3.4 shows the evolution of cost function to the iteration number. For both cases, the cost function is reduced significantly while with the prior of parabolic profile the minimization is more efficient and converged in the first five iterations. In concrete, the cost function  $J$  reduces from 32386 to 80 in the case with parabolic prior, and the ratio  $r_J \approx 0.0025$ , while for the prior with flat inlet profile, the cost function  $J$  reduces from 57607 to 114 and  $r_J \approx 0.002$ . The norm of discrepancy between numerical prediction and reference with first guessed parabolic inlet velocity is reduced from 0.0155 to 0.0031 and  $r_{J_{ob}} \approx 0.20$  while the discrepancy for the case with the flat inlet velocity profile can be reduced from 0.0191 to 0.0030 and  $r_{J_{ob}} \approx 0.157$ .

The contour plots of the velocity  $U$  field with first guessed parabolic velocity are presented in Figure 3.5. The visible improvements can be observed near the inlet and the favorable pressure gradient region. However, in the adverse pressure gradient region, the prediction is not improved with optimal inlet velocity, which is not surprising since it is a consensus that RANS model cannot give good predictions with confidence when it encountered strong adverse

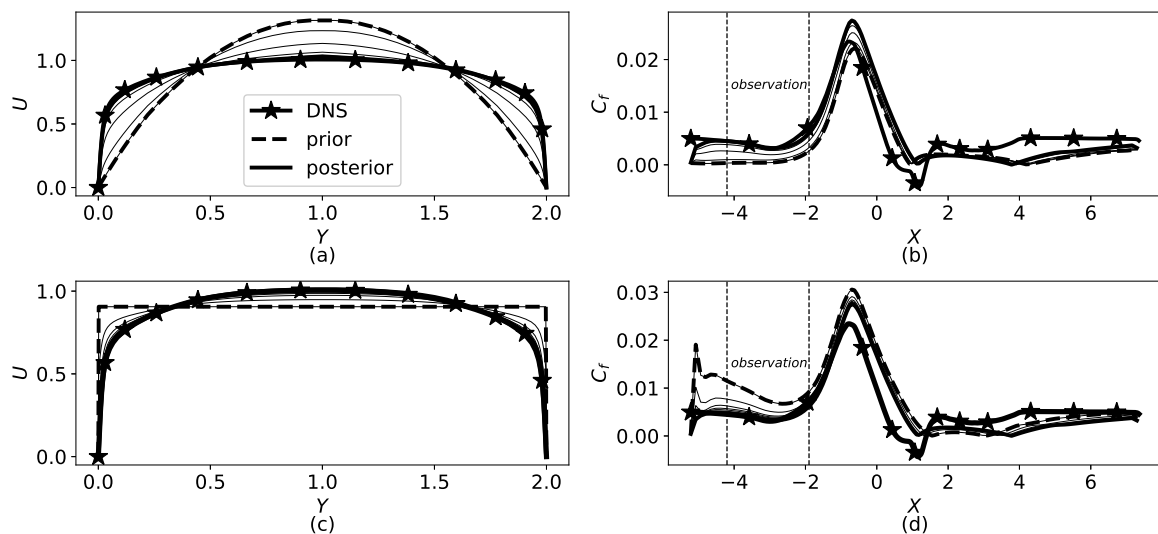


Figure 3.3: Data assimilation results about the inferred inlet velocity and the prediction in  $C_f$ : (a) (b) for the prior of parabolic velocity; (c) (d) for the prior of flat velocity

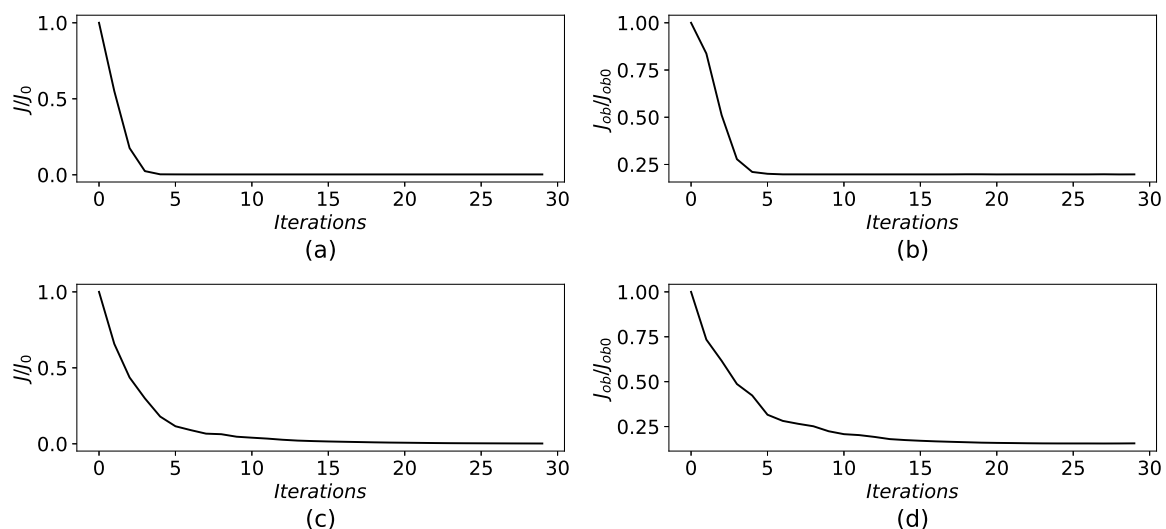


Figure 3.4: Data assimilation results of cost function  $J$  and  $J_{ob}$ : (a)(b) for the prior of parabolic inlet velocity; (c)(d) for the prior of flat inlet velocity

pressure gradient. A large-scale separation after the summit of the bump can be seen in RANS calculation, whereas in the DNS solution the reattachment occurs in the downstream near the starting point of separation and thus there is no noticeable separation. In other words, the prediction of velocity  $U$  in the adverse pressure gradient region is insensitive to the inlet velocity, and the poor prediction may be due to the RANS model inadequacy. This section is mainly to explore the applicability of data assimilation to optimize inlet velocity, so the

uncertainty in the model is not concerned.

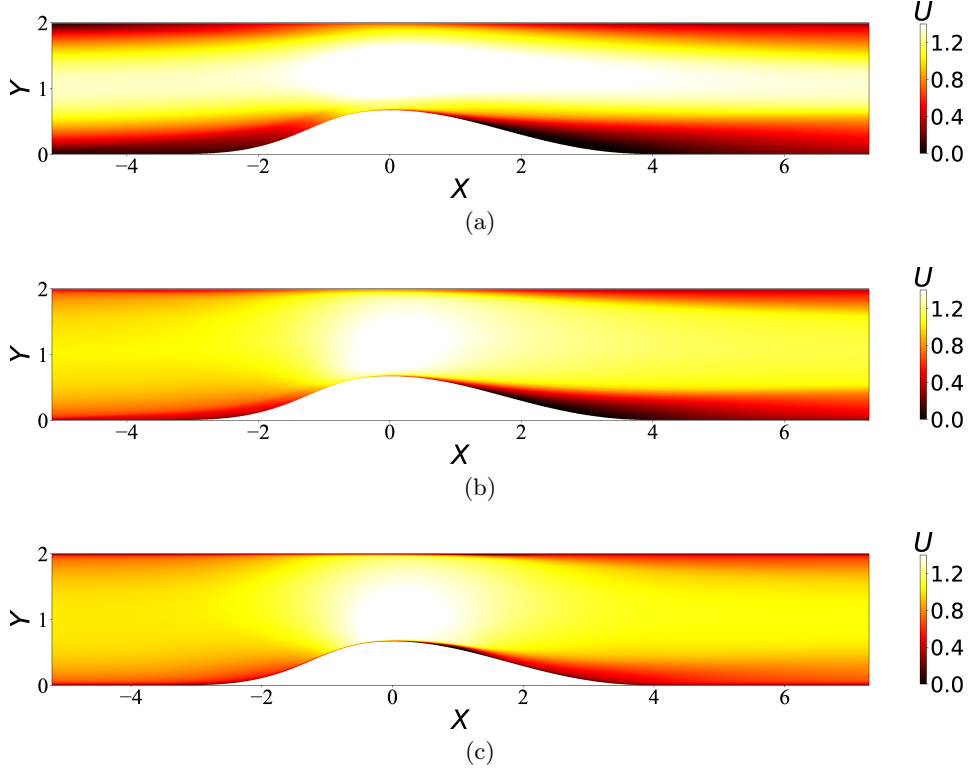


Figure 3.5: Velocity  $U$  field with the first guess of parabolic velocity for prior(a), posterior(b) and DNS(c)

### 3.4.2 Venturi

The second case is for Venturi channel, which is extensively used in the investigations of turbulent cavitating flows [30] [19]. The field information near the throat is quite challenging to be captured by current RANS model due to abrupt curvature change. In this work, the data assimilation approach is applied to infer the proper inlet velocity in non-cavitating flow by assimilating one velocity profile from experimental data.

#### 3.4.2.1 Flow condition

The experiments were conducted by I Khlifa et al. [82]. Through applying ultrafast X-Ray imaging into the turbulent flows, the velocity was measured within a Venturi-type test section with  $18^\circ$  convergence angle and  $8^\circ$  divergence angle. The cross-section in the entry of the Venturi is a rectangle of  $17mm \times 4mm$ , and the height of the throat is  $15.34mm$ . In the experiment, the flux rate is  $55.5L/min$ , representing the entry bulk velocity at  $13.6m/s$ . Reynolds number is  $2.3 \times 10^5$ . The time-averaged velocity  $u$  is obtained by averaging all the instantaneous stream-wise velocity processed from the high speed photography images. For the numerical

setup, the structured mesh is generated with 200 grid in the stream-wise direction and 70 grids in the normal to the wall direction. The  $y^+$  of the first grid near the wall is ranged from 1 to 3. The mesh of the venturi-type section is shown in Figure 3.6.

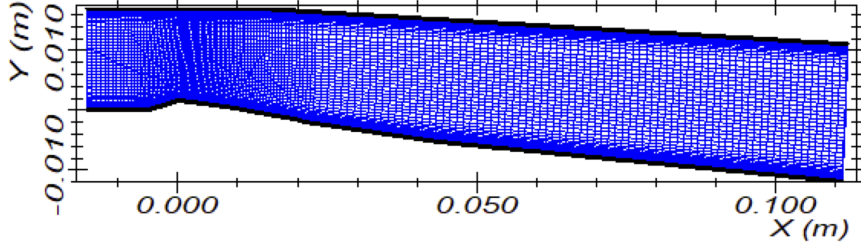


Figure 3.6: Mesh of the Venturi-type section

However, since the measured area is in the adverse pressure gradient region where the velocity field is not sensitive to the inlet condition, the data assimilation experiment within Venturi turned out to be a failure. The results are presented in Appendix A.2. In view of this, we simplified the Venturi geometry as a divergent channel with the resolution domain starting from the throat of the Venturi section. Thus the measured field is quite close to the inlet, and the flow status can be very sensitive to the inlet condition. The structured mesh is generated with 131 cells in the  $x$ -wise direction and 70 cells in the  $y$ -wise direction.

#### 3.4.2.2 Data assimilation setup

In the Venturi-type section, the measured window is placed near the bottom wall and quite small compared to the height of the channel. Therefore, only the inlet velocity profile adjacent to the bottom wall is considered as the input parameters, and the velocity in the other area is fixed at constant 1.1 to keep the flux consistent. The dimension of the input parameters is 20. The velocity at the first grid is also fixed at  $2 \times 10^{-3}$  to have a reasonable  $y^+$ .

As for the observation, the velocity field can be captured by the PIV experimental measurements while other turbulent quantities of interest on the wall such as skin friction coefficient are not straightforward to measure. Hence, we regarded the velocity profile at  $x = 0.0008m$  as the observation which is quite close to the inlet boundary, thereby ensuring that the velocity at this specific position can be affected flexibly by inlet condition. The ensemble size, in this case, is set as 20. The variance  $\sigma(x)$  is constructed based on the discrepancy of the RANS simulation and experimental velocity profile at the observed position and the added multiplication is  $10^{-5}$ . The standard deviation of observation is  $\sigma_o = 10^{-6}$ , which represents high confidence in the experimental data since the observed position and the inlet is almost linearly correlated, and thus the inverse problem is well posed for this case.

### 3.4.2.3 Results

Figure 3.7 shows the assimilated and prior results for inlet velocity and the observed velocity profiles. Figure 3.7(a) presents the evolution of inferred inlet velocity profile every 5 iterations, while Figure 3.7(b) presents the improved prediction on the velocity profile at  $x = 0.0008m$ . It can be seen that EnVar method can reconstruct the inlet velocity to fit quite well with the reference velocity profile at the specific position near the inlet.

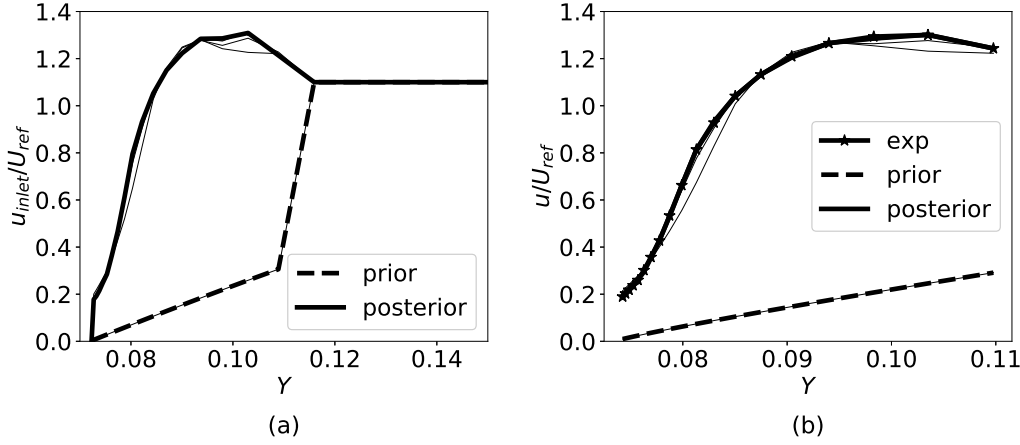


Figure 3.7: Data assimilation results of velocity at inlet(a) and velocity at  $x = 0.0008m$ (b)

Figure 3.8 shows that the evolution of cost function with respect to the iterations. The cost function  $J$  is reduced significantly from  $5.2 \times 10^{11}$  to  $1.4 \times 10^8$  after 20 iterations with ratio  $r_J$  of  $2.7 \times 10^{-4}$  and  $r_{J_{ob}}$  of  $2 \times 10^{-5}$ .

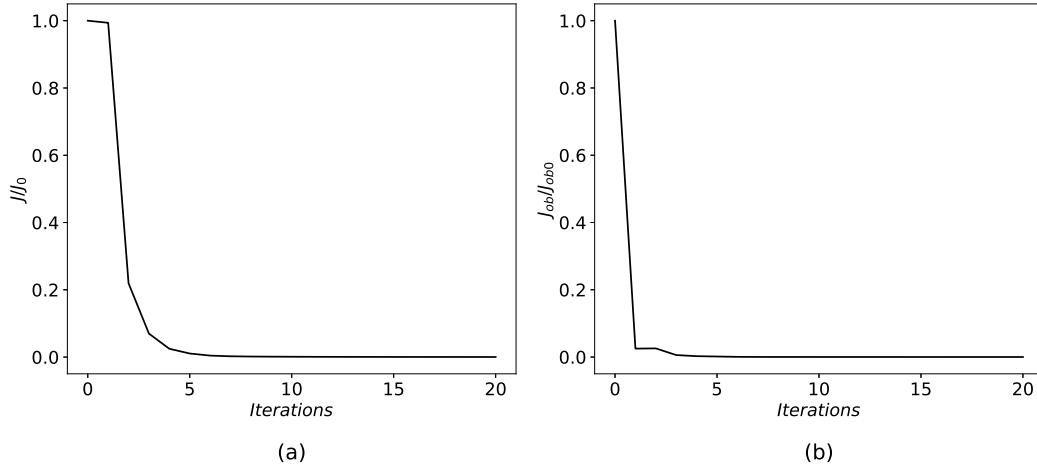


Figure 3.8: Data assimilation results of cost function  $J$ (a) and  $J_{ob}$ (b)

Figure 3.9 presents the contour plots of velocity  $u$  of prior, posterior and experiment. Noticeable improvements can be seen in the observed position  $x = 0.0008m$  comparing to the prior. However, in the other areas, the flow status is entirely different, since substantially the flows in Venturi cannot be represented with the divergent channel.

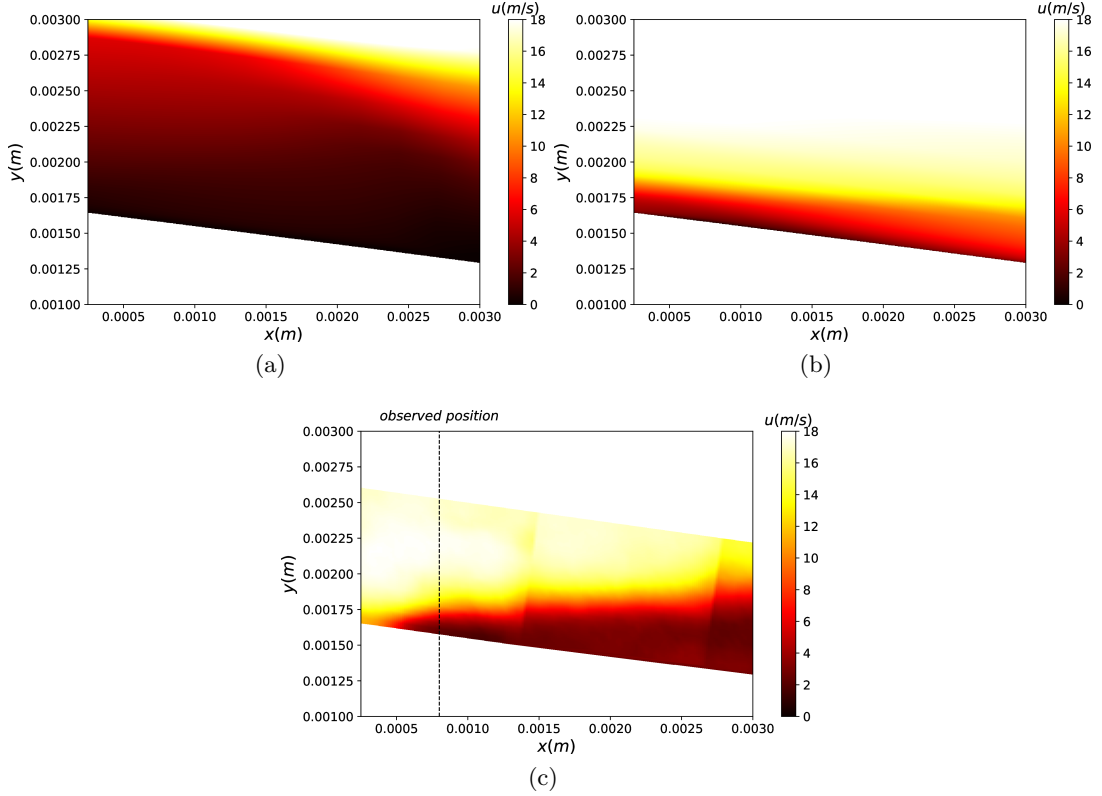


Figure 3.9: Velocity  $u$  field for prior(a), posterior(b) and experiment(c)

### 3.5 Model correction

As illustrated in section 4.2, in Venturi-type section the measured field is mainly in the adverse pressure gradient region, where the velocity is insensitive to the inlet condition, and the RANS method is incapable of making accurate prediction due to the convex curvature. Therefore, in this section, the RANS model-form uncertainty is considered through the field inversion approach [129]. The conventional  $k$  and  $\omega$  transport equation in  $k - \omega$  SST model is inadequate especially in the presence of adverse pressure gradient. Thus, the underlying source term is introduced in the  $k - \omega$  SST model by three different means depending on where the correction terms are inserted (TKE equation or  $\omega$  equation). The sensitivity of these corrections concerning the observation is analyzed, and accordingly, the correction fields are inferred through solving the inverse problem with EnVar approach. The summary of DA experiments for model correction

inference is presented in Table 3.2.

$\alpha$	$dim(\alpha)$	$y$	$N_{en}$	$r_J$	$r_{Job}$
$\beta_c$ in $k$ equation	1200			0.43	0.17
$\beta_c$ in $\omega$ equation	1200	TKE and $u$	50	0.25	0.13
$\beta_c$ in $k$ and $\omega$ equation	2400			0.087	0.13

Table 3.2: Summary of DA experiments for model correction inference

### 3.5.1 Correction in $k$ equation

#### 3.5.1.1 Data assimilation setup

In the TKE transport equation of the  $k - \omega$  SST model, the sum of turbulent-transport term and pressure diffusion term is represented through Boussinesq assumption in analogy to molecular transport process [142] which probably result in poor prediction for complex flows. The correction variable  $\beta_c$  is introduced in front of the production term in TKE transport equation to account for the model uncertainty as:

$$(3.13) \quad \frac{\partial k}{\partial t} + \frac{\partial(u_j k)}{\partial x_j} = \beta_c P - \beta^* \omega k + \frac{\partial}{\partial x_j}[(\nu + \sigma_k \nu_t) \frac{\partial k}{\partial x_j}],$$

which is equivalent to introduce a source term  $(1 - \beta_c) \times P$  in the TKE transport equation. Thus with data assimilation, the flow status can be recovered through finding out the optimal correction field to have a good agreement with reference data.

Since the measurement region is only near the throat, in order to reduce the dimension of input space and guarantee that the inferred correction and observation are locally correlated, the range of input parameters are confined in the area with extension to the observed region instead of the whole computational domain. The correction variables are well imposed on the mesh grids. The dimension of input parameters is 1200 with 40 points along the  $x$ -wise direction and 30 points along the  $y$ -wise direction.

As for the observation, four profiles on the velocity  $u$  and TKE are concerned. For each profile, there are 24 measurement points. Given that the numerical solution is imposed on the mesh points while the experimental data is on a uniform Cartesian grid, to compare the numerical resolution with the measurements, each experimental data is interpolated on the numerical mesh points. Besides, since the initial discrepancy of velocity and TKE causes the weight of the two observed quantities on the cost function to be different, TKE is normalized by multiplying the ratio of the initial discrepancy between prediction and reference data in velocity to that in TKE, thereby keeping them in the consistent range.

For the data assimilation setup, as it is not practical to draw all the samples for high dimension case, we drew 50 samples with truncated Singular Value Decomposition(SVD) which can capture more than 99 percent of the variance. The standard deviation of observation

$\sigma_o$  is  $10^{-1}$ . It is noted that the large observation error represents the experimental instinct uncertainty from both measurements and post-processing[82]. Moreover, because the model error is not considered in this work, it can be regarded as the whole process error including the data error as well as the model error. Also, the strong non-linearity for this case will increase the ill-posedness of the optimization problem, hence for the ensemble-based methods, the inflation on the observation error covariance matrix is commonly adopted to regularize the problem. The large observation error here can be regarded as the implicitly inflated one. The variance field as shown in Figure 3.10 is constructed through interpolation based on the discrepancy between RANS results and very sparse experimental data in TKE where the added correction term has a direct impact. And the multiplication of the variance is taken as  $1 \times 10^{-3}$ . The first guessed input parameter is set as 1 in the domain of interest.

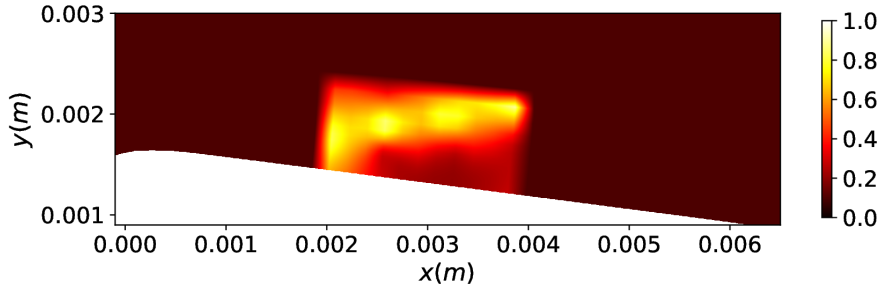


Figure 3.10: Variance  $\sigma(x)$  of  $\beta_c$  in TKE transport equation

### 3.5.1.2 Results

Figure 3.11 shows the reduction of cost function values with respect to iterations. It can be seen that the data assimilation process is well converged and the cost function is reduced significantly in the first 20 iterations from  $5.1 \times 10^5$  to around  $2.2 \times 10^5$  with the descending ratio of 0.43, while  $J_{ob}$  is decreased with a ratio of around 0.17 at the end of optimization.

Figure 3.12 is the comparison of TKE and stream-wise velocity  $u$  among the prior, posterior and experimental data along profiles. The profiles of prior TKE are quite distant from the reference profiles. The RANS model cannot capture the high TKE near the wall and throat region. After the data assimilation process, a noticeable improvement can be seen comparing to prior, and the prediction in TKE has a good agreement with experimental data especially at the first two positions as shown in Figure 3.12(b). However, from Figure 3.12(a) the prediction on velocity  $u$  is not quite improved. The correction embedded in the TKE transport equation may not have substantial effects on the observed velocity, that is to say, the perturbations



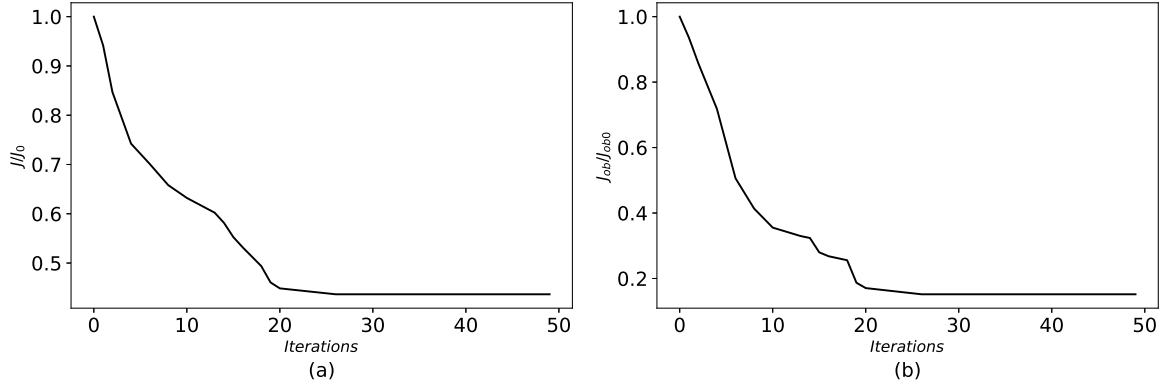


Figure 3.11: Data assimilation results of cost function  $J$ (a) and  $J_{ob}$  (b)

on the corrections can impact significantly on the prediction of TKE obviously, but have no sufficient influences on velocity  $u$ .

The contour plots of posterior TKE and velocity  $u$  with correction in the  $k$  transport equation are shown in Figure 3.22(c)(d). The apparent improvement can be found in TKE, and the region near the wall with high TKE can be recovered. However, for the velocity, no apparent improvements can be seen, and the relatively low value in the region near the wall cannot be captured even though with the correction in the  $k$  equation.

### 3.5.2 Correction in $\omega$ equation

#### 3.5.2.1 Data assimilation setup

The specific dissipation  $\omega$  transport equation in  $k - \omega$  SST turbulence model is heavily modelled with an ad-hoc form. The underlying source term in this equation is also probably responsible for the poor predictive performance on the velocity and TKE. In this subsection the correction  $\beta_c$  is introduced in  $\omega$  transport equation as the following formula:

$$(3.14) \quad \frac{\partial \omega}{\partial t} + \frac{\partial(u_j \omega)}{\partial x_j} = \beta_c \frac{\gamma}{\mu_t} P - \beta \omega^2 + \frac{\partial}{\partial x_j} [(\nu + \sigma_\omega \nu_t) \frac{\partial \omega}{\partial x_j}] + S_{sst}$$

The range of input parameters and observations are the same in section 5.1 as well as the ensemble size. The standard deviation of observation is also taken as  $10^{-1}$ . The variance  $\sigma(x)$  is taken based on the discrepancy between RANS and experimental data on velocity  $u$  since the correction in  $\omega$  transport equation can have strong correlations with velocity based on our prior study. The multiplication on variance  $\sigma(x)$  is  $1 \times 10^{-3}$ . The variance field is shown in Figure 3.14. The first guessed input parameter is set as 1 in the inferred domain as well.

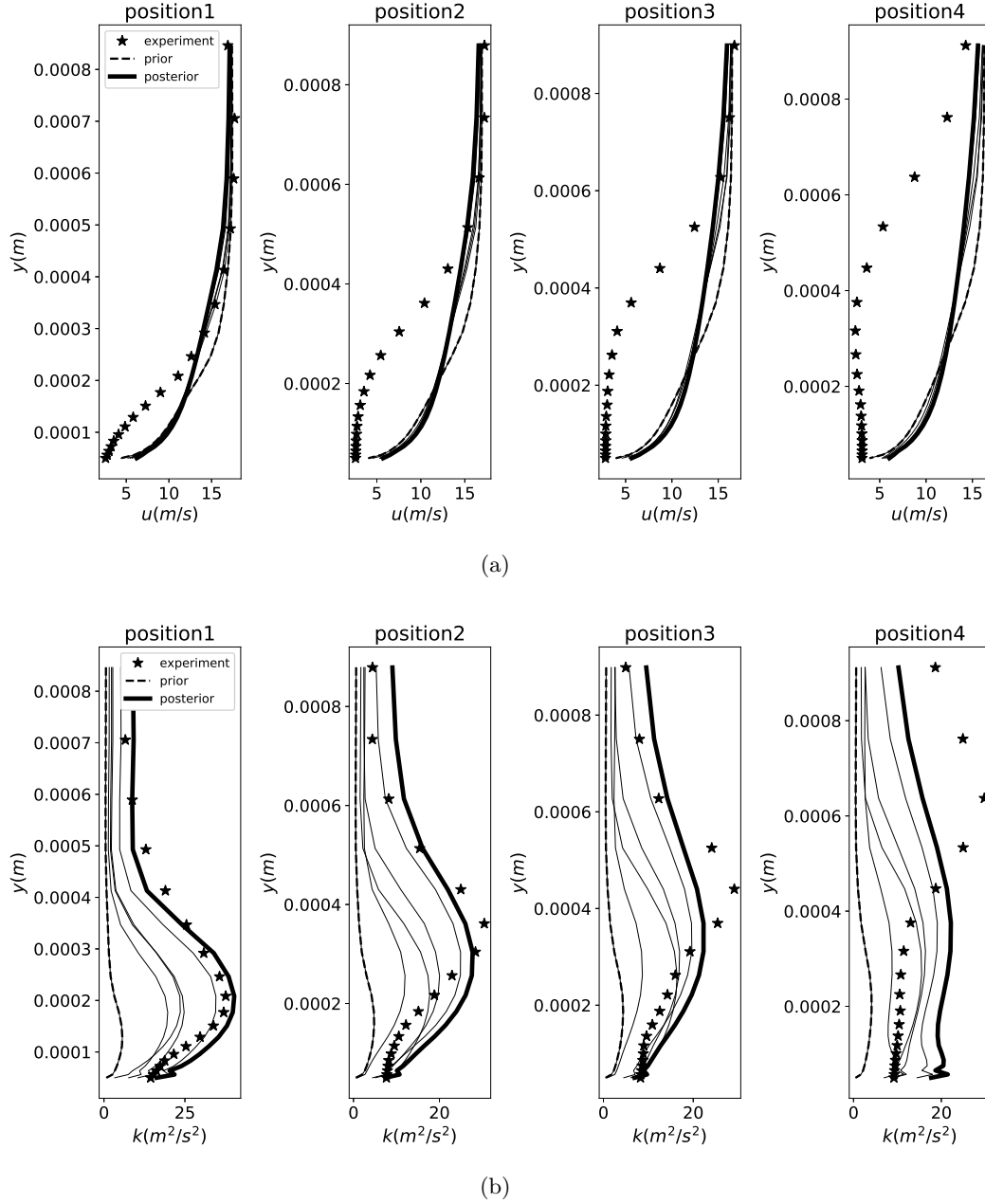


Figure 3.12: Comparison in velocity  $u$  (a) and TKE (b) along profiles among prior, posterior and experiment

### 3.5.2.2 Results

Figure 3.15 shows that the convergence curve of the cost function with correction in the  $\omega$  equation. It can be seen that the ratio of cost function  $J$  can reduce to 0.13 and for  $J_{ob}$  it can decline to 0.25. And after approximately 30 iterations, no visible improvement can be reached.

Figure 3.16 presents the evolution of RANS prediction in observation space. With the

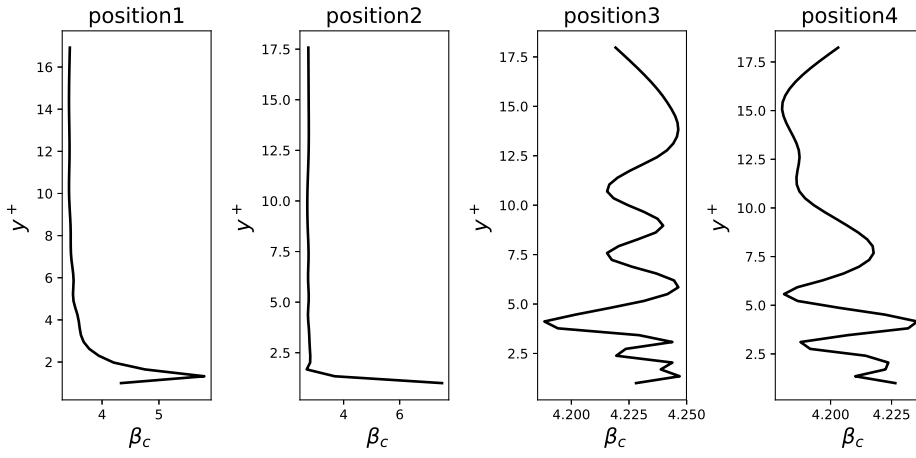


Figure 3.13: Inferred  $\beta_c$  profiles

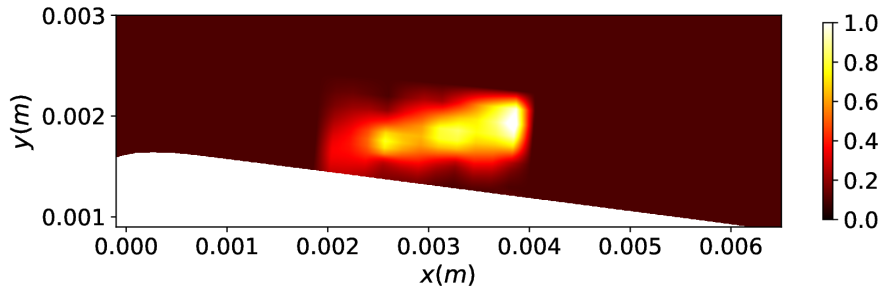


Figure 3.14: variance  $\sigma(x)$  of  $\beta_c$  in  $\omega$  transport equation

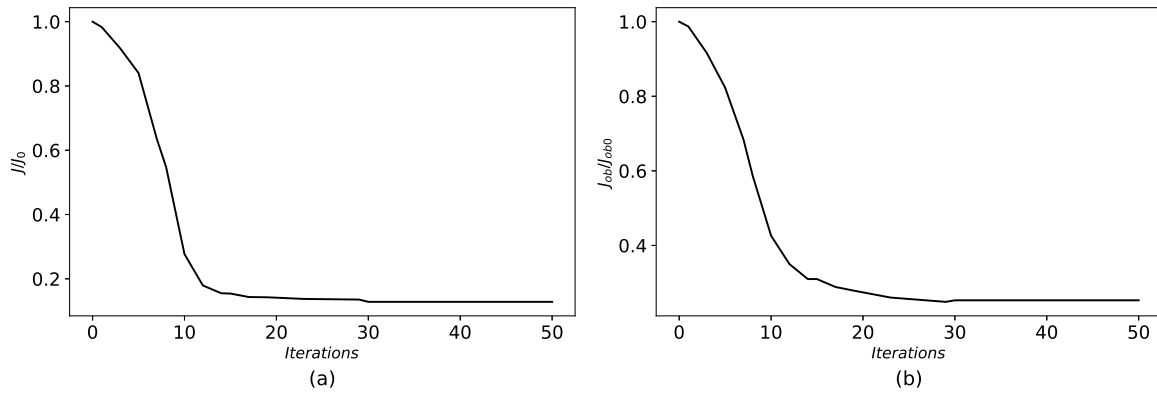


Figure 3.15: data assimilation results in cost function  $J(a)$  and  $J_{ob}(b)$

correction in the  $\omega$  transport equation, the stream-wise velocity  $u$  can be significantly improved even though TKE becomes inferior. With the velocity approaching the experimental data, the gradient of velocity near the wall is gradually reduced which results in the production term in the TKE transport equation related to the velocity gradient decrease accordingly. That is why it can be observed that the improvements in velocity  $u$  and TKE are mutually impeded: Once the prediction on velocity  $u$  is improved, the velocity gradient near the wall will become reduced, which results in the reduction of TKE and the further departure from the experimental measurements. The contour plots of the posterior with correction in the  $\omega$  equation are presented in Figure 3.22(e)(f). The velocity field is well reconstructed comparing to the experiments, especially in the upstream.

### 3.5.3 Correction in $k$ and $\omega$ equation

#### 3.5.3.1 Data assimilation setup

Because of the corrections in the TKE and special dissipation transport equation having dominant effects on the prediction of TKE and velocity  $u$  respectively, in this subsection the correction terms are introduced simultaneously in TKE and  $\omega$  transport equation. The input space has 2400 dimensions including correction variables in both TKE and dissipation transport equation. Other parameters are uniform with the former subsections.

#### 3.5.3.2 Results

Figure 3.18 shows that the results of the cost function with corrections in both  $k$  and  $\omega$  equations. It can be seen that the value of cost function reduces significantly within 45 iterations with ratio  $r_J$  of 0.087 and  $r_{J_{ob}}$  of 0.13. Compared with the previous cases, the efficiency of EnVar method decrease as the dimension of input parameters is increased. Figure 3.19 presents the evolution of the velocity  $u$  and TKE profiles by comparison with prior and experimental data. The predictions in both  $u$  and TKE is improved; however, the improvements of the predictions in the two observation are mutually restrained, which leads to that the further optimization of the velocity would deteriorate the prediction on TKE.

From the contour plots in Figure 3.22(g)(h), the apparent improvement on the prediction of velocity  $u$  and TKE can be seen comparing to prior. However, there is still a significant departure from the experiments. The reason why the optimized results cannot get further close to the reference data may be due to two aspects: first the experimental data has its instinct uncertainty including the measurement noise, insufficiency resolution and so on; secondly, it has been noted that the primary source of uncertainties in the RANS model is from Reynolds stress. The correction in the scalar  $k$  and  $\omega$  equation is still under the frame of linear eddy-viscosity assumption; hence it can only concern the magnitude of Reynolds stress tensor but cannot take the orientation of Reynolds stress into considerations. In other words, the impact of these

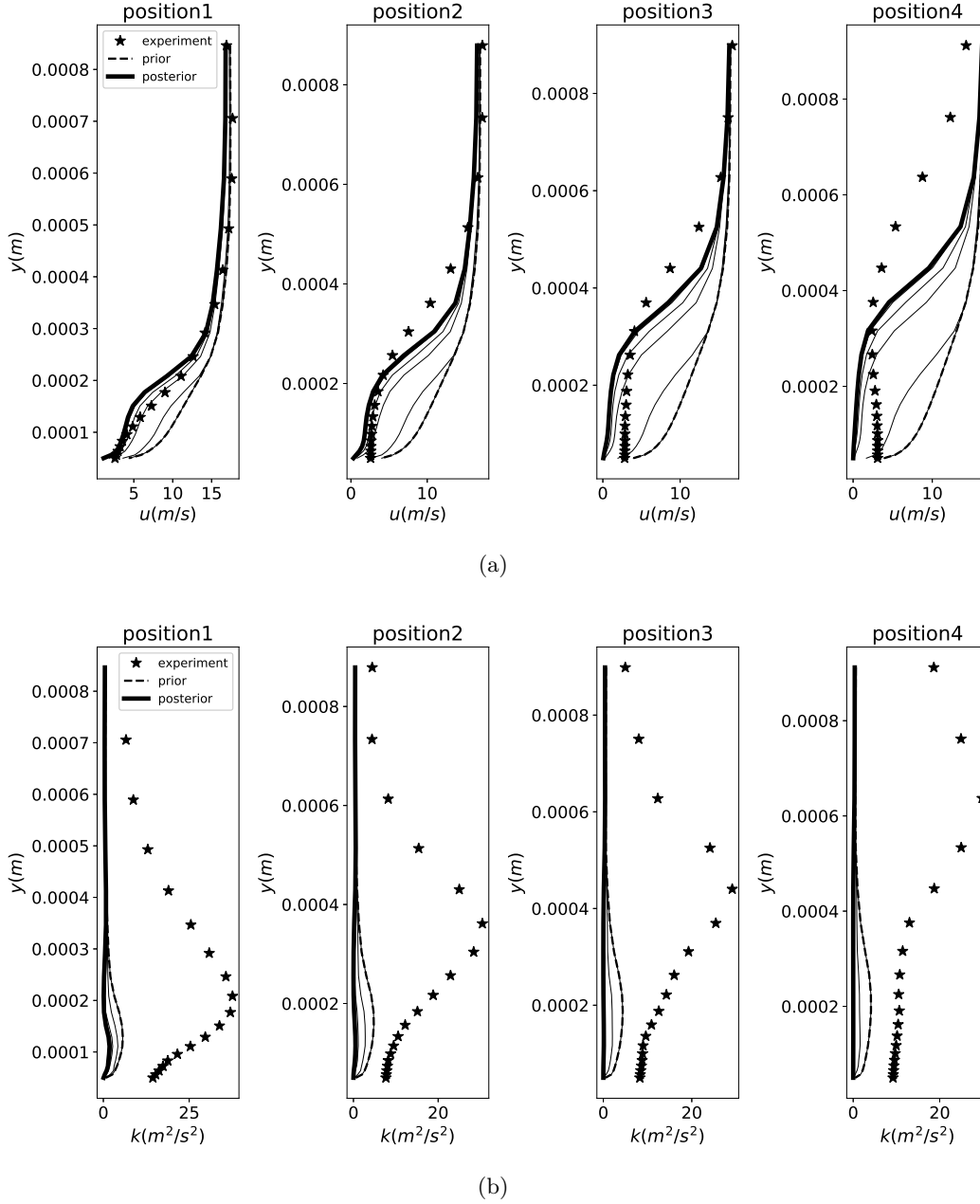
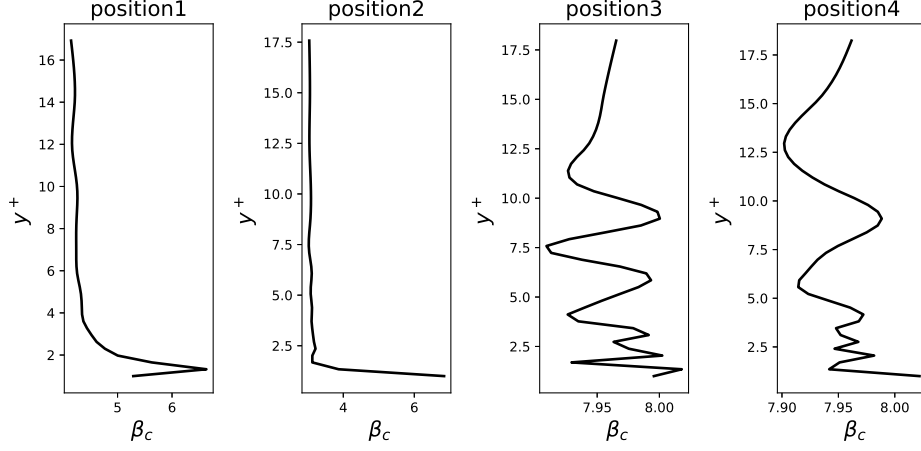
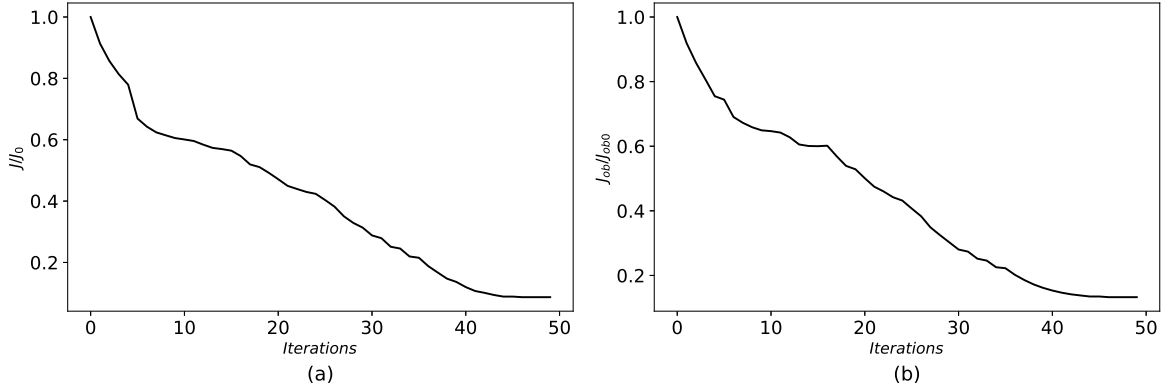


Figure 3.16: Comparison in velocity  $u$  (a) and TKE (b) along profiles among prior, posterior and experiment

corrections on the observations may be not sufficient to represent the structural uncertainty in the RANS model. To this end, this work can be extended to the framework in [148] to infer the uncertainties directly in the Reynolds stress term. Moreover, the measured TKE may be difficult to be replicated by the modeled TKE since the modeled TKE cannot be equivalent to the "true" TKE in a real flow.

Figure 3.13 3.17 3.20 3.21 are the inferred model correction profiles at the corresponding


 Figure 3.17: Inferred  $\beta_c$  profiles

 Figure 3.18: Data assimilation results of cost function  $J(a)$  and  $J_{ob}$  (b)

position for each case. Generally, the production term in TKE and dissipation transport equation are both increased by the introduced corrections. With the production term in  $k$  equation increasing, the resolution on the TKE increase as well. Thus, the prediction on  $k$  in the near wall region can be improved significantly comparing to the initially underestimated value. However for the region away from the wall, the production term itself becomes trivial, and thus TKE will reduce the sensitivity to the multiplicative correction of the production term; hence the assimilated results are almost similar to prior, especially for the case with corrections in both  $k$  and  $\omega$  transport equation. Also, the resolution on  $\omega$  gets increased with the optimal correction in the  $\omega$  equation, which leads to that the modeled Reynolds stress tend to decrease, while the velocity near the wall is reduced accordingly and get close to the experimental measurements. Nevertheless, in the area far from the wall, the inferred correction is also increased but has few effects on velocity since the region is in the outer layer where the Reynolds stress is not dominant.

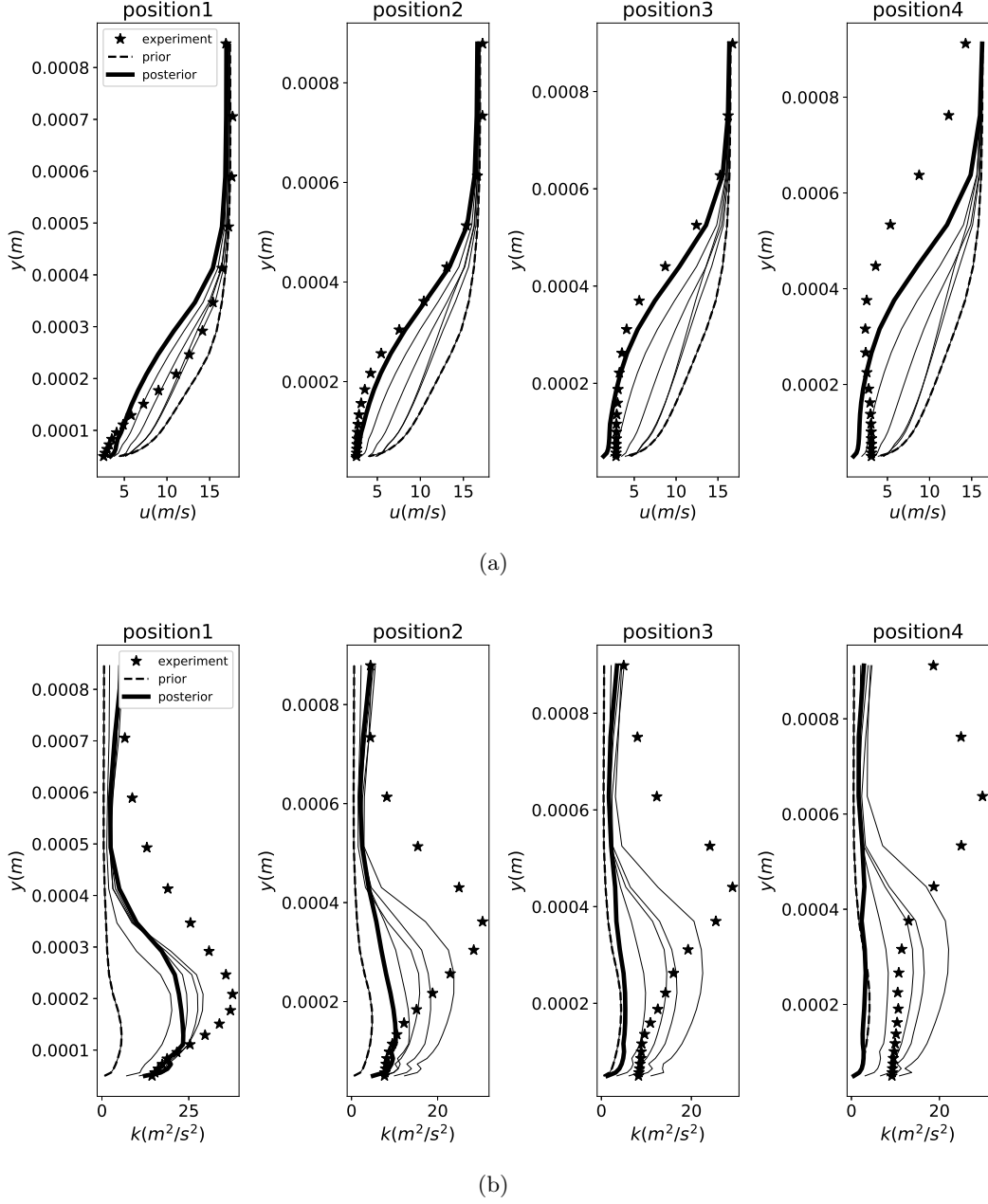
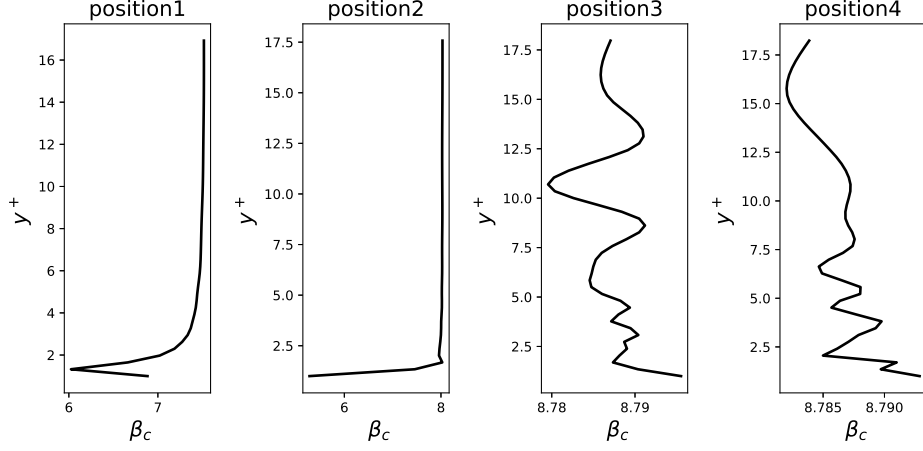
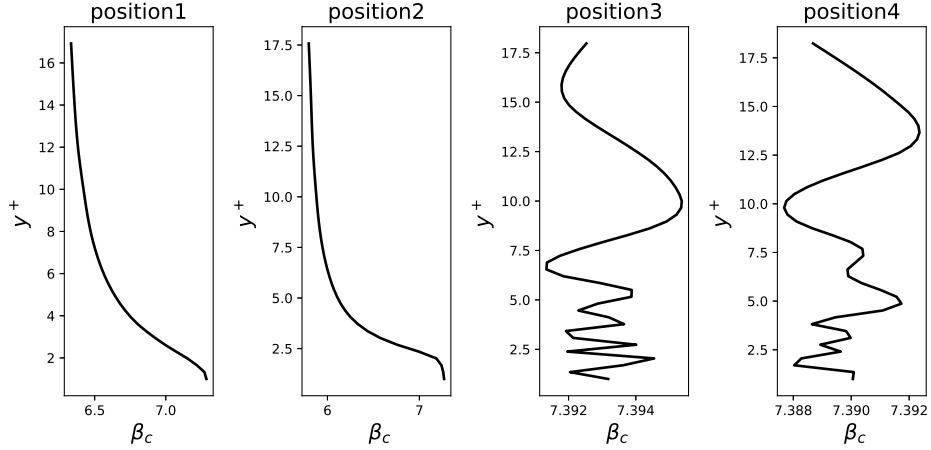


Figure 3.19: Comparison in velocity  $u$  (a) and  $k$  (b) along profiles among prior, posterior and experiment

### 3.6 Conclusion

The ensemble-based variational method is presented to optimize RANS simulation by inferring improved inlet velocity and underlying model corrections in  $k - \omega$  SST model. This approach combines the variational data assimilation method and ensemble Kalman method by transforming the MAP as the optimal control problem and meanwhile using the ensemble


 Figure 3.20: Inferred  $\beta_c$  profiles in  $k$  equation

 Figure 3.21: Inferred  $\beta_c$  profiles in  $\omega$  equation

technique to estimate prior statistics so that it can sustain the advantages of both robustness and intrusiveness.

Firstly, two representative flows in the convergent-divergent channel, the turbulent flow in the WallTurb Bump where DNS resolution is available and non-cavitating flow in Venturi-type section with the X-rays experimental observation, were tested with the proposed data assimilation approach to infer the ambiguous inlet velocity profile. With improved inlet velocity, the field of velocity  $u$  can be reconstructed in good agreement with reference data mainly near the inlet region, while the velocity  $u$  in the APG region is not quite sensitive to the inlet condition. Further, the underlying model corrections in  $k - \omega$  SST model were inferred for the non-cavitating flow in Venturi. The sensitivity of the correction term in the  $k$  and the  $\omega$  equation is analyzed respectively. The predictions in velocity  $u$  and TKE both can be improved with corrections in the  $k$  and  $\omega$  equation but still have large discrepancies comparing to the



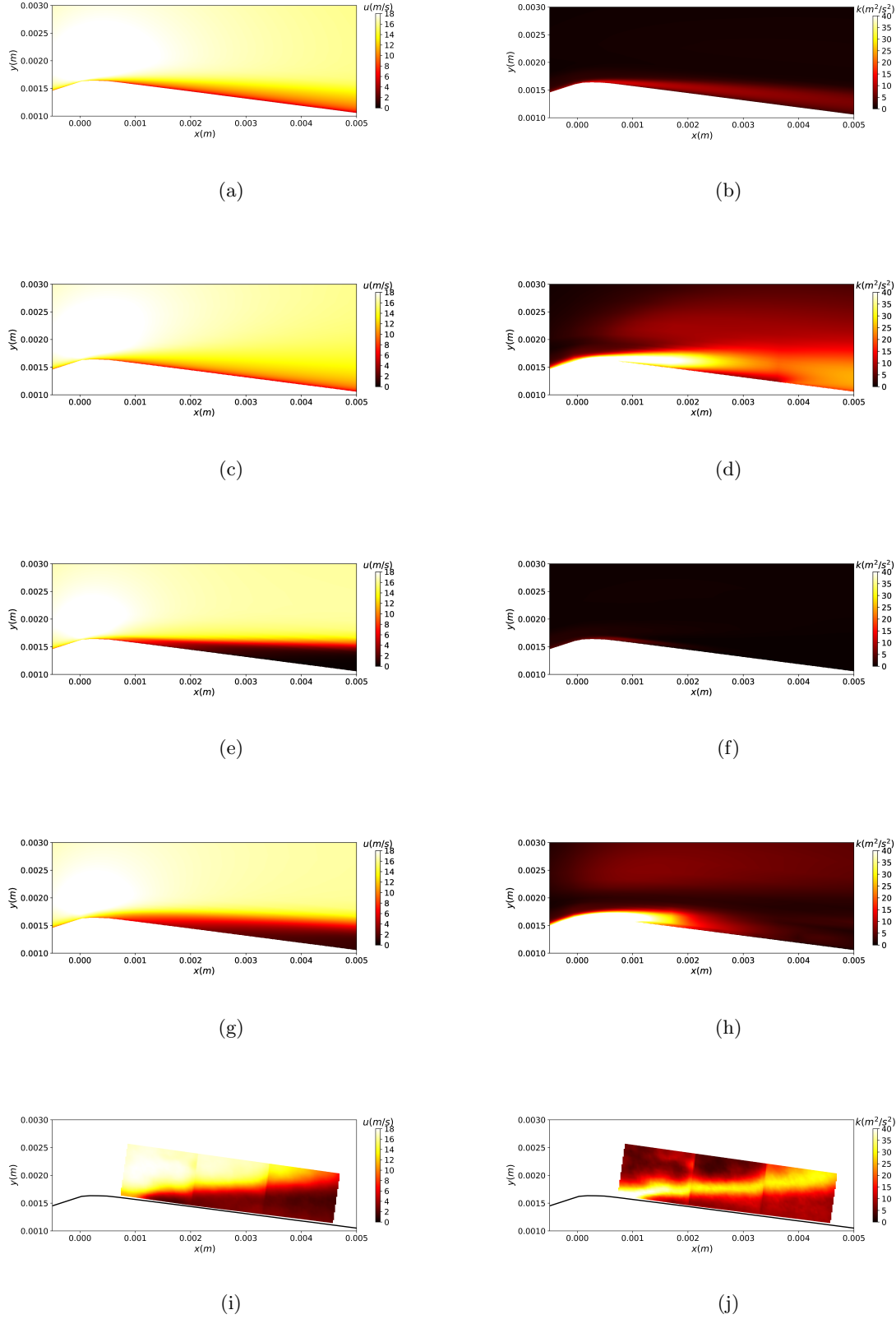


Figure 3.22: Contour plots of velocity  $u$  (first column) and TKE (second column): (a)(b) prior; (c)(d) posterior with correction in  $k$  transport equation; (e)(f) posterior with correction in  $\omega$  transport equation; (g)(h) posterior with correction in both  $k$  and  $\omega$  transport equation; (i)(j) experiment

experiments which may be due to the insufficiency of the correction in the frame of Boussinesq hypothesis. The robustness of ensemble-based variational method for the inverse problem in complex turbulent flows is demonstrated.

In light of the limitation of the RANS model-form uncertainty under the frame of linear eddy viscosity assumption, current work is being conducted to explore the applicability of this data assimilation scheme to quantify and reduce uncertainties in Reynolds stress directly. Also, the EnVar method used in this work is the standard incremental ensemble version, where the background error covariance is estimated with low-rank linear approximation and independent between consecutive data assimilation iterations. The ensemble update with consideration of the associated error covariance update will be investigated in future work.[150] Besides, the method utilizes the limited ensemble realizations to estimate the sensitivity matrix which may result in that the optimization process is prone to diverge especially for the high dimension problem. Hence, the regularization technique will be explored to be introduced in this data assimilation scheme to address this issue. Moreover, the machine learning technique will be explored to extract the model knowledge based on the inferred source term field which can be expected to be used for industrial applications.[130]

## Chapter 4

# Regularization of Ensemble Kalman Method for Inverse Problems

### 4.1 Introduction

Inverse problems are frequently encountered in computational physics applications such as complex fluid flows where physical fields need to be inferred. A classic example of inverse problems is to estimate the stationary background flow velocity field from the concentration of passive scalars (e.g., pollutant or dye) that are advected by, and diffusing within, the fluid [13]. The data that are available and used in such an inversion are often partial, noisy observations of the concentration field. The inverse problem is motivated by the fact that concentrations are often easier to measure than velocities. The forward problem corresponding to the above-mentioned inverse problem is computing the concentration field  $\mathbf{z}(\mathbf{x})$ , where  $\mathbf{x}$  denotes spatial coordinates, by solving the steady-state advection–diffusion equation

$$(4.1) \quad \mathbf{u} \cdot \nabla \mathbf{z} - \kappa \nabla^2 \mathbf{z} = 0$$

with a given background velocity field  $\mathbf{u}(\mathbf{x})$ , along with other auxiliary constraints such as boundary conditions and physical properties (e.g., diffusivity  $\kappa$ ) of the passive scalar. Hence, the partial differential equation (PDE)-based forward model above implies a functional mapping  $\mathcal{M} : \mathbf{u} \mapsto \mathbf{z}$ , or more concisely,  $\mathbf{z} = \mathcal{M}(\mathbf{u})$ . Another example of solving inverse problems is the data assimilation used for weather forecasting, where partial, time-dependent observations of the atmosphere (e.g., wind speed, temperature, humidity) and numerical simulations are jointly used to infer the full initial state of the system. Inverse problems are typically many times more expensive to solve than the corresponding forward problems. This is not only due to the limited amount of observation data compounded by the uncertainties therein, but also due to the nonlinearity of the PDE-governed system and its high-dimensional state space that leads to ill-posed inverse problems.

The example of inferring background velocities can be posed as an optimization problem, i.e., finding a velocity field  $\mathbf{u}^{\text{opt}}$  that leads to a concentration field best matching the observations ( $\mathbf{z}^{\text{obs}}$ ) at the measured locations. That is,

$$(4.2) \quad \mathbf{u}^{\text{opt}} = \arg \min_{\mathbf{u}} \|\tilde{\mathcal{H}}[\mathcal{M}(\mathbf{u})] - \mathbf{z}^{\text{obs}}\|^2,$$

where  $\mathcal{M}(\mathbf{u})$  involves solving the PDE for the concentration,  $\tilde{\mathcal{H}}$  is the observation operator (e.g., extracting values at the observed locations from the concentration field), and  $\|\cdot\|$  denotes a norm in a Hilbert space (e.g.,  $L_2$  norm in Euclidean space or that weighted by the state covariance). In a terminology consistent with that used in the data assimilation community, the velocity field to be inferred is referred to as the state ( $\mathbf{x}$ ), and the measured concentrations called observations ( $\mathbf{y}$ ). We further define  $\mathcal{H} \equiv \tilde{\mathcal{H}} \circ \mathcal{M}$  as a composition of the model operator  $\mathcal{M}$  and the observation operator  $\tilde{\mathcal{H}}$ . The inverse problem above can thus be written as:

$$(4.3) \quad \mathbf{x}^{\text{opt}} = \arg \min_{\mathbf{x}} J \quad \text{with} \quad J(\mathbf{x}) = \|\mathcal{H}[\mathbf{x}] - \mathbf{y}\|^2,$$

where  $J(\mathbf{x})$  is the cost function to be minimized, which corresponds to the discrepancy between the model outputs and the observations.

#### 4.1.1 Adjoint- vs. ensemble-based inversion methods

In order to solve the optimization problem in the field inversion, the gradient descent method or one of its variants is often used, where the search of the optimal solution is guided by following the local gradient  $\partial J / \partial \mathbf{x}$  of the cost function  $J$  with respect to the control parameter  $\mathbf{x}$ . Note that  $\mathbf{x}$  usually resides in the space of very high dimensions (corresponding to the number of degrees of freedom of the discretized velocity field in the above example, which can be in the order of millions). A highly efficient way to compute such a derivative is the adjoint method [56], where the derivative is obtained by solving an adjoint equation at a cost similar to solving the PDEs in the forward model (referred to as primal equation). Adjoint methods have been used for different fluid mechanics problems. Dow and Wang [37] proposed an adjoint-based Bayesian inversion method to quantify the structural uncertainty in Reynolds-averaged Navier–Stokes simulations. Gronsks et al. [61] adopted the variational method to infer the inflow and initial condition for a problem using direct numerical simulation (DNS) of the Navier–Stokes equations. Papadimitriou and Papadimitriou [116] applied a Bayesian framework coupled with a high-order adjoint approach to quantify the uncertainty in the parameters in the Spalart–Allmaras turbulence model [133]. Singh and Duraisamy [129] proposed an approximate Bayesian inference framework based on the adjoint method to infer the multiplicative correction term in the Spalart–Allmaras model and the  $k$ – $\omega$  model [141]. Foures et al. [51] used the adjoint-based variational method and Lagrange multipliers to reconstruct the full velocity field from coarse-grid particle image velocimetry (PIV) measurements of velocity magnitude from

only part of the domain. They imposed the Reynolds-averaged Navier–Stokes equations as a constraint in the minimization and used the Reynolds stress divergence as a control parameter. Recently, Beneddine et al. [7] further extended this technique to the reconstruction of the unsteady behavior of a round jet at a Reynolds number of  $Re = 3300$  from the mean flow field and unsteady measurements at a single point. Meldi and Poux [100] integrated the Kalman filter into the structure of a segregated CFD solver and imposed the zero-divergence condition for the velocity field. They further proposed model reduction strategies to reduce the computational costs within the Kalman analysis. The framework has been used to reconstruct different flow configurations including three-dimensional unsteady flows [100] with comprehensive sensitivity analysis performed [99].

A major shortcoming of the adjoint method, however, is the effort required to develop the adjoint solver. For the discrete adjoint method, which is the most commonly used adjoint method in computational fluid dynamics (CFD) applications, this involves differentiating each operation (i.e., each line of code) in the primal solver [55, 109]. This is a laborious process and a daunting task for complex simulation codes such as CFD solvers. Taking CFD for example, while some codes intended for design and optimization have been developed with adjoint capability [e.g., 8, 38], many other popular solvers are not equipped with a native, production-level adjoint capability. Most notably, the CFD code OpenFOAM [113] does not have any native discrete adjoint solver capabilities. Although there have been efforts to build one for OpenFOAM based on automatic differentiation [135], it is not yet at a production level at this time.

The limited availability of physical simulation codes with adjoint capability has prompted the inverse modeling community to develop ensemble-based, derivative-free optimization methods. The iterative ensemble Kalman method proposed by Iglesias et al. [71] is among such attempts for general inverse problems. In the data assimilation community, ensemble methods [47–49] have been developed to complement or replace the traditional variational (adjoint) methods (e.g., 3DVar, 4DVar) [25, 53]. In ensemble methods, the covariance estimated from the ensemble is used in lieu of the derivatives to guide the optimization. A number of primal simulations with different samples of the system states are run, which is in contrast to solving adjoint equations along with the primal equations. A critical advantage of ensemble methods over adjoint methods is that it is non-intrusive, i.e., the forward model (primal solver) does not need to be changed, and adjoint solvers are not needed. Many works have used ensemble methods for inverse problems in fluid mechanics. For instance, Kato and Obayashi [79] leveraged the ensemble Kalman filter to infer the value of empirical parameters in the Spalart–Allmaras turbulence model and demonstrated the effectiveness of ensemble Kalman methods for CFD problems. Mons et al. [107] applied different ensemble-based methods including the ensemble Kalman filter to infer the inlet and initial conditions for CFD simulations and thus reconstruct the unsteady flow around a cylinder. Xiao et al. [148] used an iterative ensemble Kalman method

to infer the Reynolds stress discrepancy field and reconstruct the velocity field accurately for flows over periodic hills as well as flows in a square duct. However, compared to adjoint methods, ensemble methods do not have the flexibility to introduce regularization to tackle ill-posed inverse problems. This shortcoming shall be examined in more detail below.

#### 4.1.2 Ill-posedness and regularization of inverse problems

We introduce the concept of ill-posedness by examining the operator  $\mathcal{H}$  in the optimization formulation of the inverse problem as in Eq. (4.3). As described above, computing the cost  $J(\mathbf{x})$  associated with the state  $\mathbf{x}$  involves

1. solving the forward model (e.g., Eq. (4.1) with the given velocity field),
2. mapping the results to observation space (e.g., sampling at specific locations), and
3. comparing with the observations  $\mathbf{y}$  to find the discrepancy.

While the advection–diffusion equation happens to be linear, in many other problems (e.g., inferring the velocity field from partial observations of itself) the model  $\mathcal{M}$  is highly nonlinear. Moreover, the operator  $\tilde{\mathcal{H}}$  typically maps a high-dimensional state space, where  $\mathcal{M}(\mathbf{x})$  is in, to a low-dimensional observation space, where  $\mathbf{y}$  is in. For example, the concentration field discretized with a mesh of millions of cells may be observed at only a few locations. Because of these two factors,  $\mathcal{H}$  typically results in a many-to-one mapping. In other words, many different velocity fields lead to the same agreement with the observations and thus the same cost  $J$ . Consequently, the inverse problem formulated as the optimization in Eq. (4.3) does not have a unique solution and is thus ill-posed.

To tackle the ill-posedness, inverse problems can be regularized by introducing an additional term  $J_r$  into the cost function  $J$  in Eq. (4.3), i.e.,

$$(4.4) \quad J = \|\mathcal{H}[\mathbf{x}] - \mathbf{y}\|^2 + J_r.$$

The term  $J_r$  serves to differentiate among the states that previously led to identical costs. Desired properties of the states that are commonly used for regularization include:

**Spatial smoothness** i.e., preferring smooth fields over non-smooth fields among the candidate states [see, e.g., 37, 114]. The corresponding cost function in Eq. (4.3) becomes  $J = \|\mathcal{H}[\mathbf{x}] - \mathbf{y}\|^2 + \lambda \|\nabla \mathbf{x}\|^2$ , where  $J_r = \lambda \|\nabla \mathbf{x}\|^2$  is the regularization term and  $\lambda$  is an algorithmic parameter corresponding to the strength of the regularization.

**Prior mean values** i.e., preferring candidate states closer to the prior mean  $\mathbf{x}_0$  over those further away [see, e.g., 129]. The regularization is  $J_r = \lambda \|\mathbf{x} - \mathbf{x}_0\|^2$ .

**Physical constraints** e.g., in the example above where the state is the background velocity, this can be preferring velocity fields that satisfy the mass conservation (divergence-free condition for incompressible flows) [66]. The regularization is thus  $J_r = \lambda \|\nabla \cdot \mathbf{x}\|^2$ . Similarly, other physical constraints include positivity of turbulent kinetic energy or eddy viscosity and realizability of Reynolds stresses [148].

There exist many more types of prior knowledge than those enumerated above. For example, one could use regularization to favor (or penalize) specific wave numbers or pattern in the field to be inferred, or to favor smaller (or larger) values in certain regions. Essentially, regularization utilizes prior knowledge on the state to be inferred to constrain the optimization process. Consequently, the regularization terms to be introduced are inevitably problem-specific and can have a wide range of forms in different applications.

Implementation of such regularization in optimization schemes is much more challenging for ensemble methods than for adjoint methods. In the adjoint-based inversion, regularization involves modifying the cost function with an additional term, which in turn may necessitate modifying the adjoint solver. This is usually straightforward (albeit laborious) process. In contrast, it has been far from clear how to implement a generic regularization in ensemble-based inversion methods. So far, a general procedure to introduce prior knowledge-based regularization to ensemble methods is still lacking. The difficulty partly stems from the fact that ensemble methods do not directly optimize a cost function. Rather, they use an analysis scheme to optimize the cost function implicitly. Nevertheless, it is well known that the adjoint-based and ensemble-based Bayesian inverse modeling methods are equivalent under some mild assumptions (e.g., Gaussian priors on the states, normal distribution of observation uncertainties, linear model) [49, 125]. Specifically, under these assumptions the maximum a posteriori (MAP) estimate from the Bayesian approach is equivalent to the minimization problem in adjoint-based methods. Therefore, one can naturally expect that the regularization methods reviewed above for adjoint methods can be equally introduced into ensemble methods for inverse modeling.

#### 4.1.3 Related works and contributions of present work

Enforcing constraints in ensemble-based methods has drawn increasing attention in the past few years, and a body of works has focused on attempting to enforce constraints in ensemble Kalman methods. Wang et al. [138] presented the projection method and the accept/reject method to constrain the estimated state and parameters. To achieve this, the former method projects the ensemble samples into the constrained space, and the latter method will reject the ensemble update and resample the model and observation errors if the updated samples violate the constraints. Prakash and Patwardhan [119] proposed a constrained ensemble Kalman method where the analysis step is formulated as solving a constrained optimization problem. Similarly, Janjić et al. [72] formulated the analysis scheme of the conventional ensemble Kalman methods as a set of quadratic programming problems and applied physical constraints to ensure

the mass conservation and non-negativity of the ensemble members. Recently, inspired by the above works, Albers et al. [2] provided a unifying framework to enforce equality and inequality constraints in ensemble Kalman methods. In their framework, the updated samples produced by the standard methods that violate the constraints are replaced by those obtained through solving a constraint optimization problem. They demonstrated the equivalence between the analysis scheme in ensemble Kalman methods and the minimization problem, as well as the well-definiteness of the constrained optimization problem.

In an alternative approach, Wu et al. [144] proposed a method where after a standard Kalman update the ensemble samples are reweighted based on the Gaussian statistical model associated with the constraint term. However, as with particle filter methods, this method is potentially susceptible to sample degeneration [93], i.e., a few samples can have large weights and dominate all other samples, reducing the effective sample size. Moreover, it is not straightforward to specify inequality constraints by using the Gaussian statistical model they adopted.

All the aforementioned methods introduce a post-processing step to enforce constraints after the analysis step of the standard ensemble Kalman methods. They require either the adjoint code to solve the constraint optimization problem or the reweighting of each sample. In our work, we propose a method that integrates constraints into the analysis scheme and involves only an algorithmic modification to the standard ensemble Kalman methods. This modification leads to a derivative-free method that incorporates constraints in a mathematically equivalent manner as the commonly used adjoint-based inversion methods, i.e., by implicit minimization of a regularized cost function.

Specifically, we propose a method to introduce general regularization terms (including but not limited to the types reviewed above) into the ensemble Kalman methods. This is achieved by deriving an analysis scheme starting from the modified cost function. The result is an analysis scheme with minor modifications to achieve the desired regularization. The derivation is valid for ensemble Kalman methods in general, including the iterative ensemble Kalman method in [71] and the ensemble Kalman filter [47, 48]. Note that we aim to derive a scheme to impose general constraints through modification of the analysis schemes. Applications to the specific type of constraints (e.g., smoothness, prior mean) as discussed above will be illustrated in further examples presented in a companion paper.

The rest of the paper is organized as follows. Section 4.2 presents the derivation of the regularized ensemble Kalman method for optimization and its implementation. Modification compared to its traditional counterpart is highlighted. Section 4.3 evaluates the proposed method on three inverse modeling problems of increasing difficulty levels ranging from optimization of a nonlinear function of scalars to inferring the closure field in the Reynolds-averaged Navier–Stokes (RANS) equations. The RANS equation closure problem is of significant importance in fluid dynamics and engineering applications since the closure models are considered the main source of uncertainty in the predictions. Finally, Section 4.4 concludes the paper.



## 4.2 Methodology

The two main approaches for solving inverse problems, adjoint-based optimization approach and maximum a posteriori (MAP) estimation based Bayesian approach, are equivalent under mild assumptions, with ensemble Kalman methods being an example of the MAP approach. The objective of this section is to bridge the gap between enforcing constraints (regularization) for the two approaches. Specifically, we show that a generic constraint introduced into the cost function for the optimization approach can be equivalently implemented as modifications to the analysis scheme of the ensemble Kalman methods.

### 4.2.1 Equivalence between optimization and maximum a posteriori approaches

The optimization approach for solving the inverse problem is presented above in Eq. (4.3). In contrast, from the Bayesian perspective, solving the inverse problem amounts to finding the probabilistic distribution  $P(\mathbf{x} | \mathbf{y})$  of the state  $\mathbf{x}$  conditioned on observation  $\mathbf{y}$ . Based on Bayes' theorem, this is:

$$(4.5) \quad P(\mathbf{x} | \mathbf{y}) \propto P(\mathbf{x})P(\mathbf{y} | \mathbf{x}),$$

where  $P(\mathbf{x})$  is the prior distribution before incorporating the observation data and  $P(\mathbf{y} | \mathbf{x})$  is the likelihood indicating the probability of observing  $\mathbf{y}$  given state  $\mathbf{x}$ . For the likelihood, the following relation is assumed between  $\mathbf{x}$  and  $\mathbf{y}$ :

$$(4.6) \quad \mathbf{y} = \mathcal{H}[\mathbf{x}] + \epsilon,$$

where  $\epsilon$  is a stochastic observation error. Estimating the full posterior distribution  $P(\mathbf{x} | \mathbf{y})$  (e.g., by using Markov Chain Monte Carlo sampling) can be prohibitively expensive, as it requires millions of evaluations of the forward model and often must resort to surrogate models [39, 40, 42, 121]. Therefore, in practical applications, one often finds the state  $\mathbf{x}$  that maximizes the posterior, which is referred to as MAP estimation [43]. The derivation assumes that both the prior and the observation noises are Gaussian processes [120], i.e.,

$$(4.7) \quad P(\mathbf{x}) = \frac{1}{\sqrt{(2\pi)^N \det(\mathbf{P})}} \exp\left(-\frac{1}{2}(\mathbf{x} - \mathbf{x}^f)^\top \mathbf{P}^{-1}(\mathbf{x} - \mathbf{x}^f)\right) \propto \exp\left(-\|\mathbf{x} - \mathbf{x}^f\|_{\mathbf{P}^{-1}}^2\right),$$

$$(4.8) \quad P(\epsilon) = \frac{1}{\sqrt{(2\pi)^D \det(\mathbf{R})}} \exp\left(-\frac{1}{2}\epsilon^\top \mathbf{R}^{-1}\epsilon\right) \propto \exp\left(-\|\mathcal{H}[\mathbf{x}] - \mathbf{y}\|_{\mathbf{R}^{-1}}^2\right).$$

where  $\mathbf{x}^f$  is the prior mean,  $\mathbf{P}$  and  $\mathbf{R}$  are the covariance matrices of the state  $\mathbf{x}$  and the observation errors  $\epsilon$ , respectively, and the norm  $\|\cdot\|_{\mathbf{W}}^2$  is defined as  $\|v\|_{\mathbf{W}}^2 = \mathbf{v}^\top \mathbf{W} \mathbf{v}$  for a vector  $\mathbf{v}$  and weight matrix  $\mathbf{W}$ . The posterior is thus

$$(4.9) \quad P(\mathbf{x} | \mathbf{y}) \propto \exp\left(-\|\mathbf{x} - \mathbf{x}^f\|_{\mathbf{P}^{-1}}^2 - \|\mathcal{H}[\mathbf{x}] - \mathbf{y}\|_{\mathbf{R}^{-1}}^2\right).$$

Maximizing the posterior amounts to minimizing its negative logarithm, i.e.,

$$(4.10) \quad \mathbf{x}^{\text{opt}} = \arg \min_{\mathbf{x}} J \quad \text{with} \quad J(\mathbf{x}) = \|\mathbf{x} - \mathbf{x}^f\|_{\mathbf{P}^{-1}}^2 + \|\mathcal{H}[\mathbf{x}] - \mathbf{y}\|_{\mathbf{R}^{-1}}^2,$$

which is equivalent to the optimization approach in Eq. (4.3) with the prior based regularization presented in Section 4.1.2.

More general regularization terms can be introduced into the cost function. These are formulated as a norm of some differentiable function  $\mathcal{G}[\mathbf{x}]$  that needs to be minimized. The cost function is then

$$(4.11) \quad J(\mathbf{x}) = \|\mathbf{x} - \mathbf{x}^f\|_{\mathbf{P}^{-1}}^2 + \|\mathcal{H}[\mathbf{x}] - \mathbf{y}\|_{\mathbf{R}^{-1}}^2 + \lambda \|\mathcal{G}[\mathbf{x}]\|_{\mathbf{W}}^2,$$

where the parameter  $\lambda$  controls the strength of the regularization, and  $\mathbf{W}$  is the weight matrix defining the norm to be minimized. For example, to promote spatial smoothness of the inferred field, the regularization term can be  $\mathcal{G}[\mathbf{x}] = \nabla \mathbf{x}$  with  $\mathbf{W}$  proportional to the discretization of the field. In light of equivalence between the two approaches, we show that the analysis scheme in ensemble Kalman methods can be derived from the optimization formulation of the inverse problem. We will reproduce such derivations below and introduce the modification needed to incorporate the constraint  $\mathcal{G}[\mathbf{x}]$  along the way.

#### 4.2.2 Derivation of the regularized ensemble Kalman method

Here we present the derivation of the regularized ensemble Kalman method. Some algebra has been omitted for brevity and ease of understanding, but the full derivations are given in B.1. In ensemble Kalman methods, the prior in Eq. (4.7) and the likelihood in Eqs. (4.6) and (4.8) are represented as ensembles  $\{\mathbf{x}_j^f\}$  and  $\{\mathbf{y}_j\}$ , respectively, where  $j = 1, \dots, M$  with  $M$  being the number of samples in the ensemble. For each pair of ensemble member  $\mathbf{x}_j^f$  and observation  $\mathbf{y}_j$ , the analysis scheme aims to find a posterior realization  $\mathbf{x}_j^a$  that minimizes the cost function  $J(\mathbf{x}_j)$ , i.e.,

$$(4.12) \quad \mathbf{x}_j^a = \arg \min_{\mathbf{x}} J \quad \text{with} \quad J(\mathbf{x}_j) = \|\mathbf{x}_j - \mathbf{x}_j^f\|_{\mathbf{P}^{-1}}^2 + \|\mathcal{H}[\mathbf{x}_j] - \mathbf{y}_j\|_{\mathbf{R}^{-1}}^2,$$

which is the ensemble-based representation of the optimization formulation in Eq. (4.10). If a regularization term is to be introduced to the cost function, the formulation in Eq. (4.12) becomes:

$$(4.13) \quad J(\mathbf{x}_j) = \|\mathbf{x}_j - \mathbf{x}_j^f\|_{\mathbf{P}^{-1}}^2 + \|\mathcal{H}[\mathbf{x}_j] - \mathbf{y}_j\|_{\mathbf{R}^{-1}}^2 + \lambda \|\mathcal{G}[\mathbf{x}_j]\|_{\mathbf{W}}^2,$$

This amounts to finding the  $\mathbf{x}_j^a$  that leads to  $\partial J / \partial \mathbf{x}_j = 0$ . For Eq. (4.13) this becomes

$$(4.14) \quad \mathbf{P}^{-1}(\mathbf{x}_j^a - \mathbf{x}_j^f) + (\mathcal{H}'[\mathbf{x}_j^a])^\top \mathbf{R}^{-1}(\mathcal{H}[\mathbf{x}_j^a] - \mathbf{y}_j) + \lambda \mathcal{G}'[\mathbf{x}_j^a]^\top \mathbf{W} \mathcal{G}[\mathbf{x}_j^a] = 0.$$

Assuming the observation operator  $\mathcal{H}$  has only modest nonlinearity, one can introduce a linearization around  $\mathbf{x}_j^f$ :

$$\begin{aligned}\mathcal{H}[\mathbf{x}_j^a] &\approx \mathcal{H}[\mathbf{x}_j^f] + \mathcal{H}'[\mathbf{x}_j^f](\mathbf{x}_j^a - \mathbf{x}_j^f), \\ \mathcal{H}'[\mathbf{x}_j^a] &\approx \mathcal{H}'[\mathbf{x}_j^f],\end{aligned}$$

where  $'$  denotes derivative with respect to the state. Similarly, we introduce two assumptions for the regularization term:

$$\mathcal{G}[\mathbf{x}^f] \approx \mathcal{G}[\mathbf{x}^a] \quad \text{and} \quad \mathcal{G}'[\mathbf{x}^f] \approx \mathcal{G}'[\mathbf{x}^a].$$

Different from  $\mathcal{H}[x]$ , we assume a convergence condition for  $\mathcal{G}[x]$  (i.e., the first derivative term is ignored) to simplify the derivation. Furthermore, we introduce the tangent linear operator  $\mathbf{H}$  for the observation operator  $\mathcal{H}$  so that  $\mathcal{H}'[\mathbf{x}] = \mathbf{H}$  and  $\mathcal{H}[\mathbf{x}] = \mathbf{H}\mathbf{x}$ . Equation (4.14) is then simplified to:

$$(4.15) \quad \mathbf{P}^{-1}(\mathbf{x}_j^a - \mathbf{x}_j^f) + \mathbf{H}^\top \mathbf{R}^{-1}(\mathbf{H}\mathbf{x}_j^f - y_j + \mathbf{H}(\mathbf{x}_j^a - \mathbf{x}_j^f)) + \lambda \mathcal{G}'[\mathbf{x}_j^f]^\top \mathbf{W} \mathcal{G}[\mathbf{x}_j^f] = 0.$$

After some algebra (details in B.1), this leads to the following analysis scheme:

$$(4.16) \quad \mathbf{x}_j^a = \mathbf{x}_j^f + \underbrace{\mathbf{P}\mathbf{H}^\top(\mathbf{R} + \mathbf{H}\mathbf{P}\mathbf{H}^\top)^{-1}(y_j - \mathbf{H}\mathbf{x}_j^f)}_{\text{Kalman correction}} - \underbrace{\mathbf{P}(\mathbf{I} + \mathbf{H}^\top \mathbf{R}^{-1} \mathbf{H}\mathbf{P})^{-1} \lambda \mathcal{G}'^\top \mathbf{W} \mathcal{G}}_{\text{regularization term}},$$

where the argument  $\mathbf{x}_j^f$  for the function  $\mathcal{G}$  and its derivative  $\mathcal{G}'$  are omitted for brevity of notation. This analysis scheme introduces two corrections to the prior realizations  $\mathbf{x}_j^f$ . The first, Kalman correction, comes from the classical ensemble Kalman methods and corresponds to the observation misfit term  $\|\mathcal{H}[\mathbf{x}_j] - y_j\|_{\mathbf{R}}^2$  in the cost function in Eq. (4.13), and the second correction corresponds to the regularization term  $\lambda \|\mathcal{G}[\mathbf{x}_j]\|_{\mathbf{W}}^2$ . Note that multiple regularization terms can be added in Eq. 4.16, each with their own function  $\mathcal{G}_i$ , weight matrix  $\mathbf{W}_i$ , and parameter  $\lambda_i$ .

The analysis scheme in Eq. (4.16) can be further simplified to facilitate interpretation and to gain insight into its relationship with that of classical Kalman update. First, we can expand the term  $-\mathbf{P}(\mathbf{I} + \mathbf{H}^\top \mathbf{R}^{-1} \mathbf{H}\mathbf{P})^{-1}$  in Eq. (4.16) to

$$-\mathbf{P} + \mathbf{P}\mathbf{H}^\top(\mathbf{R} + \mathbf{H}\mathbf{P}\mathbf{H}^\top)^{-1}\mathbf{H}\mathbf{P}$$

by using the Woodbury formula [63] (see details in B.1). Following the convention in the data assimilation literature, we write the Kalman gain matrix  $\mathbf{K} = \mathbf{P}\mathbf{H}^\top(\mathbf{R} + \mathbf{H}\mathbf{P}\mathbf{H}^\top)^{-1}$ . Consequently, the Kalman correction term and the regularization term become

$$(4.17) \quad \mathbf{K}(y_j - \mathbf{H}\mathbf{x}_j^f) \quad \text{and} \quad -\lambda \mathbf{P}\mathcal{G}'^\top \mathbf{W} \mathcal{G} + \mathbf{K}\mathbf{H}\lambda \mathbf{P}\mathcal{G}'^\top \mathbf{W} \mathcal{G},$$

respectively. We further denote

$$(4.18) \quad \delta = -\lambda \mathbf{P}\mathcal{G}'^\top \mathbf{W} \mathcal{G},$$

with which the analysis scheme Eq. (4.16) then takes the following simplified form:

$$(4.19) \quad \mathbf{x}_j^a = \mathbf{x}_j^f + \delta + \mathbf{K}(\mathbf{y}_j - \mathbf{H}(\mathbf{x}_j^f + \delta)),$$

or alternatively written as a two-step scheme:

$$(4.20a) \quad \tilde{\mathbf{x}}_j^f = \mathbf{x}_j^f + \delta,$$

$$(4.20b) \quad \mathbf{x}_j^a = \tilde{\mathbf{x}}_j^f + \mathbf{K}(\mathbf{y}_j - \mathbf{H}\tilde{\mathbf{x}}_j^f).$$

Note that Eq. (4.20b) has the same form as the analysis scheme of regular ensemble Kalman methods, i.e.,  $\mathbf{x}_j^a = \mathbf{x}_j^f + \mathbf{K}(\mathbf{y}_j - \mathbf{H}\mathbf{x}_j^f)$ . In other words, the regularized analysis scheme introduces a pre-correction  $\delta$  to the state vector  $\mathbf{x}_j^f$  to obtain  $\tilde{\mathbf{x}}_j^f$  (see Eq. (4.20a)). This pre-correction is what enforces the desired constraints. This is then followed by the Kalman correction (Eq. (4.20b)) to assimilate the observations. To enforce multiple constraints simultaneously, the regularization term can be written as a sum as follows:

$$\delta = - \sum_p \lambda_p \mathbf{P} \mathcal{G}_p'^T \mathbf{W}_p \mathcal{G}_p,$$

where the subscript  $p$  denotes index of different constraints. A case with multiple regularization terms is shown in Section 4.3.1. The proposed regularized ensemble Kalman method is schematically illustrated in Fig. 4.1 by using ensemble Kalman filtering (EnKF) procedure as an example, where our modification to the baseline EnKF is highlighted.

### 4.2.3 Implementing regularization procedure for an iterative ensemble Kalman method

As presented above the regularized Kalman update is general for the numerous ensemble Kalman methods, including the ensemble Kalman filter and the ensemble Kalman smoother. In the test cases in this paper, we use an iterative ensemble Kalman method to solve steady-state inverse problems iteratively. The analysis step is modified to incorporate the regularized update derived above. The analysis step is further modified here to overcome the effects of sample collapse on the regularization term and to avoid the dominance of the regularization term during early iterations. The details of this regularized iterative ensemble Kalman method used are presented below. The method described below differs from the iterative ensemble Kalman method for steady problems [71] only in the pre-correction step in the analysis. The proposed method requires only a small algorithmic modification. The unmodified method is used as a baseline for the test cases in Section 4.3.

Sample collapse is a common issue when using ensemble Kalman methods [48]. Moreover, for iterative methods on stationary systems, the observation data are used repeatedly, which further exacerbates the sample collapse problem. This is partly addressed by perturbing the observations (based on the observation error) at each iteration in addition to perturbing them

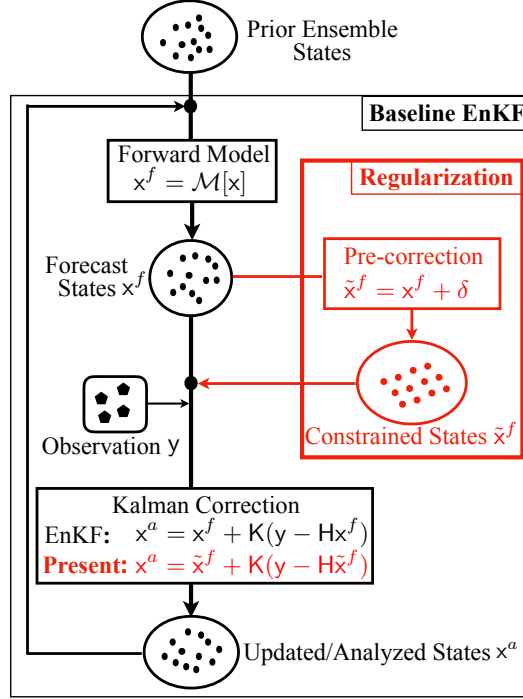


Figure 4.1: Schematics of ensemble Kalman methods by using ensemble Kalman filtering (EnKF) as example. The proposed regularization scheme consists of an additional correction  $\delta$ , defined in Eq. (4.17), to the forecast states  $x^f$  before the Kalman correction. Such a correction enforces constraints and is equivalent to penalty term  $\lambda \|\mathcal{G}[x]\|_W^2$  in adjoint methods as in Eq. (4.11). Our contribution that differentiates the present method to baseline ensemble Kalman methods is highlighted in red/grey box. The Kalman correction in the regularized EnKF has the identical form as that in standard EnKF except that it acts on the pre-corrected states  $\tilde{x}^f$ .

for each sample. Once the samples collapse, the covariance matrix  $\mathbf{P}$  approaches zero, and the regularization parameter  $\lambda$  has to be very large in order to keep the regularization effective (i.e., to keep it of a similar order of magnitude as the data discrepancy term. To overcome this issue further, we recast the pre-correction term  $\delta$  in Eq. 4.18 as follows:

$$(4.21) \quad \delta = -\frac{\chi}{\|\mathbf{P}\|_F} \mathbf{P} \mathcal{G}^\top \mathbf{W} \mathcal{G},$$

where  $\|\mathbf{P}\|_F$  is the Frobenius norm of matrix  $\mathbf{P}$ . Compared to the original derivation, we have written the algorithmic parameter as

$$(4.22) \quad \lambda \equiv \chi / \|\mathbf{P}\|_F.$$

Essentially, parameter  $\lambda$  is dynamically adjusted based on  $\|\mathbf{P}\|_F$  with  $\chi$  kept constant. In doing so, only the “direction” of the covariance matrix  $\mathbf{P}$  (i.e., information on the correlation of the samples) is preserved, which overcomes the detrimental effects of sample collapse on the added constraint. This makes it more intuitive to choose the algorithmic constant  $\chi$ .

During the first few iterations of an iterative method, a large penalty parameter can lead to the regularization term being dominant and consequently the observations being ignored. For this reason, the parameter  $\chi$  is further modeled using a ramp-up function as

$$(4.23) \quad \chi(i) = 0.5\chi_0 \left( \tanh \left( \frac{i-S}{d} \right) + 1 \right),$$

where  $\chi_0$  is the maximum value of  $\chi$  and  $i$  denotes the iteration step. The parameters  $S$  and  $d$  control the slope of the ramp-up curve and are chosen to be 5 and 2, respectively, for all test cases in this paper.

In the iterative ensemble Kalman method, the forward model  $\mathcal{M}$  is not linearized, and an iterative method is used to deal with this nonlinearity. Rather than linearizing

$$(4.24) \quad \mathcal{H} \equiv \tilde{\mathcal{H}} \circ \mathcal{M} \approx \mathbf{H},$$

only the observation operator is linearized, as  $\tilde{\mathcal{H}} \approx \tilde{\mathbf{H}}$ . Given the prior distribution of the state vector  $P(\mathbf{x})$ , observation values  $\mathbf{y}$  and error covariance matrix  $\mathbf{R}$ , and the constraint function  $\mathcal{G}$  with the weight matrix  $\mathbf{W}$  and parameter  $\lambda$ , the following steps are taken:

**1. (Sampling step)**

Generate initial ensemble of state vectors, consisting of  $M$  samples  $\{\mathbf{x}_j^{(0)}\}_{j=1}^M$ , from the prior distribution of the states.

**2. (Prediction step)**

For each sample, run the forward model to obtain the modeled observable fields.

**3. (Analysis step)**

i) Estimate the sample mean  $\bar{\mathbf{x}}^{(i)}$  and covariance  $\mathbf{P}^{(i)}$  as:

$$(4.25) \quad \bar{\mathbf{x}}^{(i)} = \frac{1}{M} \sum_{j=1}^M \mathbf{x}_j^{(i)},$$

$$(4.26) \quad \mathbf{P}^{(i)} = \frac{1}{M-1} \mathbf{X}^{(i)} (\mathbf{X}^{(i)})^\top,$$

where  $\mathbf{X}^{(i)}$  denotes the matrix formed by stacking the mean-subtracted sample vectors, i.e.,  $\mathbf{X}^{(i)} = \left[ (\mathbf{x}_1^{(i)} - \bar{\mathbf{x}}^{(i)}), \dots, (\mathbf{x}_M^{(i)} - \bar{\mathbf{x}}^{(i)}) \right]$ .

ii) Compute the Kalman gain matrix

$$(4.27) \quad \mathbf{K}^{(i)} = \mathbf{P}^{(i)} \mathbf{H}^\top (\mathbf{R} + \mathbf{H} \mathbf{P}^{(i)} \mathbf{H}^\top)^{-1}$$

iii) Generate an ensemble of observations  $\{\mathbf{y}_j^{(i)}\}_{j=1}^M$  from the joint normal distribution  $\mathcal{N}(\mathbf{y}, \mathbf{R})$ .

iv) For each sample, constrain the state  $\mathbf{x}$  with a pre-correction  $\delta$  as:

$$(4.28a) \quad \delta_j^{(i)} = -\lambda \mathbf{P}^{(i)} (\mathcal{G}'[\mathbf{x}_j^{(i)}])^\top \mathbf{W} \mathcal{G}[\mathbf{x}_j^{(i)}],$$

$$(4.28b) \quad \tilde{\mathbf{x}}_j^{(i)} = \mathbf{x}_j^{(i)} + \delta_j^{(i)},$$

with the regularization parameter  $\lambda$  determined from Eqs. (4.22) and (4.23).

v) For each sample, update the constrained state  $\tilde{\mathbf{x}}$ :

$$(4.29) \quad \mathbf{x}_j^{(i+1)} = \tilde{\mathbf{x}}_j^{(i)} + \mathbf{K}^{(i)} \left( \mathbf{y}_j^{(i)} - \mathbf{H} \tilde{\mathbf{x}}_j^{(i)} \right).$$

4. Return to step 2 until the ensemble is statistically converged.

We emphasize that the procedure described above differs from the baseline ensemble Kalman methods *only* in the additional pre-correction step in Eq. (4.28). That is, the proposed regularization only requires such small algorithmic modification to existing ensemble Kalman methods and is thus very straightforward to implement. The Python code for the proposed method and the test case from Section 4.3.1 are provided in a publicly available GitHub repository [154].

#### 4.2.4 Generality and possible extensions to other ensemble Kalman methods

In Section 4.2.3, we described how the proposed regularized Kalman update was implemented for the specific iterative method used in the test cases in this paper. However, we emphasize that it can be implemented into other ensemble Kalman methods straightforwardly. As an example take the ensemble Kalman filter used in data assimilation. The fields inferred are the initial conditions of the fields observed, and the forward model propagates these fields through time. The observations occur at different times and are assimilated as they occur. Similar to the method above the forward model is not linearized, but unlike the method above only a single analysis is done at each time. Because of these differences, the specific implementation for the two methods would obviously be different, but the modification to the analysis step will be the same in all cases. Similarly, the specific methods for dealing with the problem of sample collapse will vary from study to study, and the choice to model the parameter  $\lambda$  as described in Section 4.2.3 is particular to this study.

### 4.3 Results

We use three different test cases to showcase the use and performance of the proposed regularized ensemble Kalman method. First, we use it for the parameter estimation problem used by Wu et al. [144], which consists of a global minimization problem and for which the true solution is known. Parameter estimation problems typically have more observations than inferred

parameters, and the inferred parameters are discrete scalars. For the case tested, however, the number of observations is of less than but of the same order of magnitude as the number of inferred parameters, making it ill-posed. For this case we test a number of different constraints and prior mean (initial guess) and show that the proposed regularized method is effective in removing the ill-posedness of the data assimilation problem, making a better inference on the parameters. Parameter estimation problems in fluid mechanics include, for instance, determining the values of empirical parameters in specific turbulence models. Second, we test a field inversion problem: the one-dimensional diffusion equation on a finite domain with boundary conditions. The quantity to be inferred is a discretization of a continuous field, which is fundamentally different from the discrete scalars inferred in the first case. In this case, the number of inferred values is much larger than the number of observations. Finally, we test the proposed method for a more complex and relevant field inversion problem: the RANS closure problem. In this case, we infer the eddy viscosity field for a two-dimensional turbulent flow over periodic hills. For all cases, we show the advantage of the proposed regularized method over the traditional Kalman method in inferring the correct parameters or field by overcoming the ill-posedness intrinsic to inversion problems.

Both parameter estimation and field inversion problems have applications in computational fluid dynamics (CFD). In the case of field inversion, an important application is inferring the correct Reynolds stress field, and this is showcased in the third test case in this section. In the case of parameter estimation, one important application is inferring the parameters for the constructive turbulence models. Typically, many of these empirical parameters have underlying constraints determined from their theoretical derivation or numerical tests. For instance, Poroseva and Bezaud [118] recommend the relationship  $\sigma_\varepsilon/\sigma_k = 1.5$  in the  $k$ - $\varepsilon$  model [77] for aerodynamic simulations. Oliver and Moser [112] used a Bayesian approach to quantify the uncertainty of model parameters and indicated that the parameter  $k$  and  $c_{v1}$  in the Spalart–Allmaras model are linear. These are equality constraints. As an example of an inequality constraint, it has been shown through numerical experiments by Ray et al. [122] that the parameters in the  $k$ - $\varepsilon$  model have to satisfy  $C_{\varepsilon 2} > C_{\varepsilon 1}$ . The physical reason behind this delineation is that the ratio  $C_{\varepsilon 2}/C_{\varepsilon 1}$  corresponds to the spreading rate of a free jet. A ratio of  $C_{\varepsilon 2}/C_{\varepsilon 1} < 1$  would lead to a contracting jet, which is non-physical [147]. Nevertheless, most current works on ensemble-based parameter inferences neglect such underlying constraints, partly because of the difficulty in enforcing constraints in existing ensemble-based inversion methods.

### 4.3.1 Parameter estimation

The first test case is the parameter estimation problem used by Wu et al. [144]. The observable quantities  $\mathbf{z} \in \mathbb{R}^2$  is a vector related to two parameters  $\boldsymbol{\omega}$  (the state to be inferred) by the



forward model  $F$  as follows:

$$(4.30) \quad \mathbf{z} = \begin{bmatrix} z_1 \\ z_2 \end{bmatrix} = F[\boldsymbol{\omega}] = \begin{bmatrix} \exp(-(\omega_1 + 1)^2 - (\omega_2 + 1)^2) \\ \exp(-(\omega_1 - 1)^2 - (\omega_2 - 1)^2) \end{bmatrix},$$

$\boldsymbol{\omega} = [\omega_1, \omega_2]^\top$  is the parameter vector, and  $F$  is the forward model. The observation map is given by

$$(4.31) \quad \mathbf{y} = H\mathbf{z} = HF[\boldsymbol{\omega}],$$

with  $H = [-1.5, -1.0]$ . Given the observation  $\mathbf{y} = -1.0005$ , the inverse problem consists of inferring the parameters  $\boldsymbol{\omega}^{\text{opt}}$  that minimize the discrepancy between the observation  $\mathbf{y}$  and model output  $F[\boldsymbol{\omega}]$  (after the latter being projected to the observation space). That is,

$$(4.32) \quad J[\boldsymbol{\omega}] = \| \mathbf{y} - HF[\boldsymbol{\omega}] \|^2,$$

$$(4.33) \quad \boldsymbol{\omega}^{\text{opt}} = \arg \min_{\boldsymbol{\omega}} J[\boldsymbol{\omega}].$$

A contour plot of  $J$  is shown in Figure 4.2. This case has two groups of local minima: (Group I) the single point at  $\boldsymbol{\omega} = (1.0, 1.0)$ , and (Group II) the circle of points defined by

$$(4.34) \quad (\omega_1 + 1)^2 + (\omega_2 + 1)^2 = \log 1.5.$$

Numerous local minima result in satisfactory agreement with the observation, which makes the inference of the true parameter  $\boldsymbol{\omega}$  challenging. Fundamentally, this results from insufficient information from the observations, and the goal of the proposed regularized method is to guide the inference to the true values of the parameters by incorporating additional sources of information. Here the robustness of the method is tested by using different constraints and three different prior means for the parameters, similar to Wu et al. [144].

#### 4.3.1.1 Case details

The ensemble Kalman method is a Bayesian data assimilation framework and requires a prior distribution for the parameters. A Gaussian process is used with mean  $\boldsymbol{\omega}_p$ , equal standard deviation  $\sigma_p = 0, 1$  for both parameters, and zero covariance. Three different prior means are tested:  $\boldsymbol{\omega}_p \in \{(-1, -1), (0, 0), (2, 2)\}$ . For the observation, the true value of the parameters is taken to be  $\boldsymbol{\omega} = (1.0, 1.0)$ , and the observation to be  $\mathbf{y} = -1.0005$  with standard deviation  $\sigma_y = 0.01$ . Three different sets of constraints are enforced: an equality constraint, an inequality constraint, and multiple inequality constraints. Combined with the three prior distributions, a total of nine constrained cases were tested in addition to three baseline cases with no constraints.

We consider three different sources of information on the quantity  $\omega_1 + \omega_2$ : equal to 2, greater than 1, and less than 3, with corresponding constraint equations:

$$(4.35) \quad h_{\text{eq}}[\boldsymbol{\omega}] = \omega_1 + \omega_2 - 2 = 0,$$

$$(4.36) \quad h_{\text{in1}}[\boldsymbol{\omega}] = -\omega_1 - \omega_2 + 1 < 0,$$

$$(4.37) \quad h_{\text{in2}}[\boldsymbol{\omega}] = \omega_1 + \omega_2 - 3 < 0.$$

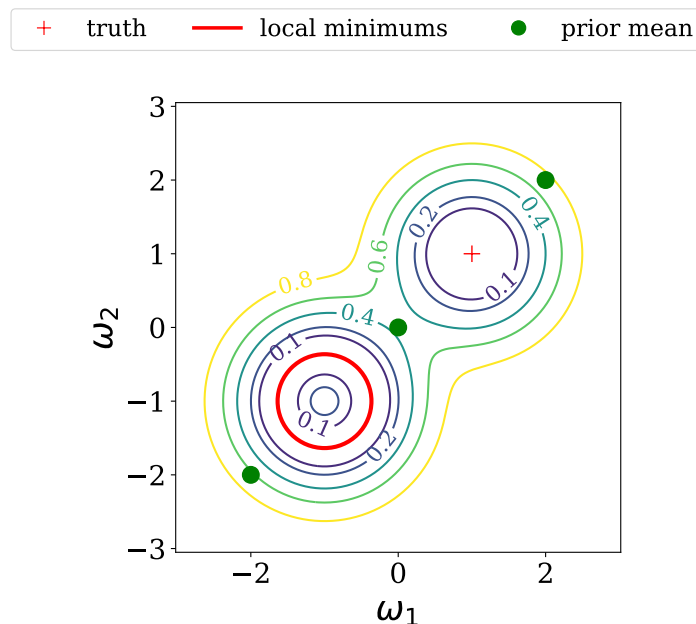


Figure 4.2: Contour plot of the discrepancy  $J[\omega]$ . The two groups of local minimums are indicated with the red/gray cross “+” (Group I) and the red/gray circle (Group II).

For inequalities of the form  $h_{in}[\omega] < 0$  a penalty function  $\phi[h_{in}[\omega]]$  of the form

$$(4.38) \quad \mathcal{G}[\omega] = \phi[h_{in}[\omega]] = \begin{cases} 0 & \text{for } h_{in}[\omega] < 0 \\ h_{in}[\omega]^2 & \text{for } h_{in}[\omega] \geq 0 \end{cases}$$

is used. The derivative can be obtained from chain-rule for  $h_{in1}[\omega]$ :

$$(4.39) \quad \mathcal{G}'[\omega] = \phi'[h_{in}[\omega]] = \begin{cases} (0, 0) & \text{for } h_{in}[\omega] < 0 \\ (-2h_{in}[\omega], -2h_{in}[\omega]) & \text{for } h_{in}[\omega] \geq 0 \end{cases}.$$

The three constraints used as regularization are summarized in Table 4.1. The last case consists of multiple inequalities and serves as an illustration of combining multiple sources of information into the framework. For the inequality constraints, the penalty function is only active when the constraint is violated. The penalties in Table 4.1 are implemented as in Eq. (4.21), with covariance set to the identity matrix  $W = I$ . A regularization parameter of  $\chi_0 = 0.1$  is used.

Table 4.1: Summary of the constraints used in the parameter estimation problem.

case	constraint type	penalty function
C1	equality	$\mathcal{G}(\omega) = h_{eq}[\omega]$
C2	inequality	$\mathcal{G}(\omega) = \phi[h_{in1}[\omega]]$
C3	multiple	$\mathcal{G}(\omega) = \phi[h_{in1}[\omega]] + \phi[h_{in2}[\omega]]$

Table 4.2: Results of the baseline and regularized inference with different constraints.

method	initial $\omega$	inferred $\omega$	$HF[\omega]$	error ( $\omega$ )	error ( $HF[\omega]$ )
truth/observation	—	(1.0, 1.0)	-1.0005	—	—
Baseline	(-2, -2)	(-1.52, -0.63)	-1.0010	(252%, 163%)	0.05%
	(0, 0)	(-1.55, -1.30)	-1.0108	(255%, 230%)	1.03%
	(2, 2)	(0.94, 0.95)	-0.9947	(6%, 5%)	0.58%
C1	(-2, -2)	(1.06, 0.93)	-0.9921	(6%, 7%)	0.84%
	(0, 0)	(1.06, 0.93)	-0.9921	(6%, 7%)	0.84%
	(2, 2)	(1.02, 0.98)	-0.9997	(2%, 2%)	0.08%
C2	(-2, -2)	(1.07, 1.03)	-0.9946	(7%, 3%)	0.59%
	(0, 0)	(0.96, 0.98)	-0.9986	(4%, 2%)	0.19%
	(2, 2)	(0.94, 0.96)	-0.9956	(6%, 4%)	0.49%
C3	(-2, -2)	(1.03, 0.94)	-0.9961	(3%, 6%)	0.44%
	(0, 0)	(1.01, 0.93)	-0.9956	(1%, 7%)	0.48%
	(2, 2)	(0.95, 0.94)	-0.9947	(5%, 6%)	0.58%

#### 4.3.1.2 Results

As a baseline, the ensemble Kalman method is used without any regularization (constraints) for each of the three prior distributions considered. The results are shown in Fig. 4.3a and Table 4.2. It is noticeable that for different priors the inference will converge to a different local minimum, with the priors with mean of  $(-2, -2)$  and  $(0, 0)$  converging to local minima belonging to Group II. Next, the proposed regularized method is tested using the equality constraint (case C1). The results are shown in Fig. 4.3b and Table 4.2. Using the equality constraint the inference converges around the truth for all three priors considered.

Similarly, the inequality constraint (case C2) is able to make the inference converge around the truth for all three priors considered, completely avoiding the Group II local minima. These results are shown in Fig. 4.3c and Table 4.2. It should be noted that the penalty term in this case is only active when the constraint is violated. This results in that while this constraint can avoid inference dropping into the local minima in Group II it cannot further enhance the optimization result, as in the case with the equality constraint. Finally, the method is tested with multiple inequality constraints (case C3) in order to showcase how to incorporate multiple sources of information. Once again, the inference converges around the truth for all three priors considered, and the results are shown in Fig. 4.3d and Table 4.2.

The errors in the inferred quantities are quantified based on the agreement with their corresponding true values. The error on quantity  $q$  is defined as:

$$(4.40) \quad \text{error} = \frac{\|q_{\text{truth}} - q_{\text{estimate}}\|}{\|q_{\text{truth}}\|}.$$

The errors on the parameters  $\omega$  and the observed point are shown in Table 4.2. For all constraints and prior means considered, the proposed regularized method can infer the parameters accurately,

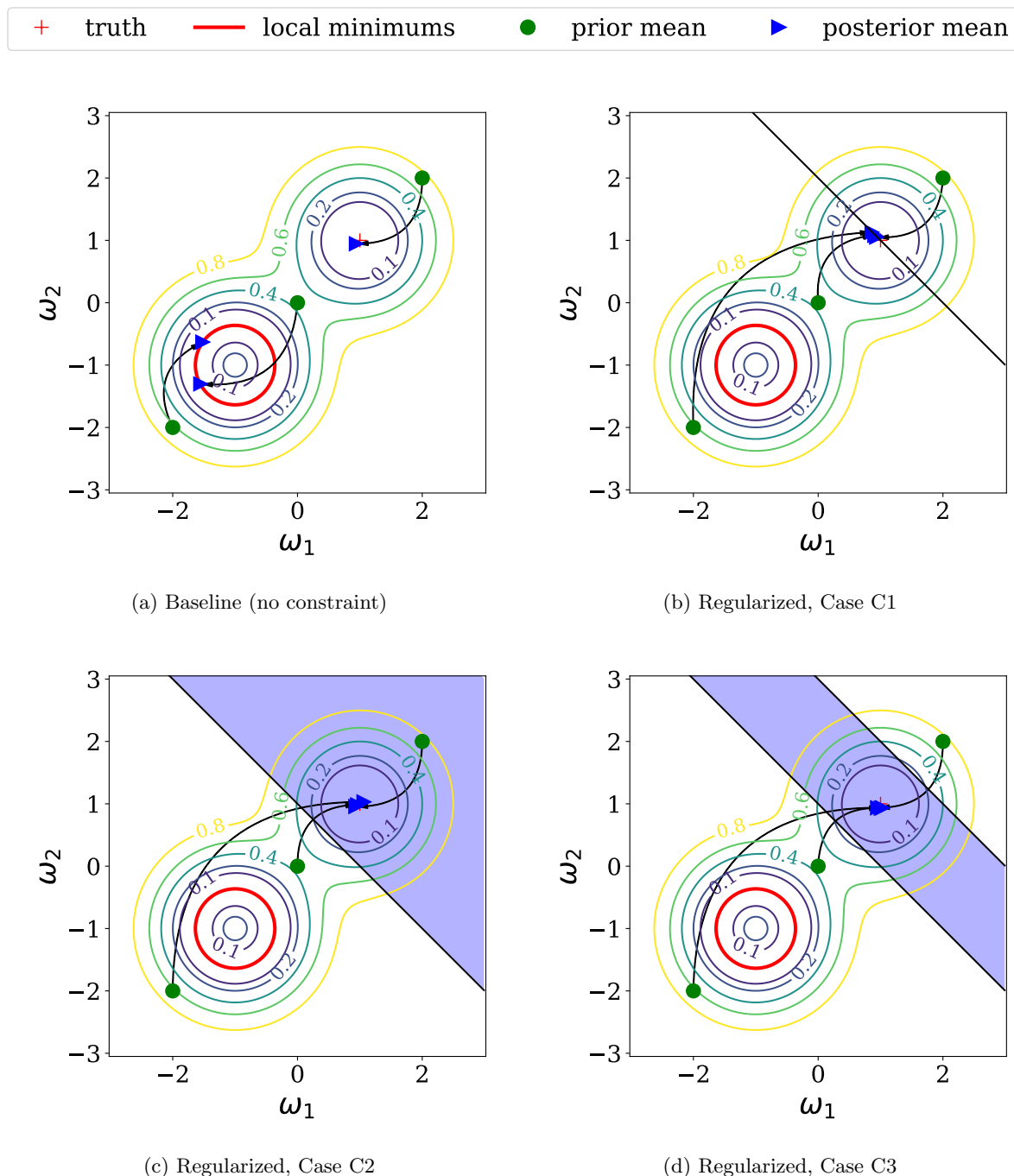


Figure 4.3: Results of parameter estimation problem using the baseline and proposed regularized methods with different constraints. For all methods three different prior means (green/gray dots) are considered. (a) Baseline case; (b) Case C2: proposed method with  $G[\omega] = h_1[\omega]$  where penalty function is indicated by the black straight line ; (c) Case C2: proposed method with  $G[\omega] = \phi[h_{in1}[\omega]]$ . The blue/gray region indicates where the constraint is inactive; (d) Case C3: proposed method with  $G[\omega] = \phi[h_{in1}[\omega]] + \phi[h_{in2}[\omega]]$ . The blue/gray region indicates where the constraint is inactive. With the baseline method, different priors converge to the different local minima. With the proposed regularized method all priors can converge to the true local minimum  $(1, 1)$ , indicated as blue/gray triangle.

comparable to the baseline case with prior mean of  $(-2, -2)$ . For the estimated observation error, all cases, including the unregularized baseline, can give a satisfactory estimation in the observation space.

It should be noted that the regularization parameter  $\chi$  in the penalty term in the cost function is inflated as in Eq. (4.23) to ensure the robustness of the analysis step. The hyper-parameters in the ramp-up function may affect the inference performance. Concretely, the parameter  $\chi_0$  has to be inflated sufficiently to regularize the inference but not so much as to ignore the observations. If the penalty term is too small it cannot drag the inference away from the erroneous local minima. The hyper-parameters  $\chi_0$ ,  $S$ , and  $d$  in Eq. (4.23) were chosen based on a parameter study. The parameter study suggests that the equality constraint is robust with a large range of parameters leading to correct inference. However, the inequality constraint was found to be significantly more sensitive to these parameters. This is due to the nature of such constraints and not caused by the intrinsic limitations of the proposed method. The equality constraint embeds more information about the truth, which can further enforce the inference to the expected point. In contrast, inequality constraints can only drag the inferred parameters out of the region where the constraint is violated but cannot further inform the inference process as the equality constraint does. Consequently, too large a penalty term may result in over-correction and lead to inference divergence, while too small a penalty term may not be sufficient to force the parameters out of the constraint-violating region and away from the undesired local minima. Detailed results of the parameter studies are presented in B.2.

### 4.3.2 Field inversion

The second test case is a field inversion case, in which observations of a field described by a partial differential equation (PDE) are used to infer a latent field in the PDE. Specifically, we infer the diffusivity field in the one-dimensional diffusion equation by observing the temperature at a few locations. As is the case in general for field inversion problems, the number of observations is much smaller than the dimensions of the discretized domain. This increases the ill-posedness of the problem and makes it challenging to infer the true latent field. We apply the proposed method to regularize the problem and demonstrate its ability to infer the correct field by incorporating additional knowledge into the inversion scheme.

The diffusion equation is given by

$$(4.41) \quad -\frac{d}{dx} \left( \mu[x] \frac{du}{dx} \right) = f[x]$$

where  $x$  is the one-dimensional spatial coordinate,  $u$  is the quantity being diffused which is considered the output observable field,  $f[x]$  is a source term in units of  $u$  per time, and  $\mu[x]$  is the diffusivity field which is regarded as the latent field to be inferred. Here we consider the diffusion of a non-dimensional quantity  $u$  (e.g., normalized by a reference value), but the equation can be used for many different applications. For instance, it could be used for heat

distribution along a rod, where  $u$  is temperature,  $f$  is distribution of heat sources, and  $\mu$  is thermal diffusivity of the material. Another common application is pollutant concentration in a fluid, where  $u$  is concentration density,  $f$  is distribution of pollutant sources, and  $\mu$  is mass diffusivity of the pollutant in that medium. We consider a domain of length  $L_x$ , a source term  $f[x] = 100 \sin(2\pi x/L_x)$ , and homogeneous boundary conditions  $u|_{x=0} = u|_{x=L_x} = 0$ . The domain is discretized into 50 equal length cells, and the equation is discretized using the central difference scheme. The output field  $u$  is observed at nine equally spaced locations  $x/L_x = 0.1, 0.2, \dots, 0.9$ , and the goal is then to infer the value of the discretized diffusivity field at each of the 50 cells.

#### 4.3.2.1 Case details

The values of the discretized diffusivity field are not independent, and some sort of spatial correlation needs to be enforced. Furthermore, diffusivity is a field with physical meaning and subject to the physical constraint that it must be non-negative. To ensure positivity, the logarithm of diffusivity  $\log[\mu/\mu_0]$  is inferred, where  $\mu_0$  is a reference diffusivity value. To enforce spatial correlation and smoothness, the field  $\log[\mu/\mu_0]$  is assumed to be a sample of a Gaussian process  $\log[\mu/\mu_0] = \mathcal{GP}(0, \mathcal{K})$  with correlation kernel  $\mathcal{K}$ . Using Karhunen-Loève (KL) decomposition the field can be written as

$$(4.42) \quad \log[\mu/\mu_0] = \sum_{i=1}^n \omega_i \sqrt{\lambda_i} \phi_i,$$

where  $\lambda_i$  and  $\phi_i$  are the eigenvalues and unit eigenvectors of the kernel  $\mathcal{K}$ , and  $\omega_i$  are coefficients. While  $n$  is theoretically equal to the discretization size, it is common to set it to a much smaller value due to the rapid decrease of the magnitude of the eigenvalues. This also results in dimensionality reduction, which can be beneficial in large 2- or 3-dimensional problems with large discretization. The problem now consists of inferring the coefficients  $\omega_i$  rather than the discretized  $\log[\mu/\mu_0]$  or  $\mu$  fields directly. We use the square exponential kernel with standard deviation  $\sigma_p$  and length scale  $l$ , which for two points  $x$  and  $x'$  is given by

$$(4.43) \quad \mathcal{K}(x, x') = \sigma_p^2 \exp\left(-\frac{\|x - x'\|^2}{l^2}\right).$$

A standard deviation of  $\sigma_p = 1.0$  is used, and the length scale is chosen as  $l = 0.02L_x$ , a relatively small value to allow for noisy inferred fields, making the problem artificially more difficult. The first five modes scaled by their respective eigenvalues are shown in Fig. 4.4. It can be seen that higher modes correspond to higher frequencies and that the magnitudes of the modes decrease slowly.

For the Bayesian inversion scheme, the prior distribution of  $\log[\mu/\mu_0]$  is considered to be the Gaussian process described earlier with uniform mean  $\mu_p[x] = \mu_0$ . A total of 80 samples are used, created using the KL decomposition in Eq. (4.42) with random coefficients with

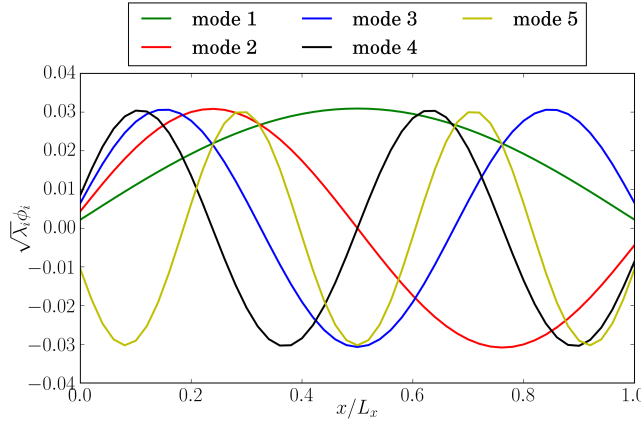


Figure 4.4: First 5 KL modes in the diffusion case scaled by their corresponding eigenvalues.

independent standard normal distributions, i.e.  $\omega_i \sim \mathcal{N}(0, 1)$ . The truth is constructed using the same decomposition in Eq. (4.42) with only the first three modes, each with coefficient equal to 1, i.e.,  $\omega_1 = \omega_2 = \omega_3 = 1.0$  and  $\omega_j = 0$  for  $j > 3$ . The observations in  $u$  are obtained by propagating this true diffusivity field through the diffusion equation and using an observation standard deviation of  $\sigma_y = 0.0001$ . Fig. 4.5 shows the prior samples for the diffusivity field as well as the propagated output field for different number of modes as will be discussed later.

The synthetic truth is constructed with only 3 modes, and the magnitude of the eigenvalues of the kernel decreases slowly due to the small length scale used in the correlation kernel. Because of these two facts, by setting the number of modes  $n$  used in the representation of the field (Eq. 4.42), we can control the dimension of the inference space and the level of ill-posedness of the problem. Specifically, if a large number of modes is used, many different diffusivity fields with increasingly different qualitative shapes can result in matching the observations in the output space. We consider as an additional source of knowledge that the first three modes are the most important, and use REnKF to embed this information into the data assimilation process. To embed this information, we use a penalty function of the form:

$$(4.44) \quad G[\omega] = \omega,$$

with a weight matrix

$$(4.45) \quad \text{diag}(0, 0, 0, 1, \dots, 1),$$

where the last  $n - 3$  modes are penalized. We use the ramp-up in Eq. (4.23) with  $\chi_0 = 10$ . With this constraint, the first three modes are not penalized while the value of the coefficients for any other modes contributes to the cost function. It is noted that this is a soft constraint, which still allows for higher modes if they contribute to improving the agreement with observations.

To test the performance of the proposed method, we perform the field inversion with both the baseline and regularized ensemble Kalman methods using different number of modes. Here

the results with 3, 5, and 20 modes are presented. In this case, the regularized method with 3 modes is equivalent to the baseline and is not repeated. Fig. 4.5 shows the prior distributions (samples) for the three test cases using an increasing number of modes. Note that with more modes there are much higher oscillations in the diffusivity fields in the prior, leading to samples that look very noisy. Nonetheless, even with the high noise all cases have similar distributions in the output field. This clearly shows the ill-posedness of this field inversion problem. Diffusivity fields that are qualitatively very different still result in very similar output fields, where the observation is made. The traditional ensemble Kalman method has no way to prefer one of these over the others as long as they match well with the observations in the output space.

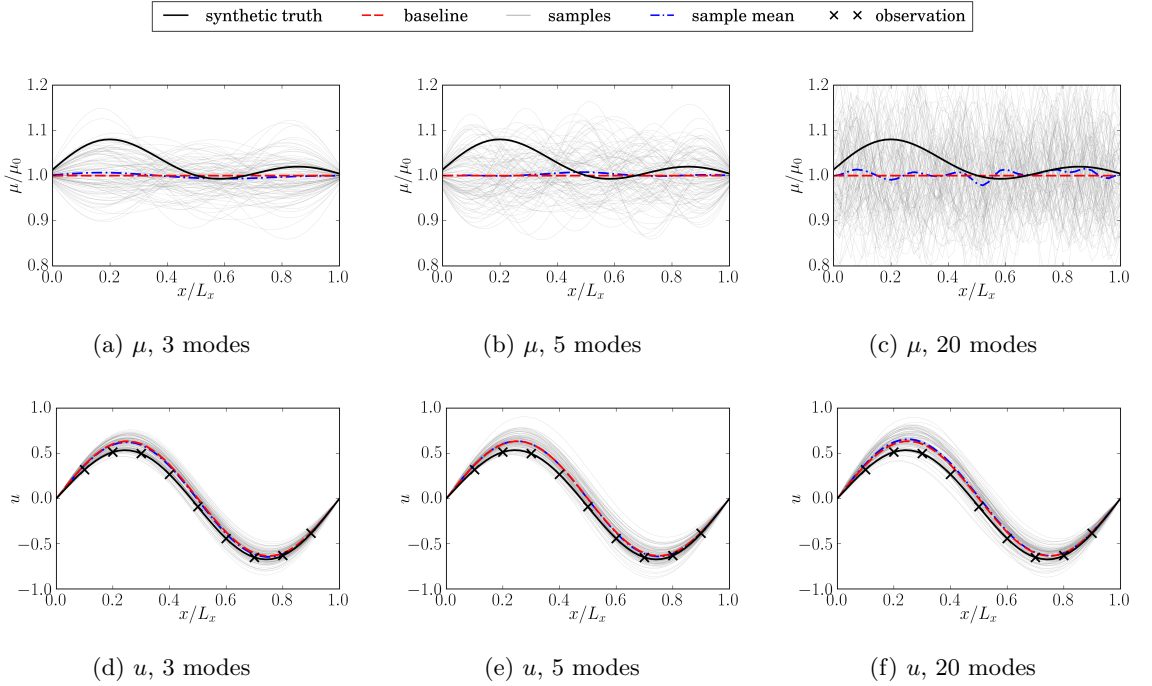


Figure 4.5: **Prior samples** of diffusivity  $\mu$  (top) and corresponding output fields  $u$  (bottom) for different number of modes.

#### 4.3.2.2 Results

The results of the inferred field  $\mu$  are shown in Figure 4.6. With different modes, both EnKF and REnKF are able to give a satisfactory agreement in the observed field, and these results are omitted since they are visually indistinguishable. The difference between the results from the different methods lies in their ability to infer the correct latent diffusivity field. The baseline method with only three modes results in the correct diffusivity field as expected, since this problem is not ill-posed. However, when there is more freedom with the increased number of modes and hence increased dimensionality of the space of possible latent fields, the baseline method infers increasingly more qualitatively wrong diffusivity fields while still matching the



observations and true output field. Incorporating the additional knowledge through the proposed regularized method results in the correct diffusivity field being inferred even in the cases with a large number of modes. This is clearly seen in Fig. 4.6.

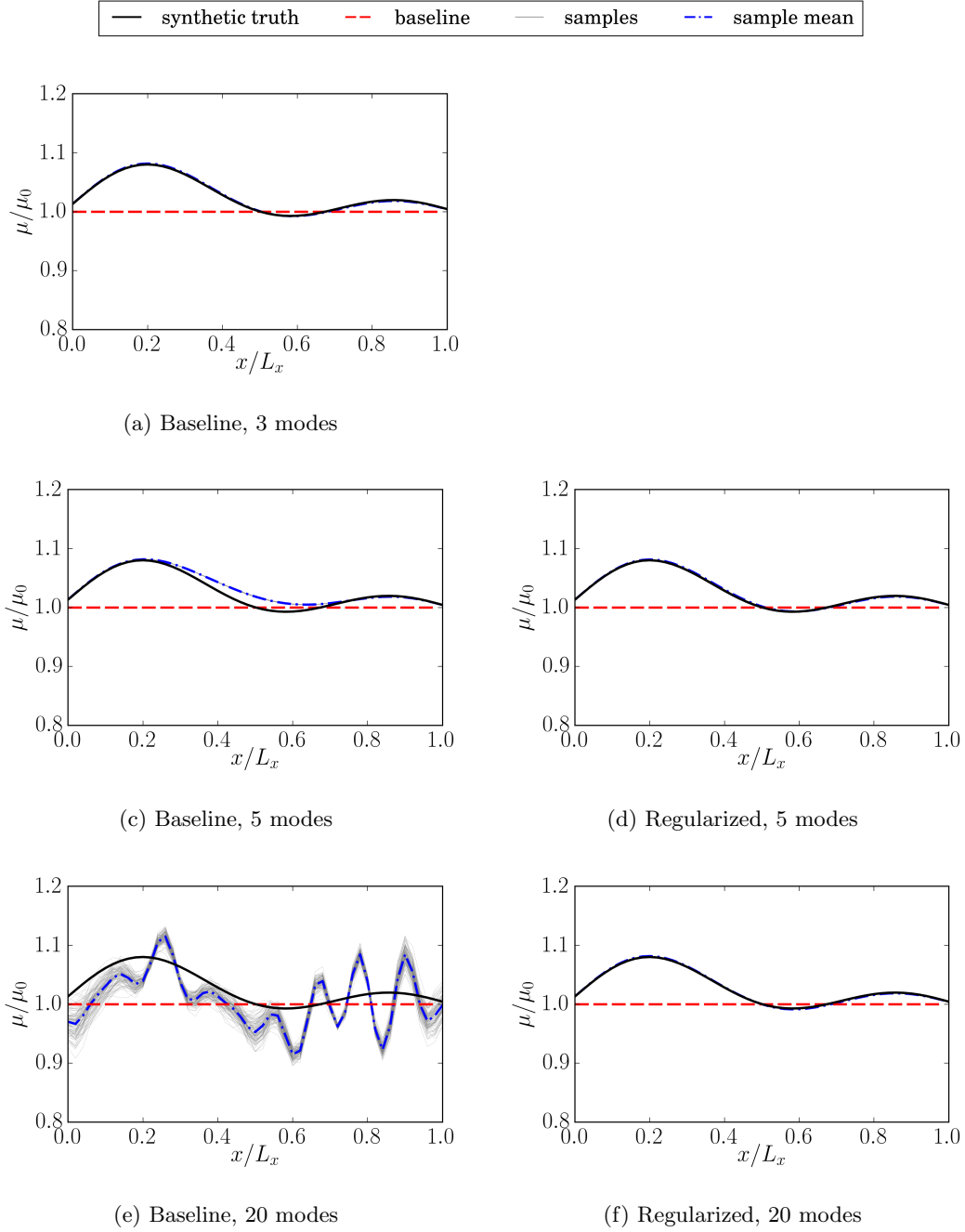


Figure 4.6: Inferred diffusivity by using the **baseline methods** (left column; panels a, b, and d) and the **proposed regularized methods** (right column; panels c and e) for different number of modes.

The inferred KL coefficients for the different methods are shown in Fig. 4.7 for the cases

with 20 modes. It is noticeable that the baseline method uses all the available modes, while the regularized method only uses the first three modes as expected. Moreover, the inferred coefficients with the regularized method have good agreement with the synthetic truth values. The errors in the inferred diffusivity for the different methods are shown in Fig. 4.8 as a function of the number of modes used in the representation. It can be seen that with increasing number of modes, the baseline method gives increasingly worse inference on the diffusivity, while with the regularized method the error remains relatively constant. The regularized method can provide satisfactory inference regardless of the number of modes used in the representation.

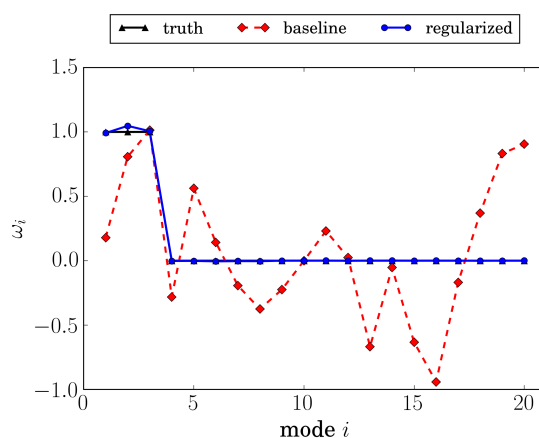


Figure 4.7: Comparison of inferred KL coefficients for **the diffusion case** by using the baseline method and the regularized method with 20 modes.

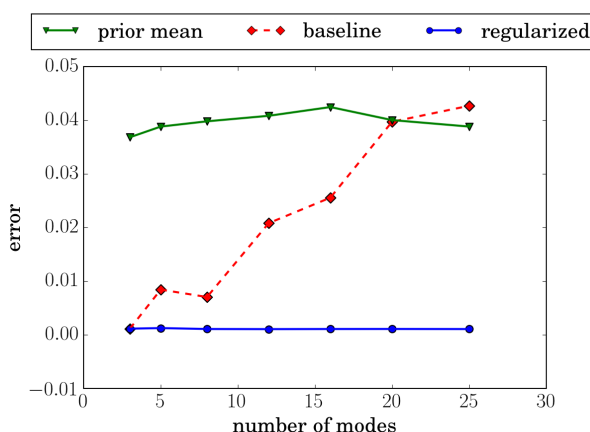


Figure 4.8: Errors in the inferred diffusivity in **the diffusion case** for the baseline method and the regularized methods as a function of number of modes used in the field representation.

### 4.3.3 RANS equations closure

As a final case we test the proposed regularized method for a field inversion problem of practical interest in fluid mechanics: closure of the Reynolds-averaged Navier–Stokes (RANS) equations. The RANS equations describe the mean flow of fluid accurately; however, they are unclosed. The Reynolds stress term requires a turbulence model, and no universally good model exists. In practice, this means that complex flows cannot be confidently predicted in regions with separation or high pressure gradients. It is therefore of tremendous interest to infer the Reynolds stress in regions where the flow is too complex to be captured by current turbulence models. This can be achieved by incorporating sparse observations using inversion schemes such as the ensemble Kalman methods. Here we consider the steady two-dimensional incompressible RANS equations with linear eddy viscosity assumption. This means that a single scalar field, the eddy viscosity field, needs to be inferred rather than the full Reynolds stress tensor field. The RANS equations can then be written as

$$(4.46a) \quad \frac{\partial U_i}{\partial x_i} = 0$$

$$(4.46b) \quad U_j \frac{\partial U_i}{\partial x_j} = -\frac{\partial p}{\partial x_i} + \frac{\partial}{\partial x_i} \left[ (\nu + \nu_t) \left( \frac{\partial U_i}{\partial x_j} + \frac{\partial U_j}{\partial x_i} \right) \right],$$

using Einstein summation notation, where  $i \in 1, 2$  denotes spatial direction,  $U$  is velocity,  $x$  is spatial coordinate,  $p$  is a pseudo pressure term,  $\nu$  is the fluid viscosity, and  $\nu_t$  is the eddy viscosity field to be inferred.

For this test case, we use the canonical flow over periodic hills [14] which has been extensively used for the investigation of numerical methods in CFD [60]. A single hill is modeled with periodic boundary conditions. The domain is discretized with 50 cells in the stream-wise direction  $x_1$  and 30 cells in the wall-normal direction  $x_2$ . The dimensionless wall distance  $y^+$  of the first cell is small enough to lie in the viscosity layer, and no wall model is used. All spatial coordinates are normalized by hill height  $H$  and all velocities by the bulk velocity  $U_b$  at the hill crest. The Reynolds number based on  $H$  and  $U_b$  is 2800.

In this case, we use OpenFOAM, an open-source CFD platform based on finite volume discretization, to simulate the incompressible, steady-state turbulent flows. The SIMPLE (Semi-Implicit Method for Pressure Linked Equations) algorithm is used to solve the RANS equations. The second-order spatial discretization schemes are applied to discretize the equations on an unstructured mesh. The prior mean and synthetic truth are both created from RANS simulations using the built-in simpleFOAM solver but with different turbulence models. The synthetic truth is obtained using the  $k$ - $\varepsilon$  model [77] and the prior mean using the Spalart–Allmaras model [133]. To propagate eddy viscosity to the velocity field, a modified solver was created that uses a constant specified eddy viscosity field rather than using a turbulence model. This modified solver is the forward model which gives the output fields (velocities and pressure) given an input field (eddy viscosity).

### 4.3.3.1 Case details

The latent field to be inferred is the eddy viscosity field  $\nu_t$ . Like the diffusivity field in the former case, the eddy viscosity is non-negative, and the same representation is used for it as for  $\mu$  in Eq. (4.42), inferring the logarithm of the field and using KL decomposition. That is,  $\log[\nu_t/\nu_{t0}] = \mathcal{GP}(0, \mathcal{K})$ , where  $\nu_{t0}$  is a reference eddy viscosity value. Again the square exponential covariance in Eq. (4.43) is used, with length scale  $l = 0.25H$  and variance  $\sigma^2 = 1.0$ . The first eight modes of the decomposition are shown in Fig. 4.9. The lower modes represent the larger scale characteristics of the constructed field, while the higher modes have more oscillations. For the prior we use the results from a RANS simulation with Spalart–Allmaras turbulence model and a standard deviation of  $\sigma_p = 1.0$ . These results are projected into the KL modes to get the prior coefficients  $\omega_i$  and 100 samples are created. The prior distribution of eddy viscosity and the propagated streamwise velocity are shown in Fig. 4.10. Note the high oscillations in the prior eddy viscosity and the relatively smooth propagated streamwise velocities, which highlights the ill-posedness of the problem. The results from a RANS simulation with  $k$ - $\varepsilon$  turbulence model are taken as the truth which is used to create synthetic observations. The observations consist of streamwise velocity  $U_1$  at 18 points, shown in Fig. 4.10b, with observation error  $\sigma_y = 0.001$ .

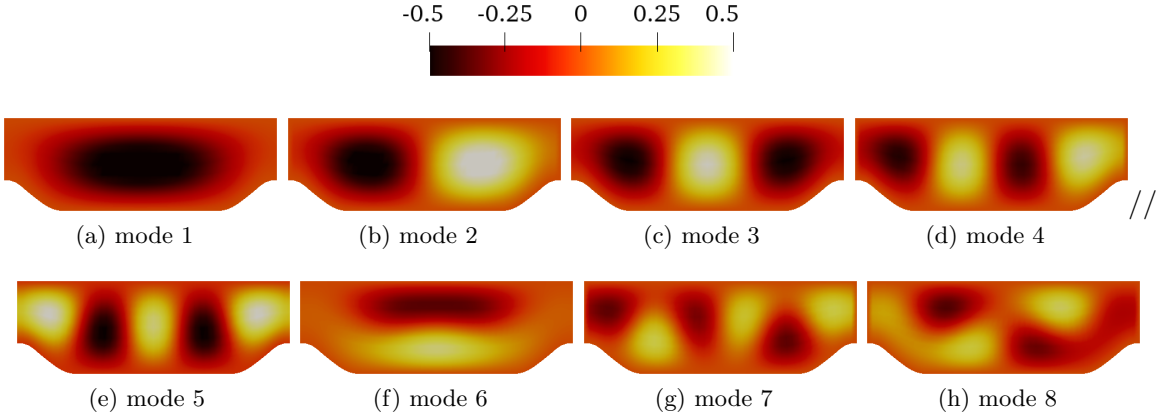


Figure 4.9: Contour plots of first 8 modes from KL decomposition for the periodic hills case. The modes are scaled by their corresponding eigenvalues.

As a baseline, the inverse problem is solved using the traditional ensemble Kalman method. As before, different number of modes are used to study cases which are progressively more ill-posed. The results for all cases are summarized but we choose to highlight the results for the case with 200 modes in more detail as a sample case. As can be seen from the prior samples in Fig. 4.10a, the eddy viscosity field can have a qualitatively very different shape from the truth and still result in satisfactory results in the observation space. This problem can be exacerbated in the inference where the inferred values of the coefficients  $\omega_i$  are not restrained unlike in the prior where they are specified to sample from a standard normal distribution. This means that

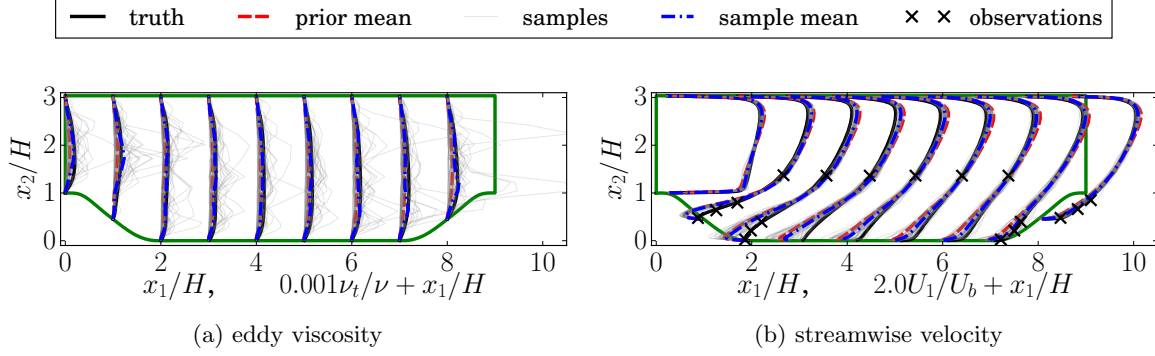


Figure 4.10: Prior realizations of eddy viscosity  $\nu_t$  and propagated streamwise velocity  $U_1$  for the periodic hills case. The locations of the observations are indicated by crosses ( $\times$ ).

the inferred coefficients for higher modes can be very large. However, the modes from the KL decomposition have intrinsic importance embedded in them, indicated by the magnitude of their corresponding eigenvalues, and while this information is used in constructing the prior samples, it is ignored in the inference step. We use this relative importance of the modes as an additional source of information to create a regularization constraint. Among equally fit candidate solutions, we will prefer the simplest one, i.e., the one that uses the fewest modes (e.g., low pass filter). We use this preference as the regularization and use the relative importance of the modes to embed this preference into the inversion through the proposed method. To achieve this, a penalty function

$$(4.47) \quad G[\omega] = \omega$$

is used with covariance  $W$  constructed from the inverse of the eigenvalues as

$$(4.48) \quad \text{diag} \left( \frac{1}{\lambda_1}, \dots, \frac{1}{\lambda_{n-1}}, \frac{1}{\lambda_n} \right)$$

A value of  $\chi_0 = 0.1$  is used for the ramp-up in Eq. (4.23).

#### 4.3.3.2 Results

The case with 200 modes is used to show the performance of the proposed regularized method. Profiles of the inferred eddy viscosity fields, as well as the propagated stream-wise velocity fields, are shown in Fig. 4.11 using both the baseline and regularized methods. The baseline method is able to improve the velocity profiles in most of the domain. The regularized method is similarly able to improve the velocity field in the entire domain. Although the baseline method improves the predicted velocity, the inferred eddy viscosity field is much farther from the true field than the prior. The inferred eddy viscosity field in Fig. 4.11a have magnitudes many times larger than the truth and exhibit much more oscillations. Embedding the additional information into inversion using the regularized method can result in improved results. The inferred field in

Fig. 4.11b is still worse than the prior, but many of the problems in the inferred field with the baseline method have been significantly reduced. Specifically, the inferred field is smoother and has smaller magnitudes. The entire inferred fields are shown in Fig. 4.12, which more clearly shows the qualitative difference between the true field and the inferred fields using either method. The field inferred with the regularized method can be seen to reduce the magnitude and number of the oscillations compared to the field inferred with the baseline ensemble Kalman method. To further improve the inferred eddy viscosity, more information such as smoothness could be embedded as constraints in the regularized ensemble Kalman method.

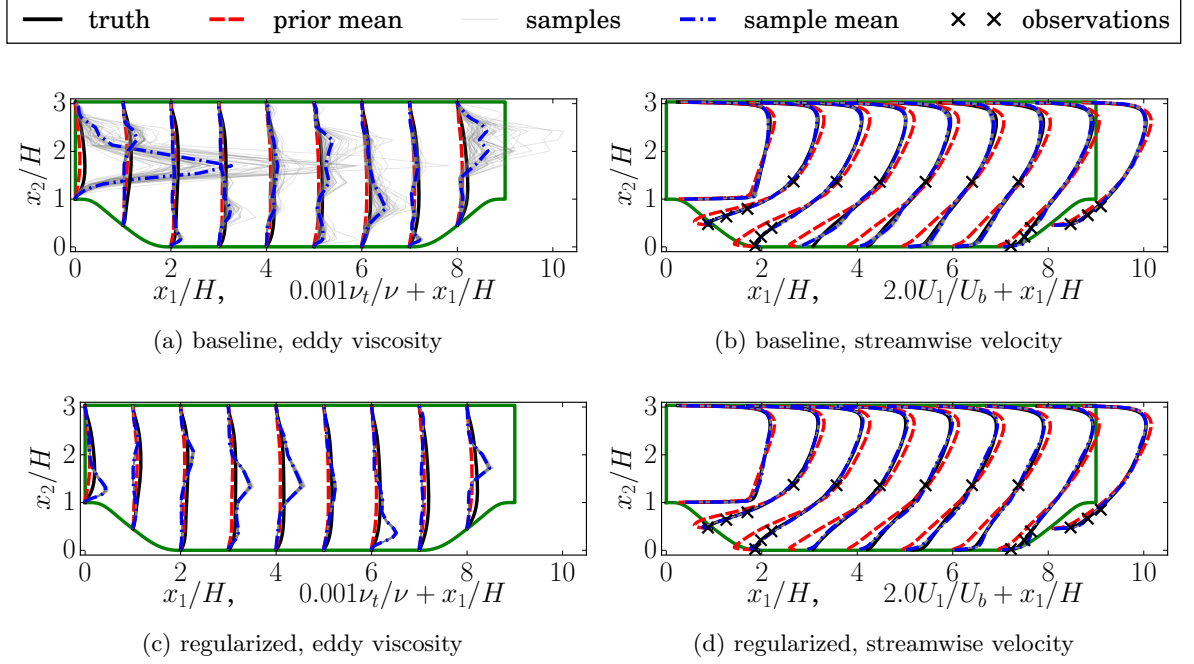


Figure 4.11: Inferred eddy viscosity field and propagated streamwise velocity field for the baseline and regularized methods using 200 modes.

The magnitudes of the inferred coefficients for both methods are shown in Fig. 4.13. The baseline ensemble Kalman method uses the modes indiscriminately, and the KL coefficients for the higher modes are still large. By contrast, the regularized method uses less of the higher modes, successfully enforcing our preference. Furthermore, the trend of the decay of magnitudes of the inferred coefficients is proportional to the eigenvalues as expected. This is due to the specified weight matrix in Eq. (4.48) penalizing each mode by the reciprocal  $1/\lambda_i$  of its respective eigenvalue.

The error in the inferred eddy viscosity is calculated using Eq. (4.40). The errors for the different methods are shown in Fig. 4.14 as a function of number of the modes used in the representation. The inference with regularized method has a lower error for all cases tested. It should be noted that this measure of error accounts for the entire field not only observation points. With too few modes, the error is large because the number of modes is insufficient to

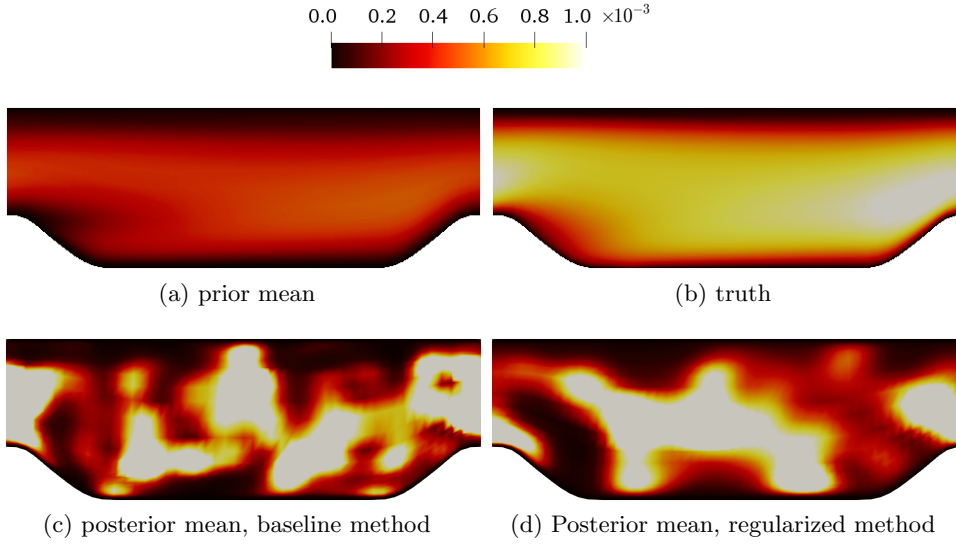


Figure 4.12: Contour plots of the inferred (posterior) eddy viscosity  $\nu_t$  with with the baseline and regularized methods using 200 modes.

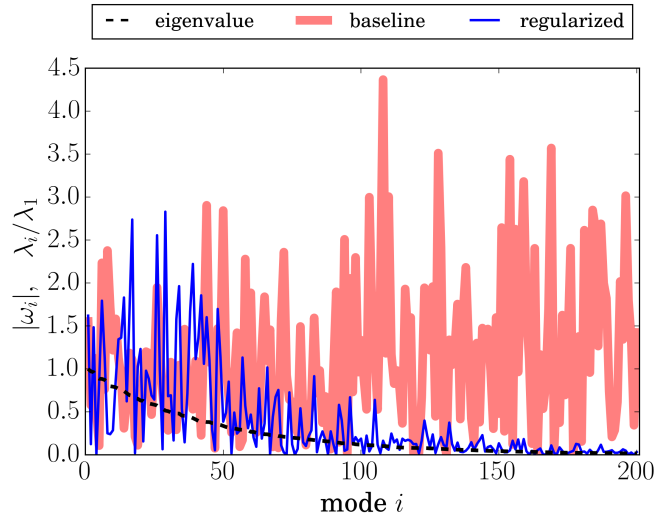


Figure 4.13: Magnitudes of the inferred KL coefficients for the periodic hills case using the baseline and regularized methods with 200 modes.

represent the field. Consequently, in order to fit the observations well, the inversion scheme drives the field in the unobserved areas to depart significantly from the truth. However, the error tends to flatten out as the number of modes is increased.

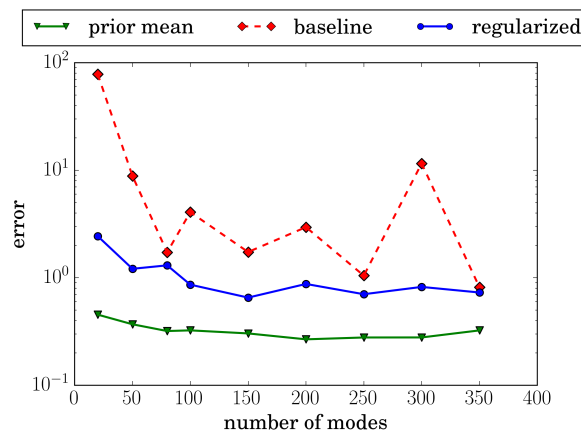


Figure 4.14: Error in the inferred eddy viscosity in the **periodic hill case** by using the baseline and regularized methods as a function of the number of modes used in the field representation. Note that a logarithmic scale is used for the errors.

## 4.4 Conclusion

Inverse problems are common and important in many applications in computational physics. They consist of inferring causal parameters in the model from observations of model output. The parameters can be scalar model parameters or physical fields, and the observations are typically sparse point observations of some, possibly different, physical fields. The most straightforward way to solve such problems is minimizing a cost function that penalizes the discrepancy of the inferred results with the observations. This cost function is minimized using gradient-based methods with the gradients computed from the adjoint of the model. However, many physical models used in practice do not have the readily available adjoint capability, and development of these capability requires significant effort. This has prompted the development of ensemble-based models, such as the ensemble Kalman methods, which are widely used in practice. Ensemble methods use the sample covariance rather than the gradient to guide the optimization. The ensemble Kalman methods implicitly solve the same minimization problem and both ensemble- and gradient-based methods are equivalent under mild assumptions.

A problem with inverse problems is that they are generally ill-posed, with many possible solutions of the parameters leading to satisfactory results in the observation space. This is typically solved by regularizing the problem by adding some additional constraint to the cost function. For instance, smoothness can be enforced by penalizing the magnitude of the gradient of the field. When directly optimizing the cost function with adjoint methods, this is straightforward to implement; however, it is not straightforward to implement such constraints in ensemble-based methods. Here we propose a regularized ensemble Kalman update capable of embedding such additional knowledge into ensemble Kalman methods. Additional constraints are added into the Bayesian formulation, and a derivative-free updating scheme is derived from



an optimization perspective. This effectively bridges the gap between the ability to regularize the problem in both classes of methods and allows for general constraints to be enforced implicitly in the data assimilation problem.

Here we presented three different cases of increasing complexity, including inferring scalar parameters as well as one- and two-dimensional fields. For the final test case we used the method to infer the closure field in the Reynolds-averaged Navier–Stokes equations, a case of significant practical importance in computational fluid dynamics. Compared to using a traditional ensemble Kalman method, the proposed method performs just as well in the observation space, but by incorporating additional knowledge as regularization, the inference in the parameter space is greatly improved. The results demonstrate that the proposed method correctly embeds the additional constraints.



## Chapter 5

# Evaluation of Iterative Ensemble Methods for Quantifying Uncertainties in Steady Flows with Limited Ensemble Sizes

### 5.1 Introduction

#### 5.1.1 Bayesian uncertainty quantification for CFD

In computational fluid dynamics (CFD) applications, Reynolds averaged Navier–Stokes (RANS) method still is the workhorse to inform the important decision-making during engineering design processes. However, RANS models cannot provide accurate results for many cases in the presence of complex turbulent flows. That necessitates quantifying uncertainties in the numerical simulations so that we could obtain additional confidence/statistics information on the simulated results [143]. The conventional approach to quantify uncertainties is to forwardly propagate the presumed uncertainty of system inputs through the system model to the quantity of interests (QoIs). There have been numerous works [37, 54, 108] and methods [67, 83, 98] developed on it. Nowadays, as the discovery of underlying information in the RANS model becomes an increasingly active topic in the CFD community, the Bayesian approach has been drawing more and more attention. With this method, we can backwardly quantify and reduce the uncertainty of QoIs as well as the system inputs (e.g., model parameters or underlying terms) through accounting for the available data from high fidelity simulations or experiments [148, 153]. The procedure is illustrated in the schematic in Fig. 5.1.

Numerous works have been conducted to apply Bayesian uncertainty quantification (UQ) approaches into diverse applications, including RANS simulations. The pioneering work of Kennedy and O’Hagan [81] presented a Bayesian calibration technique to quantify different

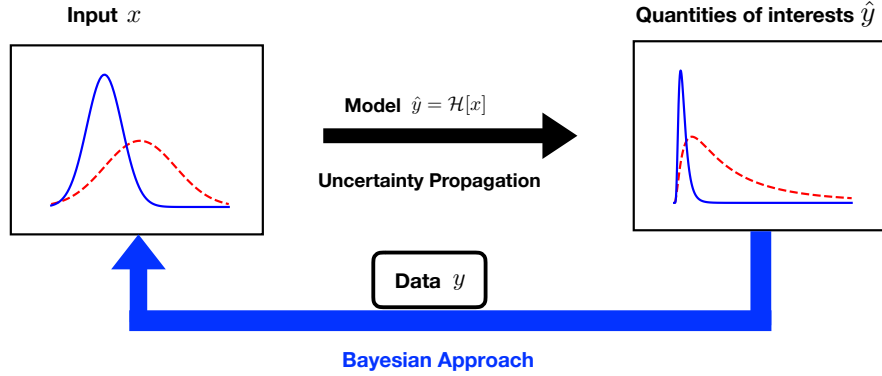


Figure 5.1: Schematic of Bayesian uncertainty quantification. Bayesian approach can combine the prior information (red dashed line) and the data to quantify the posterior uncertainty (blue solid line) in the quantities of interest as well as the input.

types of uncertainties for complex models. Cheung et al. [22] applied the Bayesian calibration framework for the Spalart–Allmaras turbulence model to calibrate the model parameters by incorporating experimental measurements. They evaluated their approach on the boundary layer flows to reduce computational costs and pointed out the necessity to develop tractable UQ approaches for computationally expensive cases. Oliver and Moser [112] further extended their work by introducing the stochastic representations for uncertainties in eddy viscosity turbulence models. The uncertainty representations based on the multiplicative error in mean velocity and the additive error in Reynolds shear stress are developed and applied into the channel flows. Edeling et al. [40] proposed a Bayesian-model-scenario-averaging (BMSA) method to estimate the  $k$ – $\epsilon$  turbulence model error for a class of boundary layer flows with different pressure gradient. More recently, Edeling et al. [43] leveraged Maximum a Posteriori (MAP) estimate to reduce the computational cost and thus make their BMSA approach applicable for complex flows.

The aforementioned works mainly focus on the simple flow cases where uncertainty propagation through CFD solver is computationally inexpensive. Hence, the Markov chain Monte Carlo (MCMC) which typically requires samples of at least  $\mathcal{O}(10^5) \sim \mathcal{O}(10^6)$  is feasible. However, it will be computationally intractable to deal with the complex flow cases of engineering interests. In order to reduce the computational cost, the conventional approach is to apply surrogate models, for instance, the polynomial chaos methods [41, 95, 152] to replace the CFD code. Nevertheless, such approach is not feasible for high dimension problems due to the curse of dimensionality. Ensemble technique has been proposed and discussed extensively for UQ problem in the data assimilation (DA) community. It can reduce significantly sample size to  $\mathcal{O}(10^2)$  and provide a satisfactory estimation of posterior uncertainty with limited samples. Therefore, the ensemble methods can potentially play a role as an approximate Bayesian UQ approach for the computationally expensive flow cases. The ensemble-based data assimilation

methods will be further discussed below.

### 5.1.2 Ensemble-based data assimilation methods

Ensemble-based DA becomes increasingly popular and has been applied to diverse contexts including fluid mechanics, weather forecasting, geoscience, and so on, due to its non-intrusiveness and robustness. Among the ensemble-based DA methods, the most extensively used one is ensemble Kalman filter (EnKF) [48]. For the CFD applications, EnKF has been leveraged to estimate uncertain parameters and model discrepancy in the RANS closure problem. For instance, Kato and Obayashi [79] explored the applicability of the EnKF method to estimate the uncertainty of empirical parameters in the Spalart–Allmaras RANS model. However, due to the strong nonlinearity of the RANS problem, we need to iteratively assimilate data even for the stationary scenario, thus enhancing the performance. To this end, Iglasias et al. [71] proposed an iterative form of the standard EnKF as a derivative-free regularized optimization method for inverse problems. In their framework, the analysis step of EnKF iterates with the artificial time for stationary systems based on the state augmentation. Xiao et al. [148] applied this iterative EnKF to quantify and reduce the RANS model-form uncertainty within the Reynolds stress. They demonstrated that the posterior mean with EnKF could have remarkably good agreement with benchmark data. The readers are referred to the recent review of Xiao and Cinnella [147] for recent progress in model-form uncertainty quantification in RANS simulations.

For highly nonlinear systems, the ill-posedness of the problem is significantly increased. To search for the optimal point, EnKF takes full gradient descent step where the linearization assumption is leveraged for simplification [49]. That possibly changes the original nonlinear problem and leads to wrong solutions. Moreover, iterative form of EnKF for UQ problems has not been fully analyzed. On the other hand, several iterative ensemble methods have been proposed and discussed for UQ of nonlinear systems in the data assimilation community, but they haven't been applied into CFD applications. For instance, Gu and Oliver [62] proposed the ensemble randomized maximum likelihood (EnRML) method to iterate the analysis step with Gauss–Newton algorithm. They applied this method in both static and dynamic problems, demonstrating the outperformance of the EnRML method than EnKF, especially for nonlinear problems. Chen and Oliver [20] treated the EnRML method as an iterative ensemble smoother and tested it on the history match problem. Similarly, Emerick and Reynolds [44] proposed the ensemble Kalman filter with multiple data assimilation (EnKF-MDA) and demonstrated it can provide better data match than EnKF with comparable computational cost. This method performs Bayesian analysis with recursion of the likelihood through inflating the observation error.

The ensemble-based DA methods mentioned above can be deduced similarly by solving the minimization problem under several assumptions (e.g., the Gaussian distribution, linearization, and ensemble gradient representation) [49]. Nevertheless, these assumptions may result in a

departure of the estimated posterior distribution from the Bayes'. Recently, several authors investigated why ensemble methods were not able to estimate uncertainties accurately. For instance, Oliver and Chen [111] reviewed the progress of MCMC, EnKF, and EnRML on the history matching problem. They summarized that the EnRML method could provide the probability distribution in better agreement with MCMC at a low computational cost, compared to the EnKF method. Ernst et al. [45] analyzed the EnKF method for nonlinear stationary systems. They demonstrated EnKF can provide the statistical information as uncertainty indicator but is not suitable for rigorous Bayesian inference. Recently, Evensen [49] derived and analyzed different ensemble methods from the view of model gradient representations, and compared the analytic gradient and the ensemble representative gradient based on several scalar cases. He concluded that none of these methods could provide the exact posterior probability density function (PDF) for highly nonlinear models, but they can serve as the uncertainty estimator at least for weakly nonlinear cases. Besides, a sufficiently large number of samples is used to obtain accurate statistical estimation in his work, and the performance of these methods with limited ensemble sizes is not fully analyzed. These iterative ensemble methods are useful for estimating uncertainties in QoIs in industrial CFD applications, and they warrant further investigations.

### 5.1.3 Objective of the present work

In this work, we present the derivations of three different ensemble-based data assimilation methods (EnKF, EnRML, and EnKF-MDA) from the optimization perspective, and compare their performances in quantifying uncertainties for RANS simulations with limited ensemble sizes. Moreover, the effect of limited ensemble sizes on the performance of each ensemble method is evaluated in a scalar case by comparison with Bayesian distribution from MCMC.

The rest of the paper is structured as follows. In Section 5.2, we give the brief derivation of the three most commonly used ensemble-based DA methods (EnKF, EnRML, and EnKF-MDA). A scalar case is presented in Section 5.3 to discuss the performance of each method with different ensemble sizes. In Section 5.4, a CFD case is tested to identify the most suitable approach to quantify the uncertainty in the RANS model. Section 5.5 concludes the paper.

## 5.2 Ensemble-based data assimilation methods

Here we summarize the brief derivation of the three different ensemble-based DA methods, namely EnKF, EnRML, and EnKF-MDA from the optimization perspective. For the clarity and without loss of generality, we assume a multi-variate state-space model with multiple observations.

### 5.2.1 Minimization problem

Consider that the system model can be expressed as:

$$(5.1) \quad \hat{y} = \mathcal{H}[\mathbf{x}],$$

where  $\mathcal{H}$  is the model function mapping the state to observation space  $\mathbb{R}^N \rightarrow \mathbb{R}^D$ ,  $\mathbf{x}$  is the state vector or input parameter  $\mathbf{x} \in \mathbb{R}^N$ , and  $\hat{y}$  is the model prediction in the observation space  $\hat{y} \in \mathbb{R}^D$ . We give an initial guess on the PDF of state  $p(\mathbf{x})$  as the prior knowledge based on Gaussian assumption. Given the data  $\mathbf{y} = \mathbf{d} + \epsilon$  where  $\mathbf{d}$  is the observation and  $\epsilon$  is the noise, the Bayesian UQ approach can find the posterior uncertainty conditioned by the observation. The Bayes' theorem can be formulated as:

$$(5.2) \quad p(\mathbf{x} | \mathbf{y}) \propto p(\mathbf{x})p(\mathbf{y} | \mathcal{H}[\mathbf{x}]).$$

It is illustrated that the posterior distribution  $p(\mathbf{x} | \mathbf{y})$  is proportional to the multiplication of the prior distribution  $p(\mathbf{x})$  and likelihood function  $p(\mathbf{y} | \mathcal{H}[\mathbf{x}])$  of data  $\mathbf{y}$  conditioned by the model  $\mathcal{H}[\mathbf{x}]$ .

With the assumption of Gaussian distribution for prior  $p(\mathbf{x})$  and likelihood  $p(\mathbf{y} | \mathcal{H}[\mathbf{x}])$ , we can express the Bayes' formula as follows:

$$(5.3) \quad p(\mathbf{x} | \mathbf{y}) \propto p(\mathbf{x})p(\mathbf{y} | \mathcal{H}[\mathbf{x}]) \propto e^{-J},$$

In the formula above,  $J$  is the cost function written as:

$$(5.4) \quad J = \frac{1}{2} (\mathbf{x}^a - \mathbf{x}^f)^\top \mathbf{P}^{-1} (\mathbf{x}^a - \mathbf{x}^f) + \frac{1}{2} (\mathcal{H}[\mathbf{x}^a] - \mathbf{y})^\top \mathbf{R}^{-1} (\mathcal{H}[\mathbf{x}^a] - \mathbf{y}),$$

where  $\mathbf{P}$  is the model error covariance,  $\mathbf{R}$  is the observation error covariance, and the superscript  $a$  and  $f$  represent the “analysis” and “forecast”, respectively. For nonlinear systems, the iterative form of data assimilation scheme is needed to enhance the optimization performance. We can write the cost function for each ensemble realization in an iterative form as:

$$(5.5) \quad J = \frac{1}{2} (\mathbf{x}_{i,j}^a - \mathbf{x}_i^f)^\top \mathbf{P}_i^{-1} (\mathbf{x}_{i,j}^a - \mathbf{x}_i^f) + \frac{1}{2} (\mathcal{H}[\mathbf{x}_{i,j}^a] - \mathbf{y})^\top \mathbf{R}^{-1} (\mathcal{H}[\mathbf{x}_{i,j}^a] - \mathbf{y}),$$

where  $i$  is the iteration number and  $j$  stands for the sample index. To obtain the true error covariance is quite difficult for most realistic cases. The ensemble-based DA methods apply the Monte Carlo technique to draw limited samples. With these samples, we can construct the ensemble representations for the model error covariance  $\mathbf{P}$  and the observation error covariance  $\mathbf{R}$  as:

$$(5.6) \quad \begin{aligned} \mathbf{P}_i &= \frac{1}{M-1} (\mathbf{X}_i - \bar{\mathbf{X}}_i) (\mathbf{X}_i - \bar{\mathbf{X}}_i)^\top, \\ \mathbf{R} &= \epsilon_i \epsilon_i^\top, \end{aligned}$$

where  $\mathbf{X} = \{\mathbf{x}_j\}_{j=1}^M$ . Note that the estimated error covariance matrix are both symmetric. Further, the maximum a posteriori (MAP) analysis can be applied to estimate the posterior distribution. That is, to maximum the posterior is equivalent to minimize the cost function  $J$ . Given that, we can derive the three different data assimilation methods, namely EnKF, EnRML, and EnKF-MDA, from the perspective of minimizing the cost function with different gradient descent techniques.

### 5.2.2 EnKF

From the cost function (5.5), we can derive the gradient as:

$$(5.7) \quad \frac{\partial J}{\partial \mathbf{x}_{i,j}^a} = \mathbf{P}_i^{-1} \left( \mathbf{x}_{i,j}^a - \mathbf{x}_{i,j}^f \right) + \left( \mathcal{H}'[\mathbf{x}_{i,j}^a] \right)^\top \mathbf{R}^{-1} \left( \mathcal{H}[\mathbf{x}_{i,j}^a] - y_j \right).$$

At the minimum of the cost function, the gradient should vanish. The formulation of EnKF can be derived by setting the gradient of cost function (5.7) to be zero as:

$$(5.8) \quad \mathbf{P}_i^{-1} \left( \mathbf{x}_j^a - \mathbf{x}_j^f \right) = - \left( \mathcal{H}'[\mathbf{x}_j^a] \right)^\top \mathbf{R}^{-1} \left( \mathcal{H}[\mathbf{x}_j^a] - y_j \right),$$

where only the terms  $\mathcal{H}'[\mathbf{x}_j^a]$  and  $\mathcal{H}[\mathbf{x}_j^a]$  are unknown. The assumption of linearization is introduced to have an estimation on the two unknown terms as:

$$(5.9a) \quad \mathcal{H}[\mathbf{x}_j^a] \approx \mathcal{H}[\mathbf{x}_j^f] + \mathcal{H}'[\mathbf{x}_j^f] \left( \mathbf{x}_j^a - \mathbf{x}_j^f \right),$$

$$(5.9b) \quad \mathcal{H}'[\mathbf{x}_j^a] \approx \mathcal{H}'[\mathbf{x}_j^f] + \mathcal{H}''[\mathbf{x}_j^f] \left( \mathbf{x}_j^a - \mathbf{x}_j^f \right),$$

where second derivative in Eq. (5.9b) can be neglected. The model gradient  $\mathcal{H}'[\mathbf{x}^f]$  can be solved with the adjoint code, but that need much extra efforts for complex systems. With ensemble technique, the model in observation space is randomized around the mean value  $\mathcal{H}[\bar{\mathbf{x}}^f]$ . After expanding  $\mathcal{H}[\mathbf{x}]$  around the ensemble mean  $\mathcal{H}[\bar{\mathbf{X}}]$  [49], we can represent  $\mathcal{H}[\mathbf{x}_j^f]$  with the model function gradient as:

$$(5.10a) \quad \mathcal{H}[\mathbf{x}_j^f] \approx \mathcal{H}[\bar{\mathbf{X}}^f] + \mathcal{H}'[\bar{\mathbf{X}}^f] \left( \mathbf{x}_j^f - \bar{\mathbf{X}}^f \right)$$

We introduce the tangent linear model  $\mathcal{H}[\mathbf{x}] = \mathbf{H}\mathbf{x}$ , and thus the gradient representation can be expressed as  $\mathbf{H}$ . Accordingly, the update step of EnKF can be derived and formulated as:

$$(5.11) \quad \mathbf{x}_{i,j}^a = \mathbf{x}_{i,j}^f + \mathbf{P}_i \mathbf{H}^\top \left( \mathbf{R} + \mathbf{H} \mathbf{P}_i \mathbf{H}^\top \right)^{-1} \left( y_j - \mathbf{H} \mathbf{x}_{i,j}^f \right).$$

Note that in EnKF the model linear operator  $\mathbf{H}$  usually is not needed to be calculated directly through reformulating  $\mathbf{P}_i \mathbf{H}^\top$  and  $\mathbf{H} \mathbf{P}_i \mathbf{H}^\top$  as:

$$(5.12a) \quad \mathbf{P}_i \mathbf{H}^\top = \frac{1}{M-1} \left( \mathbf{X}_i - \bar{\mathbf{X}}_i \right) \left( \mathcal{H}[\mathbf{X}_i] - \mathcal{H}[\bar{\mathbf{X}}_i] \right)^\top,$$

$$(5.12b) \quad \mathbf{H} \mathbf{P}_i \mathbf{H}^\top = \frac{1}{M-1} \left( \mathcal{H}[\mathbf{X}_i] - \mathcal{H}[\bar{\mathbf{X}}_i] \right) \left( \mathcal{H}[\mathbf{X}_i] - \mathcal{H}[\bar{\mathbf{X}}_i] \right)^\top.$$

Further details of the derivation are presented in C.1.



### 5.2.3 EnRML

The ensemble randomized maximum likelihood method [62] is to update the initial guessed state vector iteratively with Gauss–Newton algorithm. The cost function can be written as:

$$(5.13) \quad J = \frac{1}{2} (\mathbf{x}_{i,j} - \mathbf{x}_{0,j})^\top \mathbf{P}_0^{-1} (\mathbf{x}_{i,j} - \mathbf{x}_{0,j}) + \frac{1}{2} (\mathcal{H}[\mathbf{x}_{i,j}] - \mathbf{y}_j)^\top \mathbf{R}^{-1} (\mathcal{H}[\mathbf{x}_{i,j}] - \mathbf{y}_j),$$

where  $\mathbf{x}_0$  is the initial guess,  $\mathbf{P}_0$  is the initially estimated model error covariance before the data assimilation process. The gradient and Hessian of the cost function (5.13) can be derived similarly as in EnKF:

$$(5.14a) \quad \frac{\partial J}{\partial \mathbf{x}_{i,j}} = \mathbf{P}_0^{-1} (\mathbf{x}_{i,j} - \mathbf{x}_{0,j}) + \mathcal{H}'[\mathbf{x}_{i,j}]^\top \mathbf{R}^{-1} (\mathcal{H}[\mathbf{x}_{i,j}] - \mathbf{y}_j),$$

$$(5.14b) \quad \frac{\partial^2 J}{\partial^2 \mathbf{x}_{i,j}} = \mathbf{P}_0^{-1} + \mathcal{H}'[\mathbf{x}_{i,j}]^\top \mathbf{R}^{-1} \mathcal{H}'[\mathbf{x}_{i,j}].$$

Instead of reaching to zero-gradient minimum directly as in EnKF, the prior  $\mathbf{x}_0$  is iteratively updated based on Gauss–Newton method as:

$$(5.15) \quad \mathbf{x}_{i,j}^a = \mathbf{x}_{i,j}^f - \gamma \left( \frac{\partial^2 J}{\partial^2 \mathbf{x}_{i,j}^f} \right)^{-1} \frac{\partial J}{\partial \mathbf{x}_{i,j}^f},$$

where  $\gamma$  is the step length parameter. The Gauss–Newton approach can reduce the step length and ease the influence of the linearization assumption during the analysis step. With the gradient (5.14a) and the Hessian (5.14b) of the cost function we can obtain the analysis scheme for the EnRML method as follows:

$$(5.16) \quad \mathbf{x}_{i,j}^a = \gamma \mathbf{x}_{0,j}^f + (1 - \gamma) \mathbf{x}_{i,j}^f - \gamma \mathbf{P}_0 \mathcal{H}'[\mathbf{x}_{i,j}^f]^\top \left( \mathbf{R} + \mathcal{H}'[\mathbf{x}_{i,j}^f]^\top \mathbf{P}_0 \mathcal{H}'[\mathbf{x}_{i,j}^f] \right)^{-1} \left( \mathcal{H}[\mathbf{x}_{i,j}^f] - \mathbf{y}_j - \mathcal{H}'[\mathbf{x}_{i,j}^f] (\mathbf{x}_{i,j}^f - \mathbf{x}_{0,j}^f) \right).$$

In the EnRML method, the model error covariance  $\mathbf{P}$  remains as the initial one and does not change with the iteration number. As a result, the sensitivity matrix  $\mathcal{H}'[\mathbf{X}]$  has to be evaluated at each iteration through:

$$(5.17) \quad \mathcal{H}'[\mathbf{X}_i] \approx (\mathcal{H}[\mathbf{X}_i] - \mathcal{H}[\bar{\mathbf{X}}_i]) (\mathbf{X}_i - \bar{\mathbf{X}}_i)^{-1}$$

The singular value decomposition (SVD) is usually used to estimate the inverse of the non-full rank matrix. The details of the derivation can be found in C.2.

### 5.2.4 EnKF-MDA

From the derivation above, EnKF can be regarded as the Gauss–Newton update but uses full step in the search direction at every iteration. That may lead to overcorrection on the state vector, particularly for the nonlinear problem. This deficiency can be alleviated through the

inflation of the observation error covariance. Motivated by this deficiency, EnKF-MDA [44] is proposed to assimilate data with an inflated observation error covariance. From the Bayesian perspective, the likelihood function in EnKF-MDA is in a recursive form as:

$$(5.18) \quad p(\mathbf{x} | \mathbf{y}) \propto p(\mathbf{x}) \prod_{i=1}^{N_{\text{mda}}} p(\mathbf{y} | \mathcal{H}[\mathbf{x}_{i-1}])^{\frac{1}{\alpha_i}},$$

where  $\sum_{i=1}^{N_{\text{mda}}} \frac{1}{\alpha_i} = 1$ ,  $N_{\text{mda}}$  is the total data assimilation iteration number, and  $\alpha$  can be chosen simply as  $N_{\text{mda}}$ . The cost function  $J$  can be expressed as:

$$(5.19) \quad J(\mathbf{x}_{i,j}^a) = \frac{1}{2} (\mathbf{x}_{i,j}^a - \mathbf{x}_{i,j}^f)^\top \mathbf{P}_i^{-1} (\mathbf{x}_{i,j}^a - \mathbf{x}_{i,j}^f) + \frac{1}{2} (d + \sqrt{\alpha_i} \epsilon_{i,j} - \mathcal{H}[\mathbf{x}_{i,j}^a])^\top (\alpha_i \mathbf{R})^{-1} (d + \sqrt{\alpha_i} \epsilon_{i,j} - \mathcal{H}[\mathbf{x}_{i,j}^a]).$$

The gradient of the cost function can be formulated as:

$$(5.20) \quad \frac{\partial J(\mathbf{x}_{i,j}^a)}{\partial \mathbf{x}_{i,j}^a} = \mathbf{P}_i^{-1} (\mathbf{x}_{i,j}^a - \mathbf{x}_{i,j}^f) + \mathcal{H}'[\mathbf{x}_{i,j}^a]^\top (\alpha_i \mathbf{R})^{-1} (d + \sqrt{\alpha_i} \epsilon_{i,j} - \mathcal{H}[\mathbf{x}_{i,j}^a]).$$

Similar to the derivation of EnKF method, we set the gradient of cost function to zero. Further, with linearization assumption (5.9) and ensemble gradient representation (5.10), we have the update scheme as:

$$(5.21) \quad \mathbf{x}_{i,j}^a = \mathbf{x}_{i,j}^f + \mathbf{P}_i \mathcal{H}'[\mathbf{x}_{i,j}^f]^\top \left( \mathcal{H}[\mathbf{x}_{i,j}^f] \mathbf{P}_i \mathcal{H}'[\mathbf{x}_{i,j}^f]^\top + \alpha_i \mathbf{R} \right)^{-1} (d + \sqrt{\alpha_i} \epsilon_{i,j} - \mathcal{H}[\mathbf{x}_{i,j}^f]).$$

By introducing the tangent linear operator  $\mathbf{H}$ , we can obtain the analysis step of EnKF-MDA as:

$$(5.22) \quad \mathbf{x}_{i,j}^a = \mathbf{x}_{i,j}^f + \mathbf{P}_i \mathbf{H}^\top \left( \mathbf{H} \mathbf{P}_i \mathbf{H}^\top + \alpha_i \mathbf{R} \right)^{-1} (d + \sqrt{\alpha_i} \epsilon_{i,j} - \mathbf{H} \mathbf{x}_{i,j}^f)$$

Given the prior distribution of QoIs to be inferred and ensemble observations with error covariance matrix  $\mathbf{R}$ , the implementation steps for the three data assimilation methods are summarized as presented in Table 5.1.

### 5.2.5 Remarks

From the derivations above, we apply the iterative form, linearization assumption, and ensemble gradient representation to obtain the derivative-free analysis scheme. Here, we give some discussions on the effects of each issue.

1. Iterative form is necessary to obtain satisfactory inference results for the inverse problem of nonlinear systems. However, the iterative EnKF takes the posterior distribution as the prior for the next iteration and uses the same observation at every analysis step for stationary systems. This may result in that the samples collapse in early iteration steps and lead to the underestimation of uncertainty. Moreover, the model error covariance for

EnKF	EnKF-MDA	EnRML
<b>a. sampling step:</b> generate initial ensemble state vectors $\{\mathbf{x}_{0,j}\}_{j=1}^M$		<b>a. sampling step:</b> 1. generate initial ensemble state vectors $\{\mathbf{x}_{0,j}\}_{j=1}^M$ ; 2. estimate the mean $\bar{\mathbf{X}}_0^f$ and model error covariance $\mathbf{P}_0$ of the ensemble.
<b>b. prediction step:</b> i) Propagate from current state $i - 1$ to next iteration level $i$ based on forward model( $i > 0$ ). $\mathbf{x}_{i,j}^f = \mathcal{F}[\mathbf{x}_{i-1,j}^a]$ ii) Estimate the ensemble mean $\bar{\mathbf{X}}_i^f$ and model error covariance $\mathbf{P}_i$ of the current iteration.		<b>b. prediction step:</b> i) Propagate from current state $i - 1$ to next iteration level $i$ based on forward model( $i > 0$ ). $\mathbf{x}_{i,j}^f = \mathcal{F}[\mathbf{x}_{i-1,j}^a]$ ii) Estimate the ensemble model gradient by (5.17).
<b>c. analysis step</b> update the state vector by (5.11) and return to step b until the convergence criteria are reached.	<b>c. analysis step</b> update the state vector by (5.22) and return to step b until the convergence criteria are reached.	<b>c. analysis step</b> update the state vector by (5.16) and return to step b until the convergence criteria are reached.

Table 5.1: Schematic comparison of EnKF, EnRML and EnKF-MDA

next iteration become quite small, and the first term in Eq. (5.5) prescribing the prior distribution will dominate the cost function. That means the data assimilation analysis does not take effects and the update only depends on the prior afterward. By contrast, the EnRML method and EnKF-MDA iterate the update step through Gauss–Newton algorithm and likelihood recursion, respectively, which can avoid the data overuse and samples collapsing.

2. Linearization assumption is introduced in our derivation for simplification. However, for strongly nonlinear systems, the linear assumptions may significantly affect the optimal solution and lead to the wrong inference results. EnKF takes a full update step to the optimal point, while the EnRML method and EnKF-MDA split one EnKF step by several small steps through Gauss–Newton method and likelihood recursion, respectively. From this point of view, the EnRML method and EnKF-MDA can alleviate the influence of linearization assumption and partly preserve the nonlinear property. Therefore, the EnRML method and EnKF-MDA are more suitable for the uncertainty quantification of stationary nonlinear systems than EnKF.
3. Another assumption, ensemble gradient representation, is leveraged in the ensemble-based DA methods as presented in our derivations. That is, the model gradient is approximated by ensemble realizations rather than derivative analytically to the state vector. This may

arise the propagated posterior distribution to be not accurate compared to the exact Bayesian distribution [49]. However, unlike the linearization assumption, the impacts of which can be eased through other optimization approaches, the effects of ensemble gradient representation are inevitable within the ensemble-based DA framework unless the adjoint method is applied to calculate the analytic gradient.

Besides, the parameter  $\gamma$  and  $N_{\text{mda}}$  concerning the length of update step are introduced in the EnRML method and EnKF-MDA, respectively. They can be constant or adaptive based on the convergence judgment. Specifically, if the discrepancy in observation space is larger than that in the last iteration, we can reduce the step length by decreasing the step length parameter  $\gamma$  or increasing inflation parameter  $N_{\text{mda}}$ . Oppositely, if the discrepancy gets reduced, we can increase the  $\gamma$  in EnRML or reduce the  $N_{\text{mda}}$  in EnKF-MDA to speed up the convergence.

### 5.3 Scalar case

First we test the three ensemble-based Bayesian UQ approaches derived in Section 5.2 on a simple case used by Evensen [49]. In his work, the effects of the model gradient representation are investigated mainly under the sufficient large sample size. Here, we focus on the effects of limited ensemble sizes and the performance of the ensemble methods with a small sample size. In this case, the computing time for the forward model is negligible. Hence, we can obtain Bayesian posterior from MCMC and ensemble methods with a large sample size for comparison.

#### 5.3.1 Problem statement

The forward model is defined as:

$$(5.23) \quad \hat{y} = 1 + \sin(\pi x) + q,$$

where  $x$  is the state variable,  $\hat{y}$  is the model output in observation space, and  $q$  is the added model error for better visualization  $q \sim \mathcal{N}(0, 0.03^2)$ . The goal is to quantify and reduce the uncertainty of  $x$  and  $\hat{y}$  with Bayesian approaches.

The Bayesian UQ approaches need the statistical information on the prior state and the observation. We assume that the state variable  $x$  and data  $y$  both obey to the Gaussian distribution as  $x \sim \mathcal{N}(0, 0.1^2)$ ,  $y \sim \mathcal{N}(1, 0.1^2)$ . Besides, we set the step length parameter  $\gamma$  in the EnRML method as 0.5 and the inflation parameter  $N_{\text{mda}}$  in EnKF-MDA as 30 to obtain convergence results. The performance of the ensemble-based DA methods is assessed with two different ensemble size of  $10^6$  and  $10^2$ , and the effects of limited ensemble sizes on the propagated uncertainties are investigated. The probability density in this case is estimated from the samples through kernel density estimation (KDE) using the Gaussian kernel.

From the derivation in Section 5.2, it has been noted that two assumptions (linearization and ensemble gradient representation) are introduced to obtain the derivative-free analysis step.

The model gradient can be represented by the analytic gradient or estimated by the ensemble samples. Although the analytic model gradient can give more accurate results compared to the ensemble gradient representation [49], it is not practical for complex models and beyond the scope of this work. Here, we focus on the ensemble gradient and also investigate the effects of ensemble sizes on the ensemble gradient.

### 5.3.2 Results

We first evaluate the performance of each ensemble-based DA method with large ensemble size  $M = 10^6$ . The joint and marginal PDFs in comparison of different ensemble methods can be seen in Fig. 5.2 and Fig. 5.3, respectively. The Bayesian benchmark is obtained based on the Markov chain Monte Carlo (MCMC) approach using the DREAM package [137]. From the results, it can be seen that all the three ensemble-based DA methods can capture the posterior mean. However, it is noticeable that the iterative EnKF method leads to overconfidence in the mean value and significantly underestimates the posterior variance compared to the exact Bayesian distribution from MCMC. In contrary, both the EnRML method and EnKF-MDA can provide an estimation on the posterior distribution in good agreement with the benchmark data. It is not surprising, since the iterative EnKF repeat using same data, while the EnRML method and EnKF-MDA can avoid data overuse by introducing the Gauss–Newton method or the observation error inflation, as we remarked in Section 5.2. In conclude, with large ensemble size, the EnRML method and EnKF-MDA can perform comparably to the MCMC, while EnKF significantly underestimate the posterior uncertainty due to data repeatedly used.

Further, we explore the effects of small ensemble size on this case and evaluate which method can outperform others with limited samples. Because for many realistic cases, the propagation with large ensemble size is computationally prohibitive, and ensemble methods typically can use less than  $10^2$  samples to describe the statistical information. Hence, we set the ensemble size to be  $10^2$ , and other set-ups are consistent with the previous. The joint PDFs results with different ensemble-based DA methods are shown in Fig. 5.4. It can be seen that with the limited ensemble size, the iterative EnKF method is similar as with the large ensemble size. Specifically, all samples converge to the observations, and the posterior distribution has a low variance. By contrast, the EnRML method and EnKF-MDA not only can capture the posterior mean value but also provide the statistical information to indicate the uncertainty with ensemble realizations. For better visualization, the marginal PDFs in comparison of the three ensemble-based DA methods with  $10^2$  samples are shown in Fig. 5.5. We can see that the EnRML method and EnKF-MDA give satisfactory estimations on the uncertainty, while the mode value with EnKF is approximately three times higher than that with MCMC. Generally, with limited ensemble size, EnKF performs similarly as with large ensemble size, which underestimate the posterior variance. The performance of EnRML and EnKF-MDA is still satisfactory but inferior to with large ensemble size.

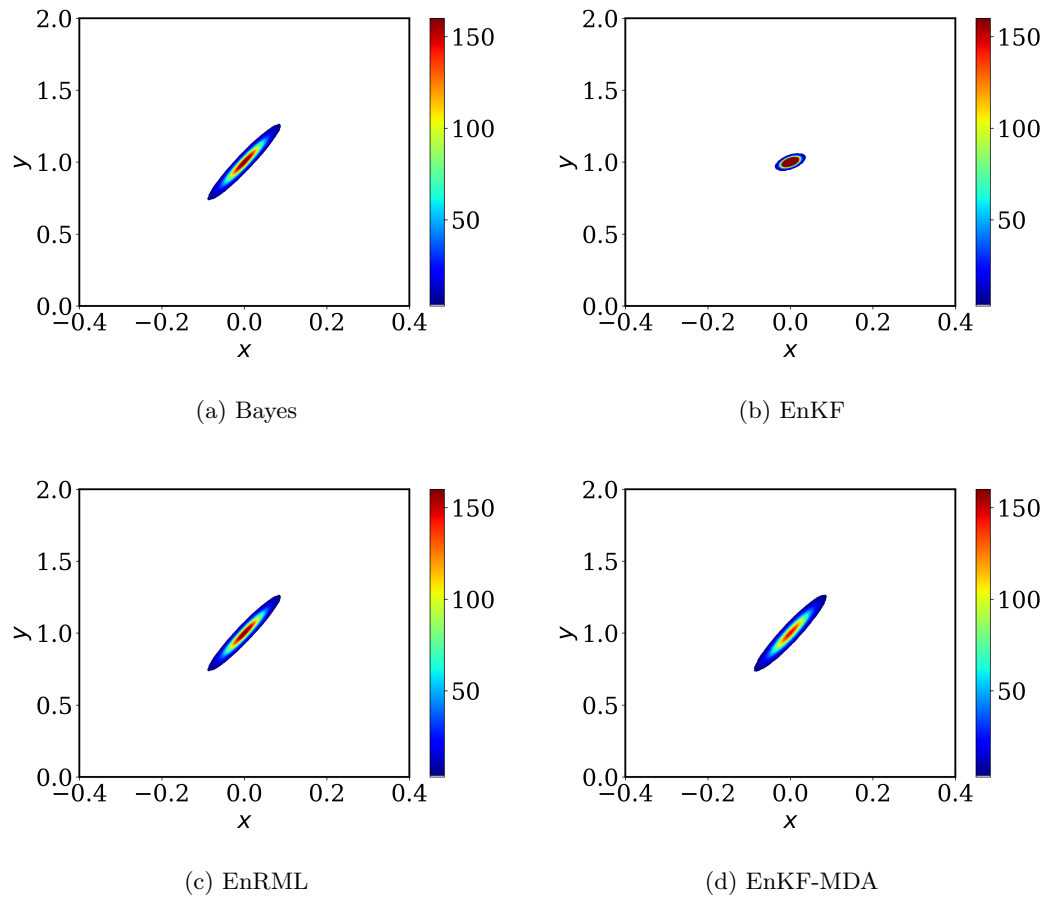


Figure 5.2: Joint PDFs with  $10^6$  samples in comparison of Bayes, EnKF, EnRML, and EnKF-MDA for the scalar case.

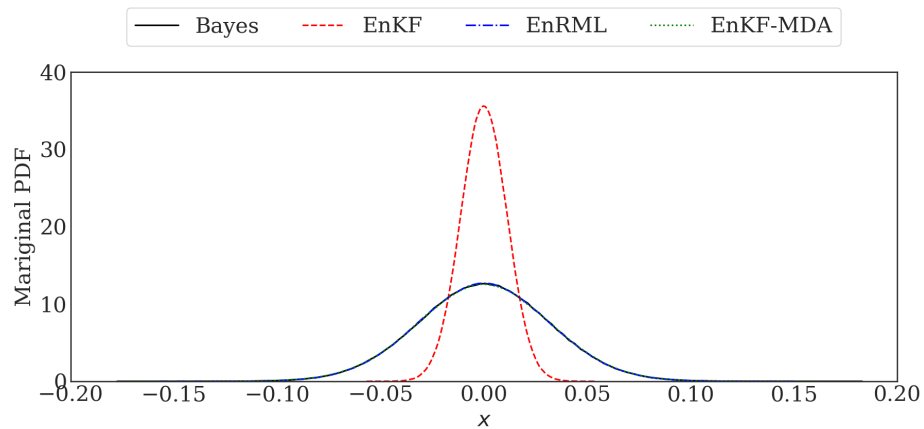


Figure 5.3: Marginal PDFs for  $x$  with  $10^6$  samples in comparison of EnKF, EnRML, EnKF-MDA, and Bayes for the scalar case.

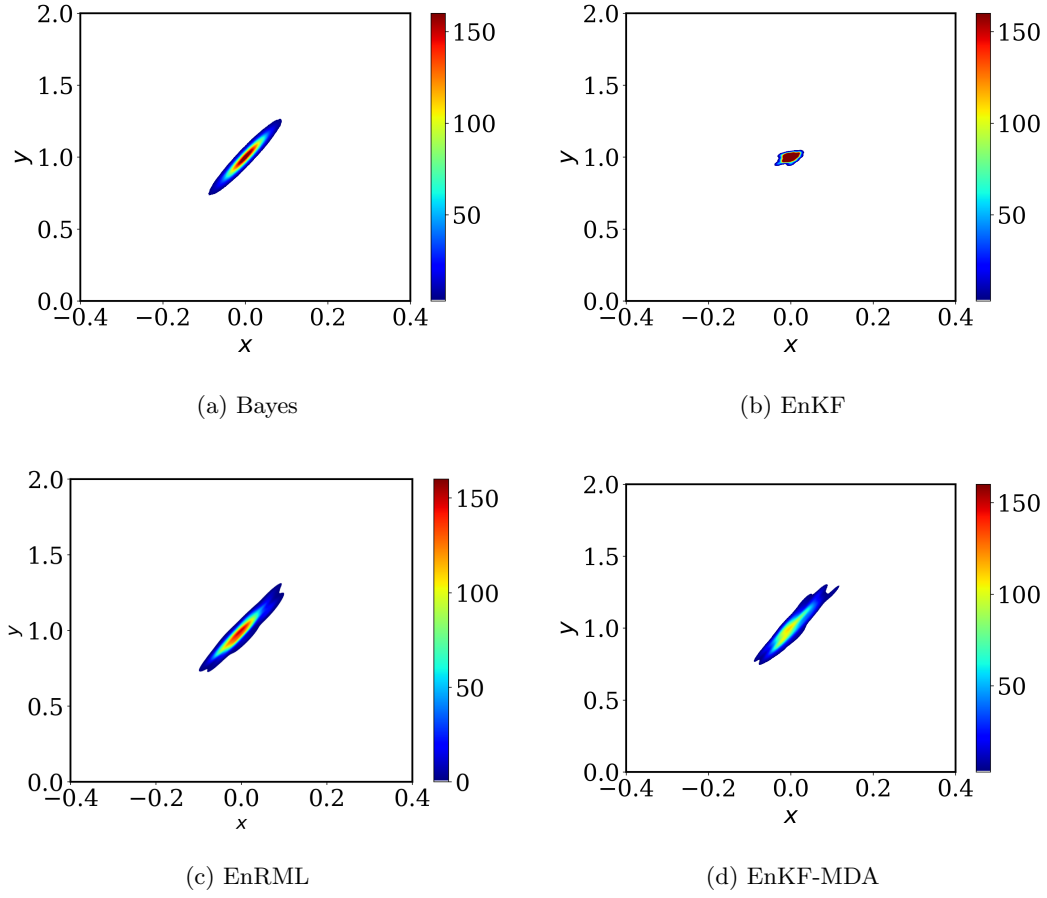


Figure 5.4: Joint PDFs with  $10^2$  samples in comparison of Bayes, EnKF, EnRML, and EnKF-MDA for the scalar case

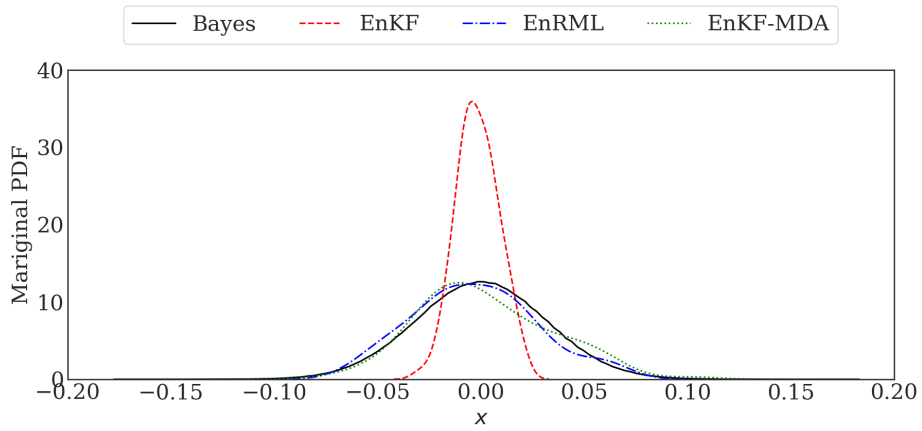


Figure 5.5: Marginal PDFs for  $x$  with  $10^2$  samples in comparison of EnKF, EnRML, EnKF-MDA, and Bayes for the scalar case.

Not surprisingly, the estimation of uncertainty with limited ensemble size slightly deviates from the Bayes'. It is probably caused by that the limited samples are inadequate to describe the statistical information and may also increase the error in estimating the model gradient, especially for the nonlinear model. To illustrate this point, we present the plots of prior joint PDF with the large and small ensemble size, as shown in Fig. 5.6. It is obvious that the small ensemble size is not sufficient to describe the prior distribution. Moreover, we give the model gradient estimated by ensemble samples in comparison with the analytic gradient. The analytic gradient of this model is  $\pi \cos \pi x$ , and the ensemble gradient can be represented by  $\frac{\sin(\pi \bar{X}) - \sin(\pi \tilde{X})}{\bar{X} - \tilde{X}}$ . Ideally, if the mean of samples on  $x$  is estimated as zero since  $x$  obey to zero-mean Gaussian distribution, we can have

$$\lim_{x \rightarrow 0} \frac{\sin(\pi x)}{\pi x} = \cos(\pi x).$$

Based on this formula, we can see that the samples close to the sample mean are approximately equal to the analytic one. Given that the model gradient is not subject to the Gaussian distribution, we use the cosine kernel to obtain the probability density, as shown in Fig. 5.7. It is noticeable that the difference between the analytic gradient and ensemble gradient can be eased with large ensemble size. The discontinuity in the case with  $10^2$  samples is mainly due to that the limited ensemble realizations are insufficient to prescribe the infinite distribution. The limited ensemble size can remarkably reduce the computational cost but arise additional errors in the statistical description and the model gradient estimation. To ensure the error in an acceptable range, the choice of the ensemble size need numerical tests. For highly nonlinear system, the reduction of errors in model gradient estimation will not benefit from large ensemble size unless the analytic gradient is adopted.

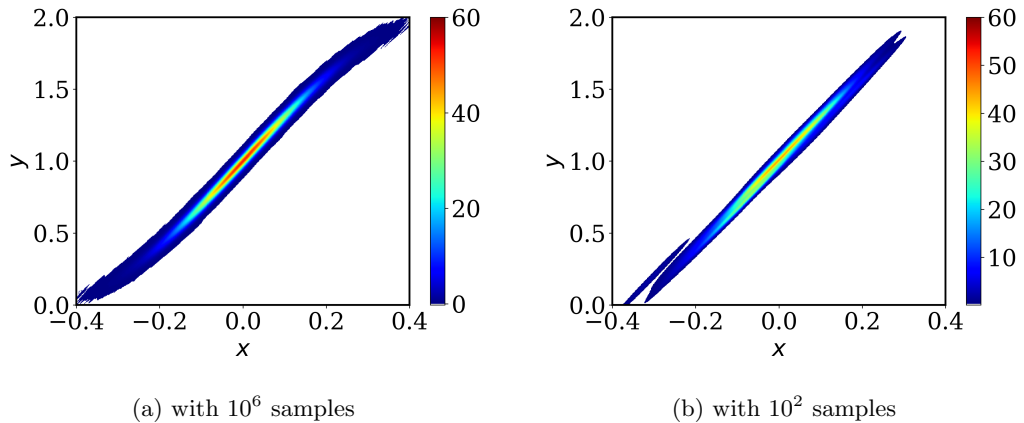


Figure 5.6: Results of prior joint PDF with large ( $10^6$ ) and small ( $10^2$ ) ensemble size for the scalar case



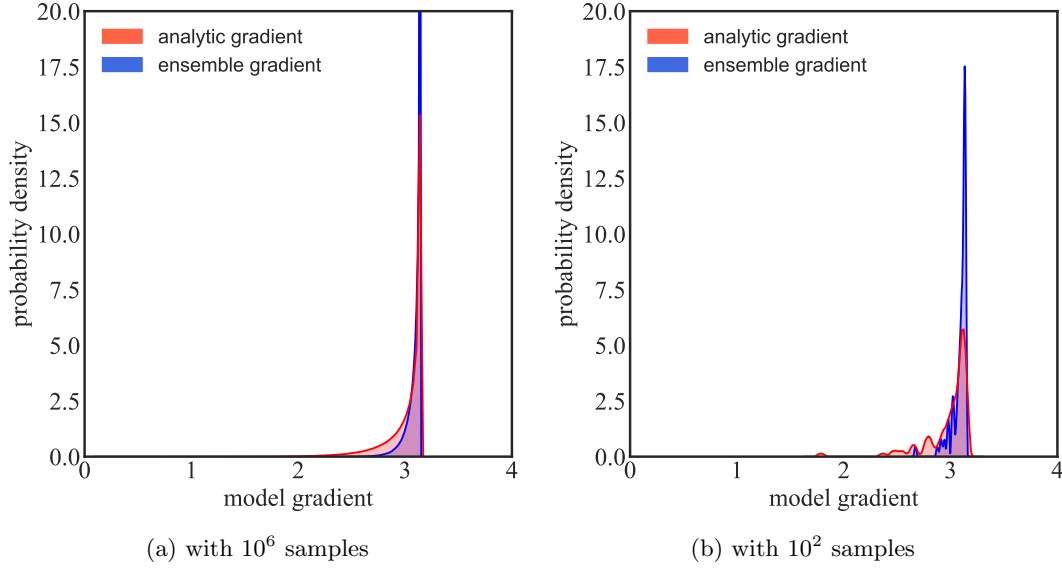


Figure 5.7: Comparison of analytic gradient and ensemble gradient. The light/pink shaded region represents analytic gradient and the dark/blue shaded region represents ensemble gradient. (a):  $10^6$  samples; (b):  $10^2$  samples

## 5.4 RANS equation

CFD is of significant importance for many engineering applications. Considering the computational cost, the RANS model is still the essential tool to characterize the turbulence behavior in CFD simulations. However, the unknown term “Reynolds stress” in RANS equations is commonly solved with different closure models under Boussinesq assumption, which will introduce the model uncertainty and reduce the confidence on the predictive performance. In this section, we apply the three ensemble-based data assimilation methods (EnKF, EnRML, and EnKF-MDA) on the RANS problem and evaluate their performance to quantify and reduce the uncertainty of the predicted velocity by incorporating the DNS data.

### 5.4.1 Problem statement

The RANS equations can be expressed as:

$$(5.24a) \quad \frac{\partial U_i}{\partial x_i} = 0$$

$$(5.24b) \quad \frac{\partial U_i}{\partial t} + \frac{\partial (U_i U_j)}{\partial x_j} = -\frac{\partial P}{\partial x_i} + \frac{1}{Re} \frac{\partial^2 U_i}{\partial x_j \partial x_j} - \frac{\partial \overline{u'_i u'_j}}{\partial x_j},$$

where  $U, P$  is the dimensionless mean velocity and pressure, and  $Re$  is the Reynolds number. In the momentum equation (5.24b),  $\tau = \overline{u'_i u'_j}$  is the Reynolds stress which is the main uncertain source in RANS simulations. The Reynolds stress from RANS simulation coupling with the

linear eddy-viscosity model is regarded as the baseline. Then we can introduce the discrepancy term  $\Delta\tau$  representing the uncertainty into the baseline as:

$$(5.25) \quad \tau = \tau^{\text{RANS}} + \Delta\tau.$$

Further, we can quantify the uncertainty in the predicted velocity with the three ensemble-based DA methods by reducing the discrepancy in Reynolds stress with observation data.

### 5.4.2 Methodology

The data assimilation framework to quantify and reduce the model-form uncertainty in Reynolds stress was proposed by Xiao et.al [148]. Here, we give a brief introduction on this methodology.

Before the data assimilation process, we represent the Reynolds stress baseline  $\tau^{\text{RANS}}$  with three discrepancy variables  $k$ ,  $\xi$ , and  $\eta$  through eigendecomposition and coordinate conversion [148]. The variable  $k$  represents the magnitude of Reynolds stress, and  $\xi$  and  $\eta$  represent the shape of the Reynolds stress. Further, the additive uncertainties  $\delta^k$ ,  $\delta^\xi$ , and  $\delta^\eta$  are injected into these projected variables as:

$$(5.26a) \quad \log k(x) = \log k^{\text{RANS}}(x) + \delta^k(x),$$

$$(5.26b) \quad \xi(x) = \xi^{\text{RANS}}(x) + \delta^\xi(x),$$

$$(5.26c) \quad \eta(x) = \eta^{\text{RANS}}(x) + \delta^\eta(x).$$

The logarithm on  $k$  is to ensure the non-negativity.

The dimension of the variable  $\log k(x)$ ,  $\xi(x)$ , and  $\eta(x)$  is consistent with the mesh grid. To infer the entire field with very sparse observation increases the ill-posedness of the problem dramatically. Hence, it is necessary to reduce the dimension of the state space. In this case, we leverage the Karhunen—Loève (K–L) expansion with truncated orthogonal modes to represent the field for each quantity to be inferred. The discrepancy variables  $\delta^k$ ,  $\delta^\xi$ , and  $\delta^\eta$  are constructed by the random field subject to zero-mean Gaussian process  $\mathcal{GP}(0, \mathcal{K})$ . The kernel function  $\mathcal{K}$  is formulated as:

$$(5.27) \quad \mathcal{K}(x, x') = \sigma(x)\sigma(x') \exp\left(-\frac{|x - x'|^2}{l^2}\right).$$

In the formula above,  $\sigma(x)$  is the variance field to indicate the region where large discrepancy is expected.  $l$  is the characteristic length. The K–L mode can be formulated as:  $\phi_i(x) = \sqrt{\hat{\lambda}} \hat{\phi}_i(x)$ , where  $\hat{\lambda}$  and  $\hat{\phi}$  are the eigenvalues and eigenvectors of the kernel  $\mathcal{K}$ , respectively. The discrepancy variables can be constructed from the deterministic K–L modes  $\phi(x)$  and random variable  $\omega$  as

follows:

$$(5.28a) \quad \delta^k(x) = \sum_{i=1}^N \omega_i^k \phi_i(x),$$

$$(5.28b) \quad \delta^\xi(x) = \sum_{i=1}^N \omega_i^\xi \phi_i(x),$$

$$(5.28c) \quad \delta^\eta(x) = \sum_{i=1}^N \omega_i^\eta \phi_i(x).$$

The prior  $\omega$  is given as zero-mean, uni-variance Gaussian random numbers. With  $\omega$  and K–L modes  $\phi(x)$ , we can reconstruct the field of each discrepancy quantity and recover the random field of Reynolds stress tensor.

Based on the Reynolds stress representation and dimension reduction presented above, the ensemble-based data assimilation can be performed to quantify and reduce the uncertainty in velocity. The procedure of the RANS model-form uncertainty quantification framework is summarized as below:

**1. Preprocessing step:**

- (1) Perform RANS simulation to obtain  $\tau^{\text{RANS}}$  as the baseline.
- (2) Project  $\tau^{\text{RANS}}$  onto the field of  $k$ ,  $\xi$ , and  $\eta$ .
- (3) Conduct K–L expansion to generate the K–L basis sets or modes  $\{\phi_i(x)\}_{i=1}^m$ , where  $m$  is the number of truncated modes.
- (4) Generate the initial value of  $\omega$  with a zero-mean uni-variance normal distribution.

**2. Data assimilation step:**

- (a) Recover the discrepancy variables of  $\delta^k$ ,  $\delta^\xi$ , and  $\delta^\eta$  with coefficient  $\omega$  and basis sets  $\phi(x)$ .
- (b) Reconstruct the ensemble realizations on  $\tau$  through mapping  $(k, \xi, \eta) \rightarrow \tau$  and solve the RANS equation to obtain the velocity field given each realization of  $\tau$ .
- (c) Perform the Bayesian analysis with data assimilation technique to reduce the uncertainty of velocity by incorporating DNS data.
- (d) Return to step (a) till the convergence criteria or maximum iteration number is reached.

### 5.4.3 Case details

The test case is turbulent flow over the periodic hill where DNS data [14] is regarded as the benchmark. The Reynolds number is 2800. The periodic boundary condition is imposed on the inlet, and the non-slip boundary condition is applied on the wall. A structured mesh is constructed with 50 cells in the stream-wise direction and 30 cells in the normal to wall direction. The number of modes for  $k$ ,  $\xi$ , and  $\eta$  is set to 8. The ensemble size is 60. The length

scale is set as constant 1 for simplification. The relative observation error is set as 0.1. We take 18 observations into account to quantify and reduce the uncertainty in velocity. The simulation results with the Launder–Sharma RANS model are regarded as the baseline. The step parameter  $\gamma$  in the EnRML method is chosen as 0.5 and the inflation parameter  $N_{\text{mda}}$  in EnKF-MDA is set as 30 to obtain the convergence results based on our calibration study. For this case, the MCMC sampling is impractical to verify the estimated posterior uncertainty due to the high dimensionality of the state space and the high costs of numerical simulation.

#### 5.4.4 Results

Through solving RANS equations given the randomized Reynolds stresses, we can obtain the prior uncertainty in the propagated velocity. The plots of the prior velocity are shown in Fig. 5.8, and the location of observation is marked. It can be seen that the space spanned by the ensemble realizations can indicate the statistical information. Also, the sample mean can have a good fit with RANS results. That is reasonable since the random field is constructed by perturbing the baseline from RANS simulation.

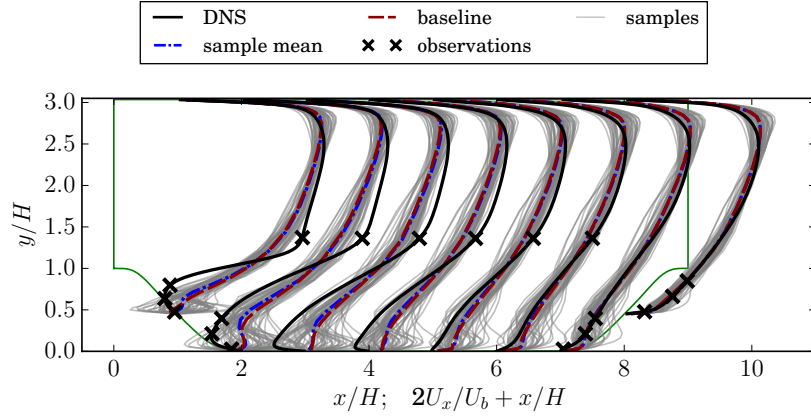


Figure 5.8: Prior ensemble realization of velocity profiles at 8 locations, in comparison to DNS and baseline. The location of observation is indicated with crosses( $\times$ ).

Further, we perform DA analysis with EnKF, the EnRML method, and EnKF-MDA to quantify uncertainties in the velocity field by incorporating the observations at the specific locations. The data assimilation results with different DA schemes are presented in Fig. 5.9. It is noticeable that with EnKF the posterior mean can fit well with DNS results. However, all samples converge to the mean value, and the variance of the posterior becomes very low. By contrast, the EnRML method and EnKF-MDA can give an estimation of the uncertainty, and the mean value also has a good fit with DNS data. Based on our derivation and evaluation in the former sections, that is probably due to that EnKF repeatedly uses the same DNS data by full Gauss–Newton steps, while the EnRML method and EnKF-MDA can be regarded to perform one EnKF step via several small analysis steps.

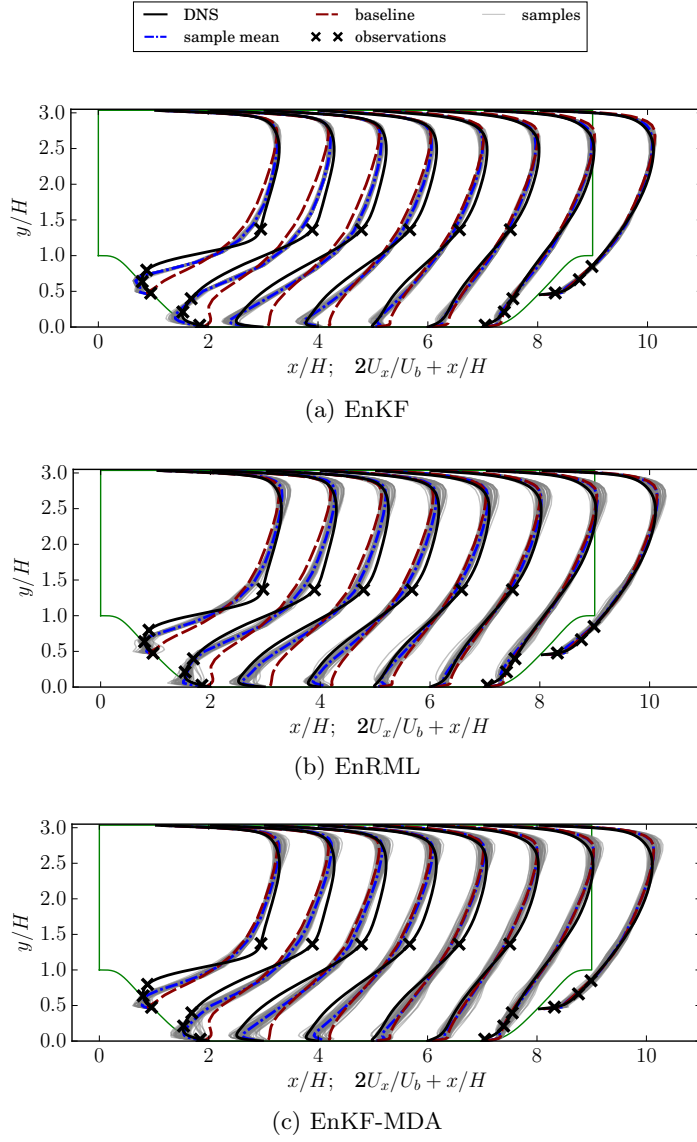


Figure 5.9: Data assimilation Results with EnKF, EnRML, and EnKF-MDA in comparison to baseline and DNS for the turbulent flow in a periodic hill.

Here we present the comparison of 95% credible interval between the prior and posterior in comparison of the three data assimilation methods. The results are shown in Fig. 5.10. It is noticeable that the posterior uncertainty with EnKF is underestimated and too much confidence is placed in the mean value. With the EnRML method and EnKF-MDA, we can have an estimation on the uncertainty indicated by samples. Besides, the uncertainty in the upper channel estimated by the EnRML method and EnKF-MDA is similar to the prior. That is reasonable since the variance  $\sigma$  in this region is low [148] and no observation is informed as well. Hence, the posterior should not change much from the prior distribution. Additionally, from the efficiency of each data assimilation technique, the EnRML method can converge in 8 iterations, while EnKF-MDA needs at least 30 iterations to converge in the inflation parameter  $N_{\text{mda}}$ . From the overall performance, the iterative EnKF loss the statistical information due to data overuse, while the other two methods can provide reasonable uncertainty information. Besides, EnRML can outperform to EnKF-MDA in the convergence speed for this CFD problem.

## 5.5 Conclusion

This paper evaluates the performance of three widely used iterative ensemble-based data assimilation methods (EnKF, EnRML, and EnKF-MDA) for UQ problems. We summarize the derivations of these ensemble methods from an optimization viewpoint. The iterative EnKF method performs several full Gauss–Newton steps during which same data is repeatedly used for the stationary scenario. The EnRML method and EnKF-MDA can iteratively approach to the optimal point with Gauss–Newton method or likelihood recursion, avoiding the data overuse and alleviating the effects of linearization approximation simultaneously. From the numerical investigation for a scalar case, we investigate the effects of limited ensemble sizes. The results show that the EnRML method and EnKF-MDA can provide a satisfactory estimation on the posterior uncertainty with limited ensemble size but inferior to that with large ensemble size. Because the limited ensemble size is not sufficient to describe the statistical information and also increase the error in the estimation of model gradient. Based on the comparison results for both scalar case and CFD case, the posterior mean with all the three methods can have a good agreement with benchmark data. However, the iterative form of EnKF discussed here which use same data repeatedly for steady problem can prompt the data fit but underestimate the posterior uncertainty. Other two methods, EnRML and EnKF-MDA, are capable of giving an estimation of posterior uncertainty. Based on our comparison study, the EnRML method is recommended since it can converge fast and provide the statistical information even in complicated CFD cases. The applicability of these ensemble methods for parameter estimation in CFD applications will be investigated in future studies.

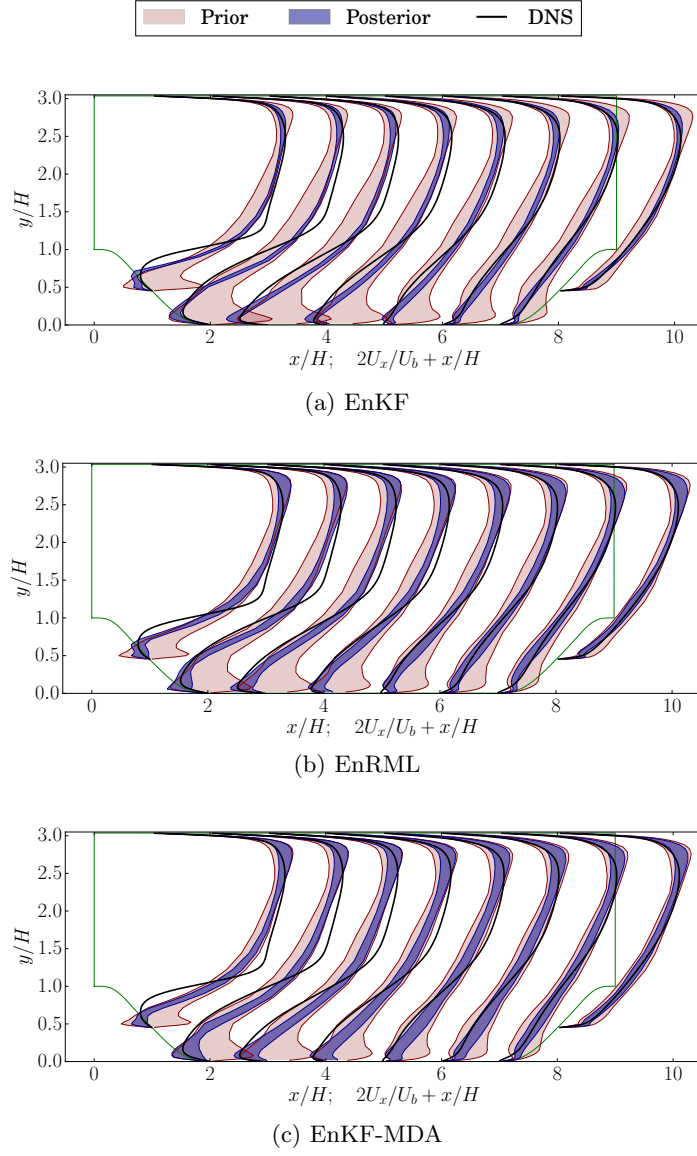


Figure 5.10: The 95% credible intervals of the prior (light/pink shaded region) and posterior (dark/blue shaded region) samples of velocity profiles for the turbulent flow in a periodic hill





## Chapter 6

# Towards for Cavitation

In this chapter, we focus on empirical improvements of the RANS model based on experimental measurements, without the use of data assimilation. It is an other way to achieve the model improvement through analyzing in details the discrepancy between numerical simulations and experiments. Although this approach mostly depends on the researcher's *intuition*, rather than a theoretical framework, we believe it's worth going in that direction in parallel, and eventually see which method of empirical modelling and data-driven modelling could provide the most efficient improvements.

### 6.1 Introduction

Cavitation is the phenomenon of liquid vaporization due to changes of local pressure. It consists in the formation of small vapor bubbles in areas of pressure drop: these bubbles expand and interact until breakup as they reach a zone of higher pressure. Turbulent cavitating flows commonly exist in many engineering applications involving high-speed flows, like rotating machinery (such as propellers and pumps), injectors, and high speed vehicle motion. In such flows, the formed cavity has underlying interactions with the turbulent flows, and different investigations have demonstrated the significant effects of cavitation on turbulent flows. Specifically, the cavitation can prompt the vortex production [75] and arise additional dissipation due to the compressibility effects [35]. Therefore, it is pivotal to gain insights on the cavitation–turbulence interaction, to improve the current turbulence model used in CFD, and eventually provide predictive modellings that would enable, for example, to test the effects of flow control to mitigate the effects of cavitation.

The mix of cavitation bubbles leads to an opaque flow which is very challenging to be measured by current experimental techniques. Hence, the numerical simulations are still the primary tool to investigate the cavitation. To simulate the cavitating flow, the widely used

approach is first to regard the cavitation region as the homogeneous mixture as:

$$(6.1) \quad \rho = (1 - \beta)\rho_l + \beta\rho_v,$$

where  $\rho$  is the mixture density,  $\beta$  is the void fraction,  $\rho_l$  and  $\rho_v$  is the density of liquid and vapor, respectively. Under this assumption, we can solve the Navier–Stokes equation coupling with a single phase model/cavitation model where the slip between the two phases is neglected. Different cavitation models have been proposed to control the mass transfer or phase change. They can be categorized by the barotropic model and the void fraction transport model based on the pressure difference or bubble dynamics. Nevertheless, these cavitation models are all obtained by empirical approaches or under ideal hypotheses. For instance, the barotropic model is firstly proposed in [149] based on the barotropic state law where the mixture density depends only on the local pressure. Numerous works have been done with this model. Coutier-Delgosha et al. used this model into different configurations, such as Venturi [26], hydrofoil [91], inducer [28], and centrifugal pump [29]. Frikha et al. [52] investigated the influence of different cavitation model including the barotropic model for the simulation of cloud cavitation in a hydrofoil. The another type of cavitation model is achieved by the void fraction transport equation as:

$$(6.2) \quad \frac{\partial \beta}{\partial t} + \nabla(\beta u) = \Pi,$$

where  $\Pi$  is the source term, which is usually divided into two terms  $m^+$  and  $m^-$ , representing vaporization and condensation process, respectively. The pioneering work to govern the phase change with transport equation is in [86]. Afterwards, different cavitation models, such as Kunz model, Merkle model, Singhal model Schnerr–Sauer model, etc. are developed to better describe the mass transfer process and widely used for diverse applications. Specifically, in the Kunz model [87] and Merkle model [104], the source terms  $\Pi$  are based on the difference between local pressure and vapor pressure. Moreover, they utilise the empirical coefficients  $C_{\text{prod}}$  and  $C_{\text{dest}}$  to control the amplitudes of evaporation or condensation of models. The difference between the two models is that the condensation in Merkle model is only activated when the local pressure is larger than the vaporisation pressure. Besides, the cavitation models, e.g., Singhal model [131] and Schnerr–Sauer model [128], are proposed where the source terms  $\Pi$  in Eq. (6.2) is deduced from the Rayleigh–Plesset equation which describes the dynamics of a single spherical bubble.

As for the turbulence simulation, the high-fidelity methods, such as large eddy simulation (LES) and direct numerical simulation (DNS), are conducted [69, 74, 157] but still computationally prohibitive for the cavitating flows. Hence, the commonly used method is still Reynolds averaged Navier–Stokes (RANS) models coupling with the cavitation model. It is well known that in RANS equations, the unknown Reynolds stress, has to be modelled under different assumptions. After decades’ developments, diverse RANS models have been proposed to address this issue. The linear eddy viscosity model therein is the most used one due to its numerical stability, which includes  $k$ – $\epsilon$ ,  $k$ – $\omega$  [141], and  $k$ – $\omega$  SST [102]. Recently, the hybrid RANS/LES

model is developed to solve RANS equations based on local turbulent length scales, such as detached eddy simulation (DES) model [132] and the scale-adaptive simulation (SAS) model [101]. Moreover, it has been observed that in the presence of cavitation, the resolved eddy viscosity with current RANS methods will be overestimated and damp the re-entrant jet, which leads to that the unsteady cavitation shedding cannot be simulated. To this end, Reboud et al. [31, 123] proposed an artificial modification (called hereafter the Reboud correction) on the eddy viscosity for unsteady cavitation. It can dramatically reduce the effective viscosity in the mixture and thus capture the shedding behaviours, but there is still no quantitative validation due to lack of experimental measurements on the turbulent quantities over the past two decades. The RANS methods coupling with Reboud correction have been investigated extensively for cavitation simulations. For instance, Coutier-Delgosha et al. [27] compared the standard and modified  $k-\epsilon$  RNG model, and  $k-\omega$  model with and without compressibility effects. They demonstrated that the Reboud correction could significantly improve the numerical simulation results and the compressibility effects have to be taken into account. Decaix and Goncalves [34] provided the comparison of a class of RANS simulation based on  $k-l$  transport equation model, including the standard  $k-l$ ,  $k-l$  SST and  $k-l$  SAS model. They suggested that the SAS model with Reboud correction could have a good agreement with experiments. However, in the above work, only one component of the bubble velocities is considered in these comparisons; hence the comparison with the velocity of the homogeneous mixture is questionable. Moreover, they mainly focus on the time-averaged velocity and void fraction. The statistical turbulent quantities in cavitating flows, such as the turbulent kinetic energy and Reynolds shear stress, are not well analyzed due to the difficulty of experimental measurements on these quantities in cavitating regime. It is well known that the Reynolds stress is the main uncertain source in RANS simulations. Hence, to understand the discrepancy between RANS simulation and experimental measurements, it is necessary to compare and analyze RANS model-form uncertainty associated with Reynolds stress.

The recent development of fast X-ray imaging in experiments [82] provides a set of reliable data for cavitating flows, including turbulent kinetic energy and Reynolds shear stress. That makes it possible to gain some insights of the cavitation/turbulence interactions and further improve current RANS models. This chapter will dedicate to compare the performance of different RANS models on the cavitating flows and investigate the effects of the Reboud correction. As a result, we propose a modified Reboud correction and validate its performance based on experimental data and numerical tests.

## 6.2 Governing equations

To simulate cavitating flows, we assume that the two phases of liquid and vapor are strongly coupled and the slip in the phases interface is neglected. Based on that, the two-phase flow is

governed by one group of RANS equations as:

$$(6.3) \quad \begin{aligned} \rho \frac{\partial u_i}{\partial t} + \rho u_j \frac{\partial u_i}{\partial x_j} &= -\frac{\partial P}{\partial x_i} + \mu \frac{\partial^2 u_i}{\partial x_j \partial x_j} - \frac{\rho \overline{\partial u'_i u'_j}}{\partial x_j} \\ \frac{\partial \rho}{\partial t} + \frac{\partial \rho u_i}{\partial x_i} &= 0, \end{aligned}$$

The mixture density  $\rho$  as defined in (6.1) is resolved with the cavitation model associated with local pressure. The Reynolds stress  $-\rho \overline{u'_i u'_j}$  in the momentum equation is estimated by turbulence model. The turbulence models and cavitation model used in the present work will be presented in the following subsections.

### 6.2.1 Turbulence models

Diverse turbulence models have been proposed over decades. Here, we mainly focus on two advanced turbulence models, namely  $k$ - $\omega$  SST and SST-SAS. In this subsection, we give a brief introduction on these models.

#### 6.2.1.1 $k$ - $\omega$ SST model

The  $k$ - $\omega$  SST is proposed by Menter [102] which combine the  $k$ - $\epsilon$  model and  $k$ - $\omega$  model. In the sub-layer of the boundary layer, the model adopts the  $k$ - $\omega$  model, while in the free shear layer away from the wall, it transforms to the  $k$ - $\epsilon$  model. Thus, this blend method can keep the respective merits of the two models where they perform the best. Moreover, the model leverages the Bradshaw assumption to ensure that the Reynolds shear stress varies as the turbulent kinetic energy, which can avoid the overestimations of the Reynolds shear stress in the adverse pressure gradient regions. The eddy viscosity is constructed by:

$$(6.4) \quad \mu_t = \frac{a_1 \rho k}{\max(a_1 \omega, S F_2)}$$

The transport equation for  $k$  and  $\omega$  is formulated as follows:

$$(6.5a) \quad \frac{\partial(\rho k)}{\partial t} + \frac{\partial(\rho u_j k)}{\partial x_j} = \rho P_k - \beta^* \rho \omega k + \frac{\partial}{\partial x_j} \left[ \left( \mu + \sigma_k \frac{\rho k}{\omega} \right) \frac{\partial k}{\partial x_j} \right]$$

$$(6.5b) \quad \frac{\partial(\rho \omega)}{\partial t} + \frac{\partial(\rho u_j \omega)}{\partial x_j} = \gamma \frac{\omega}{k} P_k - \beta \rho \omega^2 + \frac{\partial}{\partial x_j} \left[ (\mu + \sigma_\omega \mu_t) \frac{\partial \omega}{\partial x_j} \right] + 2(1 - F_1) \frac{\rho \sigma_{\omega 2}}{\omega} \frac{\partial k}{\partial x_j} \frac{\partial \omega}{\partial x_j},$$

where

$$(6.6a) \quad F_2 = \tanh \left[ \left[ \max \left( \frac{2\sqrt{k}}{\beta^* \omega y}, \frac{500\nu}{y^2 \omega} \right) \right]^2 \right],$$

$$(6.6b) \quad P_k = \min \left( \tau_{ij} \frac{\partial U_i}{\partial x_j}, 10\beta^* k \omega \right).$$

The limiter  $10\beta^*k\omega$  on the turbulent kinetic energy (TKE) production is recommended by Menter [103]. The blend function  $F_1$  is defined as:

$$(6.7) \quad F_1 = \tanh \left\{ \left\{ \min \left[ \max \left( \frac{\sqrt{k}}{\beta^*\omega y}, \frac{500\nu}{y^2\omega} \right), \frac{4\sigma_{\omega 2}k}{CD_{k\omega}y^2} \right] \right\}^4 \right\},$$

where

$$(6.8) \quad CD_{k\omega} = \max \left( 2\rho\sigma_{\omega 2} \frac{1}{\omega} \frac{\partial k}{\partial x_i} \frac{\partial \omega}{\partial x_i}, 10^{-10} \right).$$

The parameters in the model are blended from the  $k$ - $\omega$  model and  $k$ - $\epsilon$  as:

$$(6.9) \quad \phi = \phi_1 F_1 + \phi_2 (1 - F_1),$$

where  $\phi_1$  stands for the constant with subscript 1 while  $\phi_2$  is the constant with subscript 2. The constants in the model are given as:

$$(6.10) \quad \begin{aligned} \gamma_1 &= \frac{5}{9}; \gamma_2 = 0.44; \alpha_1 = \frac{5}{9}; \alpha_2 = 0.44; \beta_1 = \frac{3}{40}; \beta_2 = 0.0828; \\ \beta^* &= \frac{9}{100}; \sigma_{k1} = 0.85; \sigma_{k2} = 1; \sigma_{\omega 1} = 0.5; \sigma_{\omega 2} = 0.856 \end{aligned}$$

### 6.2.1.2 Scale-adaptive simulation model

The scale-adaptive simulation (SAS) model is proposed by Menter and Egorov [101]. They introduced the von Karman length-scale into the turbulent scale equation. Thus, the SAS model can dynamically self-adjust to resolve the turbulent structure with unsteady Reynolds averaged Navier–Stokes equations based on the von Karman length scale. The approach can provide a LES-like behavior in the detached flow regions as DES model, but without explicit grid dependence in the RANS regime. The formulation of the eddy viscosity and the transport equations are same as the  $k$ - $\omega$  SST model, except that a term  $Q_{\text{SAS}}$  is added in right hand of the special dissipation  $\omega$  transport equation (6.5b). The  $Q_{\text{SAS}}$  is defined as:

$$(6.11) \quad Q_{\text{SAS}} = \rho \max \left[ \zeta_2 \kappa S^2 \left( \frac{L}{L_{vK}} \right)^2 - C \cdot \frac{2k}{\sigma_\phi} \max \left( \frac{1}{\omega^2} \frac{\partial \omega}{\partial x_j} \frac{\partial \omega}{\partial x_j}, \frac{1}{k^2} \frac{\partial k}{\partial x_j} \frac{\partial k}{\partial x_j} \right), 0 \right]$$

In the formula above,  $L$  is the modelled length scale and the  $L_{vK}$  is the von–Karman length scale which is defined as:

$$(6.12a) \quad L = \sqrt{k} / \left( c_\mu^{1/4} \cdot \omega \right)$$

$$(6.12b) \quad L_{vK} = \frac{\kappa S}{|U''|}$$

$$(6.12c) \quad |U''| = \sqrt{\frac{\partial^2 U_i}{\partial x_k^2} \frac{\partial^2 U_i}{\partial x_j^2}}$$

The model constants are given as:

$$(6.13) \quad C = 2, \quad \alpha = 0.8, \quad \zeta_2 = 3.51, \quad \sigma_\phi = 2/3.$$

The added SAS term can be considered as a source term in the  $\omega$  equation. It can detect the regions of the instabilities based on the local turbulent length scale and adjust the turbulent dissipation to reduce the turbulent viscosity.

### 6.2.2 Reboud correction

Cavitating flows are usually highly unstable with fluctuations at various scales. The unsteady cavitation typically have periodic behaviours with four different stages in each cycle, as shown in Fig. 6.4. The cavitation first expands along the wall and form the cloud cavitation. Then the downstream cavity detaches from the wall and is driven by the main stream to the wake, eventually breaking up in the zone of high pressure.

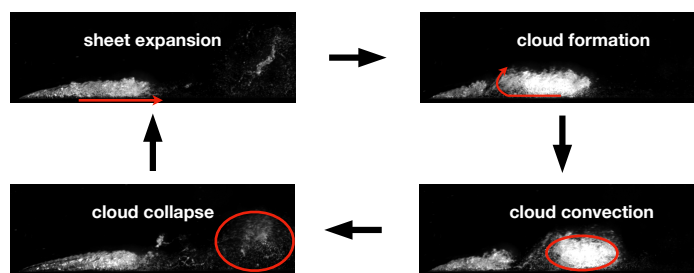


Figure 6.1: a cycle of cavitation behaviour

Cloud cavitation is characterized by a primary large scale instability based on the periodical shedding of the rear part of the cavity. However, the conventional RANS models cannot capture the shedding behaviour, because the eddy viscosity in the cavitation region is overestimated and that will block the re-entrant jet which is main factor to arise the bubble separation. In order to capture the shedding behaviour, Reboud et al. [123] imposed an artificial modification  $f(\rho)$  on the original eddy viscosity as a multiplicative correction. The modification can reduce dramatically the eddy viscosity in the cavitation regime based on the vaporization extent. The formulation can be expressed as:

$$(6.14) \quad f(\rho) = \rho_v + (1 - \beta)^n(\rho_l - \rho_v).$$

The plot of  $f(\rho)$  is shown in Fig. 6.2. When the void fraction is equal to zero,  $f(\rho)$  equals the liquid density, as in the original model. Oppositely, when the void fraction decreases down to 1,  $f(\rho)$  will be the vapor density. For intermediate values of void fraction, the function reduces significantly the original modelled eddy viscosity once there occurs the cavitation. Different investigations have been carried out and demonstrate the success of this modification for different geometries [31, 75, 155]. With this modification, the periodical behavior can be correctly reproduced, usually with the right frequency.

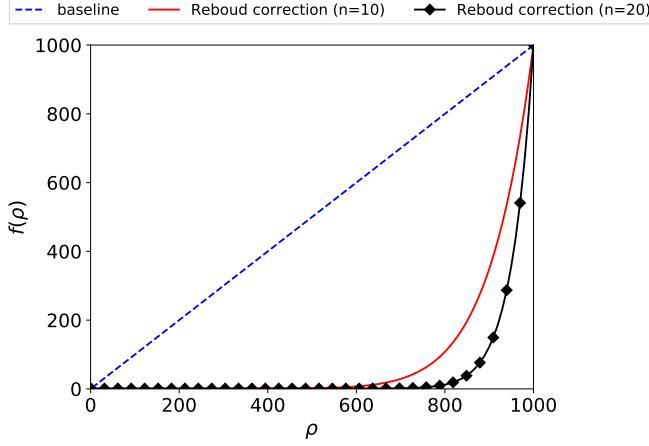


Figure 6.2: Plot of the Reboud correction function

### 6.2.3 Phase model

Regarding the phase model, we take the homogeneous assumption to treat the cavitation region as a mixture. Further, we apply the barotropic state law to describe the phase change due to its robustness. However, the barotropic model has some drawbacks. For instance, it is assumed that the cavitation phenomenon is isothermal, and thermodynamic effects are neglected. On the other hand, the barotropic law relates the pressure to the void fraction directly, and the void fraction varies immediately with change of pressure, which is not physical since the time of phase change is not taken into account. Despite the limitations of barotropic model, a systematical good agreement between the barotropic model and transport equation based model is obtained. [52] Hence, basically there is no major improvement in using the transport equation model.

In the barotropic state model, the Tait equation and the perfect gas law are utilized for the pure liquid and vapor, respectively, to estimate the relationship between the pressure and the density. The formulations are shown as:

$$(6.15) \quad \begin{aligned} \frac{\rho_l}{\rho_{\text{ref}}} &= \sqrt[7]{\frac{P + P_0}{P_{\text{ref}}^T + P_0}}, \\ \frac{P}{\rho_v} &= C, \end{aligned}$$

where  $P_{\text{ref}}^T$  and  $\rho_{\text{ref}}$  is the reference pressure and density,  $P_0 = 3 \times 10^8$ . In the mixture interval, the state law is characterized with a sinusoidal transition. The maximum slope is defined by  $1/A_{\min}^2$ , where  $A_{\min} = \partial P / \partial \rho$ . The plots are shown in Fig. 6.3 with two different  $A_{\min}$ .

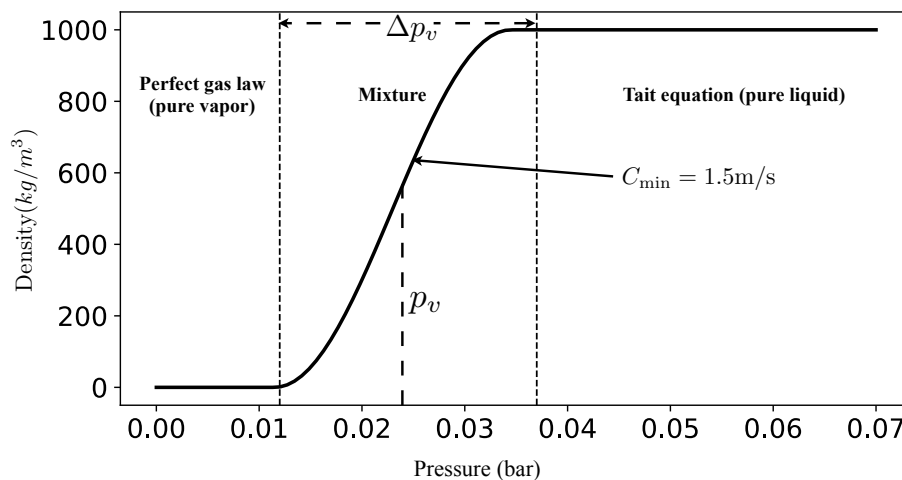


Figure 6.3: Plot of barotropic state law for the mixture

## 6.3 Numerical evaluation of current SST-based models

### 6.3.1 Numerical setup

The numerical simulations are conducted in an home-made two-dimensional CFD code, which is developed and validated over decades [31, 32, 58]. In the code, the second-order implicit scheme is used for temporal discretization, and the finite volume method is applied for the spatial discretization. The second-order scheme will locally switch to the first order in the region in presence of large pressure gradient to prevent the numerical oscillations. The oscillation-free second-order HPLA scheme [156] is leveraged to estimate the convection term, and the central differencing scheme is adopted for the diffusion term. The SIMPLE algorithm [117] is used to solve the coupling of pressure and velocity.

The Venturi geometry is commonly used for the investigation of cavitation phenomenon. Khlifa et al. [82] conducted the particle image velocimetry (PIV) experiments in a small Venturi-type section through applying the ultra-fast X-rays imaging. The Venturi channel has a convergent angle of 18 degree and a divergent angle of 8 degree as presented in Fig. 6.4. The inlet section is a rectangular with  $17mm \times 4mm$ . The height of the throat is  $15.34mm$ . The flux of the flow condition is  $35.09L/min$ . The inlet velocity can be obtained as  $8.6m/s$ . The cavitation number is defined based on outlet pressure as:

$$(6.16) \quad \sigma = \frac{P_{out} - P_{ref}}{\frac{1}{2}\rho U_{ref}^2}$$

In this case, the cavitation number is 1.15 and the Reynolds number is  $1.9 \times 10^5$ . The cavity length is estimated around  $10mm$  and the shedding frequency is around  $210Hz$ . The 2D RANS equations coupling with barotropic model are resolved to predict the cavitating flow. Since the flow field is observed from one side in the experiment, the processed results can be regarded



as the plane-averaged resolution. For the numerical setup, the mesh in the computational domain has 260 cells in the stream-wise direction and 117 cells in the normal to wall direction. The uniform velocity is imposed at the computational domain inlet, and the static pressure is imposed at the outlet. Along the solid boundary, wall function is applied and the  $y$  plus in the first mesh adjacent to the wall is range from 15 to 20. Based on previous works [27, 35], the mesh is adequate to simulate cavitation in such Venturi type section. The artificial parameter  $n$  in the Reboud correction is taken as 20 to have shedding frequency in good agreement with experiments.

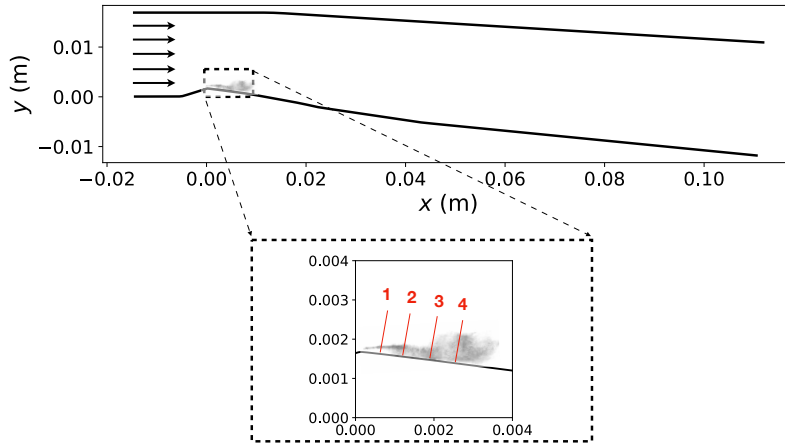


Figure 6.4: The geometry of the Venturi-type section. The red, numbered line in the enlarged window indicate the profiles for comparison.

### 6.3.2 Comparison results

In this subsection, attention is focused on the comparison between the turbulent quantities derived from the x-ray imaging experiments and the numerical predictions obtained with the aforementioned turbulence models. The cavitation number is slightly adjusted down to 1.12 (against 1.15 in the experiments) to obtain the shedding frequency and cavity length in good agreement with the experimental data. The results are summarized in Table 6.1.

turbulence model	cavitation number	cavity length (mm)	shedding frequency (Hz)
$k-\omega$ SST	1.12	10	230
SST-SAS	1.12	10	222
exp	1.15	10	210

Table 6.1: Summary of simulation results with different turbulence model with comparison to the experiments

The plots of the time evolution of cavity shape are presented as in Fig. 6.5. We can see that both the RANS models arise the periodic shedding. Besides, for both the  $k-\omega$  SST and SST-SAS, there is a small area of sheet cavity attached on the wall near the throat, and the cavity is expanded based on that.

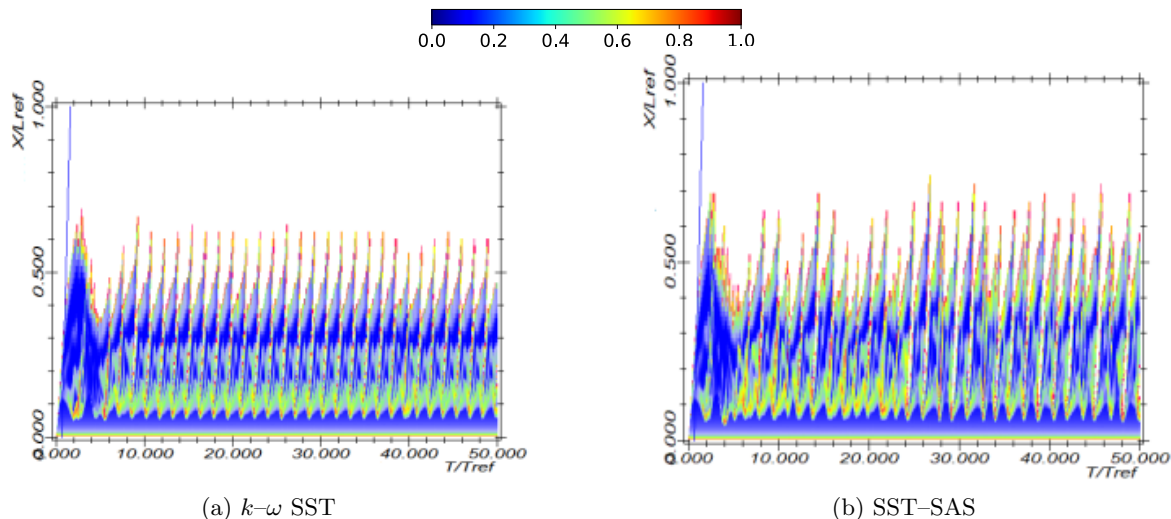


Figure 6.5: Time evolution of cavity shape with different turbulence models. The color indicate the minimum void fraction in each cross section, from the Venturi throat.

Fig. 6.6 represents the time-averaged composition of the cavitation area, i.e., the mixture density, obtained with the two turbulence models and compared to the experiments. It can be seen that the shape of the cavity is not well predicted. The position of detached cavity is very upstream relative to the numerical simulation. The lowest density in the simulation reaches to below  $300\text{kg/m}^3$ , while experimental observation capture the minimum density at around  $600\text{kg/m}^3$ . The separated cavity in the numerical prediction is reattached in the downstream and the total attached part is longer than the experimental measurements.

The contour plots of turbulent kinetic energy with comparison to experiments are presented in Fig. 6.7. Both the  $k-\omega$  SST and SST-SAS method can capture the high turbulent kinetic energy areas. However, at the downstream, the value is overestimated near the wall. The comparison along profiles is shown in Fig. 6.8. At the first position, the turbulent kinetic energy can have a good fit with the experiments. As for the downstream, the TKE from the numerical simulation decrease slowly, while from the experiment it is significantly decreased, which leads to the large discrepancy between the numerical simulation and experiments.

The results in Reynolds shear stress are shown in Fig. 6.9. It is noticeable that both the turbulence models give a very low Reynolds shear stress compared to the experiments. Fig. 6.10 presents the comparison results in the Reynolds shear stress along profiles. With Reboud correction, we can have a good estimation in Reynolds shear stress in the downstream near the wall region, which can reduce the damping of re-entrant jet flow and induce the shedding

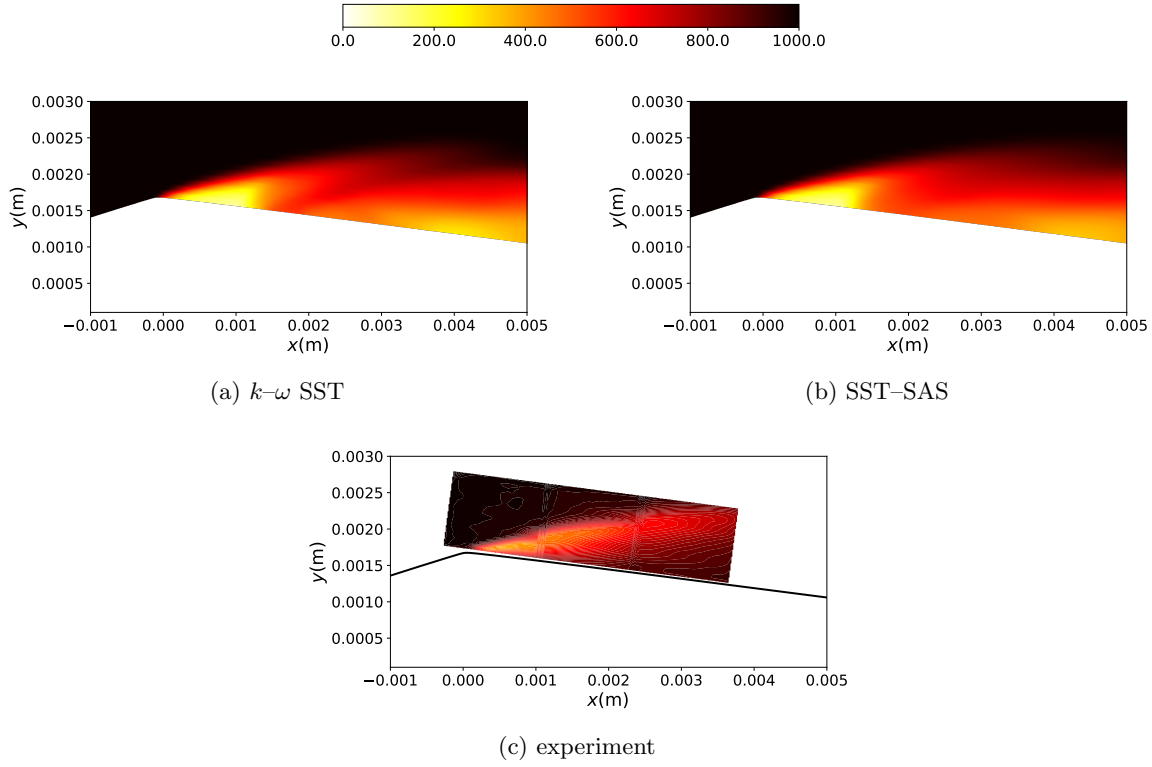


Figure 6.6: Shape of time-averaged cavity.

behaviours. However, it may reduce the Reynolds shear stress in the region away from the wall which leads to a large departure from the experiments.

To investigate the effects of Reboud correction, we recalculate the Reynolds shear stress without the Reboud correction. The results are shown in Fig. 6.11. It can be seen that without Reboud correction, both models can capture the region near the wall where exist high Reynolds shear stress. The comparison with experiments along profiles is shown in Fig. 6.12. At the first position, a good agreement with experiments can be observed. While approaching to the downstream, there will be a large discrepancy in the region near the wall, probably due to the discrepancy in TKE as shown in Fig. 6.8.

### 6.3.3 Discussion

The numerical results show that  $k-\omega$  shear stress transport based methods cannot simulate accurately the Reynolds shear stress which is the main uncertainty source in the RANS model. As for the reasons, it can be due to many aspects. First, Reynolds shear stress is directly related to TKE. In the first position, the TKE is well estimated, and it is possible to have a good prediction in Reynolds shear stress without Reboud correction, compared to experimental data. However, after position 2, the TKE are not correctly predicted. Specifically, TKE is significantly higher than that from experiment near the wall, which maybe responsible for the too large

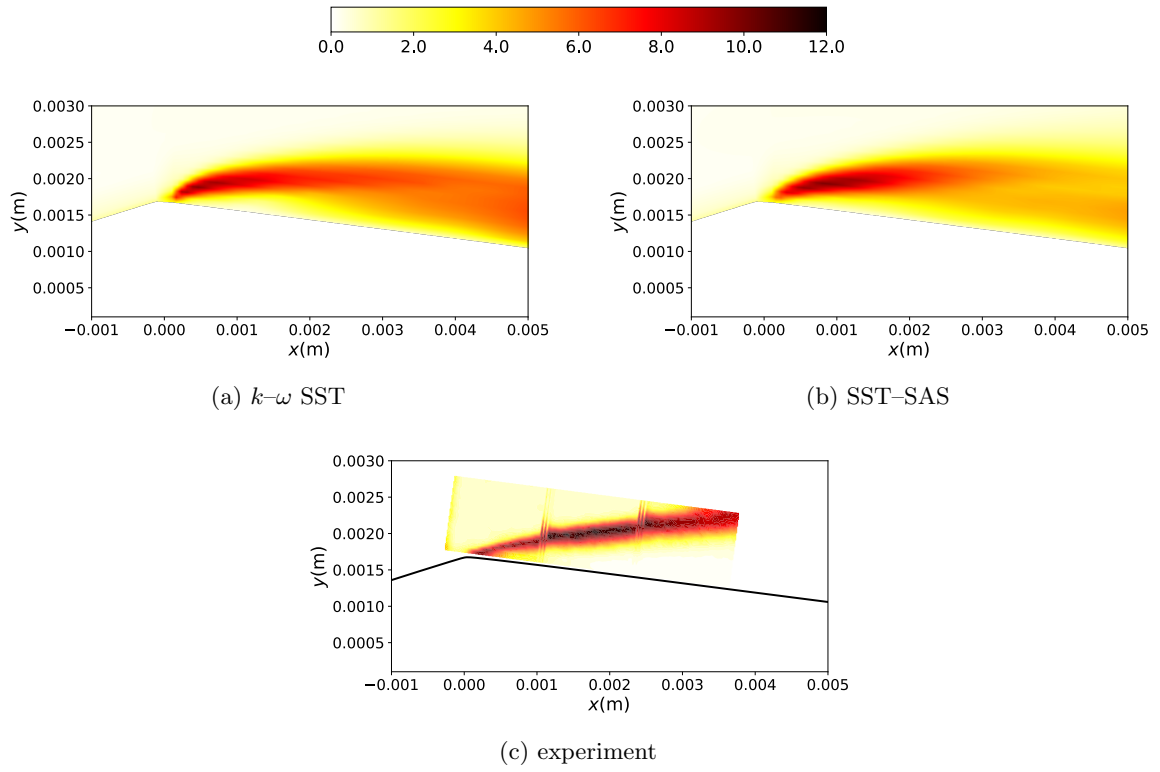


Figure 6.7: The contour plots of time-averaged turbulent kinetic energy with different turbulence models compared to the experiments.

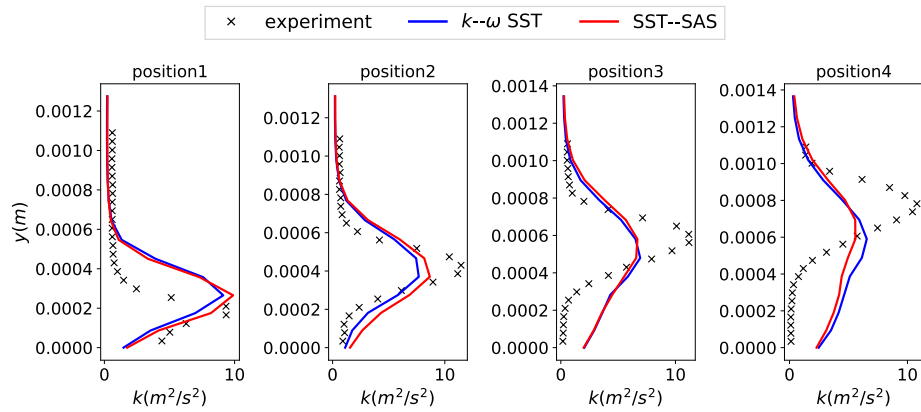


Figure 6.8: Comparison in turbulent kinetic energy between the different turbulent models and experiments with Reboud correction along profiles.

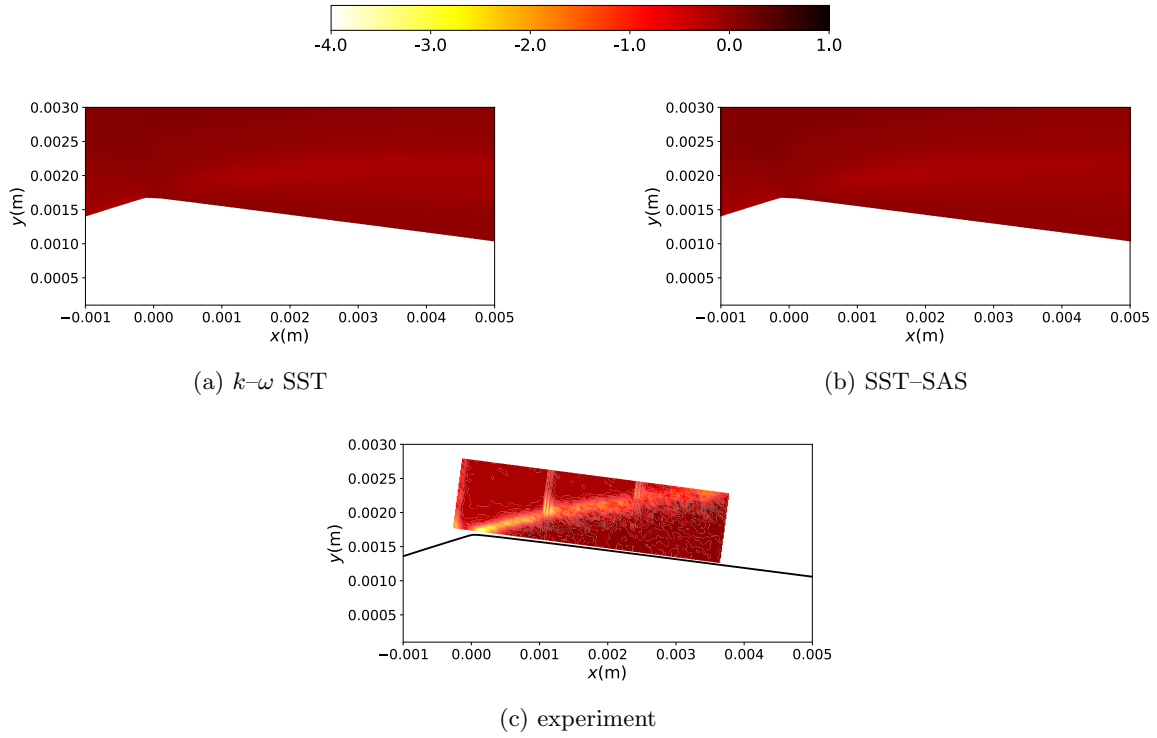


Figure 6.9: Time-averaged Reynolds shear stress with Reboud correction.

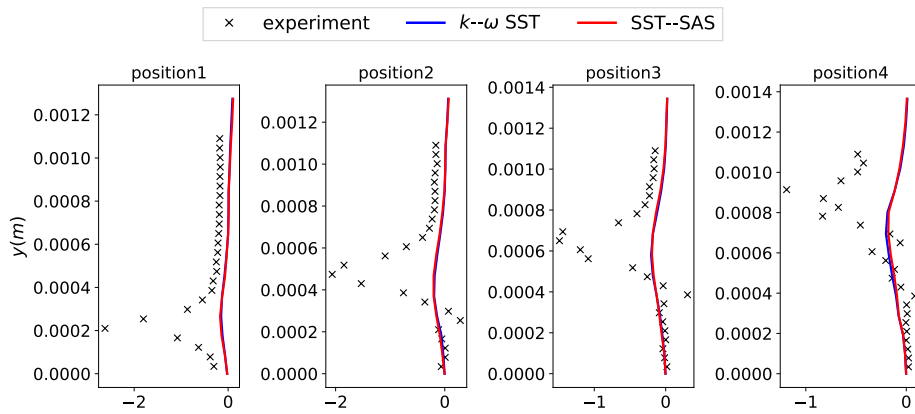


Figure 6.10: Comparison in Reynolds shear stress between the different turbulent models and experiments with Reboud correction.

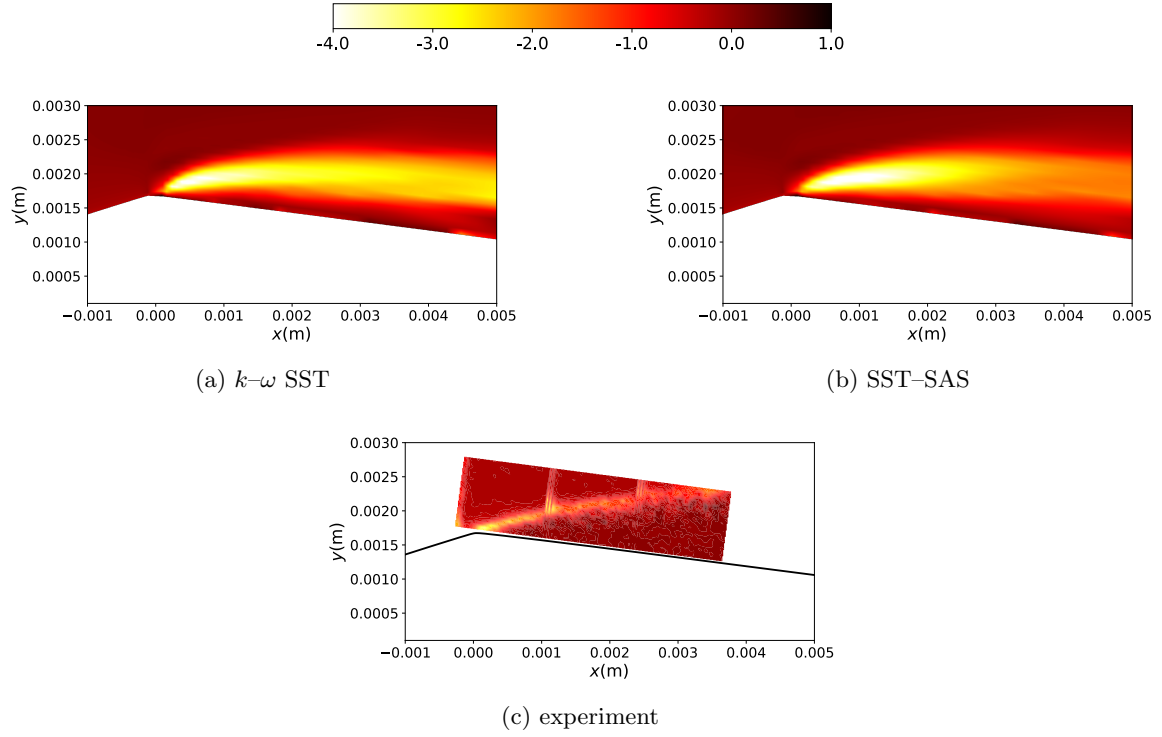


Figure 6.11: time-averaged Reynolds shear stress without Reboud correction.

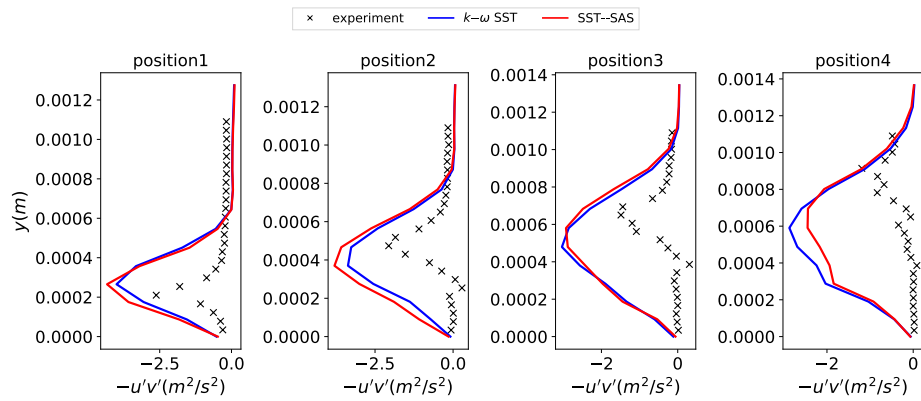


Figure 6.12: Comparison in Reynolds shear stress between the different turbulence models and experiments without Reboud correction.

Reynolds shear stress near the wall in Fig 6.12. The Reboud correction can reduce the Reynolds shear stress in the whole cavity region and lead to a good agreement with experiments near the wall. But in the region away from the wall where there exists large Reynolds shear stress, the Reboud correction deteriorates the prediction.

On the other hand, cavitation can enlarge the turbulent boundary layer thickness and result in the reduction of the TKE as well as Reynolds shear stress, since the cavity damps the main stream velocity. However, this cannot be well captured by the present turbulence models, as shown in the above numerical simulations. Moreover, Reboud correction reduces the Reynolds shear stress significantly in the entire cavitation occurring region. Nevertheless, depending only on the mixture density may lead to wrong correction, as the cavity shape is not accurately simulated in many cases (Fig. 6.6). It can capture the low Reynolds shear stress near the wall but will deteriorate results in the phase interface regime where high shear stress is expected from the experimental observation. To this end, a better modification is possible to be achieved based on enforcing the estimation of boundary layer thickness instead of only depending on the simulated mixture density.

## 6.4 Modified Reboud correction

In  $k$ - $\omega$  shear stress transport based model, the eddy viscosity in the boundary layer is modified based on Bradshaw assumption. That is, the ratio of Reynolds shear stress and TKE is constant as:

$$(6.17) \quad \frac{-u'v'}{k} = c,$$

where  $c$  is 0.31 for the incompressible turbulent flows. However, for the turbulent cavitating flow, the ratio has to be reduced from the experimental observation [1]. In the work of [34], a reduced constant  $c$  is adopted to improve the simulation and compared to the Reboud correction. They use the constant 0.3 for the non-cavitating regime, while in the two-phase areas the constant  $c$  is reduced to 0.1 or 0.2. It is demonstrated that with the reduced ratio  $c$ , it can also capture the periodic behaviours as with Reboud correction and give a comparable prediction on velocity. With our experimental measurements, we calculate the ratio of the Reynolds shear stress and TKE, and compare to the Bradshaw assumption and the Reboud correction at two different measured windows as shown in Fig. 6.13. The first window is range from  $x = 0$  to  $x = 0.0013$ , the second window is range from  $x = 0.0013$  to  $x = 0.0026$ .

The comparison results for the two windows are shown in Fig. 6.14. It is obvious that both the Reboud correction and the Bradshaw assumption with  $c = 0.1$  have large discrepancy with experimental measurements.

Although the Reboud correction can have better agreement with the experiments and reduce the eddy viscosity thus to alleviate the blockage of the re-entrant jet, the numerical investigations in Section 6.3 indicate that the Reboud correction can reduce the eddy viscosity

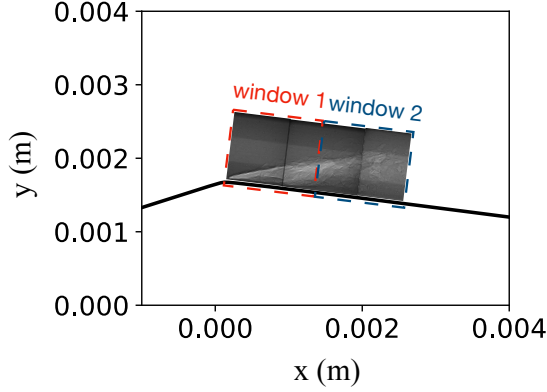
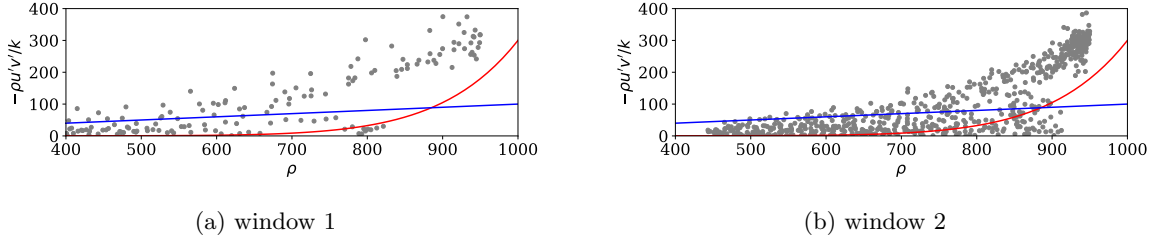


Figure 6.13: The schematic of two measured window for comparison


 Figure 6.14: The comparison of the Reboud correction with  $n = 10$  (red line), the Bradshaw assumption with  $c = 0.1$  (blue line) and experimental data (grey dots)

near the wall thus arise the shedding behaviours, but in the areas away from the wall, it will worsen the prediction. The reason is most likely due to that the phase model and the RANS model cannot predict accurately the cavity shape. Also, the effects of slip velocity in the phases interface are not considered in current models. In the experiments, we can see that the turbulent kinetic energy and Reynolds shear stress is high in the interface of the mixture and pure liquid. That may be caused by the slip velocity at the phase interface which increase the turbulent kinetic energy production and Reynolds shear stress as well.

In light of the fact that the cavity shape may be not simulated accurately, it is problematic to reduce the eddy viscosity only depending on the mixture density. Also, the constant exponent  $n$  in the Reboud correction (6.14) reduces the turbulent viscosity to same extent as long as they have same void fraction, which leads to the current correction cannot cover most of the experimental data. Moreover, the Bradshaw assumption is deduced in the boundary layer, while the Reboud correction does not consider the effects of boundary layer. It has been noted that the cavitation will enlarge the boundary layer. Accordingly, we analyze four available experimental measurements with different flow conditions. Herein two flows have similar cavitation number but different Reynolds number, and three flows have similar Reynolds number while different cavitation number. We estimate the thickness of cavitating mixing layer based on  $u = 0.9u_{max}$



and fit the slope as shown in Fig. 6.15.

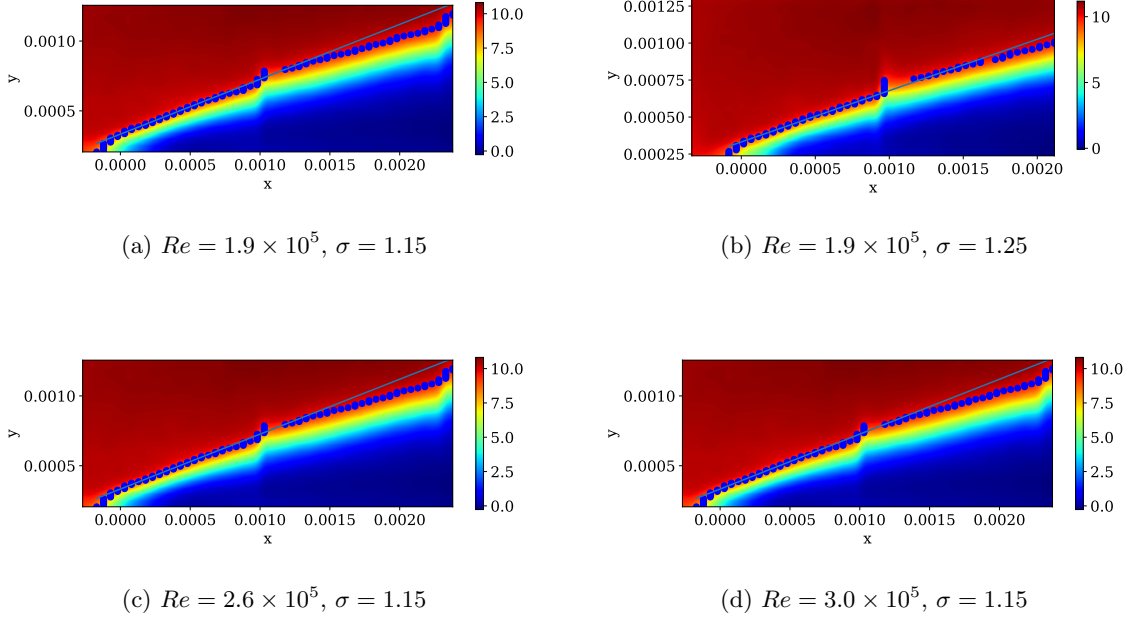


Figure 6.15: Fitting slope of the cavitating mixing layer

case	Re	$\sigma$	cavity length (mm)	slope (exp)	slope (Eq. (6.18) )
1	$1.9 \times 10^5$	1.15	10	0.42	0.40
2	$1.9 \times 10^5$	1.25	5	0.36	0.36
3	$2.6 \times 10^5$	1.15	6	0.39	0.37
4	$3.0 \times 10^5$	1.15	7	0.38	0.36

Table 6.2: Summary of slope of cavitating mixing layer for four different flow condition with comparison of experimental data and the results of fitting formula.

Based on the experimental data, we give a boundary layer estimate as:

$$(6.18) \quad \delta = \frac{5.2}{\sigma Re^{1/5}} \Delta x_i,$$

where  $\Delta x_i$  is the distance to the cavitation inception point. With this formula, the estimated slope of cavitating mixing layer can have a good agreement with experiment as shown in Table 6.2. With the estimated boundary layer thickness, we proposed a modified eddy viscosity model to trigger the eddy viscosity reduction within the boundary layer. The empirical parameter  $n$  in the Reboud correction is modified as in the formula:

$$(6.19) \quad N = \frac{n-1}{2} \tanh C(\delta - y) + \frac{n+1}{2},$$

where  $C$  is the hyper-parameter and taken as 1000,  $n$  is the original parameter in the Reboud correction, and  $y$  is the distance to the wall.

## 6.5 Validation

To validate the new eddy viscosity model, we first compare the proposed modification with experimental data in the ratio of Reynolds shear stress and TKE at the two separated measured windows. By using the experimental data, we can calculate the ratio of the time-averaged Reynolds shear stress and TKE directly. Regarding the original and modified Reboud correction, the ratio is calculated with  $0.3f(\rho)$ . For the conventional Bradshaw assumption, it adopts  $c\rho$  with a reduced  $c = 0.1$ . The comparison results at the first window and second window are shown in Fig. 6.16 and Fig. 6.17, respectively. It is noticeable that the proposed modification can have a better agreement with experimental measurements compared to the original Reboud correction.

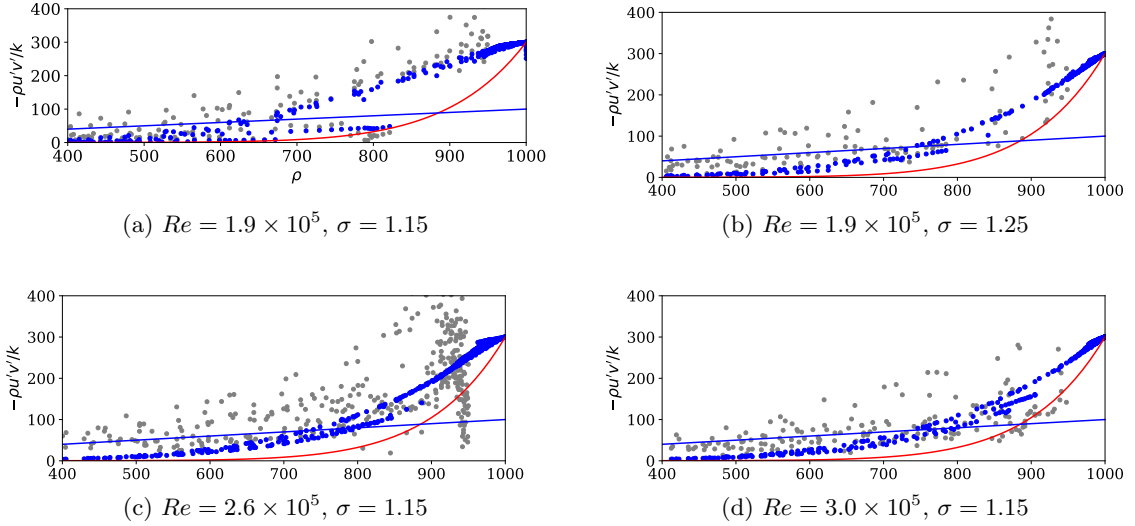


Figure 6.16: Experimental comparison at window 1. Red line: the Reboud correction with  $n = 10$ ; blue line: the Bradshaw assumption with  $c = 0.1$ ; grey dots: experimental data; blue dots: modified Reboud correction.

Further, to validate the modification, we apply the new eddy viscosity correction into the four numerical test cases in Table 6.2. The simulation results in the Reynolds shear stress are presented in Fig. 6.18. It can be seen that for all the cases the results can remarkably fit well with experimental data in  $-u'v'$  compared to the original one. The new modification can improve significantly the prediction in Reynolds shear stress, and also capture the unsteady shedding behaviours.

However, although the Reynolds shear stress can be captured with the modified eddy viscosity model, the resolved velocity and mixture density is not improved. We chose the case 1 as example since in this case we can have the similar Strouhal number as in the measurement. The results are presented in Fig. 6.19. It may be due to many aspects. First, this work are based on 2D simulations, but cavitating flow, especially cloud cavitation, is typical 3D phenomenon. It

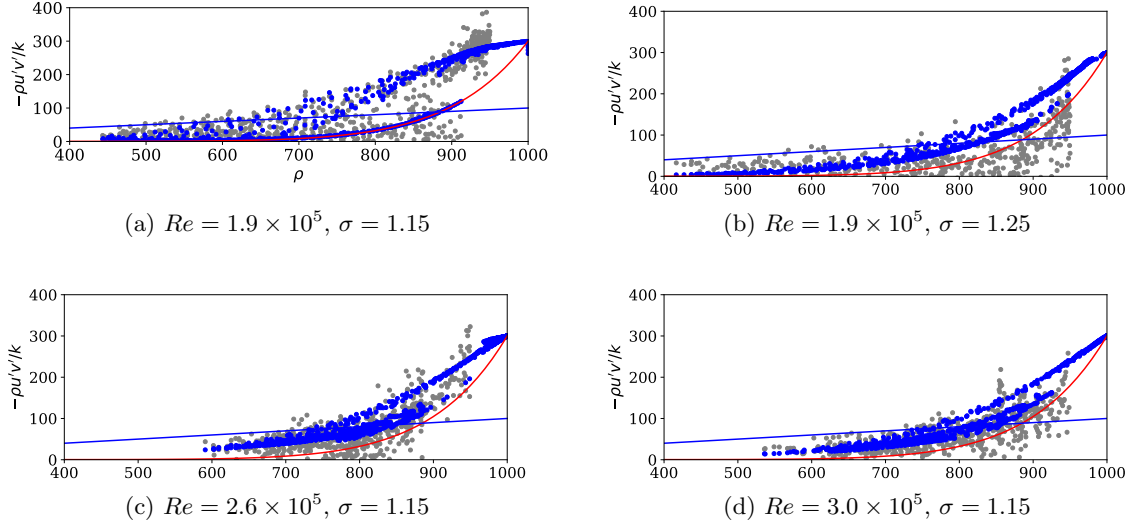


Figure 6.17: Experimental comparison at window 2: Red line: the Rebound correction with  $n = 10$ ; blue line: the Bradshaw assumption with  $c = 0.1$ ; grey dots: experimental data; blue dots: modified Rebound correction.

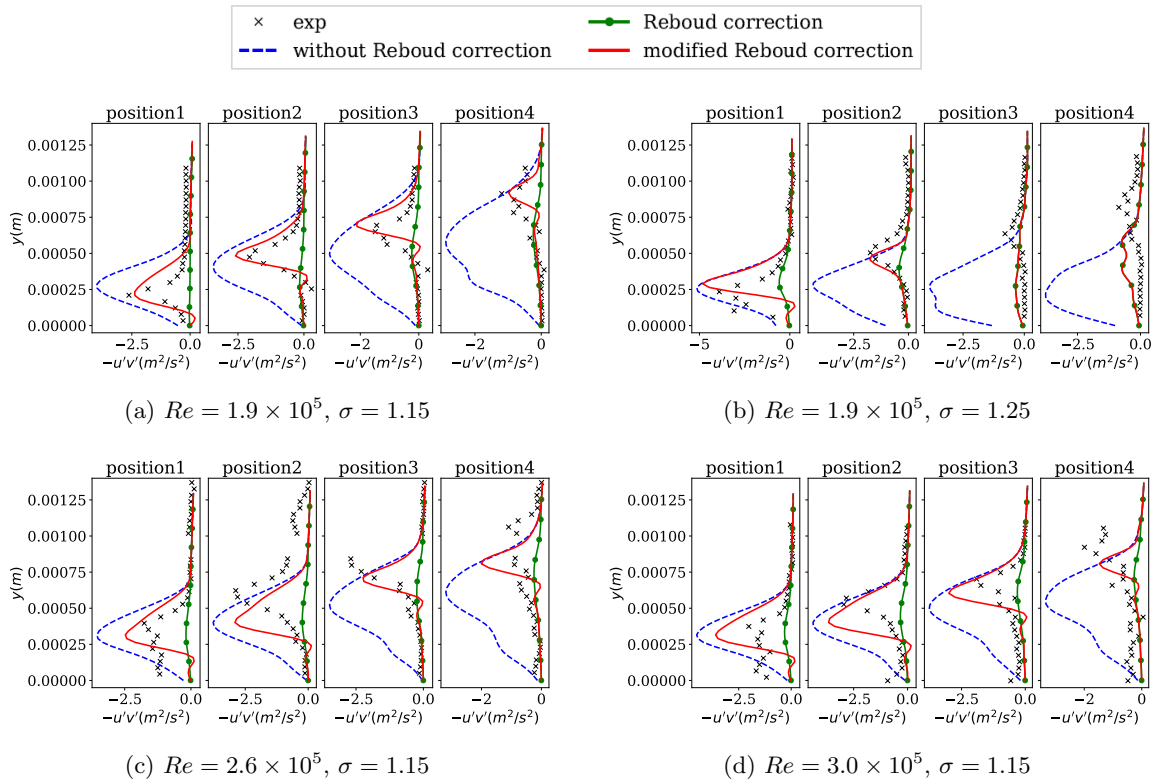


Figure 6.18: Numerical comparison of the modified Rebound correction with experiment and original Rebound correction in Reynolds shear stress.

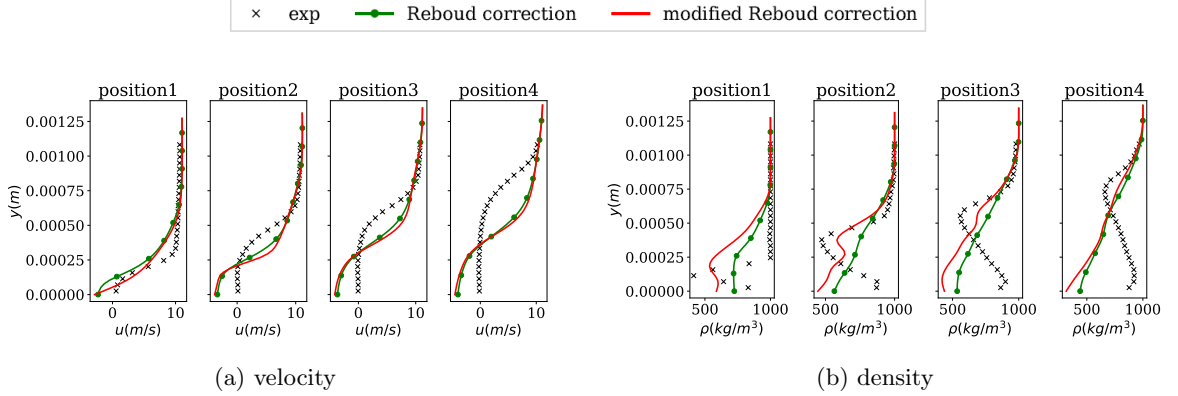


Figure 6.19: Comparison in velocity and density with modified Reboud correction and original Reboud correction.

has been demonstrated that the 3D simulation with LES model and same cavitation model can perform remarkably well for cloud cavitation [57], and the 3D simulation is essential to capture the cavitation–vortex interaction [74] and provide accurate shape of shedding cavitation [139]. Also, the present cavitation model is not sufficiently accurate to model the phase changes, which may result in the underestimation of density near the wall. Specifically, in the experiment, the cavity in the downstream (i.e., position 3 and position 4) is detached from the wall, and the liquid occupy the regime below the cavity. While in the simulation, the cavitation detachment at the near downstream is not captured. Moreover, the RANS equation is coupled with cavitation model in terms of the mixture density. From the RANS equation, the too low mixture density near the wall will overestimate the effects of the adverse pressure gradient near the wall. That may be responsible for the significant reverse velocity in the numerical simulation. The discrepancy in pressure term may be dominant in the RANS model, and the improvement in Reynolds stress is negligible. Further investigation need be conducted to consider both the RANS model and cavitation model. At last, it may be due to the ill-conditioned RANS equations. [145] That is, the small errors in the Reynolds stress can lead to large discrepancy in the velocity.

## 6.6 Conclusion

In this work, we investigate numerically the effects of cavitation on the turbulent quantities, i.e., turbulent kinetic energy and Reynolds shear stress, by comparing with the reliable X-ray experimental data. The numerical results with  $k-\omega$  SST and SST-SAS model indicate that Reboud correction can improve the results near the wall. While it approaches to the area away from wall, the Reboud correction will deteriorate the prediction. This is possibly due to the inaccurate predicted cavity shape, which leads to that the Reboud correction reduce the Reynolds stress dramatically in all the cavity region. Moreover,  $k-\omega$  SST based models

adopt the Bradshaw assumption in the boundary layer, while cavity can enlarge the boundary layer and this effect is not considered in the current model. To this end, we give an empirical estimation on the boundary layer thickness in cavitating flows. Based on that, we proposed a model to adjust the empirical exponent  $n$  in the Reboud correction. That is, to active the eddy viscosity correction, it has to be within not only the cavity but also the estimated boundary layer. The validations with experimental data and numerical test both show that the modified model can have a good agreement with experimental data in the Reynolds shear stress.

However, the velocity and density with the modified eddy viscosity model is not improved. That may be due to the inaccurate mixture density by cavitation model. In future investigations, further validations will be conducted with latest X-ray experimental data. Also, the data-driven approach, such as data assimilation, will be applied to reduce the data mismatch by inferring optimal model corrections in both turbulence model and cavitation model from experimental data.



## Chapter 7

# Conclusions and Perspectives

### 7.1 Conclusions

Cavitating flows are multiphase flow typically with adverse pressure gradient, large density gradient, flow separation and recirculation. While it is well known that the current RANS models cannot handle the flow with these characteristics. That will significantly affect the predictive performance of RANS methods for cavitation simulations. To this end, the present work intends to optimize the RANS models to better predict the flow with separation and adverse pressure gradient, and ultimately improve the prediction for cavitating flows.

The data assimilation technique has been widely used for state estimation, inverse problem, and so on. In this work, we explore to adopt this approach to optimize the RANS modelling. We first give a brief review of the existing data assimilation techniques with emphasis on the used methods in this work. In Section 3, a hybrid data assimilation method, namely the ensemble-based variational method, is applied to CFD simulation in the convergent-divergent channel with the attempt of introducing the DA method into cavitating flows. The prediction results are improved through inferring optimal inlet velocity and underlying model corrections. However, the inferred fields of model corrections are not accurate and physical, i.e., with large departure from the original value and high oscillation, due to the ill-posedness of the inverse problem. Moreover, the EnVar method only concerns the posterior mean, and the uncertainty of the inferred value cannot be quantified. To address these issues, in the following two sections, the ill-posedness and uncertainty quantification with ensemble-based DA methods are further investigated. In Section 4, we propose a novel data assimilation method with regularization for the field inversion problem. It is derived based on the conventional ensemble Kalman filter (EnKF) method, and we test this novel method in three cases which cannot be tackled by the conventional method. The results show the remarkable improvement for the inference results and demonstrate the outperformance of the proposed method comparing to the standard EnKF. In Section 5, three ensemble-based data assimilation methods, namely ensemble Kalman filter, ensemble randomized maximal likelihood, and ensemble Kalman filter–multiple data

assimilation, are evaluated for the uncertainty quantification problem from an optimization viewpoint. These methods are applied to quantify the uncertainty of quantities of interest (i.e., velocity) through perturbing the Reynolds stress. The simulation results suggest that the EnRML method performs best to quantify the uncertainty due to its high efficiency and satisfactory performance.

In the aforementioned sections, we investigate the applicability of the data assimilation technique mainly for the non-cavitating turbulent flows. In Section 6, for the cavitating flow, we conduct the numerical investigation with different existing turbulence models, including  $k-\omega$  SST and SST-SAS, with the comparison of the experimental data. Based on the simulation results and experimental measurements, we propose a modification on the empirical parameter  $n$  in the Reboud correction. The results show that the modified correction can take into account the effects of compressibility on the boundary layer and provide accurate results in the Reynolds shear stress, compared to experimental data.

## 7.2 Perspectives

Cavitation is a very complicated phenomenon, where conventional physical modeling is challenging to capture the dynamic behaviors accurately. Data-driven approach based on data assimilation and machine learning, is promising to make a way to extract the underlying model information directly from experimental measurements, and thus gain physical insights into the cavitation process. For future investigations, we envision that the data-driven approaches, including data assimilation and machine learning, can be introduced into cavitation problems to assist the modeling of both turbulence and cavitation. Generally, we can use the data assimilation method to extract the model information from data, e.g., to infer the latent field concerning the Reynolds stress. Further, the machine learning technique can be utilized to construct predictive models for the inferred quantities of interest to augment the turbulence modeling. The schematic diagram can be illustrated as in Fig. 7.1.

The current studies discussed the issue of ill-posedness and uncertainty quantification we encountered when applying the DA technique into the reconstruction of the steady non-cavitating flows. The proposed regularised ensemble Kalman method can well remove the ill-posedness of the inverse problem, and the ensemble randomized maximum likelihood (EnRML) method and ensemble Kalman filter with multiple data assimilation (EnKF-MDA) are suggested for the UQ in CFD applications. To further improve the data assimilation scheme, it is feasible to deduce the regularized EnRML method or EnKF-MDA, thus to address the ill-posedness and uncertainty quantification simultaneously in the near future.

On the other hand, the present work about the data assimilation mainly focuses on the steady case. As the cavitation is a typical dynamic problem, the applicability of data assimilation for cavitation problems warrants further investigations. First, uncertainty sources in cavitation



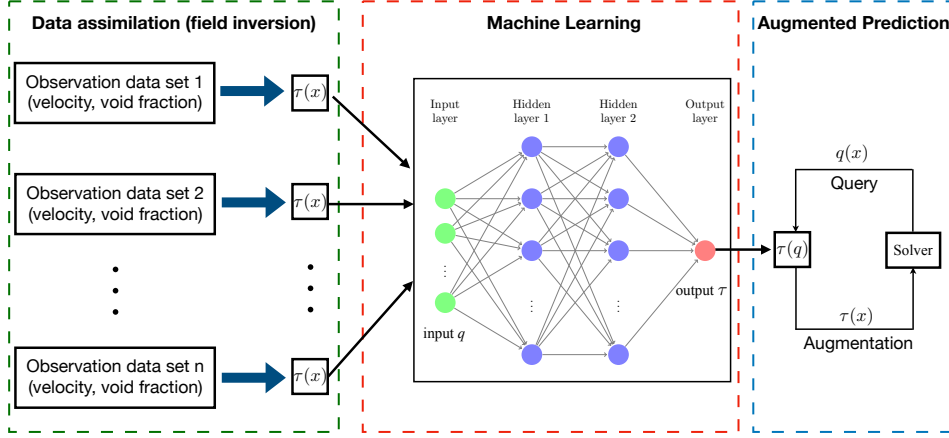


Figure 7.1: The schematic diagram of data-driven modeling with data assimilation and machine learning

simulations have at least two aspects: one is the Reynolds stress in the RANS model, and another one is the mass transfer source term in the cavitation model. The Reynolds stress discrepancy can be decomposed into several scalar fields to represent the magnitude, shape, and orientation of the stress tensor, as in Section 5. Also, it can be represented under the linear eddy viscosity assumption. Specifically, we can quantify the uncertainty in the eddy viscosity as in Section 4 or infer the auxiliary model source terms in the constitutive transport equation as in Section 3. Besides, considering the computational cost, we can start from 2D simulation to investigate the applicability of data-driven method into the cavitating flow. Even though the 2D simulations have some limitations to capture the cavitation behavior, it is still meaningful to produce a better model for the 2D scenario which can provide satisfactory predictions at a low computational cost.

Moreover, we can determine the optimal empirical model parameters in current turbulence models. As for the mass transfer source term in the cavitation model, we can also use data assimilation to infer the optimal model parameters in the cavitation models based on the experimental data in void fraction and velocity. On the other hand, with the reliable high-fidelity X-ray transient experimental data, we can obtain phase-averaged data and directly construct the mass transfer source term based on the void fraction transport equation. Once the uncertainty term is inferred through the data assimilation or constructed from the experimental data, machine learning can be leveraged to build a mapping from the different flow conditions to the inferred model uncertain terms, which can also contain the information about the dynamics. The input feature for machine learning can include the Reynolds number, cavitation number, turbulence kinetic energy, Reynolds stress, vorticity, mean strain rate, void fraction gradient, and so on. In addition, the selection of these input feature is critical to obtain an efficient machine learning framework, and unsupervised learning can be leveraged to optimize the feature selections. [16, 105]

Aside from the data-driven modeling for the cavitating flow, it is also worthy of future investigations to gain further physical insights into cavitation-turbulence interaction. In Section 6, we consider the effects of the cavitation on the boundary layer and make specific modification on the current RANS model to improve the prediction on the Reynolds shear stress. However, the results in velocity and void fraction are not greatly improved, most likely due to the inaccurate prediction on void fraction. Hence, given that the strong correlation between turbulence and cavitation, it is necessary first to apply other advanced cavitation model to have a good prediction on the cavity shape, and then improve cavitation and turbulence model simultaneously in the future investigations.

## Appendix A

# Comparison of optimization methods and test case in Venturi with EnVar method

### A.1 Comparison between BFGS and Newton-CG

In the framework of ensemble-based variational method as presented in Chapter 3, the performance of the minimization method BFGS and Newton-CG is compared in the case of inlet velocity inference for Bump geometry. Figure A.1 presents the evolution of cost function  $J$  to the iteration with different prior inlet velocity (parabolic or flat velocity profile). Even though both methods can result in a similar reduction in cost function after 16 iterations for the case with parabolic inlet velocity, Newton CG is faster and more robust compared to BFGS. And for the case with flat one, the BFGS method cannot reach similar results as Newton-CG within 30 iterations.

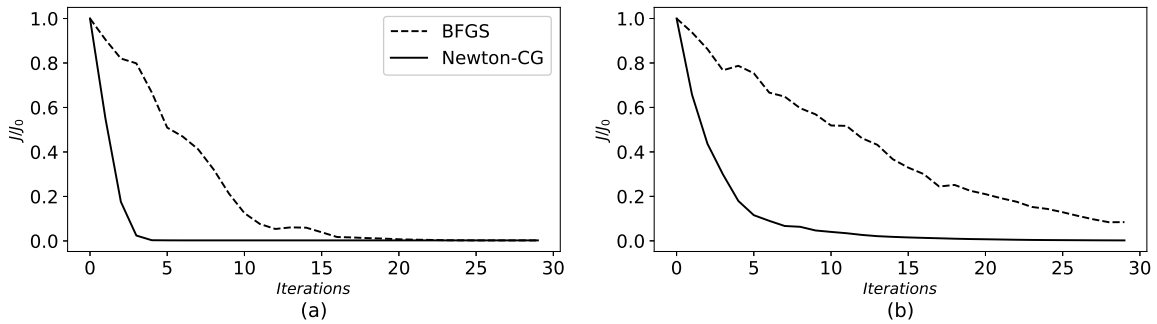


Figure A.1: evolution of cost function between BFGS and Newton-CG. left: with parabolic inlet velocity; right: with flat inlet velocity

Figure A.2 presents the inference of the inlet velocity and the predictions in  $C_f$  accordingly. Comparing to the results with Newton CG presented in Chapter 3, it is apparent that the eventually inferred velocity with Newton CG has a better agreement with DNS especially in the case with the flat velocity.

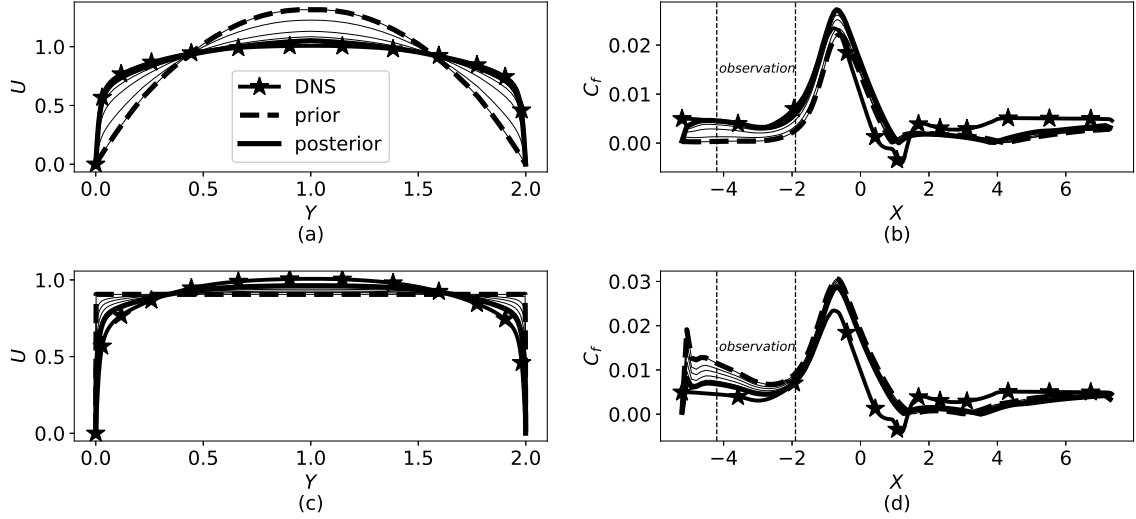


Figure A.2: Results in inference of inlet velocity and prediction in  $C_f$  : (a) (b) for prior parabolic velocity; (c) (d) for prior flat velocity

## A.2 Test case of inlet velocity inference in Venturi

We conducted a test case to infer inlet velocity in Venturi-type section. The input parameters are the inlet velocity at the first 30 grids adjacent to the bottom wall. The prior is given as the parabolic curve. The results are shown in Figure A.3.

It can be seen that the cost function cannot be further reduced after three iterations and the inferred velocity get almost stagnant, which concludes that the velocity at the region near the throat of Venturi is not sensitive to the inlet velocity especially to the velocity near the wall.

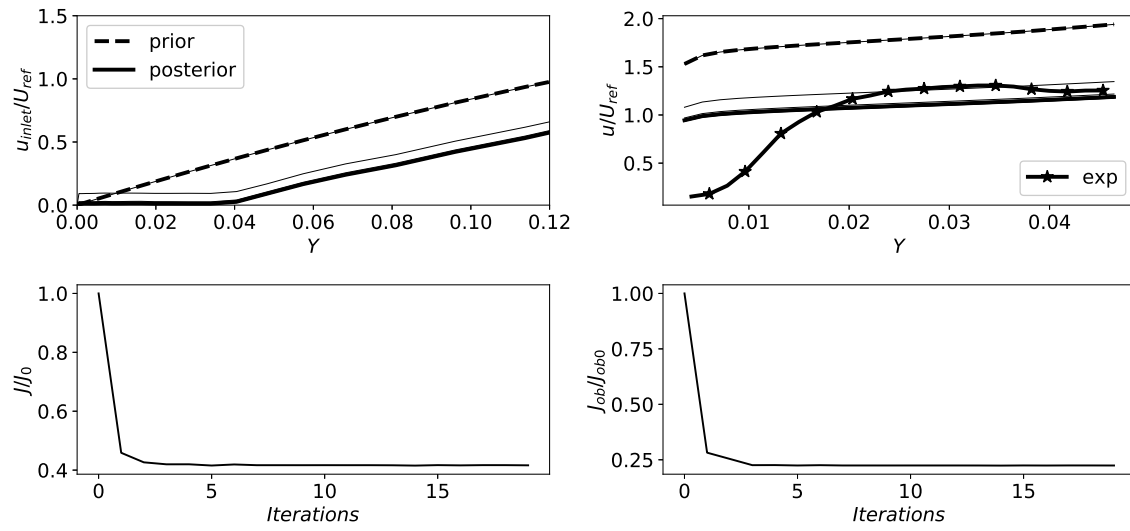


Figure A.3: Data assimilation results to infer the inlet velocity in Venturi



## Appendix B

# Derivation of REnKF and sensitivity study of algorithmic parameters

### B.1 Derivation of regularized ensemble Kalman method

The detailed derivation of the regularized ensemble Kalman method is presented here. The cost function with regularization term can be formulated as:

$$(B.1) \quad J[\mathbf{x}_j^a] = (\mathbf{x}_j^a - \mathbf{x}_j^f)^\top \mathbf{P}^{-1}(\mathbf{x}_j^a - \mathbf{x}_j^f) + (\mathcal{H}[\mathbf{x}_j^a] - \mathbf{y}_j)^\top \mathbf{R}^{-1}(\mathcal{H}[\mathbf{x}_j^a] - \mathbf{y}_j) + \lambda(\mathcal{G}[\mathbf{x}_j^a]^\top \mathbf{W}\mathcal{G}[\mathbf{x}_j^a])$$

The gradient of the cost function can be derived as:

$$(B.2) \quad \frac{\partial J[\mathbf{x}_j^a]}{\partial \mathbf{x}_j^a} = \mathbf{P}^{-1}(\mathbf{x}_j^a - \mathbf{x}_j^f) + (\mathcal{H}'[\mathbf{x}_j^a])^\top \mathbf{R}^{-1}(\mathcal{H}[\mathbf{x}_j^a] - \mathbf{y}_j) + \lambda(\mathcal{G}'[\mathbf{x}_j^a])^\top \mathbf{W}\mathcal{G}[\mathbf{x}_j^a]$$

To minimize the cost function, we set the gradient (B.2) to be zero, and have:

$$(B.3) \quad \mathbf{P}^{-1}(\mathbf{x}_j^a - \mathbf{x}_j^f) + (\mathcal{H}'[\mathbf{x}_j^a])^\top \mathbf{R}^{-1}(\mathcal{H}[\mathbf{x}_j^a] - \mathbf{y}_j) + \lambda(\mathcal{G}'[\mathbf{x}_j^a])^\top \mathbf{W}\mathcal{G}[\mathbf{x}_j^a] = 0$$

The unknown terms  $\mathcal{H}[\mathbf{x}_j^a]$  and  $\mathcal{H}'[\mathbf{x}_j^a]$  are estimated via linearization as:

$$(B.4a) \quad \mathcal{H}[\mathbf{x}_j^a] \approx \mathcal{H}[\mathbf{x}_j^f] + \mathcal{H}'[\mathbf{x}_j^f](\mathbf{x}_j^a - \mathbf{x}_j^f),$$

$$(B.4b) \quad \mathcal{H}'[\mathbf{x}_j^a] \approx \mathcal{H}'[\mathbf{x}_j^f],$$

respectively. With the linearization assumption, we can reformulate the equation (B.3) as:

$$(B.5a) \quad \mathbf{P}^{-1}(\mathbf{x}_j^a - \mathbf{x}_j^f) = -(\mathcal{H}'[\mathbf{x}_j^f])^\top \mathbf{R}^{-1}(\mathcal{H}[\mathbf{x}_j^f] + \mathcal{H}'[\mathbf{x}_j^f](\mathbf{x}_j^a - \mathbf{x}_j^f) - \mathbf{y}_j) - \lambda(\mathcal{G}'[\mathbf{x}_j^f])^\top \mathbf{W}\mathcal{G}[\mathbf{x}_j^f]$$

Similarly, we introduce linearization to the constraint term as:

$$(B.6) \quad \mathcal{G}[\mathbf{x}_j^f] \approx \mathcal{G}[\mathbf{x}_j^a] \quad \text{and} \quad \mathcal{G}'[\mathbf{x}_j^f] \approx \mathcal{G}'[\mathbf{x}_j^a].$$

Note that we consider a convergence condition for  $\mathcal{G}[\mathbf{x}_j^a]$  for simplification. Furthermore, we introduce the tangent linear operator  $\mathbf{H}$  so that  $\mathcal{H}[\mathbf{x}] = \mathbf{H}\mathbf{x}$  and  $\mathcal{H}'[\mathbf{x}] = \mathbf{H}$ . Thus (B.5a) can be formulated and rearranged as:

$$(B.7a) \quad \mathbf{P}^{-1}(\mathbf{x}_j^a - \mathbf{x}_j^f) + \mathbf{H}^\top \mathbf{R}^{-1}(\mathbf{H}\mathbf{x}_j^f + \mathbf{H}(\mathbf{x}_j^a - \mathbf{x}_j^f) - \mathbf{y}_j) + \lambda(\mathcal{G}')^\top \mathbf{W}\mathcal{G}[\mathbf{x}_j^f] = 0$$

$$(B.7b) \quad \mathbf{x}_j^a = \mathbf{x}_j^f + \mathbf{P}(I + \mathbf{H}^\top \mathbf{R}^{-1} \mathbf{H} \mathbf{P})^{-1} \mathbf{H}^\top \mathbf{R}^{-1}(\mathbf{y}_j - \mathbf{H}\mathbf{x}_j^f) - \mathbf{P}(I + \mathbf{H}^\top \mathbf{R}^{-1} \mathbf{H} \mathbf{P})^{-1} \lambda(\mathcal{G}')^\top \mathbf{W}\mathcal{G},$$

where the argument  $\mathbf{x}_j^f$  of function  $\mathcal{G}$  and its derivative  $\mathcal{G}'$  are omitted for brevity of notation. Consider the following equation:

$$(B.8) \quad \mathbf{H}^\top (I + \mathbf{R}^{-1} \mathbf{H} \mathbf{P} \mathbf{H}^\top) = (I + \mathbf{H}^\top \mathbf{R}^{-1} \mathbf{H} \mathbf{P}) \mathbf{H}^\top.$$

Based on that, taking the left multiplication  $(I + \mathbf{H}^\top \mathbf{R}^{-1} \mathbf{H} \mathbf{P})^{-1}$  and right multiplication  $(I + \mathbf{R}^{-1} \mathbf{H} \mathbf{P} \mathbf{H}^\top)^{-1}$  for both sides, we can obtain:

$$(B.9) \quad (I + \mathbf{H}^\top \mathbf{R}^{-1} \mathbf{H} \mathbf{P})^{-1} \mathbf{H}^\top = \mathbf{H}^\top (I + \mathbf{R}^{-1} \mathbf{H} \mathbf{P} \mathbf{H}^\top)^{-1}.$$

By substituting  $(I + \mathbf{H}^\top \mathbf{R}^{-1} \mathbf{H} \mathbf{P})^{-1} \mathbf{H}^\top$  in (B.7b) with  $\mathbf{H}^\top (I + \mathbf{R}^{-1} \mathbf{H} \mathbf{P} \mathbf{H}^\top)^{-1}$  based on Eq. (B.9), we can derive:

$$(B.10a) \quad \mathbf{x}_j^a = \mathbf{x}_j^f + \mathbf{P}(I + \mathbf{H}^\top \mathbf{R}^{-1} \mathbf{H} \mathbf{P})^{-1} \mathbf{H}^\top \mathbf{R}^{-1}(\mathbf{y}_j - \mathbf{H}\mathbf{x}_j^f) - \mathbf{P}(I + \mathbf{H}^\top \mathbf{R}^{-1} \mathbf{H} \mathbf{P})^{-1} \lambda(\mathcal{G}')^\top \mathbf{W}\mathcal{G}$$

$$(B.10b) \quad = \mathbf{x}_j^f + \mathbf{P} \mathbf{H}^\top (I + \mathbf{R}^{-1} \mathbf{H} \mathbf{P} \mathbf{H}^\top)^{-1} \mathbf{R}^{-1}(\mathbf{y}_j - \mathbf{H}\mathbf{x}_j^f) - \mathbf{P}(I + \mathbf{H}^\top \mathbf{R}^{-1} \mathbf{H} \mathbf{P})^{-1} \lambda(\mathcal{G}')^\top \mathbf{W}\mathcal{G}$$

$$(B.10c) \quad = \mathbf{x}_j^f + \mathbf{P} \mathbf{H}^\top (\mathbf{R} + \mathbf{H} \mathbf{P} \mathbf{H}^\top)^{-1} (\mathbf{y}_j - \mathbf{H}\mathbf{x}_j^f) - \mathbf{P}(I + \mathbf{H}^\top \mathbf{R}^{-1} \mathbf{H} \mathbf{P})^{-1} \lambda(\mathcal{G}')^\top \mathbf{W}\mathcal{G}.$$

Finally, expand  $(I + \mathbf{H}^\top \mathbf{R}^{-1} \mathbf{H} \mathbf{P})^{-1}$  in the last term of Eq.(B.10c) with the Woodbury formula [63] as:

$$(B.11) \quad (I + \mathbf{H}^\top \mathbf{R}^{-1} \mathbf{H} \mathbf{P})^{-1} = I - \mathbf{H}^\top (\mathbf{R} + \mathbf{H} \mathbf{P} \mathbf{H}^\top)^{-1} \mathbf{H} \mathbf{P}.$$

By substituting Eq. (B.11) into Eq. (B.10c), we have:

$$(B.12) \quad \mathbf{x}_j^a = \mathbf{x}_j^f + \mathbf{P} \mathbf{H}^\top (\mathbf{R} + \mathbf{H} \mathbf{P} \mathbf{H}^\top)^{-1} (\mathbf{y}_j - \mathbf{H}\mathbf{x}_j^f) - \lambda \mathbf{P} \mathcal{G}'^\top \mathbf{W}\mathcal{G} + \mathbf{P} \mathbf{H}^\top (\mathbf{R} + \mathbf{H} \mathbf{P} \mathbf{H}^\top)^{-1} \mathbf{H} \mathbf{P} \lambda \mathcal{G}'^\top \mathbf{W}\mathcal{G}.$$

Furthermore, combine the second and last term in the right hand side of Eq. (B.12), and we can deduce the regularized analysis scheme as:

$$(B.13) \quad \mathbf{x}_j^a = \mathbf{x}_j^f + \mathbf{P} \mathbf{H}^\top (\mathbf{R} + \mathbf{H} \mathbf{P} \mathbf{H}^\top)^{-1} (\mathbf{y}_j - \mathbf{H}\mathbf{x}_j^f + \lambda \mathbf{H} \mathbf{P} \mathcal{G}'^\top \mathbf{W}\mathcal{G}) - \lambda \mathbf{P} \mathcal{G}'^\top \mathbf{W}\mathcal{G}.$$

By further denoting Kalman gain  $\mathbf{K}$  and the correction  $\delta$  by the following:

$$(B.14) \quad \mathbf{K} = \mathbf{P} \mathbf{H}^\top (\mathbf{R} + \mathbf{H} \mathbf{P} \mathbf{H}^\top)^{-1},$$

$$(B.15) \quad \delta = -\lambda \mathbf{P} \mathcal{G}'^\top \mathbf{W}\mathcal{G},$$

the final analysis scheme for the regularized ensemble Kalman method reads:

$$(B.16) \quad \mathbf{x}_j^a = \mathbf{x}_j^f + \delta + \mathbf{K}(\mathbf{y}_j - \mathbf{H}(\mathbf{x}_j^f + \delta))$$



## B.2 Sensitivity studies of algorithmic parameters in regularization

As implemented in Chapter 4 the regularization parameter  $\lambda$  has three hyper-parameters:  $\chi_0$ ,  $S$ , and  $d$ . We take  $\chi_0 = 0.1$ ,  $S = 5$ , and  $d = 2$  as reference and investigate the effects of different  $\chi_0$ ,  $S$ , and  $d$ , respectively. The inferred parameters with different tunable parameters ( $\chi_0$ ,  $S$ , and  $d$ ) for an equality constraint are shown in Table B.1. It can be seen that with an equality constraint, the proposed method is robust, and there is a large range of hyper-parameters that result in good inference.

Table B.1: Summary of inferred parameter  $\omega$  with different  $\chi_0$ ,  $S$ , and  $d$  for the equality constraint (Case C1) in the parameter estimation problem. The values in bold indicate the reference.

parameter	value	prior $(-2, -2)$	prior $(0, 0)$	prior $(2, 2)$
$\chi_0$	0.01	(0.86, 1.07)	(0.81, 1.14)	(0.93, 1.04)
	<b>0.1</b>	(1.06, 0.93)	(1.06, 0.93)	(1.02, 0.98)
	0.5	(0.94, 1.05)	(0.94, 1.05)	(0.98, 1.00)
	1.0	(1.05, 0.94)	(0.94, 1.06)	(1.02, 0.98)
$S$	1	(0.92, 1.08)	(1.07, 0.92)	(0.98, 1.02)
	<b>5</b>	(1.06, 0.93)	(1.06, 0.93)	(1.02, 0.98)
	20	(1.09, 0.90)	(1.07, 0.92)	(1.04, 0.94)
	50	(0.86, 1.13)	(0.91, 1.08)	(1.05, 0.94)
$d$	0.1	(1.08, 0.91)	(1.07, 0.92)	(1.01, 0.98)
	<b>2</b>	(1.06, 0.93)	(1.06, 0.93)	(1.02, 0.98)
	10	(1.09, 0.90)	(1.08, 0.91)	(1.00, 0.98)
	50	(1.10, 0.89)	(0.91, 1.08)	(1.02, 0.98)

However, with inequality constraints the method is not as robust as with equality constraints. The results are shown in Table B.2. With an inequality constraint, the method is more sensitive to these hyper-parameters. If the inequality constraint overcorrects the inferred parameters and then turns off, this can lead to the inference diverging.

Table B.2: Summary of inferred parameter  $\omega$  with different  $\chi_0$ ,  $S$ , and  $d$  for the inequality constraint (Case C2) in the parameter estimation problem. The values in bold indicate the reference.

parameter	value	prior $(-2, -2)$	prior $(0, 0)$	prior $(2, 2)$
$\chi_0$	0.01	(0.07, 0.07)	(0.91, 0.96)	(0.95, 0.96)
	<b>0.1</b>	(1.07, 1.03)	(0.96, 0.98)	(0.94, 0.96)
	0.5	(0.83, 0.98)	(1.07, 0.94)	(0.94, 0.94)
	1.0	Diverge	Diverge	Diverge
$S$	1	Diverge	(1.07, 0.92)	(0.95, 0.96)
	<b>5</b>	(1.07, 1.03)	(0.96, 0.98)	(0.94, 0.96)
	20	(0.31, 0.31)	(0.87, 1.07)	(0.95, 0.93)
	50	(0.29, 0.29)	(1.00, 0.96)	(0.95, 0.96)
$d$	0.1	(0.19, 0.19)	Diverge	(0.94, 0.95)
	<b>2</b>	(1.07, 1.03)	(0.96, 0.98)	(0.94, 0.96)
	10	Diverge	(0.99, 0.93)	(0.97, 0.95)
	50	(1.01, 0.87)	(0.96, 1.04)	(0.96, 0.94)

## Appendix C

# Derivation of EnKF and EnRML

### C.1 Derivation of EnKF

The cost function and its gradient for the iterative EnKF are formulated as:

$$(C.1a) \quad J = \frac{1}{2} \left( \mathbf{x}_{i,j}^a - \mathbf{x}_{i,j}^f \right)^\top \mathbf{P}_i^{-1} \left( \mathbf{x}_{i,j}^a - \mathbf{x}_{i,j}^f \right) + \frac{1}{2} \left( \mathcal{H}[\mathbf{x}_{i,j}^a] - \mathbf{y} \right)^\top \mathbf{R}^{-1} \left( \mathcal{H}[\mathbf{x}_{i,j}^a] - \mathbf{y} \right),$$

$$(C.1b) \quad \frac{\partial J}{\partial \mathbf{x}_{i,j}^a} = \mathbf{P}_i^{-1} \left( \mathbf{x}_{i,j}^a - \mathbf{x}_{i,j}^f \right) + \mathcal{H}'[\mathbf{x}_{i,j}^a]^\top \mathbf{R}^{-1} \left( \mathcal{H}[\mathbf{x}_{i,j}^a] - \mathbf{y}_j \right).$$

We approximate the unknown terms  $\mathcal{H}[\mathbf{x}^a]$  and  $\mathcal{H}'[\mathbf{x}^a]$  in Eq. (C.1b) with the linear assumption as:

$$(C.2a) \quad \mathcal{H}[\mathbf{x}_j^a] \approx \mathcal{H}[\mathbf{x}_j^f] + \mathcal{H}'[\mathbf{x}_j^a] \left( \mathbf{x}_j^a - \mathbf{x}_j^f \right),$$

$$(C.2b) \quad \mathcal{H}'[\mathbf{x}_j^a] \approx \mathcal{H}'[\mathbf{x}_j^f] + \mathcal{H}''[\mathbf{x}_j^f] \left( \mathbf{x}_j^a - \mathbf{x}_j^f \right),$$

where the second derivation can be neglected. Further, we set the gradient of the cost function to be zero and substitute with Eq. (C.2) as:

$$(C.3) \quad \mathbf{P}_i^{-1} \left( \mathbf{x}_{i,j}^a - \mathbf{x}_{i,j}^f \right) = -\mathcal{H}'[\mathbf{x}_{i,j}^f]^\top \mathbf{R}^{-1} \left( \mathcal{H}[\mathbf{x}_{i,j}^f] + \mathcal{H}'[\mathbf{x}_{i,j}^f] \left( \mathbf{x}_{i,j}^a - \mathbf{x}_{i,j}^f \right) - \mathbf{y}_j \right).$$

We expand  $\mathcal{H}[\mathbf{x}]$  around the ensemble mean as:

$$(C.4a) \quad \mathcal{H}[\mathbf{x}_j^f] \approx \mathcal{H}[\bar{\mathbf{X}}^f] + \mathcal{H}'[\mathbf{x}_j^f] \left( \mathbf{x}_j^f - \bar{\mathbf{X}}^f \right).$$

Afterwards, we assume that  $\mathcal{H}[\mathbf{x}] = \mathbf{H}\mathbf{x}$ , where  $\mathbf{H}$  is the tangent linear operator. The model function gradient  $\mathcal{H}'[\mathbf{x}^f]$  can be estimated directly with the linear operator  $\mathbf{H}$  based on Eq. C.4. Hence, Eq. (C.3) can be formulated and rearranged as:

$$(C.5a) \quad \mathbf{P}_i^{-1} \left( \mathbf{x}_{i,j}^a - \mathbf{x}_{i,j}^f \right) = -\mathbf{H}^\top \mathbf{R}^{-1} \left( \mathbf{H}\mathbf{x}_{i,j}^f + \mathbf{H}(\mathbf{x}_{i,j}^a - \mathbf{x}_{i,j}^f) - \mathbf{y}_j \right),$$

$$(C.5b) \quad \mathbf{x}_{i,j}^a = \mathbf{x}_{i,j}^f + \mathbf{P}_i \left( \mathbf{I} + \mathbf{H}^\top \mathbf{R}^{-1} \mathbf{H} \mathbf{P}_i \right)^{-1} \mathbf{H}^\top \mathbf{R}^{-1} \left( \mathbf{y}_j - \mathbf{H}\mathbf{x}_{i,j}^f \right).$$

Set  $Q = R^{-1}HP_i$  and we have:

$$(C.6a) \quad H^\top (I + QH^\top) = (I + H^\top Q) H^\top,$$

$$(C.6b) \quad (I + H^\top Q)^{-1} H^\top = H^\top (I + QH^\top)^{-1}.$$

Now back to Eq. (C.5b), substituting  $(I + H^\top R^{-1}HP_i)^{-1}H^\top$  with  $H^\top (I + R^{-1}HP_i H^\top)^{-1}$  based on Eq. (C.6b), we can derive:

$$(C.7a) \quad \mathbf{x}_{i,j}^a = \mathbf{x}_{i,j}^f + P_i H^\top (I + R^{-1}HP_i H^\top)^{-1} R^{-1} (y_j - H\mathbf{x}_{i,j}^f),$$

$$(C.7b) \quad \mathbf{x}_{i,j}^a = \mathbf{x}_{i,j}^f + P_i H^\top (R + HP_i H^\top)^{-1} (y_j - H\mathbf{x}_{i,j}^f).$$

Eq. (C.7b) is the iterative formulation for the analysis step of the EnKF method.

## C.2 Derivation of EnRML

To derive the analysis scheme of ensemble randomized maximal likelihood method, we start from the gradient and Hessian of the cost function as:

$$(C.8a) \quad \frac{\partial J}{\partial \mathbf{x}_{i,j}} = P_0^{-1} (\mathbf{x}_{i,j} - \mathbf{x}_{0,j}) + \mathcal{H}'[\mathbf{x}_{i,j}]^\top R^{-1} (\mathcal{H}[\mathbf{x}_{i,j}] - y_j),$$

$$(C.8b) \quad \frac{\partial^2 J}{\partial \mathbf{x}_{i,j}^2} = P_0^{-1} + \mathcal{H}'[\mathbf{x}_{i,j}]^\top R^{-1} \mathcal{H}'[\mathbf{x}_{i,j}].$$

In the EnRML method, the state vector  $\mathbf{x}$  is updated with Gauss–Newton method as:

$$(C.9) \quad \mathbf{x}_{i,j}^a = \mathbf{x}_{i,j}^f - \gamma \left( \frac{\partial^2 J}{\partial \mathbf{x}_{i,j}^2} \right)^{-1} \frac{\partial J}{\partial \mathbf{x}_{i,j}}.$$

Through directly introducing the gradient and Hessian formulation into Eq. (C.9), we can have:

$$(C.10) \quad \begin{aligned} \mathbf{x}_{i,j}^a = & \mathbf{x}_{i,j}^f - \gamma \left( P_0^{-1} + \mathcal{H}'[\mathbf{x}_{i,j}^f]^\top R^{-1} \mathcal{H}'[\mathbf{x}_{i,j}^f] \right)^{-1} \left( P_0^{-1} (\mathbf{x}_{i,j}^f - \mathbf{x}_{0,j}^f) + \mathcal{H}'[\mathbf{x}_{i,j}^f]^\top R^{-1} (\mathcal{H}[\mathbf{x}_{i,j}^f] - y_j) \right), \\ & - \gamma \left( I + P_0 \mathcal{H}'[\mathbf{x}_{i,j}^f]^\top R^{-1} \mathcal{H}'[\mathbf{x}_{i,j}^f] \right)^{-1} \left( \mathbf{x}_{i,j}^f - \mathbf{x}_{0,j}^f + P_0 \mathcal{H}'[\mathbf{x}_{i,j}^f]^\top R^{-1} (\mathcal{H}[\mathbf{x}_{i,j}^f] - y_j) \right). \end{aligned}$$

By expanding the last term, we obtain:

$$(C.11) \quad \begin{aligned} \mathbf{x}_{i,j}^a = & \mathbf{x}_{i,j}^f - \gamma \left( I + P_0 \mathcal{H}'[\mathbf{x}_{i,j}^f]^\top R^{-1} \mathcal{H}'[\mathbf{x}_{i,j}^f] \right)^{-1} \left( \mathbf{x}_{i,j}^f - \mathbf{x}_{0,j}^f \right) \\ & - \gamma \left( I + P_0 \mathcal{H}'[\mathbf{x}_{i,j}^f]^\top R^{-1} \mathcal{H}'[\mathbf{x}_{i,j}^f] \right)^{-1} P_0 \mathcal{H}'[\mathbf{x}_{i,j}^f]^\top R^{-1} (\mathcal{H}[\mathbf{x}_{i,j}^f] - y_j). \end{aligned}$$

We can further derive from (C.11) via Woodbury formula as follows:

$$(C.12) \quad \begin{aligned} \mathbf{x}_{i,j}^a = & \mathbf{x}_{i,j}^f - \gamma \left( I - P_0 \mathcal{H}'[\mathbf{x}_{i,j}^f]^\top \left( R + \mathcal{H}'[\mathbf{x}_{i,j}^f] P_0 \mathcal{H}'[\mathbf{x}_{i,j}^f]^\top \right)^{-1} \mathcal{H}'[\mathbf{x}_{i,j}^f] \right) \left( \mathbf{x}_{i,j}^f - \mathbf{x}_{0,j}^f \right) \\ & - \gamma \left( I + P_0 \mathcal{H}'[\mathbf{x}_{i,j}^f]^\top R^{-1} \mathcal{H}'[\mathbf{x}_{i,j}^f] \right)^{-1} P_0 \mathcal{H}'[\mathbf{x}_{i,j}^f]^\top R^{-1} (\mathcal{H}[\mathbf{x}_{i,j}^f] - y_j). \end{aligned}$$

After expanding the second term at right hand and rearranging, we can have:

$$(C.13) \quad \begin{aligned} \mathbf{x}_{i,j}^a = & \gamma \mathbf{x}_{0,j}^f + (1 - \gamma) \mathbf{x}_{i,j}^f + \gamma \mathbf{P}_0 \mathcal{H}'[\mathbf{x}_{i,j}^f]^\top \left( \mathbf{R} + \mathcal{H}'[\mathbf{x}_{i,j}^f] \mathbf{P}_0 \mathcal{H}'[\mathbf{x}_{i,j}^f]^\top \right)^{-1} \mathcal{H}'[\mathbf{x}_{i,j}^f] \left( \mathbf{x}_{i,j}^f - \mathbf{x}_{0,j}^f \right) \\ & - \gamma \left( \mathbf{I} + \mathbf{P}_0 \mathcal{H}'[\mathbf{x}_{i,j}^f]^\top \mathbf{R}^{-1} \mathcal{H}'[\mathbf{x}_{i,j}^f] \right)^{-1} \mathbf{P}_0 \mathcal{H}'[\mathbf{x}_{i,j}^f]^\top \mathbf{R}^{-1} \left( \mathcal{H}[\mathbf{x}_{i,j}^f] - y_j \right) \end{aligned}$$

Set  $\mathbf{Q} = \mathbf{P}_0 \mathcal{H}'[\mathbf{x}]^\top$ , and we deduce:

$$(C.14a) \quad \mathbf{Q} \mathbf{R}^{-1} (\mathbf{R} + \mathcal{H}'[\mathbf{x}] \mathbf{Q}) = (\mathbf{I} + \mathbf{Q} \mathbf{R}^{-1} \mathcal{H}'[\mathbf{x}]) \mathbf{Q},$$

$$(C.14b) \quad (\mathbf{I} + \mathbf{Q} \mathbf{R}^{-1} \mathcal{H}'[\mathbf{x}])^{-1} \mathbf{Q} \mathbf{R}^{-1} = \mathbf{Q} (\mathbf{R} + \mathcal{H}'[\mathbf{x}] \mathbf{Q})^{-1}.$$

Finally, by substituting Eq. (C.14b) into Eq. (C.13), we can obtain the analysis step for the EnRML method as:

$$(C.15) \quad \mathbf{x}_{i,j}^a = \gamma \mathbf{x}_{0,j}^f + (1 - \gamma) \mathbf{x}_{i,j}^f - \gamma \mathbf{P}_0 \mathcal{H}'[\mathbf{x}_{i,j}^f]^\top \left( \mathbf{R} + \mathcal{H}'[\mathbf{x}_{i,j}^f]^\top \mathbf{P}_0 \mathcal{H}'[\mathbf{x}_{i,j}^f] \right)^{-1} \left( \mathcal{H}[\mathbf{x}_{i,j}^f] - y_j - \mathcal{H}'[\mathbf{x}_{i,j}^f] \left( \mathbf{x}_{i,j}^f - \mathbf{x}_{0,j}^f \right) \right).$$



# Appendix D

## List of publications

This chapter presents a list of journal publications and participations in international conferences related to the work presented in this thesis.

### Publications

- Xinlei Zhang, Thomas Gomez, and Olivier Coutier-Delgosha. Bayesian optimisation of RANS simulation with ensemble-based variational method in convergent-divergent channel. *Journal of Turbulence* (2019): 1-26. DOI: 10.1080/14685248.2019.1622016
- Xinlei Zhang, Carlos Michélen-Ströfer, Heng Xiao. Regularization of Ensemble Kalman Method for Inverse Problem. submitted, 2019. (arXiv:1910.01292)
- Xinlei Zhang, Heng Xiao, Thomas Gomez, Olivier Coutier-Delgosha, Evaluation of Iterative Ensemble Method for Quantifying Uncertainties in Steady Flow with Limited Ensemble Sizes. submitted, 2019.
- Carlos Michélen-Ströfer, Xinlei Zhang, Heng Xiao, Olivier Coutier-Delgosha. Enforcing Boundary Conditions on Latent Fields in Bayesian Inversion of PDE-Based Fields. submitted, 2019. (arXiv:1911.06683)

### Conference

- Xinlei Zhang, Olivier Coutier-Delgosha, Thomas Gomez, Heng Xiao. Bayesian optimization of RANS simulation with Ensemble based Variational method in convergent-divergent channel. *Bulletin of the American Physical Society*, Atlantic, USA, Nov 18-20, 2018.
- Xinlei Zhang, Thomas Gomez, Heng Xiao, Olivier Coutier-Delgosha. Optimization of cavitating flows simulation with data driven approach: from data assimilation to machine learning. *Proceedings of the 10th Symp. on Cavitation CAV2018*, Baltimore, USA, May 14-16, 2018.





# Bibliography

- [1] V. AESCHLIMANN, S. BARRE, AND H. DJERIDI, *Velocity field analysis in an experimental cavitating mixing layer*, Physics of Fluids, 23 (2011), p. 055105.
- [2] D. J. ALBERS, P.-A. BLANCQUART, M. E. LEVINE, E. E. SEYLABI, AND A. M. STUART, *Ensemble Kalman methods with constraints*, Inverse Problems, (2019).
- [3] J. L. ANDERSON, *An adaptive covariance inflation error correction algorithm for ensemble filters*, Tellus A: Dynamic Meteorology and Oceanography, 59 (2007), pp. 210–224.
- [4] M. ASCH, M. BOCQUET, AND M. NODÉ, *Data assimilation: methods, algorithms, and applications*, vol. 11, SIAM, 2016.
- [5] R. N. BANNISTER, *A review of forecast error covariance statistics in atmospheric variational data assimilation. I: Characteristics and measurements of forecast error covariances*, Quarterly Journal of the Royal Meteorological Society, 134 (2008), pp. 1951–1970.
- [6] S. BARRE, J. ROLLAND, G. BOITEL, E. GONCALVES, AND R. F. PATELLA, *Experiments and modeling of cavitating flows in venturi: attached sheet cavitation*, European Journal of Mechanics-B/Fluids, 28 (2009), pp. 444–464.
- [7] S. BENEDDINE, R. YEGAVIAN, D. SIPP, AND B. LECLAIRE, *Unsteady flow dynamics reconstruction from mean flow and point sensors: An experimental study*, Journal of Fluid Mechanics, 824 (2017), pp. 174–201.
- [8] R. T. BIEDRON, J.-R. CARLSON, J. M. DERLAGA, P. A. GNOFFO, D. P. HAMMOND, W. T. JONES, B. KLEB, E. M. LEE-RAUSCH, E. J. NIELSEN, M. A. PARK, ET AL., *FUN3D Manual: 13.5*, (2019).
- [9] M. BOCQUET, *Localization and the iterative ensemble Kalman smoother*, Quarterly Journal of the Royal Meteorological Society, 142 (2016), pp. 1075–1089.
- [10] M. BOCQUET AND P. SAKOV, *Combining inflation-free and iterative ensemble Kalman filters for strongly nonlinear systems*, Nonlinear Processes in Geophysics, 19 (2012), pp. 383–399.

- [11] —, *Joint state and parameter estimation with an iterative ensemble Kalman smoother*, Nonlinear Processes in Geophysics, 20 (2013), pp. 803–818.
- [12] —, *An iterative ensemble Kalman smoother*, Quarterly Journal of the Royal Meteorological Society, 140 (2014), pp. 1521–1535.
- [13] J. BORGGAARD, N. E. GLATT-HOLTZ, AND J. A. KROMETIS, *A Bayesian approach to estimating background flows from a passive scalar*, arXiv preprint arXiv:1808.01084, (2018).
- [14] M. BREUER, N. PELLER, C. RAPP, AND M. MANHART, *Flow over periodic hills—numerical and experimental study in a wide range of Reynolds numbers*, Computers & Fluids, 38 (2009), pp. 433–457.
- [15] G. BURGERS, P. JAN VAN LEEUWEN, AND G. EVENSEN, *Analysis scheme in the ensemble Kalman filter*, Monthly weather review, 126 (1998), pp. 1719–1724.
- [16] D. CAI, C. ZHANG, AND X. HE, *Unsupervised feature selection for multi-cluster data*, in Proceedings of the 16th ACM SIGKDD international conference on Knowledge discovery and data mining, ACM, 2010, pp. 333–342.
- [17] M. CALLENAERE, J.-P. FRANC, J.-M. MICHEL, AND M. RIONDET, *The cavitation instability induced by the development of a re-entrant jet*, Journal of Fluid Mechanics, 444 (2001), pp. 223–256.
- [18] B. CHARRIÈRE, J. DECAIX, AND E. GONCALVÈS, *A comparative study of cavitation models in a Venturi flow*, European Journal of Mechanics-B/Fluids, 49 (2015), pp. 287–297.
- [19] B. CHARRIÈRE AND E. GONCALVES, *Numerical investigation of periodic cavitation shedding in a Venturi*, International Journal of Heat and Fluid Flow, 64 (2017), pp. 41–54.
- [20] Y. CHEN AND D. S. OLIVER, *Ensemble randomized maximum likelihood method as an iterative ensemble smoother*, Mathematical Geosciences, 44 (2012), pp. 1–26.
- [21] Y. CHEN, D. S. OLIVER, ET AL., *History matching of the Norne full-field model with an iterative ensemble smoother*, SPE Reservoir Evaluation & Engineering, 17 (2014), pp. 244–256.
- [22] S. H. CHEUNG, T. A. OLIVER, E. E. PRUDENCIO, S. PRUDHOMME, AND R. D. MOSER, *Bayesian uncertainty analysis with applications to turbulence modeling*, Reliability Engineering & System Safety, 96 (2011), pp. 1137–1149.

- [23] C. COLBURN, J. CESSNA, AND T. BEWLEY, *State estimation in wall-bounded flow systems. Part 3. the ensemble Kalman filter*, Journal of Fluid Mechanics, 682 (2011), pp. 289–303.
- [24] P. COURTIER, E. ANDERSSON, W. HECKLEY, D. VASILJEVIC, M. HAMRUD, A. HOLLINGSWORTH, F. RABIER, M. FISHER, AND J. PAILLEUX, *The ECMWF implementation of three-dimensional variational assimilation (3D-Var). I: Formulation*, Quarterly Journal of the Royal Meteorological Society, 124 (1998), pp. 1783–1807.
- [25] P. COURTIER, J.-N. THÉPAUT, AND A. HOLLINGSWORTH, *A strategy for operational implementation of 4D-Var, using an incremental approach*, Quarterly Journal of the Royal Meteorological Society, 120 (1994), pp. 1367–1387.
- [26] O. COUTIER-DELGOSHA, R. FORTES-PATELLA, AND J. REBOUD, *Simulation of unsteady cavitation with a two-equation turbulence model including compressibility effects*, Journal of Turbulence, 3 (2002), pp. 58–65.
- [27] O. COUTIER-DELGOSHA, R. FORTES-PATELLA, AND J.-L. REBOUD, *Evaluation of the turbulence model influence on the numerical simulations of unsteady cavitation*, Journal of Fluids Engineering, 125 (2003), pp. 38–45.
- [28] O. COUTIER-DELGOSHA, R. FORTES-PATELLA, J.-L. REBOUD, N. HAKIMI, AND C. HIRSCH, *Numerical simulation of cavitating flow in 2D and 3D inducer geometries*, International Journal for Numerical Methods in Fluids, 48 (2005), pp. 135–167.
- [29] O. COUTIER-DELGOSHA, R. FORTES-PATELLA, J.-L. REBOUD, M. HOFMANN, AND B. STOFFEL, *Experimental and numerical studies in a centrifugal pump with two-dimensional curved blades in cavitating condition*, Journal of Fluids Engineering, 125 (2003), pp. 970–978.
- [30] O. COUTIER-DELGOSHA, J. REBOUD, AND Y. DELANNOY, *Numerical simulation of the unsteady behaviour of cavitating flows*, International journal for numerical methods in fluids, 42 (2003), pp. 527–548.
- [31] —, *Numerical simulation of the unsteady behaviour of cavitating flows*, International journal for numerical methods in fluids, 42 (2003), pp. 527–548.
- [32] O. COUTIER-DELGOSHA, B. STUTZ, A. VABRE, AND S. LEGOUPIL, *Analysis of cavitating flow structure by experimental and numerical investigations*, Journal of Fluid Mechanics, 578 (2007), pp. 171–222.
- [33] L. D’AGOSTINO AND M. V. SALVETTI, *Fluid dynamics of cavitation and cavitating turbopumps*, Springer Science & Business Media, 2008.

- [34] J. DECAIX AND E. GONCALVES, *Time-dependent simulation of cavitating flow with  $k$ - $l$  turbulence models*, International Journal for Numerical Methods in Fluids, 68 (2012), pp. 1053–1072.
- [35] ———, *Compressible effects modeling in turbulent cavitating flows*, European Journal of Mechanics-B/Fluids, 39 (2013), pp. 11–31.
- [36] N. DITTAKAVI, A. CHUNEKAR, AND S. FRANKEL, *Large eddy simulation of turbulent-cavitation interactions in a Venturi nozzle*, Journal of Fluids Engineering, 132 (2010), p. 121301.
- [37] E. DOW AND Q. WANG, *Quantification of structural uncertainties in the  $k$ - $\omega$  turbulence model*, in 52nd AIAA/ASME/ASCE/AHS/ASC Structures, Structural Dynamics and Materials Conference 19th AIAA/ASME/AHS Adaptive Structures Conference 13t, 2011, p. 1762.
- [38] T. D. ECONOMON, F. PALACIOS, S. R. COPELAND, T. W. LUKACZYK, AND J. J. ALONSO, *SU2: An open-source suite for multiphysics simulation and design*, AIAA Journal, 54 (2015), pp. 828–846.
- [39] W. EDELING, P. CINNELLA, AND R. P. DWIGHT, *Predictive RANS simulations via Bayesian model-scenario averaging*, Journal of Computational Physics, 275 (2014), pp. 65–91.
- [40] W. EDELING, P. CINNELLA, R. P. DWIGHT, AND H. BIJL, *Bayesian estimates of parameter variability in the  $k$ - $\epsilon$  turbulence model*, Journal of Computational Physics, 258 (2014), pp. 73–94.
- [41] W. EDELING, R. P. DWIGHT, AND P. CINNELLA, *Simplex-stochastic collocation method with improved scalability*, Journal of Computational Physics, 310 (2016), pp. 301–328.
- [42] W. N. EDELING, G. IACCARINO, AND P. CINNELLA, *Data-free and data-driven RANS predictions with quantified uncertainty*, Flow, Turbulence and Combustion, 100 (2018), pp. 593–616.
- [43] W. N. EDELING, M. SCHMELZER, R. P. DWIGHT, AND P. CINNELLA, *Bayesian predictions of Reynolds-averaged Navier–Stokes uncertainties using maximum a posteriori estimates*, AIAA Journal, 56 (2018), pp. 2018–2029.
- [44] A. A. EMERICK AND A. C. REYNOLDS, *Ensemble smoother with multiple data assimilation*, Computers & Geosciences, 55 (2013), pp. 3–15.
- [45] O. G. ERNST, B. SPRUNGK, AND H.-J. STARKLOFF, *Analysis of the ensemble and polynomial chaos Kalman filters in Bayesian inverse problems*, SIAM/ASA Journal on Uncertainty Quantification, 3 (2015), pp. 823–851.

- [46] G. EVENSEN, *Sequential data assimilation with a nonlinear quasi-geostrophic model using Monte Carlo methods to forecast error statistics*, Journal of Geophysical Research: Oceans, 99 (1994), pp. 10143–10162.
- [47] ———, *The ensemble Kalman filter: Theoretical formulation and practical implementation*, Ocean dynamics, 53 (2003), pp. 343–367.
- [48] ———, *Data assimilation: the ensemble Kalman filter*, Springer Science & Business Media, 2009.
- [49] ———, *Analysis of iterative ensemble smoothers for solving inverse problems*, Computational Geosciences, 22 (2018), pp. 885–908.
- [50] B. F. FARRELL AND P. J. IOANNOU, *State estimation using a reduced-order Kalman filter*, Journal of the Atmospheric Sciences, 58 (2001), pp. 3666–3680.
- [51] D. P. FOURES, N. DOVETTA, D. SIPP, AND P. J. SCHMID, *A data-assimilation method for Reynolds-averaged Navier–Stokes-driven mean flow reconstruction*, Journal of Fluid Mechanics, 759 (2014), pp. 404–431.
- [52] S. FRIKHA, O. COUTIER-DELGOSHA, AND J. A. ASTOLFI, *Influence of the cavitation model on the simulation of cloud cavitation on 2D foil section*, International Journal of Rotating Machinery, 2008 (2008).
- [53] P. GAUTHIER, M. TANGUAY, S. LAROCHE, S. PELLERIN, AND J. MORNEAU, *Extension of 3DVAR to 4DVAR: Implementation of 4DVAR at the meteorological service of Canada*, Monthly weather review, 135 (2007), pp. 2339–2354.
- [54] A. GEL, R. GARG, C. TONG, M. SHAHNAM, AND C. GUENTHER, *Applying uncertainty quantification to multiphase flow computational fluid dynamics*, Powder technology, 242 (2013), pp. 27–39.
- [55] M. B. GILES, M. C. DUTA, J.-D. M-UACUTE, AND N. A. PIERCE, *Algorithm developments for discrete adjoint methods*, AIAA Journal, 41 (2003), pp. 198–205.
- [56] M. B. GILES AND N. A. PIERCE, *An introduction to the adjoint approach to design*, Flow, Turbulence and Combustion, 65 (2000), pp. 393–415.
- [57] A. GNANASKANDAN AND K. MAHESH, *A numerical method to simulate turbulent cavitating flows*, International Journal of Multiphase Flow, 70 (2015), pp. 22–34.
- [58] E. GONCALVES, M. CHAMPAGNAC, AND R. FORTES PATELLA, *Comparison of numerical solvers for cavitating flows*, International Journal of Computational Fluid Dynamics, 24 (2010), pp. 201–216.

- [59] N. J. GORDON, D. J. SALMOND, AND A. F. SMITH, *Novel approach to nonlinear/non-Gaussian Bayesian state estimation*, in IEE proceedings F (radar and signal processing), vol. 140, IET, 1993, pp. 107–113.
- [60] M. S. GRITSKEVICH, A. V. GARBARUK, J. SCHÜTZE, AND F. R. MENTER, *Development of DDES and IDDES formulations for the  $k$ - $\omega$  shear stress transport model*, Flow, Turbulence and Combustion, 88 (2012), pp. 431–449.
- [61] A. GRONSKIS, D. HEITZ, AND E. MÉMIN, *Inflow and initial conditions for direct numerical simulation based on adjoint data assimilation*, Journal of Computational Physics, 242 (2013), pp. 480–497.
- [62] Y. GU, D. S. OLIVER, ET AL., *An iterative ensemble Kalman filter for multiphase fluid flow data assimilation*, Spe Journal, 12 (2007), pp. 438–446.
- [63] W. W. HAGER, *Updating the inverse of a matrix*, SIAM Review, 31 (1989), pp. 221–239.
- [64] T. M. HAMILL AND C. SNYDER, *A hybrid ensemble Kalman filter–3D variational analysis scheme*, Monthly Weather Review, 128 (2000), pp. 2905–2919.
- [65] T. M. HAMILL, J. S. WHITAKER, AND C. SNYDER, *Distance-dependent filtering of background error covariance estimates in an ensemble Kalman filter*, Monthly Weather Review, 129 (2001), pp. 2776–2790.
- [66] Y. HE AND D. XIU, *Numerical strategy for model correction using physical constraints*, Journal of Computational Physics, 313 (2016), pp. 617–634.
- [67] S. HOSDER, R. WALTERS, AND R. PEREZ, *A non-intrusive polynomial chaos method for uncertainty propagation in cfd simulations*, in 44th AIAA aerospace sciences meeting and exhibit, 2006, p. 891.
- [68] P. L. HOUTEKAMER AND H. L. MITCHELL, *A sequential ensemble Kalman filter for atmospheric data assimilation*, Monthly Weather Review, 129 (2001), pp. 123–137.
- [69] B. HUANG, Y. ZHAO, AND G. WANG, *Large eddy simulation of turbulent vortex-cavitation interactions in transient sheet/cloud cavitating flows*, Computers & Fluids, 92 (2014), pp. 113–124.
- [70] X.-Y. HUANG, Q. XIAO, D. M. BARKER, X. ZHANG, J. MICHALAKES, W. HUANG, T. HENDERSON, J. BRAY, Y. CHEN, Z. MA, ET AL., *Four-dimensional variational data assimilation for WRF: Formulation and preliminary results*, Monthly Weather Review, 137 (2009), pp. 299–314.
- [71] M. A. IGLESIAS, K. J. LAW, AND A. M. STUART, *Ensemble Kalman methods for inverse problems*, Inverse Problems, 29 (2013), p. 045001.

- [72] T. JANJIC, D. McLAUGHLIN, S. E. COHN, AND M. VERLAAN, *Conservation of mass and preservation of positivity with ensemble-type Kalman filter algorithms*, Monthly Weather Review, 142 (2014), pp. 755–773.
- [73] A. JESUS, J. L. AZEVEDO, AND J.-P. LAVAL, *Large eddy simulations and RANS computations of adverse pressure gradient flows*, in 51st AIAA Aerospace Sciences Meeting including the New Horizons Forum and Aerospace Exposition, 2013, p. 267.
- [74] B. JI, X. LUO, R. E. ARNDT, X. PENG, AND Y. WU, *Large eddy simulation and theoretical investigations of the transient cavitating vortical flow structure around a NACA66 hydrofoil*, International Journal of Multiphase Flow, 68 (2015), pp. 121–134.
- [75] B. JI, X. LUO, R. E. ARNDT, AND Y. WU, *Numerical simulation of three dimensional cavitation shedding dynamics with special emphasis on cavitation–vortex interaction*, Ocean Engineering, 87 (2014), pp. 64–77.
- [76] B. JI, X.-W. LUO, X.-X. PENG, AND Y.-L. WU, *Three-dimensional large eddy simulation and vorticity analysis of unsteady cavitating flow around a twisted hydrofoil*, Journal of Hydrodynamics, 25 (2013), pp. 510–519.
- [77] W. JONES AND B. E. LAUNDER, *The prediction of laminarization with a two-equation model of turbulence*, International Journal of Heat and Mass Transfer, 15 (1972), pp. 301–314.
- [78] R. E. KALMAN, *A new approach to linear filtering and prediction problems*, Journal of basic Engineering, 82 (1960), pp. 35–45.
- [79] H. KATO AND S. OBAYASHI, *Approach for uncertainty of turbulence modeling based on data assimilation technique*, Computers & Fluids, 85 (2013), pp. 2–7.
- [80] H. KATO, A. YOSHIZAWA, G. UENO, AND S. OBAYASHI, *A data assimilation methodology for reconstructing turbulent flows around aircraft*, Journal of Computational Physics, 283 (2015), pp. 559–581.
- [81] M. C. KENNEDY AND A. O’HAGAN, *Bayesian calibration of computer models*, Journal of the Royal Statistical Society: Series B (Statistical Methodology), 63 (2001), pp. 425–464.
- [82] I. KHLIFA, A. VABRE, M. HOČEVAR, K. FEZZAA, S. FUZIER, O. ROUSSETTE, AND O. COUTIER-DELGOSHA, *Fast X-ray imaging of cavitating flows*, Experiments in Fluids, 58 (2017), p. 157.
- [83] O. KNIO AND O. LE MAITRE, *Uncertainty propagation in CFD using polynomial chaos decomposition*, Fluid dynamics research, 38 (2006), p. 616.

- [84] P. KOUKOUVINIS, H. NASERI, AND M. GAVAISES, *Performance of turbulence and cavitation models in prediction of incipient and developed cavitation*, International Journal of Engine Research, 18 (2017), pp. 333–350.
- [85] L. KUBAN, J.-P. LAVAL, W. ELSNER, A. TYLISZCZAK, AND M. MARQUILLIE, *Les modeling of converging-diverging turbulent channel flow*, Journal of Turbulence, (2012), p. N11.
- [86] A. KUBOTA, H. KATO, AND H. YAMAGUCHI, *A new modelling of cavitating flows: a numerical study of unsteady cavitation on a hydrofoil section*, Journal of fluid Mechanics, 240 (1992), pp. 59–96.
- [87] R. F. KUNZ, D. A. BOGER, D. R. STINEBRING, T. S. CHYCZEWSKI, J. W. LINDAU, H. J. GIBELING, S. VENKATESWARAN, AND T. GOVINDAN, *A preconditioned Navier–Stokes method for two-phase flows with application to cavitation prediction*, Computers & Fluids, 29 (2000), pp. 849–875.
- [88] J.-P. LAVAL, C. BRAUD, G. FOURNIER, AND M. STANISLAS, *Large-eddy simulations of control of a separated flow over a 2D bump by means of pulsed jets*, Journal of Turbulence, (2010), p. N52.
- [89] D. H. LE, A. A. EMERICK, A. C. REYNOLDS, ET AL., *An adaptive ensemble smoother with multiple data assimilation for assisted history matching*, Spe Journal, 21 (2016), pp. 2–195.
- [90] K. H. LEE, L. CORTELEZZI, J. KIM, AND J. SPEYER, *Application of reduced-order controller to turbulent flows for drag reduction*, Physics of Fluids, 13 (2001), pp. 1321–1330.
- [91] J.-B. LEROUX, O. COUTIER-DELGOSHA, AND J. A. ASTOLFI, *A joint experimental and numerical study of mechanisms associated to instability of partial cavitation on two-dimensional hydrofoil*, Physics of fluids, 17 (2005), p. 052101.
- [92] H. LI, E. KALNAY, AND T. MIYOSHI, *Simultaneous estimation of covariance inflation and observation errors within an ensemble Kalman filter*, Quarterly Journal of the Royal Meteorological Society: A journal of the atmospheric sciences, applied meteorology and physical oceanography, 135 (2009), pp. 523–533.
- [93] T. LI, S. SUN, T. P. SATTAR, AND J. M. CORCHADO, *Fight sample degeneracy and impoverishment in particle filters: A review of intelligent approaches*, Expert Systems With Applications, 41 (2014), pp. 3944–3954.



- [94] C. LIU, Q. XIAO, AND B. WANG, *An ensemble-based four-dimensional variational data assimilation scheme. Part I: Technical formulation and preliminary test*, Monthly Weather Review, 136 (2008), pp. 3363–3373.
- [95] X. MA AND N. ZABARAS, *An adaptive hierarchical sparse grid collocation algorithm for the solution of stochastic differential equations*, Journal of Computational Physics, 228 (2009), pp. 3084–3113.
- [96] J. MANDEL, E. BERGOU, S. GÜROL, S. GRATTON, AND I. KASANICKY, *Hybrid Levenberg–Marquardt and weak-constraint ensemble Kalman smoother method*, Nonlinear Processes in Geophysics, 23 (2016), pp. 59–73.
- [97] M. MARQUILLIE, J.-P. LAVAL, AND R. DOLGANOV, *Direct numerical simulation of a separated channel flow with a smooth profile*, Journal of Turbulence, (2008), p. N1.
- [98] L. MATHELIN, M. Y. HUSSAINI, T. A. ZANG, AND F. BATAILLE, *Uncertainty propagation for a turbulent, compressible nozzle flow using stochastic methods*, AIAA journal, 42 (2004), pp. 1669–1676.
- [99] M. MELDI, *Augmented prediction of turbulent flows via sequential estimators*, Flow, Turbulence and Combustion, 101 (2018), pp. 389–412.
- [100] M. MELDI AND A. POUX, *A reduced order model based on Kalman filtering for sequential data assimilation of turbulent flows*, Journal of Computational Physics, 347 (2017), pp. 207–234.
- [101] F. MENTER AND Y. EGOROV, *The scale-adaptive simulation method for unsteady turbulent flow predictions. Part 1: theory and model description*, Flow, Turbulence and Combustion, 85 (2010), pp. 113–138.
- [102] F. R. MENTER, *Two-equation eddy-viscosity turbulence models for engineering applications*, AIAA journal, 32 (1994), pp. 1598–1605.
- [103] F. R. MENTER, M. KUNTZ, AND R. LANGTRY, *Ten years of industrial experience with the SST turbulence model*, Turbulence, heat and mass transfer, 4 (2003), pp. 625–632.
- [104] C. L. MERKLE, *Computational modelling of the dynamics of sheet cavitation*, in Proc. of the 3rd Int. Symp. on Cavitation, Grenoble, France, 1998, 1998.
- [105] P. MITRA, C. MURTHY, AND S. K. PAL, *Unsupervised feature selection using feature similarity*, IEEE transactions on pattern analysis and machine intelligence, 24 (2002), pp. 301–312.

- [106] T. MIYOSHI, *The Gaussian approach to adaptive covariance inflation and its implementation with the local ensemble transform Kalman filter*, Monthly Weather Review, 139 (2011), pp. 1519–1535.
- [107] V. MONS, J.-C. CHASSAING, T. GOMEZ, AND P. SAGAUT, *Reconstruction of unsteady viscous flows using data assimilation schemes*, Journal of Computational Physics, 316 (2016), pp. 255–280.
- [108] H. N. NAJM, *Uncertainty quantification and polynomial chaos techniques in computational fluid dynamics*, Annual review of fluid mechanics, 41 (2009), pp. 35–52.
- [109] E. J. NIELSEN, B. DISKIN, AND N. K. YAMALEEV, *Discrete adjoint-based design optimization of unsteady turbulent flows on dynamic unstructured grids*, AIAA Journal, 48 (2010), pp. 1195–1206.
- [110] T. O’HERN, *An experimental investigation of turbulent shear flow cavitation*, Journal of fluid mechanics, 215 (1990), pp. 365–391.
- [111] D. S. OLIVER AND Y. CHEN, *Recent progress on reservoir history matching: a review*, Computational Geosciences, 15 (2011), pp. 185–221.
- [112] T. A. OLIVER AND R. D. MOSER, *Bayesian uncertainty quantification applied to RANS turbulence models*, Journal of Physics: Conference Series, 318 (2011), p. 042032.
- [113] OPENCFD, *OpenFOAM User Guide*, 2018.  
See also <http://www.opencfd.co.uk/openfoam>.
- [114] S. OSHER, M. BURGER, D. GOLDFARB, J. XU, AND W. YIN, *An iterative regularization method for total variation-based image restoration*, Multiscale Modeling & Simulation, 4 (2005), pp. 460–489.
- [115] E. OTT, B. R. HUNT, I. SZUNYOGH, A. V. ZIMIN, E. J. KOSTELICH, M. CORAZZA, E. KALNAY, D. PATIL, AND J. A. YORKE, *A local ensemble Kalman filter for atmospheric data assimilation*, Tellus A: Dynamic Meteorology and Oceanography, 56 (2004), pp. 415–428.
- [116] D. I. PAPADIMITRIOU AND C. PAPADIMITRIOU, *Bayesian uncertainty quantification of turbulence models based on high-order adjoint*, Computers & Fluids, 120 (2015), pp. 82–97.
- [117] S. PATANKAR, *Numerical heat transfer and fluid flow*, CRC press, 2018.
- [118] S. POROSEVA AND H. BÉZARD, *On ability of standard  $k-\epsilon$  model to simulate aerodynamic turbulent flows*, CFD J, 9 (2001), pp. 464–470.

- 
- [119] J. PRAKASH, S. C. PATWARDHAN, AND S. L. SHAH, *Constrained state estimation using the ensemble Kalman filter*, in 2008 American Control Conference, IEEE, 2008, pp. 3542–3547.
- [120] C. E. RASMUSSEN, *Gaussian processes in machine learning*, in Summer School on Machine Learning, Springer, 2003, pp. 63–71.
- [121] J. RAY, S. LEFANTZI, S. ARUNAJATESAN, AND L. DECHANT, *Bayesian parameter estimation of a  $k$ - $\epsilon$  model for accurate jet-in-crossflow simulations*, AIAA Journal, 54 (2016), pp. 2432–2448.
- [122] ———, *Learning an eddy viscosity model using shrinkage and Bayesian calibration: A jet-in-crossflow case study*, ASCE-ASME Journal of Risk and Uncertainty in Engineering Systems, Part B: Mechanical Engineering, 4 (2018), p. 011001.
- [123] J.-L. REBOUD, B. STUTZ, AND O. COUTIER-DELGOSHA, *Two phase flow structure of cavitation: experiment and modeling of unsteady effects*, in 3rd International Symposium on Cavitation CAV, vol. 26, 1998.
- [124] E. D. N. RUIZ AND A. SANDU, *A derivative-free trust region framework for variational data assimilation*, Journal of Computational and Applied Mathematics, 293 (2016), pp. 164–179.
- [125] P. SAKOV, G. EVENSEN, AND L. BERTINO, *Asynchronous data assimilation with the EnKF*, Tellus A: Dynamic Meteorology and Oceanography, 62 (2010), pp. 24–29.
- [126] P. SAKOV, D. S. OLIVER, AND L. BERTINO, *An iterative EnKF for strongly nonlinear systems*, Monthly Weather Review, 140 (2012), pp. 1988–2004.
- [127] C. SARRAF, Y. AIT BOUZAD, H. DJERIDI, M. FARHAT, F. DENISET, AND J.-Y. BILLARD, *Effect of cavitation on the structure of the boundary layer in the wake of a partial cavity*, tech. rep., 2006.
- [128] J. SAUER AND G. H. SCHNERR, *Unsteady cavitating flow—a new cavitation model based on a modified front capturing method and bubble dynamics*, in Proceedings of 2000 ASME Fluid Engineering Summer Conference, vol. 251, 2000, pp. 1073–1079.
- [129] A. P. SINGH AND K. DURAISAMY, *Using field inversion to quantify functional errors in turbulence closures*, Physics of Fluids, 28 (2016), p. 045110.
- [130] A. P. SINGH, S. MEDIDA, AND K. DURAISAMY, *Machine-learning-augmented predictive modeling of turbulent separated flows over airfoils*, AIAA Journal, (2017), pp. 2215–2227.

- [131] A. K. SINGHAL, M. M. ATHAVALE, H. LI, AND Y. JIANG, *Mathematical basis and validation of the full cavitation model*, Journal of fluids engineering, 124 (2002), pp. 617–624.
- [132] P. R. SPALART, *Detached-eddy simulation*, Annual review of fluid mechanics, 41 (2009), pp. 181–202.
- [133] P. R. SPALART AND S. R. ALLMARAS, *A one-equation turbulence model for aerodynamic flows.*, AIAA Paper, (1992), pp. 1992–439.
- [134] S. SYMON, N. DOVETTA, B. J. MCKEON, D. SIPP, AND P. J. SCHMID, *Data assimilation of mean velocity from 2D PIV measurements of flow over an idealized airfoil*, Experiments in fluids, 58 (2017), p. 61.
- [135] M. TOWARA AND U. NAUMANN, *A discrete adjoint model for OpenFOAM*, Procedia Computer Science, 18 (2013), pp. 429–438.
- [136] Y. TRÉMOLET, *Incremental 4D-Var convergence study*, Tellus A: Dynamic Meteorology and Oceanography, 59 (2007), pp. 706–718.
- [137] J. A. VRUGT, *Markov chain Monte Carlo simulation using the DREAM software package: Theory, concepts, and MATLAB implementation*, Environmental Modelling & Software, 75 (2016), pp. 273–316.
- [138] D. WANG, Y. CHEN, AND X. CAI, *State and parameter estimation of hydrologic models using the constrained ensemble Kalman filter*, Water Resources Research, 45 (2009).
- [139] Y. WANG, C. HUANG, X. FANG, X. YU, X. WU, AND T. DU, *Cloud cavitating flow over a submerged axisymmetric projectile and comparison between two-dimensional RANS and three-dimensional large-eddy simulation methods*, Journal of Fluids Engineering, 138 (2016), p. 061102.
- [140] G. WELCH, G. BISHOP, ET AL., *An introduction to the Kalman filter*, (1995).
- [141] D. C. WILCOX, *Turbulence Modeling for CFD*, DCW Industries, 3 ed., 2006.
- [142] D. C. WILCOX ET AL., *Turbulence modeling for CFD*, vol. 2, DCW industries La Canada, CA, 1998.
- [143] F. D. WITHERDEN AND A. JAMESON, *Future directions in computational fluid dynamics*, in 23rd AIAA Computational Fluid Dynamics Conference, 2017, p. 3791.
- [144] J. WU, J.-X. WANG, AND S. C. SHADDEN, *Adding constraints to Bayesian inverse problems*, in Proceedings of the AAAI Conference on Artificial Intelligence, vol. 33, 2019, pp. 1666–1673.

- 
- [145] J. WU, H. XIAO, R. SUN, AND Q. WANG, *Reynolds-averaged Navier–Stokes equations with explicit data-driven Reynolds stress closure can be ill-conditioned*, Journal of Fluid Mechanics, 869 (2019), pp. 553–586.
- [146] X. WU, *Inflow turbulence generation methods*, Annual Review of Fluid Mechanics, 49 (2017), pp. 23–49.
- [147] H. XIAO AND P. CINNELLA, *Quantification of model uncertainty in RANS simulations: a review*, Progress in Aerospace Sciences, (2019).
- [148] H. XIAO, J.-L. WU, J.-X. WANG, R. SUN, AND C. ROY, *Quantifying and reducing model-form uncertainties in Reynolds-averaged Navier–Stokes simulations: A data-driven, physics-informed Bayesian approach*, Journal of Computational Physics, 324 (2016), pp. 115–136.
- [149] J. Y. DELANNOY, *Two phase flow approach in unsteady cavitation modelling*, in Proceedings of the Spring Meeting of the Fluids Engineering Division, 1990.
- [150] Y. YANG, C. ROBINSON, D. HEITZ, AND E. MÉMIN, *Enhanced ensemble-based 4DVar scheme for data assimilation*, Computers & Fluids, 115 (2015), pp. 201–210.
- [151] F. ZHANG, M. ZHANG, AND J. A. HANSEN, *Coupling ensemble Kalman filter with four-dimensional variational data assimilation*, Advances in Atmospheric Sciences, 26 (2009), pp. 1–8.
- [152] J. ZHANG AND S. FU, *An efficient Bayesian uncertainty quantification approach with application to  $k$ - $\omega$ - $\gamma$  transition modeling*, Computers & Fluids, 161 (2018), pp. 211–224.
- [153] X. ZHANG, T. GOMEZ, AND O. COUTIER-DELGOSHA, *Bayesian optimisation of RANS simulation with ensemble-based variational method in convergent-divergent channel*, Journal of Turbulence, (2019), pp. 1–26.
- [154] X. ZHANG, C. MICHELÉN-STRÖFER, H. XIAO, AND O. COUTIER-DELGOSHA, *Code and examples for regularized EnKF*.  
[https://github.com/XinleiZhang/REnKF\\_parameter\\_estimation](https://github.com/XinleiZhang/REnKF_parameter_estimation).
- [155] L. ZHOU AND Z. WANG, *Numerical simulation of cavitation around a hydrofoil and evaluation of a RNG  $\kappa$ - $\varepsilon$  model*, Journal of Fluids Engineering, 130 (2008), p. 011302.
- [156] J. ZHU, *A low-diffusive and oscillation-free convection scheme*, Communications in applied numerical methods, 7 (1991), pp. 225–232.
- [157] A. ŽNIDARČIČ AND O. COUTIER-DELGOSHA, *New algorithm for fast DNS simulations of cavitating flows using homogeneous mixture approach*, 2016.

## BIBLIOGRAPHY

---

- [158] D. ZUPANSKI, *A general weak constraint applicable to operational 4DVAR data assimilation systems*, Monthly Weather Review, 125 (1997), pp. 2274–2292.

## Optimisation de la Modélisation RANS des Écoulements Cavitants

**RESUME :** Des écoulements cavitants turbulents se produisent dans de nombreuses applications pratiques telles que les pompes et les propulseurs navals. Dans ces dispositifs, l'implosion des bulles de cavitation combinée à des instabilités à différentes échelles engendrent des effets nuisibles majeurs comme des fluctuations du débit, du bruit, des vibrations et de l'érosion. Il est donc essentiel de prédire correctement ces instabilités, afin de réduire leurs conséquences. Pour simuler les écoulements cavitants turbulents, l'approche la plus couramment utilisée est « Reynolds Averaged Navier-Stokes » (RANS) couplée à des modèles de cavitation homogènes, en raison du faible coût de calcul. Cependant, il est généralement admis que les modèles RANS ne sont pas précis pour les écoulements caractérisés par des gradients de pression adverses conduisant à des séparations et des recirculations. Cette limitation conduit à la mauvaise prédiction des interactions entre la cavitation et la turbulence. Par conséquent, il est nécessaire de quantifier et de réduire les incertitudes dans les modèles RANS, pour améliorer les performances prédictives, soit par une approche empirique, soit par des méthodes d'assimilation de données (DA). Dans cette thèse, nous étudions les performances de différentes méthodes pour des écoulements turbulents dans le but final de les appliquer aux écoulements cavitants. Plus précisément, une méthode hybride variationnelle d'ensemble est appliquée pour reconstruire le champ d'écoulement dans un canal convergent-divergent, en déduisant une vitesse optimale d'entrée et des corrections de modèle à partir de données d'observation. En outre, nous avons proposé une méthode de Kalman d'ensemble régularisée, capable d'appliquer des contraintes de régularisation pour des problèmes inverses mal posés. En outre, diverses méthodes d'assimilation d'ensembles sont évaluées pour la quantification de l'incertitude dans les applications CFD. Enfin, une nouvelle modification empirique de la viscosité turbulente est proposée pour les écoulements cavitants sur la base de mesures expérimentales.

**Mots clés :** Cavitation, Optimisation, RANS, CFD, Assimilation de données

## Optimization of RANS Modelling of Cavitating Flows

**ABSTRACT:** Turbulent cavitating flows occur in many engineering practical applications such as pumps and propellers. In these devices, the collapse of the cavitation bubbles combines with instabilities at multiple scales produce major detrimental effects like flow rate fluctuations, noise, vibrations, and erosion. It is thus essential to accurately predict the behavior of unsteady cavitation, thereby reducing their consequences for the machinery. To simulate the turbulent cavitating flows, the most commonly used approach is still the Reynolds-averaged Navier-Stokes (RANS) method coupled with homogeneous cavitation models, due to its computational tractability. However, it is a consensus that the RANS models are not accurate for the complex flows in the presence of adverse pressure gradients leading to flow separation and recirculation. This limitation leads to the poor prediction on the interactions between cavitation and turbulence in cavitating flows. Hence, it is necessary to quantify and reduce the uncertainties in the RANS model and thus improve the predictive performance, either with an empirical approach or data assimilation (DA) methods. In this thesis, we investigate the applicability of such methods for turbulent flows with the objective of introducing the data-driven method into cavitating flows. Specifically, we first apply the hybrid DA method, ensemble based variational method, to reconstruct the flow field in convergent-divergent channel, through inferring optimal inlet velocity and model corrections from observation data. Further, we proposed a regularized ensemble Kalman method capable of enforcing the regularization constraints for ill-posed inverse problems. Also, various ensemble-based DA methods are evaluated for uncertainty quantification in CFD applications. Finally, a new empirical modification of the turbulent viscosity is proposed for cavitating flows based on experimental measurements.

**Keywords :** Cavitation, Optimization, RANS, CFD, Data assimilation

